Doppler ultrasound tracking instrument for monitoring blood flow

Marco Antônio von Krüger

Thesis submitted for the degree of
Doctor of Philosophy

from
the Division of Medical Physics, Faculty of Medicine
University of Leicester

October 2000

The work on which this thesis is based is my own independent work except where acknowledged

Marco Antônio von Krüger
October 2000

Doppler ultrasound tracking instrument for monitoring blood flow

Marco Antônio von Krüger

Abstract

There are situations, during surgery, in the immediate post-operative period, and in neonatal and adult intensive care units, where monitoring the blood supply to a certain organ or region of the body could be of great value. Doppler ultrasound has great potential for monitoring blood flow velocity because it is a reliable, noninvasive method and produces results in real time. In addition, the development of Doppler technology associated with the recent progress of electronics and computerization has widened the range of information that can be extracted from the Doppler signal. Despite its great potential, there are difficulties which prevent the establishment of blood flow monitoring as a valuable clinical tool. Amongst these difficulties the one which appears to be the most important is the problem of fixing the transducer to the patient in order to prevent misalignment between ultrasound beam and vessel caused by patient movement. A Doppler tracking instrument which is able to adjust its beam direction automatically to ensure correct alignment between the beam and vessel would be valuable in overcoming this difficulty. The work described in this thesis led to the design, construction, and testing of hardware and software for such an instrument, which consists of a feedback controlled phased array transceiver, driving a one dimension array continuous wave Doppler transducer. With its operation it was possible to demonstrate the principle of Doppler tracking, which can open a wide area of monitoring to clinical ultrasound. From the construction point of view, this equipment was useful in identifying some guide lines to be followed in order to turn it into a device which can be used as a clinical tool.

Acknowledgments

I would like to acknowledge:
Prof. David H. Evans for his supervision, friendship, continuous support and for sharing with me his dream of an 'intelligent' Doppler transducer as a step towards the establishment of blood flow monitoring, and for entrusting to me part of its realisation.
Graham Aucott for his fundamental contribution to this project with the conception of the DUPAT and to David Heaton for its professional construction.
Mike Squires and John Brooks for applying their mechanical craftsmanship in support of this work; especially for the help in the effort to push forward the limits of miniaturization and precision of the array transducer.
Lingke Fan for adapting the software of the DSP 32C board analyzer to suit the requirements of the feedback loop.
John Gittins for his work in upgrading the Beam Plotting Tank hardware and software and the adaptation of its acquisition programs for other tests.
David Simpson for his invaluable and continuous guidance on the Matlab environment and for his assistance in the optimization of the programs.
Stephanie Deverson for her lasting companionship and help with the preparation of blood mimicking fluid.
Paul Handley and Jamie Dicks for sharing with me their experience of HP-VEE programming.
Daniel Rose for his help in plotting the acoustic fields.
Ronney Panerai for his constant support in almost all aspects of my life in Leicester and for his suggestions on the writing of this thesis.
Fernando S. Schlindwein for many explanations and for suggestions on the writing of this thesis
Steve Bentley and Harry Hall for their help in the acquisition of materials employed in this work and for their continuous assistance with my laboratory needs.
Glen Bush for his smooth management of the lost and forever missed Medical Physics Network, and for his help in the harsh new times of the dynasty of Royal 4, Royal 7 and Royal 9.
Tina Craig and Lea Bickerdike for the secretarial work related to this thesis.
Ali, Fatima, Rehana, Dominique, Emma and Lorna for their daily companionship and friendship.
The Department of Medical Physics as a whole for the general comprehensive support I have received here. To be member of staff in this Department has been a pleasure and a privilege.
Programa de Engenharia Biomédica da COPPE /UFRJ for their patience and particularly Wagner C. A. Pereira and Tereza F. Nobre for representing me during my absence.
My wife Wanda, for her solidarity, inspiration and for enduring my long absence from home in order to finish this thesis, with such courage and serenity.
My son Rodrigo and my daughter Cristina for their companionship in this pursuit which is older than their years and for understanding so many sacrifices in name of its finishing.
My parents Lourdes and Walter for their ever present confidence, support and assistance.
Friends and family for the enjoyment of their supporting presence, either virtual or in person.
Fundação Coordenação de Aperfeiçoamento de Pessoal de Nível Superior - Capes for providing my air tickets.
Our Lady of Aparecida (saint patron of Brazil) for helping me to overcome the last obstacle towards the end of this thesis: myself.

Doppler ultrasound tracking instrument for monitoring blood flow

List of symbols and abbreviations

Symbols

α	intensity attenuation coefficient, or phase difference between two electrical signals
β	phase difference (function of the geometry only) between two acoustic waves with the same frequency meeting at a point P
ϑ	angle between incident wave and scattered wave
θ	angle between the axis of the acoustic field and any azimuth direction ('in plane')
ψ	angle between the axis of the acoustic field and any elevation direction ('out of plane')
γ	angle of the sinc function representing the effect of diffraction in the acoustic field generated by a finite source
ω	angular velocity
ν	absorption coefficient
κ	compressibility
ρ	density
φ	Doppler angle, or derating factor
ε	permitivity of a piezoelectric material
ϕ	phase difference between two acoustic waves with the same frequency meeting at a point P
δ	phase of an acoustic wave expressed in fractions of a wavelength
λ	wavelength
γ_ρ	mean density factor of a scattering region
γ_k	mean compressibility factor of a scattering region
A	amplitude of the acoustic field from a point source
A_1	amplitude of the acoustic field resultant of one element of an array of line sources
A_n	amplitude of the acoustic field resultant from a generic point in a line source
A_P	amplitude of the acoustic field at a generic point P
A_{Pl}	amplitude of the acoustic field at the point P resulting from a line source of length l
A_R	amplitude of the acoustic field resulting from contributions of two or more sources
c	velocity of wave propagation
D	displacement current
d	distance between two acoustic sources, or the pitch of an array, or the piezoelectric charge coefficient, or the transmitting coefficient (4.1, 4.7, 4.8)
$D(\theta)$	function describing of the amplitude profile of the diffracted acoustic field as a function of the azimuth angle
$D(\psi)$	function describing of the amplitude profile of the diffracted acoustic field as a function of the elevation angle
ds	distance along the lateral movement executed by the transducer during the SDS and DDS tests
E	electric field
e	piezoelectric constant (4.3)
f	frequency

f_c	central frequency
f_d	Doppler frequency
$fmax$	maximum frequency of the Doppler signal corresponding to maximum particle velocity
f_p	parallel resonant frequency of piezoelectric material
f_r	received frequency (RF)
f_s	series resonant frequency of piezoelectric material
f_t	transmitted frequency (RF)
g	piezoelectric voltage coefficient, or receiving coefficient (4.2, 4.8)
h	piezoelectric constant (4.4)
I	intensity
ID	signal to noise ratio index
I_P	intensity of the acoustic field at a generic point P
I_R	intensity of the acoustic field resulting from the contribution of two or more sources
I_{RD}	intensity of the acoustic field resulting from the contribution of two or more line sources taking into account the effect of the diffraction
I_{RDP}	intensity of the acoustic field resulting from the contribution of two or more line sources taking into account the effect of projection and diffraction
I_{RP}	intensity of the acoustic field resulting from the contribution of two or more line sources taking into account the effect of projection
IWM	intensity weighted mean
K	bulk modulus
k	wave number or coupling coefficient (4.11)
m	the sequence of integers
M_0	zeroth moment (TP)
M_1	first moment
MI	mechanical index
N	number point sources, or mean value of scatterers per unit volume (1.8)
N_e	number of elements of an array
p	excess pressure caused by the acoustic wave
$P(\theta)$	function describing of the amplitude profile of the projected acoustic field as a function of azimuth angle
$P(\psi)$	function describing of the amplitude profile of the projected acoustic field as a function of elevation angle
$P(f)$	power spectrum
q_1	arbitrary multiplication factor to adjust the threshold level of the signal/noise detection
q_2	arbitrary multiplication factor to adjust the sensitivity of the signal/noise index
s	elastic compliance
S	strain
T	period of a wave, or stress (4.3, 4.4, 4.7, 4.8)
t	time interval
TAV_{30}	period averaged over thirty consecutive cycles
TI	Thermal index
TIB	Thermal index - bone
TIC	Thermal index - cranial
TIS	Thermal index - soft tissues

TP	total power signal
TPcdB	total power conditioned signal in dB scale
TPr	total power raw signal
TR	threshold value to classify signal to noise ratio index
*T*SDT$_3$	standard deviation of period calculated over three consecutive cycles
t_w	time interval of a Doppler signal which corresponds to a single spectrum in the sonogram
U_e	total applied electrical energy
U_{ED}	dielectric energy
U_{e-m}	the electrical energy converted to mechanical energy
U_M	mutual energy
U_m	total applied mechanical energy
U_{m-e}	the mechanical energy converted to electrical energy
U_{ST}	elastic energy
V	volume
W	time averaged output power
w	width of the array element
x	distance
Z	impedance

Abbreviations

ALARA	As Low As Reasonably Achievable
BMF	Blood Mimicking Fluid
BPT	Beam Plotting Tank
CW	Continuous Wave
DACB	Data Acquisition and Control Board
DDS	Dynamic Doppler Steering test
DSP	Digital Signal Processor
DUPAT	Doppler Ultrasound Phased Array Transceiver
PCB	Printed Circuit Board
PRF	Pulse Repetition Frequency
PW	Pulsed Wave
RF	Radio Frequency
SDS	Static Doppler Steering test

Chapter 1

Introduction

1.1 Introduction

Doppler ultrasound is a technique for non-invasively measuring blood flow velocity in the human body. Since the introduction of the technique in the late 1950s and 1960s (Satomura 1959, Franklin et al 1961, 1963, McLeod 1967, Wells 1969) it has gained widespread clinical acceptance, and is now routinely incorporated into many diagnostic ultrasound examinations.

Currently the technique is usually used to make short-term measurements of blood flow and blood flow velocity, however since the method is non-invasive it has potential applications in the long term monitoring of changes in blood flow, and reports have appeared in the literature describing a number of possible applications (Greisen et al 1984, Rabe et al 1990, Thrush and Evans 1990, Fenton et al 1990, Anthony et al 1991, Coughtrey et al 1992, Holestrom-Westas et al 1992, Brennan et al 1991, 1992, Larsen et al 1994, Kofke 1999).

Long term monitoring of many physiological parameters (e.g. temperature, blood pressure, ECG and respiration) are vital in many intensive care situations where they give important information about the patient's clinical status, and can give warning of potentially hazardous changes. Monitoring can also be of great utility for observing the response to drugs and other interventions in research applications.

There are however situations, during surgery, in the immediate post-operative period, and in neonatal and adult intensive care units, where monitoring the blood supply to a certain organ or region of the body could be of great value.[1] Blood flow measurement is more challenging than the measurement of many other physiological parameters and several different techniques have been employed, for example fluorescein dye infusion, hydrogen clearance, ^{133}xenon, thermal diffusion, microvascular Doppler ultrasonography, and noninvasive Doppler ultrasonography (Evans et al 1989a, 1989e, Thrush and Evans 1990, Brennan et al 1992, Kofke 1999).

---

[1] *Monitoring cerebral blood flow (CBF) in the immediate pre-operative period (according to Kofke "often the most physiologically stressing period during an operative procedure") the anesthetist can observe the effect of anaesthetics and intubation maneuvers on CBF. Monitoring CBF during surgery permits the observation of the repercussions on cerebral perfusion of drugs and anaesthetics, operative procedures, important cardiac events like fibrillation and arrhythmias, variations in the blood pressure, and increases in intracranial pressure (ICP). It also permits the detection of air and particulate embolism. During the post operative period monitoring CBF gives information about the recovery from anaesthesia which actually starts during the surgical procedures; it can also be used in the detection of embolism and in general to provide information about cerebral perfusion during the recovery period. (Kofke 1999, Hennerici and Meairs al 1999). Cerebral blood flow (CBF) monitoring of neonates can help to detect acute events resulting from ventilatory and pharmacological manipulation. It can also detect clinical deterioration and important changes correlated with the development of ischaemia or cerebral haemorrhage (Evans et al 1989a, Fenton et at 1990, Rabe et al 1990, Anthony et al 1991, Coughtrey et al 1992). Graft monitoring can provide early detection of failing grafts, studying the effects of postoperative procedures and pharmacological interventions. (Dahnoun et al 1990, Thrush and Evans 1990, Brennan et al 1990, Brennan et al 1992).*

Amongst these techniques, noninvasive Doppler monitoring appears to be the most promising. However even this method presents difficulties, and the most significant appears to be the problem of fixing the ultrasound transducer/beam so as to provide continuous high quality signals irrespective of patient movement (Fenton et al 1990, Michel et al 1993, Kofke 1999). The problem of maintaining a fixed alignment between transducer and vessel arises from the way the transducer is usually held in position, i.e: attached to the patient's skin, which is inherently soft, flexible and movable, and consequently unable to provide a rigid and still support. As a result the transducer can be easily displaced and, if subject to any external force, may move so as to lose correct alignment with the vessel.

Several attempts of minimizing the transducer movement to maintain a fixed alignment between transducer and vessel have been adopted, with variable degree of success. They range from adhesive tapes and bandages to more elaborate flexible fixtures embracing larger portions of the body contour. The literature on transcranial Doppler applications is particularly rich in examples (Anthony et al 1991, Bode 1991, Saliba et al 1991a-1991b, Michel et al 1993, Kofke 1999) and there are also reports in the case of lower limb vein graft monitoring (Thrush and Evans 1990).

A more attractive approach would be to design a transducer which would change the ultrasound beam direction so as to track the position of a blood vessel as small relative movements between the body and transducer occur. The purpose of the work described in this thesis was to explore the possibility of constructing a continuous wave Doppler ultrasound system that will continuously adjust the ultrasound beam so as to maintain an optimal Doppler signal.

Such a system will be feedback controlled. It will consist of: a steereable Doppler traducer, the electronics to drive it, and a feedback loop capable of controlling the beam direction based on the real time analysis of the incoming Doppler signal. It will not necessarily require complex and expensive equipment and can be incorporated in a wide range of machines from the very simple to the very sophisticated.

It is somehow surprising that the idea of a tracking Doppler flow meter has not yet been fully implemented. The necessary technology has been available for some time, and a tracking system could have been evolved using duplex technologies which have been available for almost 20 years. During the last decade medical ultrasound has benefited from tremendous progress in electronics, computerization and transducer technology (Wittingham 1997, Evans and McDicken 2000). There has also been considerable development in the understanding the physical principles of blood flow measurement by Doppler ultrasound, and in the design and improvement of the processing methods required to extract clinical information from the Doppler signal. As a result the aim of producing a system capable of performing the apparently trivial action of a human operator may seem a small step, however it represents an important advance in overcoming a difficulty which appears to be one of the major reasons why monitoring applications have not become firmly established with Doppler ultrasound. The ability to monitor blood flow once established could open up a wide variety of new opportunities.

1.2 Plan of the thesis

This thesis describes the design, construction and testing of a Doppler tracking system which is able to successfully adjust the Doppler transducer beam direction to maintain an adequate Doppler signal when relatively small displacement of the transducer occurs.

This thesis is divided into nine chapters. Chapter one presents the introduction and the basic principles of ultrasound and its application in medicine. Chapter two presents the analysis of the Doppler signal as a function of the alignment between the transducer and blood vessel. Chapter three describes the overall design of the Doppler tracking system to be constructed, taking into account the practical requirements and limitations of a particular application. Chapter four describes the theory of transducer construction with an emphasis on array transducers. Chapter five describes the construction of the transducer employed in the present work. Chapter six describes the electronics developed to process the RF Doppler signal and to drive the transducer steering both on transmission and on reception. Chapter seven describes the feedback loop responsible for the tracking action. Chapter eight presents the tests at each stage of the construction and the test of the whole system. Chapter nine discusses the results and limitations of the system.

1.3 Ultrasound

1.3.1 Physical principles of ultrasound

The physical principles of waves and ultrasound have been described by many authors (Hueter et al 1955, Kinsler et al 1962, Feynman et al 1963, Wells 1977). What follows is a brief summary of some of the most important concepts which form a basis for developments described later.

Ultrasound is a historical classification of any sound with a frequency above 20 kHz, the frequency considered to be the limit of the hearing capacity of the human. In diagnostic medicine, ultrasound is usually taken to imply frequencies of between around 2 MHz and 20 MHz, although some modern applications use still higher frequencies.

Sound can be described as waves of density fluctuation propagating in a physical medium. Inside the volume where the wave is propagating, the particles[2] compressed in high density regions expand exerting a force on the ones in the neighboring lower density regions, displacing them from their equilibrium position and creating further regions of high density. This dynamic process, starting from the point where the first density difference was created is repeated indefinitely and the energy is transported further and further away, successively exchanging between potential and kinetic forms.

The behavior of the wave both in space and time domains is described by the wave equation:[3]

---

[2] *A particle is defined here as the volume of the medium small enough to be assumed of constant density. (Kinsler and Frey 1962).*

[3] *For the sake of simplicity the wave equation presented here refers to the particular case of a plane wave propagating in one direction, the deformation produced in the medium by the wave is inside the elastic region, which means that there are no ruptures or permanent deformations, and that the propagation velocity is independent of amplitude and frequency (Kinsler and Frey 1962).*

$$\frac{\partial^2 U}{\partial x^2} = \frac{1}{c^2}\frac{\partial^2 U}{\partial t^2} \qquad (1.1)$$

where U represents any parameter of the medium altered by the wave, t is time, x is distance, and c is the velocity of propagation. c links the two sides of the wave equation because velocity relates time and space. c is also a function of the mechanical properties of the medium which are relevant to wave propagation: elastic properties and density which are respectively related to the capacity of the medium to store potential and kinetic energy.

From an acoustic point of view, biological soft tissues behave like liquids, and in a liquid the propagation velocity can be expressed as:

$$c \cong \sqrt{\frac{K}{\rho}} \qquad (1.2)$$

where K is the bulk modulus, (compressibility per unit volume), and ρ is the density of the medium, (mass per unit volume).

In the process of wave propagation, the particles in the region of higher density and higher pressure exert a force, which is a combined effect of inertial and elastic forces on the particles in the adjacent region. This force meets a resistance, which is also a combined consequence of the inertia of the particles and the medium reaction against compression. In a homogeneous medium, in the direction of propagation there will always be a condition of continuous opposition between the acting and reacting forces allowing a complete momentum transfer. The response of the medium to the disturbing action of a propagating wave, is called the impedance given by:

$$Z = \rho c \tag{1.3}$$

Z is a characteristic of a medium and ultimately is a function of density and elasticity. Whenever a wave meets a discontinuity in Z, reflection and refraction take place. In the simplest case, when an ideal plane wave propagating in a medium *1* reaches an infinite plane boundary in a medium *2*, the ratio of the transmitted energy to the incident energy is given by:

$$\frac{I_t}{I_i} = \frac{4Z_2Z_1\cos\theta_i\cos\theta_t}{(Z_2\cos\theta_i + Z_1\cos\theta_t)^2} \tag{1.4}$$

The ratio of the reflected energy to the incident energy is given by:

$$\frac{I_r}{I_i} = \left(\frac{Z_2\cos\theta_i - Z_1\cos\theta_t}{Z_2\cos\theta_i + Z_1\cos\theta_t}\right)^2 \tag{1.5}$$

where I_i, I_t and I_r are the intensity of the incident, transmitted and reflected energies respectively, Z_1 and Z_2 are the impedances of the two media, and θ_i and θ_t are the incidence and transmitted angles respectively.

In the time domain, waves can be classified according to their frequency content; they may present a wide range of shapes, from a sinusoid to a short pulse. The waves relevant to the present work are continuous and almost sinusoidal. From the propagation point of view it is possible to assume they have a single frequency f, a period $T = \frac{1}{f}$ and the wavelength $\lambda = cT$. Whenever a wave is to be employed as a probing tool the wavelength becomes an important factor because smaller wavelengths provide better resolution.

Unfortunately higher frequency also means a higher attenuation and smaller penetration. It is therefore necessary to find a compromise between resolution and penetration, and in the case of biological tissues the size of the internal structures of interest brings this compromise to the low MHz frequency band which is the most useful medical ultrasound range. (Fig. 1.1)

Attenuation of an acoustic wave is a broad concept describing the observed decrease in intensity along its propagation direction as result of absorption, scattering, reflection, refraction, and beam divergence.

In the case of a plane wave in a boundless medium, the attenuation is a function of absorption and scattering and then purely a characteristic of the medium. The Intensity Attenuation Coefficient of a medium for a given frequency can be expressed in dB by the equation:

$$\alpha = \frac{10}{x}\log\left(\frac{I_2}{I_1}\right) \tag{1.6}$$

where α is the intensity attenuation coefficient of the medium, x is the distance between position *1* and *2* along the direction of propagation, and I_1 and I_2 are wave intensity at the positions *1* and *2* respectively

Absorption accounts for acoustical energy conversion to heat and there are many different mechanisms involved. In the case of biological tissues, in the low megahertz range, the relaxation processes at the molecular level are the most significant mechanisms (Hussey 1975, Wells 1977). The absorption coefficient (ν) is dependent on frequency and may be written:

$$\nu \propto f^{e} \tag{1.7}$$

where the exponent e depends on the material. For biological tissues e varies between one and two depending on the tissue.

When the size of the discontinuity is of the order of magnitude or smaller than the wavelength, the ultrasound is said to be scattered. In this case the discontinuities behave like secondary sources of ultrasound which is propagated in all directions. The intensity and the spatial distribution of the scattered energy are complicated functions of compressibility, density, dimension, geometry and distribution of scatterers. The present work is concerned with biological tissues and particularly blood, which can be described as a suspension of cells and particles in plasma, here considered as a homogeneous fluid. The particles having acoustic properties different from the plasma present a scattering cross section to an ultrasonic wave. Amongst these, the erythrocytes are the most significant scatterers because of their relative higher concentration. A simple model to evaluate the relative contribution of the main factors involved in the generation of ultrasound scattering by blood is presented by Morse and Ingard (1968). This model consists in a region $\boldsymbol{R}$ of volume V where a cloud of spherical scatters of radius $\boldsymbol{a}$ much smaller than λ are randomly distributed. The dimensions of $\boldsymbol{R}$ are much larger than λ. The average number of scatters per unit volume inside $\boldsymbol{R}$ is N, the mean distance between scatterers is not larger than λ, the compressibility is κ, the density of the spheres is ρ, and the distance of $\boldsymbol{R}$ from the measurement point $\mathbf{r}$ is also much larger than the dimensions of $\boldsymbol{R}$.

In this model, assuming just simple scattering, the proportionality between the incident acoustic energy I_i and the scattered energy I_{is} generated can be expressed by:

$$I_{is} \propto I_i \left(NV \frac{k_0^4 a^6}{r^2} \left| \gamma_k + \gamma_\rho \cos\vartheta \right|^2 \right) \tag{1.8}$$

where: $k_0 = \omega\sqrt{\rho_0 \kappa_0}$ where ω is the angular velocity, ρ_0 and κ_0 respectively the density and compressibility of the medium between scatterers, **r** is the distance from **R**, γ_κ and γ_ρ are respectively the compressibility and density factors of the scatterers and ϑ is the angle of measurement.

The interference between the scattered waves generated by each scatterer interfere with each other introducing a directionality which will be proportional to

$$\left(\frac{k_R}{k_0}\right)^4 \left(k_R a \sin\frac{1}{2}\vartheta\right)^2 \exp\left(-2k_R^2 a^2 \sin^2\frac{1}{2}\vartheta\right) \tag{1.9}$$

where: $k_R = \omega\sqrt{\rho_R \kappa_R}$ and $\omega = 2\pi f$ is the angular velocity and ρ_R and κ_R respectively the density and compressibility of the scattering region.

For the present work the relevant information to be drawn from this model are:

- The scattering is a function of the fourth power of the frequency.
- Scattering causes part of the energy propagating in the forward direction to be redirected sideways and backwards.

As for any movement, waves must be defined in relation to a reference. We can always consider two reference points when describing a wave, the position of the source and the position of the receiver. When the source and receiver are separated by a fixed distance, the wave frequency at both positions is the same, however when there is a relative movement the frequency at the receiver will be different from the frequency at the source. This phenomena is known as Doppler effect described by the equation (Evans et al 1989):

$$f_d = f_t - f_r = \frac{2 f_t v \cos\theta}{c} \tag{1.10}$$

where: f_d, f_t and f_r are the difference, transmitted and received frequencies respectively, v is the relative velocity between transmitter and receiver, and θ is the angle between the direction of the motion and the ultrasound beam. The higher the transmitted frequency the larger the Doppler shift corresponding to a target velocity and consequently the better the velocity discrimination. The choice of the transmitted frequency is also a compromise between velocity discrimination and attenuation. The relation between f_d, f_t and v is presented in Figure 1.2.

1.3.2 Ultrasound in medicine

Ultrasound can be claimed to be non-invasive since the transducer can be applied to the surface of the body and at diagnostic levels is regarded as producing no harm. Ultrasound is not comparable to ECG, temperature or pressure measurement where the energy detected is generated naturally inside the body. The origin of ultrasound energy is external, it penetrates the body where in fact it always interacts with the tissues. It sets particles in motion, it produces localized pressures, it causes deformations, it can produce cavitation, it can produce micro streaming, and it is partly converted to heat.

More important than the consideration of whether or not a technique is invasive is to define to what extent its interaction leads to modifications in tissues and whether or not such modifications are permanent. The structures of the tissues and molecules are able to support pressures and deformations up to a certain level without suffering any permanent modification. Small temperature rises are also considered innocuous. Ultrasound dosimetry is the study of the methods and techniques for measuring exposure and energy deposition rate. The proposed use of the ultrasound will determine the dose of ultrasound the patient receives.

1.3.2.1 Therapy

The threshold between diagnostic and therapeutic ultrasound is essentially defined as the region in which the energy deposition in tissue starts to became important. In this region and upwards the best understood effect of ultrasound is the energy deposition in the form of heat. Ultrasound can be focused in order to produce localized heat in a region of the body. The focusing can be achieved either by the use of acoustic lenses or by irradiating from different positions. The amount of heat produced can be adjusted in order to produce an improvement of blood circulation and an increase in metabolism which is the rationale for using ultrasound in physiotherapy. In this case either continuous or pulsed wave is employed, the frequency is generally in the range of 0.5 MHz to 3 MHz and the intensity is in the range of 0.05 to 15 W/cm^2.

At even higher dose rates the thermal effects can produce temperature increases that can cause protein denaturation. In addition to the thermal effects ultrasound can produce cavitation and micro streaming which can cause cell rupture. Localized high intensities of ultrasound are used in hyperthermia for treatment of tumors, lithotripsy, the treatment of Meniere's disease, and in ophthalmology and surgery. (Wells 1977, Duck and Martin 1993).

1.3.2.2 Diagnostic

The more important applications of ultrasound in medicine are diagnostic. In diagnosis it is the effect of the medium on the ultrasound wave that is harnessed. In this case the effect of ultrasonic energy in tissue should be kept as low as possible.

The rapid increase of the use of diagnostic ultrasound in medicine is always renewing the discussion about safety levels. Many new applications require longer exposure times and in some applications higher doses are proposed in order to improve the signal to noise ratio. Over the years new studies about dosimetry and safety levels are produced and disseminated in reports, recommendations and norms updating the information in order to keep up with new equipment and applications. (DHSS 1979, AIUM/NEMA 1981, 1992, AIUM 1985-1987, 1991, IEC 1991 a/b/c, NCRP 1983, 1992, FDA 1993). The safety levels are normally defined in terms of intensity and exposure time. For the case of continuous wave, intensity values below 0.1 W/cm^2 are considered safe. (Evans et al 1989b, Duck and Martin 1993).

As the main motivation of the present work is to contribute to the establishment of long term monitoring, and as this is an application where special attention must be paid to patient safety, an appendix on safety is presented at the end of this thesis.

As ultrasound penetrates the tissues, its propagation is characterized by a continuous process of interactions. In addition to the absorption process already discussed the ultrasonic wave is progressively transformed into refracted, reflected and scattered waves which can also be shifted in frequency. Different soft tissues have slightly different impedances as a consequence of their different propagation velocities and densities (Wells 1977, Evans et al 1989). Individual tissues are not completely homogeneous, they present characteristic textures reflected in impedance fluctuation, and in addition tissues can also move. The flow of back-scattered and reflected energy detected by a receiver contains information about the position, characteristics and movements of the tissue along the wave propagation path. This is what makes ultrasound a diagnostic tool.

1.3.2.2.1 Pulse Echo Applications

In pulse echo applications, the same transducer which is used to emit the pulses, acts as a receiver and in the time interval between pulses detects the reflected and backscattered energy. As explained in section 1.2.1, ultrasound propagates in a medium with a characteristic speed for that medium. In soft biological tissues, which have a high percentage of water, this propagation speed is around 1540 m/s.

The simplest pulse echo application, called A-mode, uses only the time interval between the pulse emission and echo, and the back-scattered energy received from the various layers of tissue in the propagation path. This time information, together with the knowledge of the propagation speed in each layer enables the calculation of the thickness of the various layers along the propagation path.

B-mode scans consists of A-mode scans associated with information about the direction of the beam in the scanning plane. The reflected and backscattered signals are used to construct two-dimensional images of the scanning plane depicting large interfaces and tissue micro-structure. If the direction of the beam is known in three dimensions it is possible to reconstruct that image for any plane.

In the case of relative movement between tissue layers it is possible to make a series of A-mode traces from the same direction collected at time intervals adequate to sample the movement. Displaying these traces side by side sequentially generates an image that enables the observation of the relative positions of the layers with time; this is called M-mode imaging.

Common to any ultrasonic imaging system is the question of resolution. The axial resolution depends on the pulse length and consequently on the frequency. The compromise between resolution and attenuation means that most medical applications of ultrasound use frequencies in the range of 2-10 MHz. However, for imaging small parts and in high resolution applications where deep penetration is not required frequencies of up to 100 MHz have been employed (Lockwood et al 1996).

Ultrasound pulse-echo imaging has experienced a long evolution since the early 1950s. Thanks to progress in transducer technology, electronics and computing the same basic physical principles can now be much more efficiently explored. It is beyond the scope of the present work to provide a general view of ultrasound imaging today. Recently, remarkable progress has been achieved in many areas such as: Real time imaging with 1D, 1.5D and 2D array transducers, composite transducers, transducer bandwidth increase, beam forming both for transmission and reception, slice thickness reduction, digital image processing, 3D scanning, ultrasonic computerized tomography, harmonic imaging and visualization of dynamic behaviour of tissue (Wittingham 1997).

1.3.2.2.2 Doppler Applications

The ability of the Doppler technique to detect and measure velocity defines the cardio-vascular area as its natural medical application field. It may be employed to detect heart and arterial wall movements, but the more important application is in the measurement of blood flow. Its most remarkable and attractive feature is the ability to non invasively detect and instantaneously measure blood velocity in a vessel. This may be achieved simply by coupling a transducer to the skin and pointing it towards that vessel.

As for pulse echo, in Doppler applications there is always a transmitter irradiating ultrasound and a receiver detecting the echoes and backscattered energy. In Pulsed Wave Doppler (PW) units the same piezo-electric element performs alternatively transmission and reception functions, while in the case of Continuous Wave (CW) units two elements are required, one for transmitting and another for receiving. The echoes and backscattered energy returning from tissues moving relative to the transducer present the Doppler shift described in equation (1.10), which can be rearranged to enable the calculation of this relative velocity.

$$v = \frac{c f_d}{2 f_i \cos\theta} \tag{1.11}$$

From (1.11), it is clear that the basic information provided by the Doppler shift is the velocity and this is why a Doppler unit is called a velocimeter.

As ultrasound wave propagates through a vessel it is backscattered by the moving scatterers found in the propagation path. In the blood the more important scatters are the erythrocytes with different degrees of rouleau formation. The Doppler shifted signals detected at the receiver represent the sum of the contribution of each scatter with its particular size and velocity.

As a whole this signal contains a range of frequencies. The amplitude of each frequency is proportional to the number of scatterers with a particular velocity. Assuming an average homogeneous distribution of scatterers and a uniformly insonated vessel it is possible to say that the Doppler power spectrum represents the velocity distribution inside the vessel.

CW Doppler units can provide velocity direction information however they are unable to provide range information. This means that they cannot provide information about the position (depth) of the moving targets. In PW Doppler, a burst of sinusoids is emitted and the receiver is gated in such way as to select the signals coming from a particular range of depths. The gate can be adjusted either to sample the entire vessel lumen or a fraction of the flow profile.

Duplex systems combine anatomical information provided by pulse echo imaging with blood flow measurement by Doppler. The operator can see in real time the image of the body section he/she is scanning. It is possible then choose the vessel from which he/she wants to measure the blood flow and steer the Doppler transducer to point to that vessel. The information can be processed either to display a sonogram or to display an image of the velocity superimposed on the pulse echo image as a colour overlay.

1.4 Summary

In this introduction the relevance of blood flow monitoring was presented and in this context, the problems related to the attachment of the transducer to the patient were described. This was followed by an introduction of the proposition of this thesis and a description of its structure. In the second part of the introduction a brief description of the basic principles of ultrasound followed by a general description of its applications in medicine was presented. The following chapters will conform to the structure described in section 1.2.

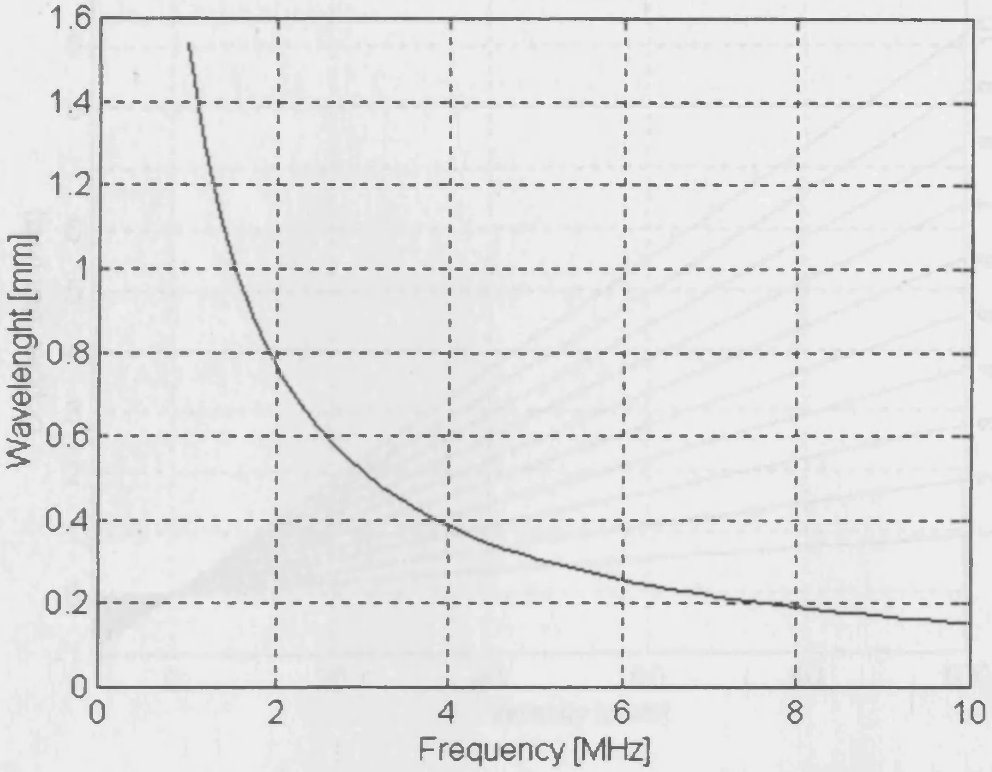

Fig. 1.1 Relationship between frequency and wavelength for a propagation speed of 1540 $m \cdot s^{-1}$ (typical value for biological soft tissues).

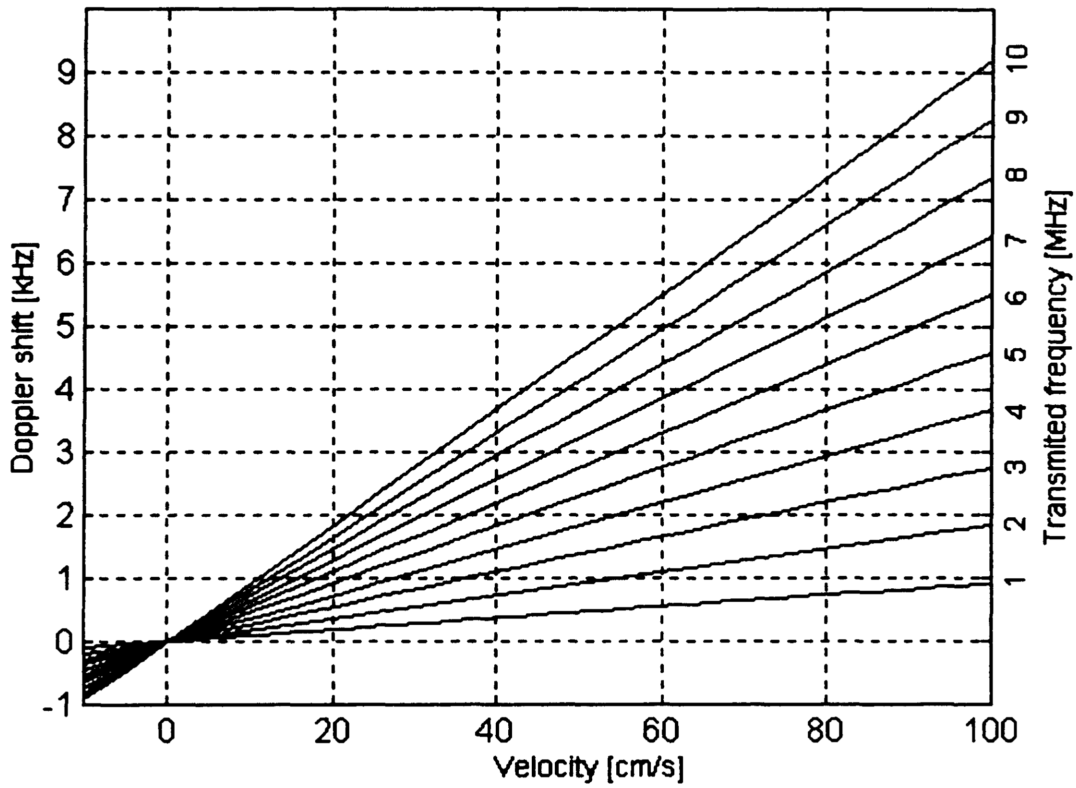

Fig. 1.2 Relationship between transmitted frequency, target velocity and Doppler shift. In the present diagram an incidence angle of 45° and a propagation speed of 1540 $m \cdot s^{-1}$ (typical values for biological soft tissues) are assumed. The range of target velocities shown spans most of the mean blood velocities found in humans.

Chapter 2

The Doppler signal as a function of insonation

2.1 Introduction

An important part of the present project consists of reproducing by computer the action performed by a human operator, who aims to optimise the quality of recording by visual or auditory feedback. This chapter examines the characteristics of the signals which may aid this process.

The first part of the chapter introduces the behaviour of blood as a scattering medium and the dynamic behaviour of arterial blood flow. This is followed by a description of the process of generation of the Doppler signal and its presentation as a sonogram. Then the relationship between alignment and insonation is discussed followed by attempts to search for objective means of defining the idea of quality in terms of alignment between transducer and vessel. Finally the parameters of the sonogram are analysed and discussed from the point of view of expressing the degree of insonation.

2.2 Blood as a scattering medium

Backscattered energy received from blood must come from some sort of inhomogenity. It is known that the most important constituents of blood with regard to ultrasound scattering are the plasma and the erythrocytes (Evans et al 1989c). Both have slightly different densities and compressibilities. Erythrocytes occupy between 36% and 54% of the blood volume and on average this represents more than 50 times the total volume of any of the other particles in blood. Because of their concentrations in blood, erythrocytes tend to aggregate forming larger structures called rouleaux (Shung 1976, Mo and Cobblod 1986, Bascon and Cobblod 1996). The aggregation forces are small compared with the shear stress present in arterial flow and therefore the rouleaux sizes are not stable and fluctuate constantly (Mo and Cobblod, 1986, Wu and Shung 1996, Bascon and Cobblod 1996). Consequently the scattering of ultrasound by blood can be better explained by a model describing blood as a mixture of plasma and rouleaux of different sizes in a dynamic process of reaggregation as a function of the shear stress (Bascon and Cobblod 1996). This model predicts the same behaviour as the one described by Morse and Ingard (1968) in chapter 1 of this thesis, in that scattering is still proportional to the fourth power of frequency (Shung et al 1976).

2.3 Blood flow profile

The flow profile in an artery undergoes periodic changes during the cardiac cycle (McDonald 1974). Additionally, it is also affected by physiological, anatomical, and pathological circumstances (Evans et al 1989d). For example, the blood flow profile changes with peripheral resistance, the proximity of a bifurcation causes asymmetry, while stenoses produce asymmetry and turbulence. The shape of the flow profile is representative of the velocity distribution; and the shear stress is smallest at the centre of the vessel, and increases with the distance from the centre. As already presented the sizes of the rouleaux depend on shear stress which means that the size and concentration of the rouleaux could change during the cardiac cycle under certain flow conditions (Bascon and Cobblod 1996). It is however generally believed that in the absence of turbulence, or very slow flow, the size of the rouleaux, and hence the backscattering cross section of the blood is virtually independent of both spatial and temporal variations (Evans and McDicken 2000).

2.4 Doppler signal

As ultrasound propagates through a vessel it is backscattered by the moving particles found in the propagation path. Because of the random spatial distribution of rouleaux the scattered ultrasound from some parts of the blood will constructively interfere and some will destructively interfere. This means that the backscattered intensity from each small volume will be slightly different and that the total backscattered intensity fluctuates with time as the blood moves through the sample volume. The Doppler shifted signal generated by insonating a blood vessel contains a range of frequencies. The mean power of each frequency is related to the number of scatterers, and the distribution within the power spectrum is a function of the insonation and of the velocity distribution inside the vessel. For the case of a uniformly insonated vessel the underlying frequency distribution represents the velocity distribution inside the vessel.

In a Doppler flowmeter, the signal detected at the receiver represents the sum of the contributions from the entire sample volume. This signal is amplified and then demodulated in order to obtain the audio signal which is free from the RF carrier and still contains the information about the blood flow velocities. The audio Doppler signal is low pass filtered in order to eliminate the high frequency noise lying outside the relevant frequency range. The lower frequencies of the audio Doppler signal are also filtered out in order to eliminate the strong low frequency signals originating from the arterial wall motion. Unfortunately, this also causes the loss of information related to the low velocity fraction of the blood flow.

It is the audio signal obtained through demodulation of the Doppler shifted RF signal, and further conditioned by the low pass and high pass filters that will be normally referred to here as the Doppler signal.

2.5 The sonogram

The Doppler signal carries the sum of the instantaneous contributions from each 'particle' crossing the beam. It can be interpreted by the human observer because in the cochlea such mixtures of signals are sorted according to frequency and weighted according to intensity. To be visually interpreted the signal needs to undergo a similar process of sorting and weighting. This is achieved by translating the Doppler signal into the frequency domain and is usually done in real time by computing the Fast Fourrier Transform (FFT) of successive segments of the Doppler signal. The segments must be short enough so that the stationarity of the blood flow may be assumed. The power spectrum $P(f)$ obtained for each segment represents the velocity distribution of the particles within the beam during the time interval t_w corresponding to the width of the segment. The spectral resolution is given by the inverse of the time interval t_w. A point on $P(f)$ corresponds to a frequency interval representing a velocity range, whilst the height of each point represents the power or the number of particles within that velocity range.

The new representation of the Doppler signal is a three dimensional image generated by displaying the successive $P(f)$ aligned in such way that a line parallel to the time axis always corresponds to the same frequency (Fig. 2.1). It is called a Sonogram and is the most complete way to display information about the blood flow carried by the Doppler signal (Evans et al 1989c).

A sequence of n spectra depicts the changes occurring in the blood flow during a period t equal to:

$$n \times t_w \tag{2.1}$$

(assuming that there is no gap or overlap between the subsequent samples). The number of $P(f)$ required to represent a cardiac cycle is a function of the chosen t_w and of the duration of the cardiac cycle. A variation in the cardiac cycle period is reflected in n and in normal sinus rhythm, such variations tend to be minor.

A single power spectrum from a single cardiac cycle shows an irregular power density known as 'speckle' which is still not completely understood. It is considered to be consequence of Rayleigh interference between wavelets emanating from scatterers in the blood but also may contain information about "true underlying velocity fluctuations" (Mo and Cobbold 1986, 1992). As already mentioned the irregular power distribution caused by the interference gives an imperfect picture of the actual instantaneous velocity distribution inside the vessel. A variety of solutions for speckle reduction have been proposed including: windowing (Oppenheim and Schafer 1975 in Hoskins et al 1990), the use of real time auto-regressive modelling (Schlindwein and Evans 1989c), and filtering (Hoskins et al 1990). Speckle reduction can cause information loss because it is difficult to distinguish interference from true underlying velocity variations (Mo and Cobbold 1992) but, for the purpose of detecting degree of insonation, this does not the present a problem.

Two three-dimensional images of a sonogram are presented in Fig. 2.1, and in order to exemplify the improvement provided by speckle reduction, the same sonogram is presented twice: Fig. 2.1 a shows a raw sonogram as obtained with the equipment developed for the present project before any processing. The granular pattern can be clearly observed. Fig. 2.1 b shows a sonogram using the same raw data but after filtering using a rectangular filter 3X3. The post-filtered sonogram is considerably smoothed, facilitating the visualisation of sonogram features.

2.6 Sonogram parameters

The advantage of the sonogram is that not only does it contains a large amount of information but also that this information is presented in such way that it can be easily identified and retrieved.

Each $P(f)$ represents the number of moving scatterers present in the volume insonated during the time interval t_w distributed according to their respective velocities.

The maximum frequency f_{max} corresponding to the maximum blood velocity in the vessel is represented by the peak in the velocity profile (fig 2.3). It should theoretically correspond to the transition between the signal and noise on the higher frequency side of the spectrum. In practice however it is necessary to take into consideration a series of factors. The spectral broadening caused by the measurement process will displace the spectrum threshold (Newhouse et al 1980, Evans et al 1989c), additionally any filtering intended either to reduce speckle or background noise will smear the edge making difficult the precise determination of the threshold (Hoskins et al 1990). In any case the detection of the threshold will always be affected by the signal-to-noise ratio.

Because there is a distribution of the velocities inside the vessel, $P(f)$ can be submitted to statistical analysis (Lynn 1989). The calculation of the cumulative sum of powers between f_{min} and f_{max} gives the zeroth moment:

$$M_0 = \int_{f\,min}^{f\,max} P(f) \cdot df \tag{2.2}$$

M_0 represents the total power (*TP*) in the Doppler spectrum during t_w and is proportional to the number of moving scatterers present in the volume insonated (Evans et al 1989c).

A piece of useful diagnostic information that can be extracted from $P(f)$ is the Intensity Weighted Mean (*IWM*) (Evans et al 1989c), which represents the average velocity in the sampled volume. Prior to its determination it is necessary to calculate the first moment (M_1) of $P(f)$: which is:

$$M_1 = \int_{f\,min}^{f\,max} P(f) \cdot f \cdot df \tag{2.3}$$

M_1 as such has no absolute physical meaning although in some circumstances it is proportional to the instantaneous volumetric flow (Saini et al 1983, Evans et al 1989c) *IWM* is calculated by dividing M_1 by M_0:

$$IWM = \frac{\int_{f\,min}^{f\,max} P(f) \cdot f \cdot df}{\int_{f\,min}^{f\,max} P(f) \cdot df} \tag{2.4}$$

IWM is the average frequency of $P(f)$ and represents the average velocity in the sampled volume. Both M_1 and *IWM* are affected by the flow profile.

The parameters presented so far were extracted from a single spectrum which corresponds to a single instantaneous measurement. A sonogram however is a sequence of such spectra and this is important because significant clinical information about the arterial blood flow is related to the way it changes during the cardiac cycle.

Excluding M_0, all other parameters here described (***fmax***, ***IWM***, M_1) are related to the blood flow profile which changes quasi-periodically over the cardiac cycle. Therefore they are usually assumed to be functions of time and presented for at least the duration of a complete cardiac cycle.

2.7 Insonation

Before discussing the dependency of the parameters of the sonogram on insonation it is convenient to discuss the meaning of insonation and its relationship with the alignment between the transducer axis and the vessel axis. While alignment is a simple geometric expression of the distance between the beam axis and the vessel axis, insonation is intended to express the amount and distribution of the ultrasonic energy effectively in the vessel lumen when a real acoustic beam is directed (with different degrees of alignment) towards a real blood vessel.

The ability to understand and model insonation more correctly has been developed over the years as a means to improve the accuracy of the extraction of information about the blood flow from the Doppler signal. It is beyond the scope of this thesis to describe these developments in detail, however it is important to enumerate the more important considerations which need to be taken into account when modelling insonation or analysing the possible sources of errors when interpreting the Doppler signal in order to extract information about blood flow.

Attenuation (Cobbold et al 1983, Hoskins et al 1991a) Doppler shifted signals are received from many different distances from the transducer. Depending on the path length these signals will suffer different degrees of attenuation and consequently contribute differently to the final sum.

The ratio between width of the beam and the width of the vessel (Lunt 1975, Evans 1982, Cobbold et al 1983, Saini et al 1983) The degree of insonation for any alignment depends on whether the width of the beam is bigger, equal to or smaller than the diameter of the vessel.

The shape and the uniformity of the beam (Evans and Parton 1981, Cobbold et al 1983, Bascom and Cobblod 1990). Real ultrasonic beams have a complex geometry with no sharp boundaries and an inhomogeneous energy distribution.

Beam vessel angle (Thompson and Aldis 1990-1996, Aldis and Thompson 1992, Hoskins et al 1991a) The vessel wall presents an interface to the incident ultrasonic wave. The amount of reflection grows as the incidence angle decreases, and below the critical angle no energy crosses this interface.

The influence of the walls in diffracting and reflecting the propagating ultrasonic energy (Thompson and Aldis 1990-1996, Aldis and Thompson 1992) The vessel wall curvature presents an interface with variable angles to the incident ultrasonic waves causing a non-uniform insonation across the section of the vessel.

2.8 The dependency of sonogram parameters on insonation.

Consider an ultrasonic beam which is perfectly aligned with a blood vessel. Consider then what occurs as the beam moves off axis. As the beam starts to move, a smaller part of the vessel lumen is sampled (Fig. 2.2). Initially signals from the region near the wall will be lost. In general these correspond to the lower velocities and a relatively smaller volumetric flow. As the misalignment increases, progressively higher velocities and flows are under-sampled up to a point where the region of peak velocity and highest flow is also lost, from then onwards the maximum velocities and flows sampled are insonated by the beam border. Eventually the sample volume will decrease up to a point where there is no insonation at all.

In order to explore these effects a simple model has been constructed to study the behaviour of ***fmax***, M_0, ***IWM*** and M_1. It represents two cases; a vessel containing flow with a parabolic profile (Fig. 2.3 a), and a vessel containing a rather blunter profile[1] (Fig. 2.3 b) A rectangular beam which has the same width as the vessel is pointed towards it. Initially both vessel and beam are perfectly aligned, then they are progressively moved apart by a lateral movement of the beam.

Such a model can not take into account the many complicating factors described in section 2.6 but will lead to a general understanding of the effect of beam misalignment

---

[1] The general form of the flow profile studied was $V = V_{max}\left(1-\left(\frac{r}{R}\right)^n\right)$ where V_{max} is the maximum velocity (at the centre of the vessel), r is the radial co-ordinate and R is the radius of the vessel. For parabolic flow $n=2$, the blunter profile was created by setting $n=4$.

on the sonogram parameters.

Fig. 2.3 c and Fig. 2.3 d present the functions ***fmax(d)***, $M_0(d)$, ***IWM(d)***, $M_1(d)$ normalised to their respective on-axis values plotted against the ratio between displacement of the beam and beam diameter.

For the case of f_{max} it can be seen that while the sampled volume contains the peak of the velocity profile there is no change in the f_{max} detected. After the peak is lost, the detected value of f_{max} falls with the same rate as the velocity profile drops towards the border of the vessel.

M_0 represents the contribution of all the scatterers in the sample volume. As the beam and vessel move apart less insonation results, proportionally less power is returned to the transducer and the power decreases monotonically as the alignment becomes worse.

In the case of ***IWM***, when small amounts of misalignment occur it is the lower velocities contributing to the mean that are lost, and therefore the IWM actually rises at first. This can also be explained by observing the behaviour of the moments M_0 and M_1 which are combined to form the ***IWM***. It can be seen from Fig. 2.3 (c and d) that both moments decrease with misalignment. However the decrease in M_0 is proportional to the volume insonated and is fundamentally a geometric function describing the changes of the intersection of the vessel and ultrasound beam with a progressive degree of misalignment, whilst the decrease in M_1 is proportional to the change in volumetric flow sampled in this changing volume. The initial decrease in the sampled volumetric flow is slower than the corresponding decrease in sample volume, and as a consequence the initial tendency of ***IWM*** is to grow. As the misalignment progresses the rate of fall in the sampled volumetric flow overtakes the rate of fall in the sampled volume and the value of the ***IWM*** drops. It can be seen from Fig. 2.3 (c and d) that this behaviour leads to a small increase before ***IWM*** starts to fall.

2.9 Discussion

The concept of Doppler signal quality already exists in the literature. The Quality index (***QI***) as employed by Hoskins et al (1990, 1991b) was shown to relate to how consistently a Doppler waveform can provide measurements of Maximum Frequency, Intensity Weighted Mean, and other envelope functions, from which Pulsatility Index (***PI***), Resistance Index (***RI***), and other Doppler indices can be calculated. The quality of the signal was analyzed as a function of beam-vessel angle, beam vessel off-set, attenuation, and signal-to-noise ratio.

The idea of quality is also employed in this chapter, however as a function of alignment and degree of insonation. As a consequence, it is primarily related to the strength of the signal and to the signal-to-noise ratio. Additionally, as this work is mainly concerned with restoring alignment, the concept of quality must be relative because a tracking system can only optimize the insonation by picking up the best signal available.

To observe the effect of the degree of insonation and background noise on sonogram parameters a series of 'in vitro' experiments were performed with a flow phantom (described in chapter seven). The experiment consisted in record a sequence of sonograms in three different situations: the beam and vessel aligned and low background noise (Fig. 2.4), the beam and vessel aligned and background noise (Fig. 2.5), the beam and vessel misaligned and low background noise. From each sequence

***M_0*, *M_1*, and *IWM* were extracted**

TP* (*M_0*)** appears a natural choice as a parameter to measure the degree of insonation. It is a function of the volume of moving blood insonated by the beam and therefore falls monotonicaly with misalignment. It is hardly sensitive to blood velocity variations and, under ideal conditions, would be almost constant during the cardiac cycle, meaning that a point measurement would be enough to measure the degree of insonation. The characteristic of being sensitive to the number of moving particles and not to their velocity making the ***TP signal in principle non responsive to the blood flow variations. This represents an important advantage because the object of monitoring is to record blood flow and the distinction between changes in blood flow and changes in insonation ensures that the tracking function is not triggered by changes in the patient condition. Under real conditions, (Fig. 2.4b), the ***TP*** signal presents irregularly spaced higher frequency variations as a result of speckle and the fluctuations in the number of scattering particles within the beam. It presents some periodicity with the cardiac cycle which is partly explained by the variation of the vessel cross section during the cardiac cycle. It also presents a decrease towards the end of diastole, and this is caused by the action of the high pass filters intended to cancel the signals from the arterial walls (Evans et al 1989c). Unfortunately these filters also cancel the low frequency signals from low velocity particles to a greater extent during diastole when the velocity distribution shows a marked drop and even reversal. Such artefacts introduced by the high pass filters produce some dependence of the measured ***TP*** signal on velocity. It is therefore necessary to question if this artefact can lead to the interpretation of the decrease in blood flow velocity (related to the patient condition), as a decrease in insonation. In practice the dependence of ***TP*** on velocity is only during that part of the cardiac cycle when the Doppler signal has a large proportion of its power below the cut-off frequency of the high pass filters; at all other times ***TP*** it is largely related to the degree of insonation and much less sensitive to velocity variations. Therefore it is always possible to process the ***TP*** signal in order to extract information about the degree of insonation which is fairly independent of velocity variations. Examples of this processing are presented in Chapter seven.

TP is also sensitive to noise because the power of the noise spectrum is added to the power of the Doppler spectrum and if the noise is random it becomes indistinguishable from the signal.

In summary, although ***TP*** appears to perform well in the results of this simple simulation, on its own it is not reliable as an absolute indicator of degree of insonation.

fmax, ***IWM***, M_1 are by definition related to velocity and consequently to the flow profile. As the profile changes with time, it is necessary to compare measurements made at the same phase of the cardiac cycle. As these parameters are observed over complete cardiac cycles it is possible to evaluate the degree of insonation from the amplitude of their cyclic excursions. Comparing the behaviour of ***fmax(d)***, ***IWM(d)***, $M_1(d)$ as shown in Fig. 2.3 it can be seen that ***IWM*** and M_1 will perform better than ***fmax*** thanks to their sensitivity to small beam displacements.

fmax, ***IWM***, M_1 are also affected by noise, but in a different way from M_0. In the absence of noise their general shapes over the cardiac cycle are both cyclic and regular. The effect of the noise is to disturb these regular patterns (Fig. 2.5). This feature can be used as an indication of the presence of noise, and even explored as a signal-to-noise (S/N) threshold of acceptance when the sequence of values of $\boldsymbol{n}$ (see equation 2.1) calculated for the successive cardiac cycles becomes unstable.

In conclusion, ***fmax***, ***IWM***, $\boldsymbol{M_1}$ can help in discriminating noise from signal. The combined use of $\boldsymbol{M_0}$, and one of those parameters can provide a more precise assessment of degree of insonation.

2.10 Summary

An analysis of the problem of extracting objective information from the Doppler signal to express the degree of vessel insonation has been presented. From the analysis of the features of the sonogram it was concluded that the degree of insonation is better analysed by a combination of two parameters extracted from the sonogram: the Total Power ($\boldsymbol{M_0}$) and another parameter capable of providing a measure of the signal-to-noise ratio, for example the intensity weighted mean ***IWM*** or the first moment ($\boldsymbol{M_1}$).

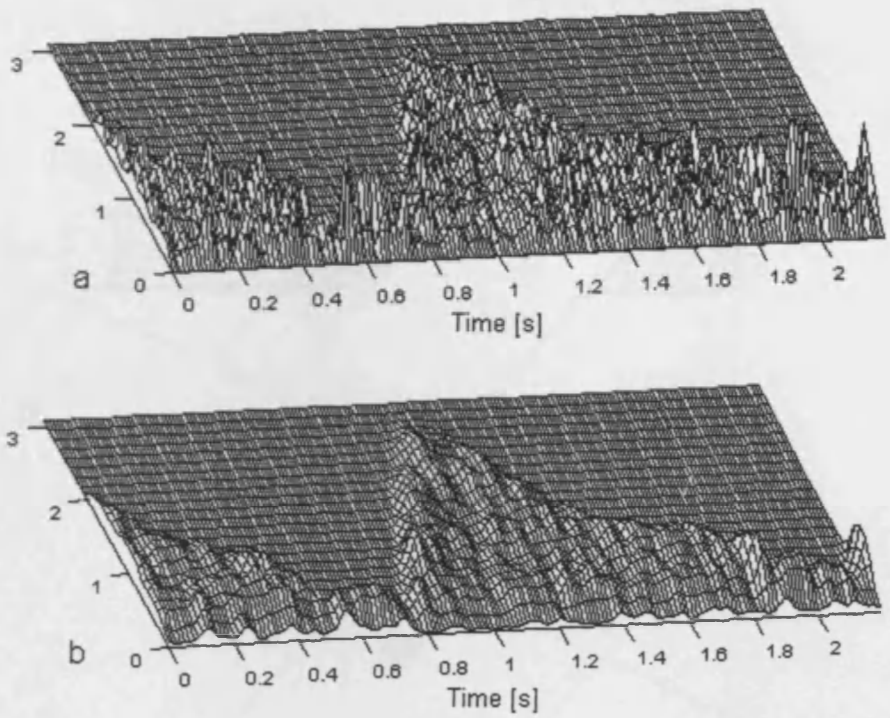

Fig. 2.1 Waterfall representation of sonogram generated by displaying the successive ***P(f)*** aligned in such way that a line parallel to the time axis always corresponds to the same frequency. Speckle reduction is exemplified by the representation of the same sonogram twice: (a) raw sonogram before any processing, the granular pattern can be clearly observed. (b) sonogram using the same raw data after filtering. The post-filtered sonogram is considerably smooth, making the visualization of sonogram features easier.

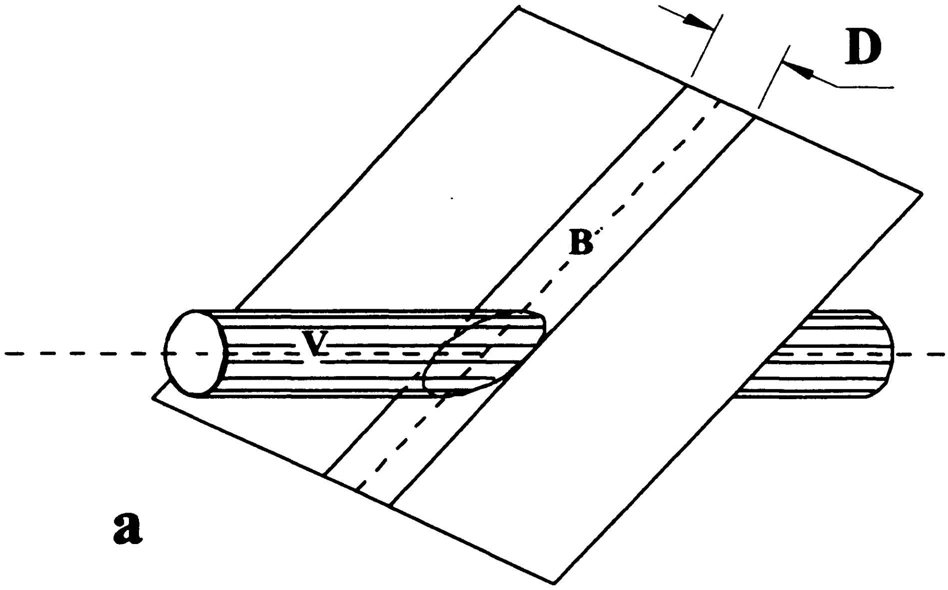

a

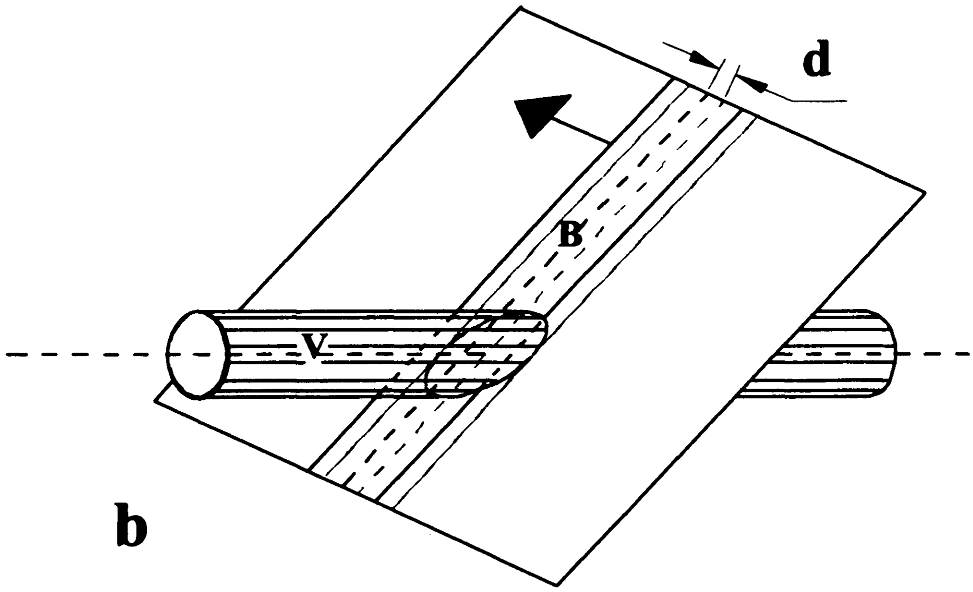

b

Fig 2.2 Schematic diagram presenting the intersection between a rectangular ultrasonic beam (**B**) and a vessel (**V**). The width of the beam and the diameter of the vessel are equal to **D**. In (a) the beam axis intersects the vessel axis. In this situation the beam is able to sample the whole vessel lumen. In (b) the beam presents an off-axis displacement **d**. In this situation part of the vessel lumen is not sampled.

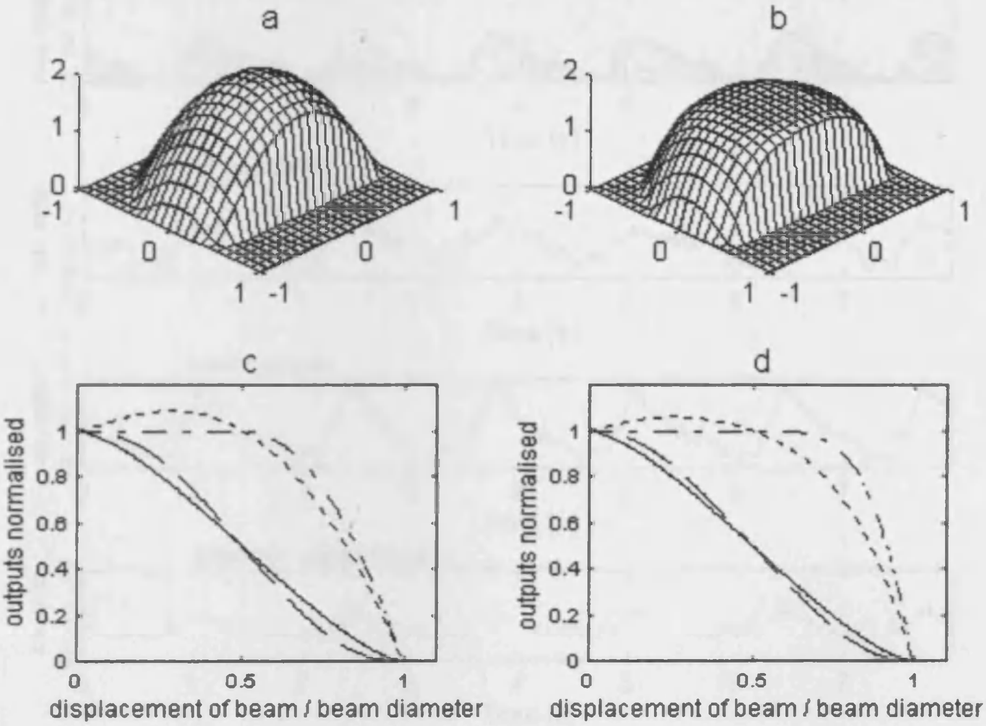

Fig. 2.3 Effect of misalignment between ultrasonic beam and vessel on ***fmax***, M_0, *IWM*, ***and*** M_1. for the case of two types of velocity profiles. (a) Parabolic velocity profile partially sampled by a rectangular beam. (b) Blunt velocity profile partially sampled by a rectangular beam. (c) M_0 (______), M_1 (_ _ _ _ _ _ _), *IWM* (........), and *fmax*(_._._._._) normalized and plotted against the ratio between beam displacement and vessel diameter. Data for parabolic velocity profile shown in (a). (d) The same as (c) for the case of the blunter velocity profile shown in (b).

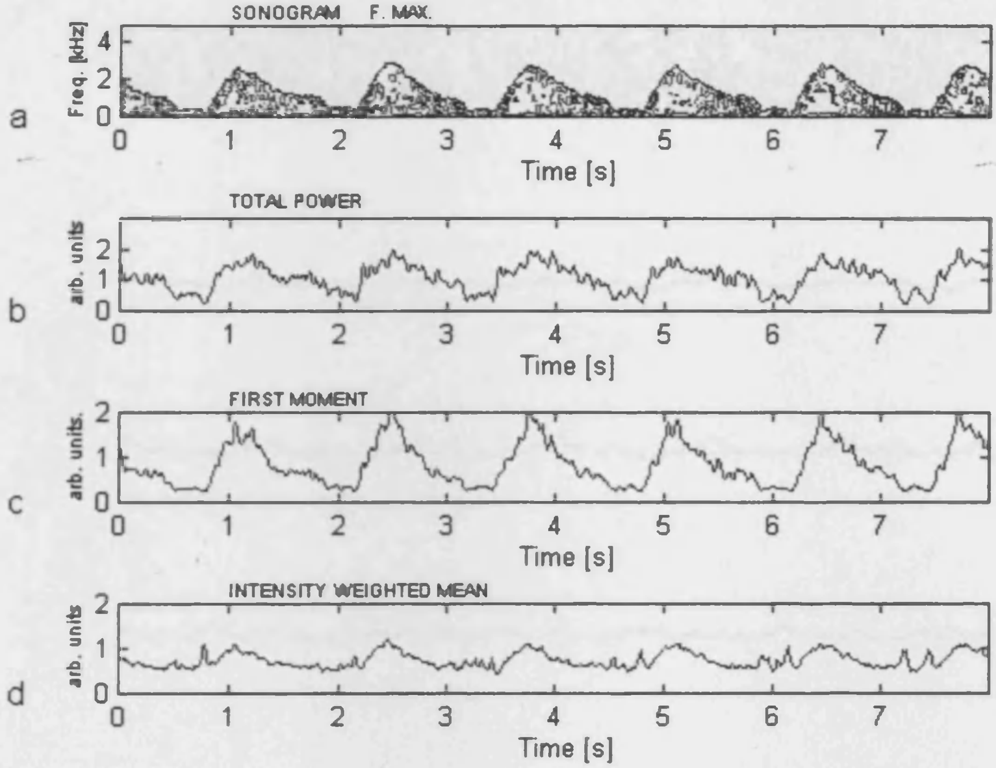

Fig. 2.4 'In vitro' experiment performed with a flow phantom to observe the behavior of a sonogram, and the parameters ***fmax***, M_0, M_1 and ***IWM*** in the case of a perfect alignment between beam and vessel and low background noise. (a) Sequence of sonograms recorded continuously over several cardiac cycles, ***fmax*** lies along the superior borderline of the sonogram. (b) The recording of M_0 extracted from the sequence presented in (a). (c) The recording of M_1 extracted from the sequence presented in (a). (d) The recording of ***IWM*** calculated from M_0, and M_1 recorded in (b) and (c).

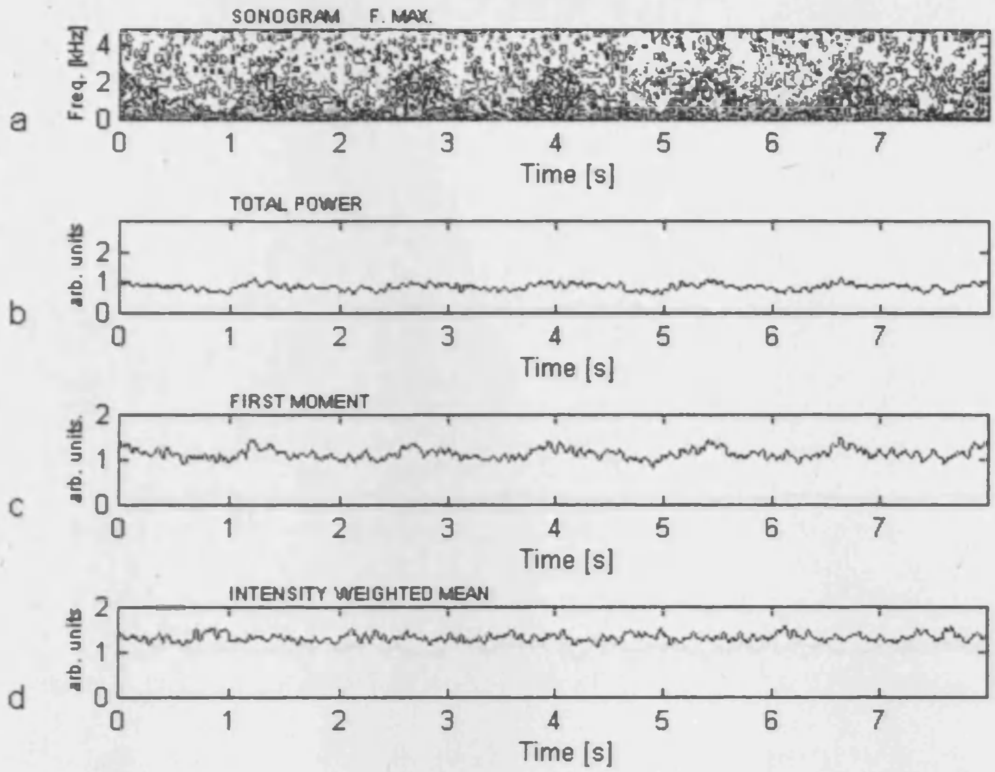

Fig. 2.5 'In vitro' experiment performed with a flow phantom to observe the behavior of a sonogram, and the parameters ***fmax***, M_0, M_1 and ***IWM*** in the case of high background noise. (a) Sequence of sonograms recorded continuously over several cardiac cycles. It is difficult to observe the outline of the sonogram. As a consequence it is also difficult to observe ***fmax***. (b) The recording of M_0 extracted from the sequence presented in (a). (c) The recording of M_1 extracted from the sequence presented in (a). (d) The recording of ***IWM*** calculated from M_0, and M_1 recorded in (b) and (c).

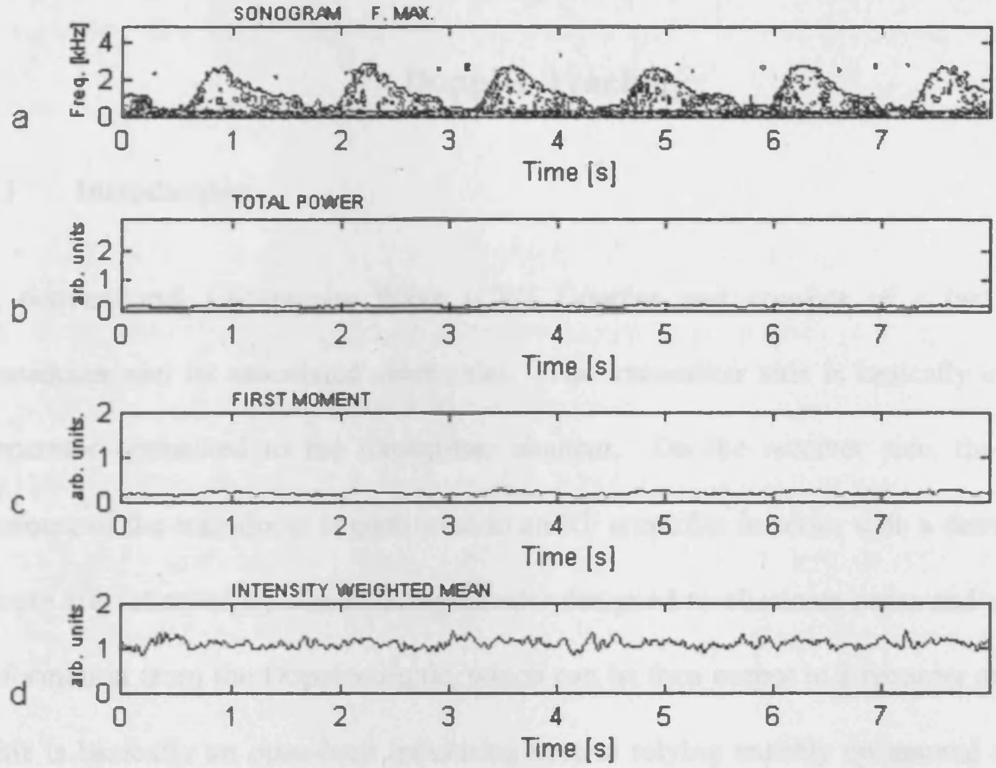

Fig. 2.6 'In vitro' experiment performed with a flow phantom to observe the behavior of a sonogram, and the parameters ***fmax***, M_0, M_1 and ***IWM*** in the case of misalignment between beam and vessel and low background noise. (a) Sequence of sonograms recorded continuously over several cardiac cycles, ***fmax*** lies the sonogram superior borderline. (b) The recording of M_0 extracted from the sequence presented in (a). (c) The recording of M_1 extracted from the sequence presented in (a). (d) The recording of ***IWM*** calculated from M_0, and M_1 recorded in (b) and (c).

Chapter 3

Doppler Tracking

3.1 Introduction

A conventional Continuous Wave (CW) Doppler unit consists of a two element transducer and its associated electronics. The transmitter side is basically a CW RF generator connected to the transmitter element. On the receiver side, the receiver element of the transducer is connected to an RF amplifier in series with a demodulator. These are followed by conditioning circuits designed to eliminate noise and unwanted information from the Doppler signal, which can be then output to a recorder or display. This is basically an open-loop measuring system relying entirely on manual operation for searching and setting the correct beam direction.

A tracking CW Doppler unit also contains a two element transducer (in the sense of transmitter and receiver) and the same associated electronics. The differences are that the transducer must be steereable and that this steering action must be feedback controlled and driven from inside the system. This is a closed-loop measuring system, and this equipment must be able to automatically hunt and track the signal which it assumes to be optimal.

To construct such a device it is necessary to replace the static CW Doppler transducer by a steereable one. This transducer will require an additional driving circuit necessary to adjust the beam direction both for transmitting and receiving. Being feedback controlled, the driving circuit requires real time information about the degree of insonation extracted from the processed input Doppler signal. This information, expressed either as a voltage level and as a logical state, when compared with pre-set stored values will generate the instructions for the activation of the hunting and tracking action.

Although the idea of Doppler tracking is general in the sense that it can be applied to many different cases, in the present work it was considered useful to focus on a typical application. This helped in defining the experimental set-up, the dimensions and shape of the transducer to be constructed, as well as the specifications of the electronics. The present study used as a working model the case of long term monitoring of blood flow in the femoro-distal grafts with Continuous Wave (CW) Doppler (Thrush and Evans 1990).

In this case the blood vessel of around 4 mm diameter runs straight, between 20 mm and 30 mm below the skin surface. The transducer is applied to the patient pointing towards the incoming flow so as to achieve an insonation angle (φ) between 30° and 60° (Fig 3.1 a). The typical movement of the transducer most likely to produce misalignment would be a composition of lateral and angular "in plane" displacements (Fig. 3.1 b and c). The ultrasonic beam direction follows the transducer movement and the beam axis moves along the plane[1] transverse to the vessel missing it. In a steereable transducer the beam is not fixed relative to the transducer housing and a compensation steering along this plane can restore the alignment.

Changes in φ caused by patient movement can also occur (Fig 3.1 d) however they

[1] Strictly speaking, depending on the kind of movement, the beam axis doesn't always move along the same plane and the surface generated by the beam axis can be plane or curved. However, for the limited range of movement particular to this application, those differences can be neglected.

should not affect the tracking too greatly because over a limited range they will cause little effect in the Doppler power. It must be noted however that changes in φ can affect the output of the monitoring device because they may be misinterpreted as a changes in the graft blood flow (equation 1.11). For example, for φ equal to 30°, changes of ± 5° cause approximately 5% variations in the flow measurement, and for φ equal to 45° changes of ±5° can cause flow measurement variations of approximately 9%. A way around this (Trush and Evans 1990), shown in Figure 3.2, would be to minimise the variations in φ by: a) Mounting the transducer in a housing that would distribute the pressure exerted by the transducer attachment over a wider body area. b) Reducing the of the tilt force exerted by the cable by placing the insertion of the cable in the transducer housing close to its base line and parallel to the skin surface.

In the present chapter the general description of a Doppler tracking system is presented. It starts from the presentation of the reasons leading to the adoption of a particular type of steereable transducer and is followed by the description of the whole apparatus as a block diagram and a brief description of its operation.

3.2 The steereable transducer

An acoustic beam can be steered either mechanically or electronically. Mechanical sector steering is straightforward and simple to understand. It can steer over a wide-angle range with high angular definition (Whittingham 1981, Fenster and Downey 1996) However as a mechanical device it has inertia, it is not agile, i.e. it can only move along a continuous sequence of positions and is unable to jump from one position to another. Additionally, considering the miniaturisation necessary for a transducer to be attached to a patient, the precision required would be demanding in terms of construction. In the area of imaging, mechanical scanners have been gradually replaced by electronic scanners which have no moving parts and are agile, i.e. capable of jumping from one position to any other without the need of passing through all intermediate positions. Electronic steering can be performed with array technology, which is booming (Whittingham 1997). Array transducers can be made in many dimensions and shapes (Bjorn et al 1995) and operated as switched linear arrays, phased arrays or the combinations of both types.

The main-stream of array transducer development is directed towards imaging applications (Miller 1983, Smith et all 1991, Withingham 1997), where high resolution is the central requirement. High resolution is achieved with wide bandwidth pulsed waves (generated by heavily damped transducers) and very narrow beams. Beamforming methods (either analogue or digital) employing arrays perform better with large numbers of elements and consequently arrays with rows of 64, 128 or 256 (Larson 1983, Withingham 1997) elements are usually employed. 1-D arrays are capable of focusing and beam steering in the azimuth direction, 1.5-D arrays constructed with three to five rows of 1-D arrays are capable of some degree of elevation steering and slice control in addition to the focusing and azimuth steering control. There are as well full 2-D arrays with as many rows as columns and capable of unrestricted electronic focusing and steering in azimuth and elevation directions (Smith 1991, Wittingham 1995, 1996, 1997).

The transducer requirements for a CW Doppler application are quite different from imaging. For CW operation non-damped piezo elements perform better, and in this case air backed ceramics are indicated. In addition, each array 'element' is actually a pair of elements: one for transmitting and one for receiving. CW Doppler array transducers are not commercially available and therefore is was necessary to develop one from scratch.

An initial consideration concerned the choice between linear and phased arrays (Bjorn et al 1995). In linear array operation, a group of elements located at a certain position on the transducer face is excited generating an acoustic field perpendicular to the transducer face. The scanning is done by selecting which group is excited and its position in the array determines the position of the main lobe axis. The scanning range of a linear array is therefore approximately the array length or area. In a phased array operation all the elements are excited simultaneously. A progressive phase difference between the signals driving the consecutive elements causes the beam to steer along the azimuth and/or elevation direction. From the point of view of simplicity a linear array represents an attractive option when compared with a phased array. However, because of its lack of angular steering it must be larger than a phased array to be able to scan over the same range and this represents a disadvantage from the miniaturisation point of view. Another advantage of the phased array is its ability to irradiate through small windows. This may not represent an advantage in the case of graft monitoring but could be very important in monitoring the middle cerebral artery. For those two reasons the phased array option was adopted.

In comparison with an imaging phased array transducer a Doppler phased array transducer would be far less complex and cheaper to built. The need to insonate the whole vessel requires a broader beam and therefore an array with a smaller number of elements would be adequate. A number of elements in the range of eight to twelve was chosen as this would lead to a light and small device adequate for miniaturisation and easy attachment to the patient. An additional benefit of a small number of elements is that the array requires cheaper cables, connectors and simpler driving circuits.

For the purposed application of graft monitoring, as already explained the alignment correction can be performed by scanning the beam in the azimuth direction alone and therefore an 1-D array will be sufficient. For other applications, for example cerebral blood flow monitoring, it would be necessary to steer both in azimuth and elevation directions, this option however is not explored in this thesis.

The transducer development for the present work is explained in detail in Chap 5. Three versions of 1-D phased array transducers designed for CW Doppler operation (transmitter and receiver) were built. The last and most advanced version has twelve elements, it was successfully employed in the Doppler tracking instrument using just eight elements. The reduction in the number of elements employed (eight instead of twelve) was adopted in order to simplify the electronics.

3.3 Doppler Ultrasound Phased Array Transceiver (DUPAT)

The electronics to drive the array transducer for its operation as a CW Doppler transducer must additionally steer the beam both for transmitting and receiving. It was designed by G. Aucott (Aucott 2001) especially for this project and constructed in the Electronics Laboratory of the Department of Medical Physics at Leicester Royal Infirmary. It was named the 'Doppler Ultrasound Phased Array Transceiver' (DUPAT) and consists basically of an array of eight individual transmitter and receiver Doppler circuits working in programmable synchronism. Each pair of transmitting and receiving circuits is connected to a pair of transmitting and receiving elements of the transducer. The beam steering for transmission can be adjusted by controlling the relative phases of the driving signals. The same set of signals are employed for the demodulation of the Doppler shifted signals detected at the receiver. By this process the demodulated signal output from the eight receivers can be added in phase. The phase relationship can be controlled externally via a digital line, and this is how the feedback control signal adjusts the steering. The DUPAT is described in detail in Chap. 6.

3.4 Feedback loop

The feedback loop can be implemented on a single board installed inside the DUPAT. However, at this stage of development, a more direct, flexible and versatile approach of employing two computers was adopted. The first machine is fitted with a DSP32C System Board (Loughborough Sound Images Ltd) operated by a Multi Channel Signal Analysis and Monitoring Program for Doppler Signal developed at the Dept of Medical Physics Leicester Royal Infirmary (Gibbons et al 1981, Prytherch and Evans 1985, Schlindwein et al 1988, Schlindwein and Evans 1989, Evans et al 1989e, Fan and Evans 1994a 1994b). The demodulated Doppler signal exported from the DUPAT is acquired at the A/D input of the DSP32C which is programmed to display the Sonogram on the computer screen and provide analogue outputs of the Intensity Weighted Mean (*IWM*) and the Total Power (*TP*).

These signals are acquired at the A/D input of a DT VPI™ interface (Data Translation DT 302) fitted in a second computer. An HP-VEE™ Visual Program operates the data acquisition, processes the signal and, through the Digital output of the interface steers the transmission and reception direction of the Array Doppler Transducer via the

DUPAT. (Fig. 3.3)

When attaching the transducer to the patient for the first time the operator overrides the feedback mechanism and sets the steering to zero by disabling the tracking program. Observing the sonogram on the computer screen or listening to the audio Doppler signal he/she is able to manually align the transducer with the vessel. The tracking program is then started and during the initialisation stage the reference values for classifying the degree of insonation are acquired. The ***TP*** signal is recorded, averaged and stored, and from its value two threshold levels are calculated, ***a*** for the detection of small misalignments, and ***b*** for larger degrees of misalignment. At the same time the mean and standard deviation of the cardiac cycle length is calculated over a period of five complete cardiac cycles extracted from the ***IWM*** waveform which is also stored and cyclically updated.

From this stage on the tracking program is ready to take over the steering control. It will then continuously monitor the ***TP*** and the duration of the cardiac cycle. In low noise conditions the monitored value of ***TP*** alone is enough to measure the degree of insonation. When the value of ***TP*** falls below the threshold ***a***, but is still above the threshold ***b***, it indicates that a small misalignment has taken place, and a small adjustment of beam direction is required. A routine to steer the beam to the neighbouring positions is activated until a new peak value of TP is found. Then the routine is disabled and a new TP reference value is calculated. When TP falls below the threshold ***b*** it means that a large misalignment has occurred and it is necessary to widen the search. Another strategy is then used based on the assumption that it is necessary to jump the neighbouring positions to recover alignment. The sequence of positions to be searched depends on the direction in which the beam is initially steered. For each of the possible starting directions there is a defined sequence of jumps to be executed in order to optimise the search. As soon the value of the detected ***TP*** rises above the threshold ***b***, the routine for small adjustments takes over and the same process already described takes place. More detail of the search strategy can be found in Chap. 7.

In high noise conditions the system can be fooled, because despite the fact that the ***TP*** value is still above the thresholds, the physiological and haemodynamic information extracted from the Doppler signal will be compromised. In this situation however the detection of the cardiac cycle period extracted from the IWM signal becomes erratic presenting non realistic values and irregular variations. The existence of such irregular variations expressed in the divergence with the stored reference values triggers an alarm indicating that with such a low signal-to-noise ratio the level ***TP*** signal is no longer a reliable indicator of insonation. As it is not possible for the equipment to correct this situation, an operator intervention is necessary.

3.5 Summary

At the present stage, the Doppler tracking system proposed is basically a working model where Doppler tracking methods can be implemented and studied. Whenever possible a provision for future developments was favoured. The block structure provides the versatility necessary for modifications, adaptations and refinements. A general description of the system has been presented. In this description details were intentionally omitted in order to emphasise a modular view. In the following chapters each part of the block diagram (Fig 3.3) will be described in detail.

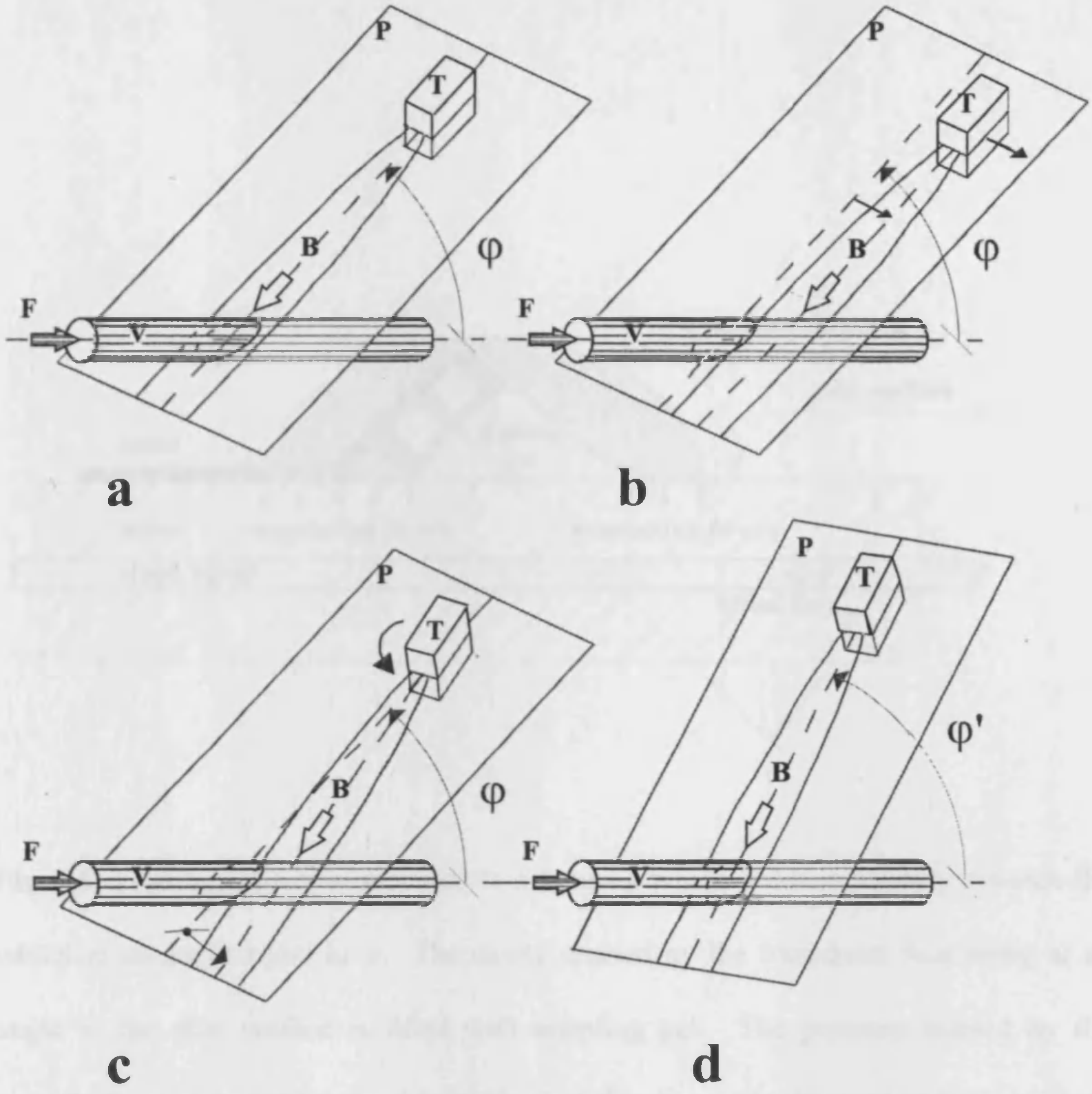

Fig. 3.1 The schematic diagram presents different orientations between transducer (T) and vessel (V). In **a**, **b** and **c** the axis of the ultrasonic beam is contained in the plane (**P**) which sections the vessel making an angle φ with the flow (**F**) axis: **a)** perfect alignment, **b)** an "in plane" misalignment caused by a lateral translation of the transducer, and **c)** an "in plane" misalignment caused by transducer rotation. **d)** an 'out of plane' transducer movement modifies the Doppler angle to φ' without causing misalignment. The general case of relative orientation between beam and blood vessel can be described as a composition between 'in plane' and 'out of plane' orientations.

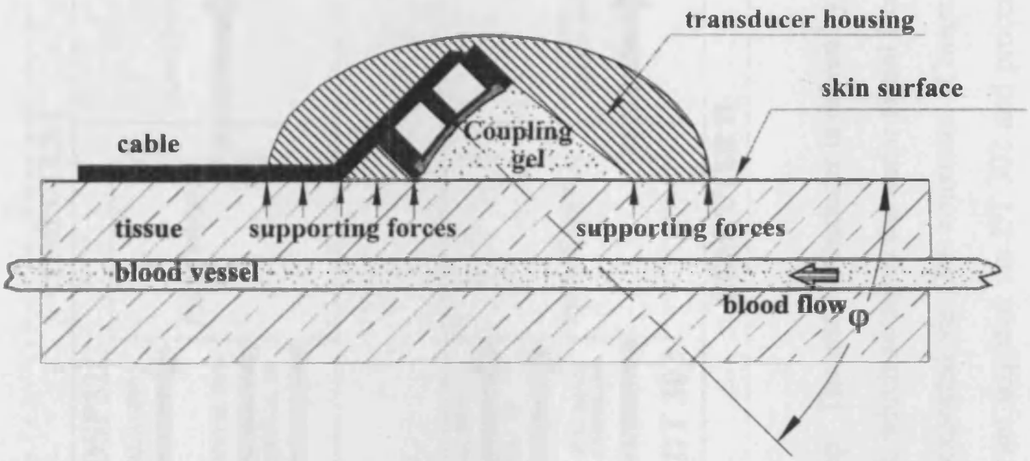

Fig 3.2 The transducer is mounted in a housing which holds it pointing towards the vessel at an angle equal to φ. The cavity created by the transducer face being at an angle to the skin surface is filled with coupling gel. The pressure exerted by the transducer and housing on the skin is distributed over a wide skin area and this tends to reduce the deformation of the supporting tissue. The insertion of the cable in the base of the transducer housing helps the attachment of the transducer to the skin surface and minimizes the titling force exerted by the cable on the transducer. These features tend to reduce variations in the value of φ.

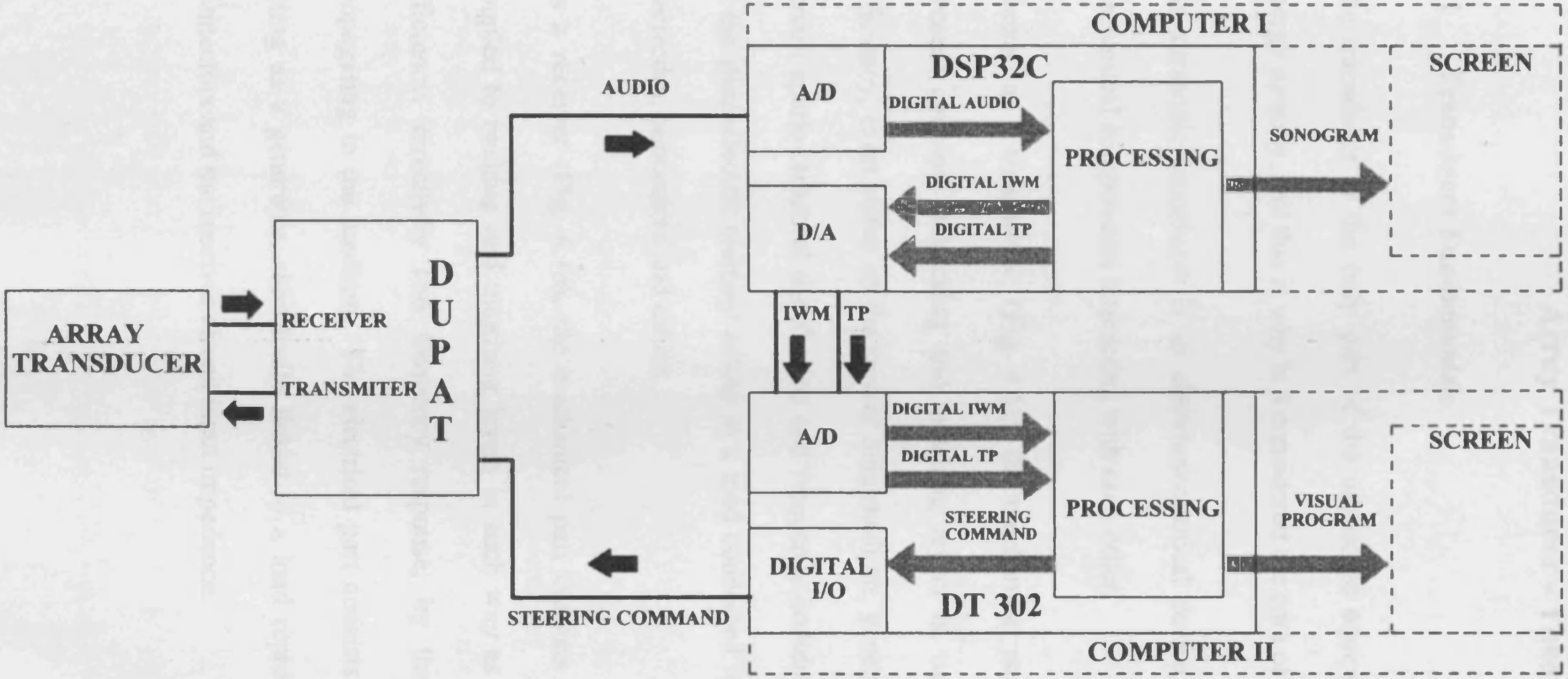

Fig. 3.3 The block diagram presents the complete tracking system as it was set-up. The array transducer is driven by the DUPAT. The feedback loop is constructed with two computers. Computer I contains the DSP32C board, which acquires the audio signal from the DUPAT and extracts the Sonogram, displayed on the computer screen, the IWM and TP signals are exported via D/A converter. Computer II contains the DT 302 board and is loaded with the HP-VEE 4.0 program. The IWM and TP signals are acquired via DT 302 and processed by the visual program displayed on the screen. The program generates the steering commands exported to the DUPAT.

Chapter 4

Array Transducer - Theory

4.1 Transducer Fundamentals

The transducer is the only part of the ultrasonic equipment to deal with ultrasonic energy directly, and this is why is it considered the core of such devices.

An ultrasonic transducer is an electromechanical device, incorporating electrical and mechanical components interacting with each other.

Viewed as a transmitter, (Fig. 4.1a), the mechanical part consists of a piezoelectric element coupled to backing and matching layers in such way as to, with a given efficiency, exert stress on the surrounding medium, generating an acoustic field with a certain spatio-temporal distribution and frequency content. The electrical part consists of the piezoelectric element acting as a load connected to a driving RF source by the electrodes, connectors and cables.

As a receiver (Fig. 4.1b), the mechanical part consists of the piezoelectric element coupled to backing and matching layers in such way as to be strained, with a given efficiency, directivity and frequency response, by the ultrasonic pressure waves propagating in the medium. The electrical part consists of the piezoelectric element acting as a generator, electrically linked to a load represented by electrodes, cables, connectors and the receiver circuit input impedance.

4.1.1 Piezoelectricity

The core of the ultrasonic transducer is the piezoelectric element. It can be made of materials like crystals, polled ferroelectric ceramics or polymers. In the present work the piezoelectric material employed was PZT (Lead Zirconate Titanate) which is still the most widely used piezo-ceramic today.

The theory of piezoelectricity is extensively described in the scientific literature (Silk, 1984, Moulson and Herbert 1990). The brief presentation here is intended only to summarise the meaning of symbols, and the notation employed in the equations directly relevant to the present work.

Piezoelectric materials exhibit a crystalline structure containing some sort of asymmetry. This results in the formation of electric dipoles with a certain degree of orientation. Any distortion in this structure (strain S) caused by mechanical action (stress T) will lead to a redistribution of charges in the lattice (displacement current D) resulting in generation of a net proportional voltage (electric field E) across the material. Conversely, a redistribution of charges in the lattice (D) caused by an external electric field (E) will produce a proportional distortion (S) in the crystalline structure applying a proportional stress (T) in the surrounding medium. The piezoelectric effects are also dependent on the temperature .

Cross-coupling effects caused by the applied electrical and mechanical stresses will determine the distribution of strain (S) and displacement current (D) in the three orthogonal directions. Because of this, to be correctly described, the piezoelectric effect requires the use of tensors. For simplicity, the tensorial notation will not be presented here.

The following equations describe the piezoelectric properties of any material in terms of the parameters $\boldsymbol{S}$, $\boldsymbol{T}$, $\boldsymbol{D}$ and $\boldsymbol{E}$ assuming temperature to be constant. $\boldsymbol{T}$ and $\boldsymbol{S}$ are fully described by second rank tensors, $\boldsymbol{D}$ and $\boldsymbol{E}$ by first rank tensors. The subscripts indicate the variables held constant.

$$\left(\frac{\partial \boldsymbol{D}}{\partial \boldsymbol{T}}\right)_{\boldsymbol{E}} = \left(\frac{\partial \boldsymbol{S}}{\partial \boldsymbol{E}}\right)_{\boldsymbol{T}} = \boldsymbol{d} \tag{4.1}$$

$$-\left(\frac{\partial \boldsymbol{E}}{\partial \boldsymbol{T}}\right)_{\boldsymbol{D}} = \left(\frac{\partial \boldsymbol{S}}{\partial \boldsymbol{D}}\right)_{\boldsymbol{T}} = \boldsymbol{g} \tag{4.2}$$

$$\left(\frac{\partial \boldsymbol{D}}{\partial \boldsymbol{S}}\right)_{\boldsymbol{E}} = -\left(\frac{\partial \boldsymbol{T}}{\partial \boldsymbol{E}}\right)_{\boldsymbol{S}} = \boldsymbol{e} \tag{4.3}$$

$$\left(\frac{\partial \boldsymbol{E}}{\partial \boldsymbol{S}}\right)_{\boldsymbol{D}} = \left(\frac{\partial \boldsymbol{T}}{\partial \boldsymbol{D}}\right)_{\boldsymbol{S}} = -\boldsymbol{h} \tag{4.4}$$

The piezoelectric properties $\boldsymbol{d}$, $\boldsymbol{g}$, $\boldsymbol{e}$ and $\boldsymbol{h}$ would be fully described by third rank tensors.

From the point of view of transducer construction and ceramic manufacturers' catalogues, the more usually quoted properties are:

d- <u>Piezoelectric Charge Coefficient</u> also known as <u>Transmitting Coefficient</u> defined as: the ratio between short circuit charge density and applied stress (Coulomb/Newton) or the ratio between strain developed and applied field (meter/Volt)

g- <u>Piezoelectric Voltage Coefficient</u> also known as <u>Receiving Coefficient</u> is defined as: the ratio between strain developed and applied charge density (meter^2/Coulomb) or the ratio between open circuit field and applied stress (Volt meter/Newton)

The properties (here represented generically as P) are described by a system of symbols and notation employing superscripts and subscripts.

$$P_{ij}^{F} \tag{4.5}$$

Superscripts (F) describe external factors like physical mounting and electrical connections:

T- Mechanically free S- Mechanically clamped

D- Electrical open circuit E- Electrical short circuit

Consistent with their crystalline asymmetric structure, many properties of piezoelectric materials are defined as function of direction. In a co-ordinate system referred to the direction of polarisation, normally designated as the Z-axis, the X, Y and Z axis in this co-ordinate system are represented respectively as directions 1, 2 and 3, and the shear about the same axes respectively as 4, 5 and 6 (Fig 4.2). These numbers are added as subscripts to the symbol representing the property. The first subscript (i) refers to the direction of the electrical field associated with the voltage applied or the charge displacement produced. The second subscript (j) gives the direction of mechanical stress or strain under consideration. For example: A transmitting coefficient d of a loose ceramic submitted to an electric field applied in the Z direction and producing a strain along the direction X is represented by $d_{31}{}^{T}$

In a piezoelectric material the ratio between Stress (T) and Strain (S) is:

$$\Delta S = s^E \Delta T + \varepsilon^T \Delta E \tag{4.6}$$

The ratio between Displacement Current (D) and the applied Electric Field (E) is:

$$\Delta D = \varepsilon^T \Delta E + d\Delta T \tag{4.7}$$

Where s the elastic compliance of the material is fully described by a fourth rank tensor and ε is the permitivity fully described by a second rank tensor. The superscripts refer to the parameters held constant, E means short circuited electrodes while T means unrestrained material. Equations 4.6 and 4.7 express the coupling between the electrical and mechanical properties linked by the piezoelectric parameter d and which can also be related to ε^T through the relation:

$$d = g\varepsilon^T \tag{4.8}$$

From the point of view of power transduction, the piezoelectric material is better characterised by the coupling factor k (Berlincourt 1964, Moulson and Herbert 1990) which represents the effective electromechanical energy conversion and can be expressed as:

$$k = \frac{U_M}{\sqrt{U_{ST} U_{ED}}} \tag{4.9}$$

or

$$k = \sqrt{\frac{U_{e-m}}{U_e}} = \sqrt{\frac{U_{m-e}}{U_m}} \tag{4.10}$$

Where U_m is the mutual energy, U_{ST} is the elastic energy, U_{ED} is the dielectric energy, U_m is the total applied mechanical energy, U_e is the total applied electrical energy, $U_{e\text{-}m}$ is the electrical energy converted to mechanical energy, and $U_{m\text{-}e}$ is the mechanical energy converted to electrical energy. Coupling factors are not tensors, however they are dependent upon the stress distribution and on boundary factors requiring the employment of subscripts in a similar way as has already been explained (4.5). Another way to characterise a piezoelectric material is through their electrical input impedance Z measured with a network analyser by sweeping the frequency and continuously recording the values of impedance Z (real) and phase α. This reveals all the resonances and anti-resonances of the device. Resonances are the natural oscillation frequencies for short circuited electrodes represented by the minima of Z and anti-resonances are the natural oscillations for open circuit electrodes represented by the maxima of Z (Moulson and Herbert 1990).

The coupling coefficient, k, can also be approximately determined from the resonant f_r and antiresonant-f_a frequencies (Berlincourt et al 1964):

$$k \cong \frac{f_a^2 - f_r^2}{f_r^2} \tag{4.11}$$

4.1.2 Mason model

The reflection of the mechanical response in the electrical output provides the basis for the electrical modelling of ceramics and transducers. The earliest model was proposed by Mason (1948). Its important contribution was the separation of electrical and mechanical parts and the employment of the analogy between a transmission line and acoustic wave propagation to represent the mechanical part. A useful simplification of this model is the representation of the electrical equivalent of an unloaded ceramic near the resonance region (Berlincourt et al 1964).

The equivalent circuit is presented in Fig. 4.3. It has two branches in parallel, branch **1** contains a capacitor C_0 and branch **2** a resistance R, an inductance L, and a capacitance C in series. The resonance occurs at the frequency causing serial resonance in the RLC circuit in branch **2** (at this frequency the impedance of the equivalent circuit is at a minimum). The antiresonance occurs at the frequency causing parallel resonance between branches **1** and **2** (at this frequency the impedance of the equivalent circuit is maximum).

4.1.3 Backing and matching

As already presented, the piezoelectric element cannot be described or analysed without taking into account the nature and conditions of its attachment to the surrounding medium, and this is true both from the electrical and mechanical point of view. The basic purpose of the transducer construction is to shape and assemble the piezo ceramic to a particular matching and backing in order to define the mechanical energy transfer.

The backing layer of a transducer is defined according to the transducer's purpose. For continuous wave (CW) operation the backing should not restrain the free oscillation of the piezoelectric material, it must be allowed to vibrate in its natural resonance frequency determined by its mechanical properties and dimensions, then for CW operation air backing is normally employed. For pulsed wave (PW) operation the backing should dampen the vibration producing a short duration broad band signal. This is achieved at the expense of transducer efficiency and should be compensated by high excitation voltages and high amplification. For PW operation the backing should be well matched with the ceramic and present a high degree of absorption. There are many different solutions to achieve this purpose and better results are achieved with more than one backing layer. Tungsten loaded epoxy is a well documented option as a matching layer between the ceramic and the absorbing layer for the purpose of improving the energy transfer (Silk 1984).

Because of the high impedance of the ceramic material there is strong reflection at the ceramic-medium interface. The employment of the matching layer to improve the efficiency of the energy transfer is now standard procedure. The maximum efficiency is achieved with odd numbers of quarter wavelengths. Single and double matching layers have been employed with success. An additional use of the matching layer is to focus the acoustic energy. Here again tungsten loaded epoxy can be employed considering its ability to be conformed by moulding and the fact that for small thicknesses it produces negligible attenuation.

From the electrical point of view, it is also possible to achieve effects equivalent to backing and matching, by manipulating the excitation signal and also tuning the input electrical impedance of the transducer. The electrical coupling provided by the electrodes and cables connecting the piezoelectric ceramic and the transmitter/receiver is also significant in the performance of the transducer.

The Mason model was adapted and employed by Kossof (1966) for studying the effects of backing and matching in transducer performance both for transmission and reception. Krimholtz et al (1970) introduced modifications to the original Mason model in order to allow a better distinction between mechanical and electrical parts and by the representation of the surrounding medium and each transducer layer by their equivalent transmission line. This makes easier the study and interpretation of transducer response by modification or addition of layers. Silk (1980, 1984) and Stepanishen (1981) extended the study to take into account the effect of three dimensional beam spreading.

4.1.4 Discussion

It is certainly useful and desirable to be able to predict the behaviour of a transducer before its construction. The successful employment of any model in predicting and explaining the behaviour of a transducer is directly dependant on the correct representation of all transducer features. From an electrical point of view, the electrical coupling provided by the electrodes and cables connecting the piezoelectric ceramic and the transmitter/receiver are significant. From a mechanical point of view dimensions and mechanical properties of all materials including electrodes and bonding layers are also significant. There is variability in the piezoelectric characteristics and in the dimensions of ceramics and electrodes. In addition, bonding layers are hard to control and characterise. As a consequence it is common to find differences in the characteristics of transducers designed and manufactured to be identical.(Silk 1984)

4.2 Phased array transducers

To achieve the tracking action required for the system, the development of a stereable transducer was essential. As already explained in the Chapter 3, a phased array transducer was chosen as the best option because:

- Electronic steering avoids the need for moving parts.

- It is agile, (it has the ability to change the direction of the beam at a speed limited only by the time interval taken by the electronic circuit to adjust the phase ratio of the driving signals)

- The transducer can be made small enough to probe into the patient through small anatomical acoustic windows, and also to be comfortably attached to the patient for long term monitoring.

4.2.1 Principles

The acoustic field generated by an array transducer is merely the sum of the acoustic fields generated by each individual element. This process can equally be thought of as the diffraction of the acoustic waves produced by the array elements.

The study of the beam formation from an array (Feynman et al 1964) can begin from a two-dimensional model where two elements, represented by point sources **1** and **2**, driven by continuous, single frequency signals $f = \frac{\omega}{2\pi}$ with a relative phase difference $\Delta\alpha$, are generating continuous waves of amplitudes A_1 and A_2 in a medium (Fig. 4.4). These waves will meet and add at a generic point ***P*** in the medium and, neglecting the effect of attenuation, the resultant amplitude A_p and intensity I_P at ***P***, will be given by:

$$A_P = A_1(\cos \omega t + \phi_1) + A_2 \cos(\omega t + \phi_2) \tag{4.12}$$

$$I_P = A_1^2 + A_2^2 + 2A_1 A_2 \cos(\phi_2 - \phi_1) \tag{4.13}$$

where ϕ_1 and ϕ_2 are the waves' phases at ***P***.

The three parts of Fig. 4.5 present three distinct situations for two sources **1** and **2**, spaced by ***d***, transmitting single frequency circular waves in a semi-space. The semi-circles centred on **1** and **2** represent the cycle repetition. They are spaced by one wavelength λ and their phases, expressed in fractions of wavelengths, are given by

$\delta = \dfrac{\lambda \cdot \alpha}{2\pi}$ where α is the phase of the signal driving a source.

When the waves from these two sources interfere with each other, what matters is their phase difference. The study of their interaction is simplified by fixing the phase of one wave at zero and varying the phase of the other, which makes the difference equal to the phase which is varying. In theory δ can assume any value but as the interference is cyclic all possible situations occur in the range between **0** and λ. In diagrams **(a)**, **(b)** and **(c)** three values of α (δ) are represented. In **(a)** α is equal to zero and in **(b)** and **(c)** it takes progressively higher values.

At any fixed point in the semi-space the phase difference between the waves remains constant as long as ***d***, λ and δ remain constant. As a consequence, for a given set of ***d***, λ and δ there is a fixed phase distribution pattern in the semi-space which will determine how the waves from ***1*** and ***2*** will interact locally. In each of the examples shown in the diagram, ***d*** and λ are constant and ***d*** is smaller than λ in all cases. The axis joining the intersection of the semicircles marks the main lobe ***L*** direction (points where the waves originating from ***1*** and ***2*** are in phase and consequently exhibiting constructive interference). It is possible to observe that as δ changes the phase distribution pattern also changes, and that there is a direct proportionality between δ and θ (the angle of ***L*** relative to the main axis). This is the principle of phased array operation. The ratio between d and λ is of obvious importance. There is a tendency to secondary lobe (L') formation for higher values of δ, and such a tendency can be counteracted by decreasing the value of d. Any secondary lobe formed shares the total output power of the transducer therefore weakening the overall transducer efficiency.

In order to construct an analytical function relating wavelength, array dimensions, angles and phases, the distances from the individual sources to a generic point P are compared (Fig. 4.6).

As far as phase is concerned it is the difference between these distances in radians that is important. For $\overline{1P} >> d$ the path length difference $(\overline{1P} - \overline{2P})$ may be written $\overline{1P} - \overline{2P} = d\sin\theta$. Such a distance multiplied by the wave number k $(k = \frac{2\pi}{\lambda})$ is converted to radians. The phase difference of the waves at P as a function of the geometry is thus:

$$\beta = \frac{2\pi}{\lambda} d\sin\theta = kd\sin\theta \tag{4.14}$$

Adding β to α, (the relative phase between the signals driving the two elements *1* and *2*), leads to a general equation for the relative phase differences between two acoustic waves at a generic point in the far field and is given by:

$$\phi = \phi_2 - \phi_1 = \alpha + \frac{2\pi}{\lambda} d\sin\theta = \alpha + kd\sin\theta \tag{4.15}$$

4.2.2 Array of point sources

In the case of an array of N_e equally spaced elements, driven by equal amplitude signals A, with gradual regular phase increments ϕ, equation (4.12) can be extended to:

$$A_R = A(\cos\omega t + \cos(\omega t + \phi) + \cos(\omega t + 2\phi) + \ldots + \cos(\omega t + (N_e - 1)\phi)) \qquad (4.16)$$

where A_R is the vectorial sum of the individual element contributions at the point P. In this sum, the vectors corresponding to each element form a regular polygonal line with N_e sides which can be inscribed in a circumference of radius r. The particular case of $N_e = 3$ is shown in the Fig. 4.7 to exemplify the general demonstration which follows.

In the representation of the vectorial sum it is always possible to identify two triangles: ***OQS*** and ***OQT***.

OQS has two sides equal to r and the third side equal to the unitary vector A opposed to the angle ϕ which can be proven to be the unitary phase increment. ***OQT*** has two sides also equal to r and the third side is equal to A_R the resultant of the sum of the N_e unitary vectors and opposed to the angle $N_e\phi$ which is the product of the number of elements and ϕ. The value of r can be expressed by:

$$r = \frac{\frac{A}{2}}{\sin\frac{\phi}{2}} \qquad \text{or} \qquad r = \frac{\frac{A_R}{2}}{\sin\frac{N_e\phi}{2}}$$

then:

$$A_R = A\frac{\sin\frac{N_e\phi}{2}}{\sin\frac{\phi}{2}} \qquad (4.17)$$

and
$$I_R = A^2 \frac{\sin^2 \frac{N_e \phi}{2}}{\sin^2 \frac{\phi}{2}} \tag{4.18}$$

From (4.15), (4.17) and (4.18):

$$A_R = A \frac{\sin \frac{N_e(\alpha + kd \sin\theta)}{2}}{\sin \frac{\alpha + kd \sin\theta}{2}} \tag{4.19}$$

$$I_R = A^2 \frac{\sin^2 \frac{N_e(\alpha + kd \sin\theta)}{2}}{\sin^2 \frac{\alpha + kd \sin\theta}{2}} \tag{4.20}$$

which are the expressions of the resultant amplitude and intensity as a function of A, N_e, α, k, d and θ.

Equations (4.19) and (4.20) provide a means for dimensioning and studying an array of N_e equally spaced points driven by equal amplitude electrical signals with gradual regular phase increments.

From equation (4.18) it is possible to see that I_R has a maximum when $\frac{\phi}{2}$ tends to zero. It is possible to demonstrate that at this position $I_R = N_e^2 A^2$. The amplitude of the subsequent maxima corresponds to $N_e\phi = m\cdot(2\pi)+\pi$ (m is the sequence of integers). Looking at Fig. 4.7, this corresponds to the case of the vector I_R turning a complete circle. The amplitudes will become progressively smaller following the slower variation of $\sin^2\frac{\phi}{2}$. The sequence of the maxima tends to a minimum at,

$\phi = m\cdot(2\pi)+\pi$, and tend to a maximum at $\phi = m\cdot(2\pi)$. For $N_e\phi = m\cdot(2\pi)$, I_R is equal to zero.

In Fig. 4.8, $\sin^2\frac{\phi}{2}$, and $\sin^2\frac{N_e\phi}{2}$, and I_R, are plotted against ϕ taking as an example the case of $N_e = 6$. In **a,** $\sin^2\frac{\phi}{2}$, and $\sin^2\frac{N_e\phi}{2}$ are plotted together. In **b,** I_R is plotted separately.

The main lobe corresponds to the case of $\frac{\phi}{2}$ tending to zero. Taking this condition to equation (4.15) $\phi = \alpha + \frac{2\pi}{\lambda}d\sin\theta = \alpha + kd\sin\theta$ (transcribed here for clarity:)

$$\phi \rightarrow 0 \qquad \text{then} \qquad \alpha = \frac{2\pi}{\lambda}d\sin\theta = kd\sin\theta \tag{4.21}$$

$$\text{or} \qquad \theta_0 = \sin^{-1}(-\frac{\alpha}{kd}) \tag{4.22}$$

Equation (4.21) expresses the main lobe condition and can be used to define any combination of θ, α, k and d satisfying this condition.

Typical shapes of $A_R(\theta)$ (dotted line) and $I_R(\theta)$ (solid line) for two distinct cases of α $(\alpha = 0^0)$ and $(\alpha \neq 0^0)$ are presented in Fig. 4.9

4.2.3 Array of line sources

As long as the dimensions of the elements can be neglected, the ideal representation of the array by point sources is applicable. However, to make a more realistic model, the dimensions of the elements must be taken into account. From this point on, instead of defining d as spacing between elements (which is correct only for the case of point sources), it is better to define d as the pitch which is the distance between the centres of neighbouring elements. This is a more general concept and applies to both cases.

In the particular case of simulating the acoustic field generated by a 1-D (one dimensional) array 'in plane', it is sufficient to take into account only the width of the element (w). This can be done by replacing each point source of the ideal model by a line with length w made up of N point sources (Fig. 4.10). The path length from each point of **1** to a generic point P in the 'in plane' is a function of the point of origin. Different path lengths will cause a phase difference between the signals arriving at P from different points in the line if it is assumed that the phase difference at the origin is zero. A_{P1} is the amplitude of the signal in P which is the resultant from the contributions of the N points forming the line **1**, it can be expressed by the following equation (similar to equation 4.16).

$$A_{P1} = A_n(\cos \omega t + \cos(\omega t + \phi) + \cos(\omega t + 2\phi) + \cdots + \cos(\omega t + (N-1)\phi)) \qquad (4.23)$$

where A_n is the amplitude of a wave from a generic point n in the line assuming that the amplitudes of the waves originating from all point sources are equal, and ϕ is the phase difference between the contribution of two consecutive points. To express ϕ as a function of w it is possible to employ equation 4.15 which represents the phase differences ϕ at a generic point P between waves originating from two points separated by a distance d. These points are driven by signals of the same frequency and phase difference α. In a 'line' representation of one element the distance d between two consecutive points depends on the value of N adopted and ranges from w to **zero** following the formula $d=w/N$. As all points in the line are driven by the same signal they are in phase. Replacing d by w/N and considering that in the line source all points are driven by the same signal, the phase difference α is zero and consequently equation 4.15 is transformed to:

$$\phi = \beta = k(w/N)sin\theta \tag{4.24}$$

In this case ϕ is equal to β which is just a function of the geometry, k is the wave number and θ the angle between the path length and the main axis (X direction). It must be mentioned that in this deduction it is assumed that the path lengths from all the point sources to P are parallel, by considering that the distance between the sources and P is much larger than the distances between the sources themselves.

For a line source model, where N tends to be large, the individual contributions A_n tend to lie along the circumference arc OT as shown in the graphical representation of equation 4.23 in Fig. 4.11 (analogous to Fig. 4.7). The set of equations 4.25 and 4.26 derived for this diagram differ from the equivalent equations (4.17) and (4.18) simply by the replacement of A_R by A_{P1} and A by A_n

$$A_{P1} = A_n \frac{\sin\frac{N\phi}{2}}{\sin\frac{\phi}{2}} \tag{4.25}$$

$$I_{P1} = A_n^2 \frac{\sin^2\frac{N\phi}{2}}{\sin^2\frac{\phi}{2}} \tag{4.26}$$

The sum of the amplitudes of the point sources A_n can be expressed by $NA_n = \sum_N A_n$

Taking: $A_n = \frac{\sum_N A_n}{N}$, $\frac{N\phi}{2} = \gamma$ and $\frac{\phi}{2} = \frac{\gamma}{N}$, equation 4.25 becomes:

$$A_{P1} = \frac{\sum_N A_n}{N} \frac{\sin\gamma}{\sin\frac{\gamma}{N}} \tag{4.27}$$

which can be rearranged to give:

$$A_{P1} = \frac{\frac{\sum_N A_n}{N}}{\sin\frac{\gamma}{N}} \sin\gamma \tag{4.28}$$

As $N \to \infty$, $\frac{\sum_N A_n}{N} \to 0$ and $\sin\frac{\gamma}{N} \to 0$ leading an indetermination of the type $\frac{0}{0}$ in equation (4.28). To solve this indetermination the L'Hopital Rule is applied (Dias 1964) and it consists of extracting the derivative in N of both terms:

$$\frac{d\left(\frac{\sum_N A_n}{N}\right)}{dN} = \sum_N A_n \frac{d\left(\frac{1}{N}\right)}{dN} = \sum_N A_n\left(-\frac{1}{N^2}\right) \tag{4.29}$$

$$\frac{d\left(\sin\frac{\gamma}{N}\right)}{dN} = \left(\cos\frac{\gamma}{N}\right)\left(-\frac{\gamma}{N^2}\right) \tag{4.30}$$

substituting (4.29) and (4.30) in (4.28):

$$A_{P1} = \frac{\sum_N A_n\left(\frac{1}{N^2}\right)}{\left(\cos\frac{\gamma}{N}\right)\left(\frac{\gamma}{N^2}\right)} \sin\gamma = \left(\sum_N A_n\right)\left(\frac{1}{\left(\cos\frac{\gamma}{N}\right)\gamma}\right) \sin\gamma \tag{4.31}$$

when $N \rightarrow \infty$, (4.31) becomes: $$A_{P1} = \left(\sum_N A_n\right)\frac{\sin\gamma}{\gamma} \tag{4.32}$$

replacing γ by $\frac{N\phi}{2}$ and expressing ϕ from (4.23), equation (4.32) becomes:

$$A_{P1} = \left(\sum_N A_n\right)\frac{\sin\frac{kw\sin\theta}{2}}{\frac{kw\sin\theta}{2}} \tag{4.33}$$

Equation (4.33) takes into account the phase differences corresponding to the different path lengths from the line source to P and expresses the resulting amplitude A_{P1} as a function of the wave number k, the element length w, and the angle θ between the path length and main axis. It is also necessary to take into account the element projection in P which is a function of θ (maximum at $\theta = 0$, falling to zero at $\theta = \pi/2$). To do that it is sufficient to multiply A_{P1} by $\cos\theta$.

In conclusion, the representation of A_1, the acoustic field amplitude profile in the 'in plane direction' generated at a point P from an element 1 of width w from a 1-D array is:

$$A_1 = A_{P1}\cos\theta = \left(\sum_N A_n\right)\frac{\sin\frac{kw\sin\theta}{2}}{\frac{kw\sin\theta}{2}}\cos\theta \tag{4.34}$$

The transformation of the initial array model constructed with point sources, to a model of an array constructed with line sources, is done by replacing the point sources by line sources. Mathematically this corresponds to replacing A in equation 4.18 by A_1 from equation 4.34. The expression for A_R in the new model is presented fully expanded in equation 4.35.

$$A_R = \left(\left(\sum_N A_n \right) \frac{\sin \frac{kw \sin\theta}{2}}{\frac{kw \sin\theta}{2}} \cos\theta \right) \left(\frac{\sin \frac{N_e(\alpha + kd \sin\theta)}{2}}{\sin \frac{\alpha + kd \sin\theta}{2}} \right) \tag{4.35}$$

Equation 4.35 can be arranged to represent $A_R(\theta)$ as the dot product between three vectors:

$$A_R(\theta) = F(\theta) \cdot D(\theta) \cdot P(\theta) \tag{4.36}$$

where

$$F(\theta) = \left(\sum_N A_n \right) \left(\frac{\sin \frac{N_e(\alpha + kd \sin\theta)}{2}}{\sin \frac{\alpha + kd \sin\theta}{2}} \right) \tag{4.37}$$

is a function representing the profile of an acoustic field generated by an array of N_e point sources, each one having output amplitude equal to $\sum_N A_n$,

and where

$$D(\theta) = \frac{\sin \frac{kw \sin\theta}{2}}{\frac{kw \sin\theta}{2}} \tag{4.38}$$

is a sinc function representing the effect of the diffraction caused by the finite size of the line source,

and where

$$P(\theta) = \cos\theta \tag{4.39}$$

is a cosine representing the effect of the projection of the line source.

The intensity I_R can be derived from 4.35 simply by making $I_R = A_R^2$ (4.40)

therefore

$$I_R(\theta) = F^2(\theta) \cdot D^2(\theta) \cdot P^2(\theta) \tag{4.41}$$

4.2.4 Cross-talk

In a real array the elements and circuits are never perfectly isolated from each other and as a consequence it is also necessary to take into account the cross-talk between elements. The cross-talk may be mechanical and/or electrical and the array behaves as if the effective dimensions of each element are larger than its real physical dimensions, as if there were an overlap between elements. The cross-talk enhances the diffraction which leads to a further attenuation of the beam and to a decrease in the transducer steering range.

In the case of the model of the 1-D array described above such a situation can be theoretically implemented in equations 4.35 and 4.38 by increasing the value of $\boldsymbol{w}$. The only assumption made in this representation of cross-talk its that of a lateral symmetry in the energy spread. It is also expected that there will be an 'apodization like' effect in the real irradiation length leading to a decrease in the irradiation distribution towards the extremities. Consequently the effective element width just represents an equivalent of the real irradiating length.

4.2.5 Modelling

In order to study the effect of $\boldsymbol{k}$, $\boldsymbol{N_e}$, $\boldsymbol{w}$, $\boldsymbol{d}$, α in $\boldsymbol{I_R}(\theta)$ a working model was constructed with a program in Matlab implementing equations (4.15, 4.37, 4.38, 4.39, 4.40 and 4.41). This model displays the maximum profiles of the acoustic fields generated by an 1-D array transducer attributing to $\boldsymbol{k}$, $\boldsymbol{N_e}$, $\boldsymbol{w}$, $\boldsymbol{d}$, α different values.

When $\boldsymbol{w} \rightarrow \mathbf{0}$, $\boldsymbol{D}(\theta)$ tends to 1, and the projection of the point source becomes independent of θ. In that case equation 4.41 reverts to the ideal case of point sources.

An array of point sources is more suitable to show the influence of variations in k, N_e, d, α in $I_R(\theta)$, and for this purpose the function $F^2(\theta, k, N_e, d, \alpha)$ is employed.

In Figures 4.12 and 4.13 the function $I_R = F^2(\theta, N_e)$ for a given set of values of k, d and α is presented. It is possible to observe the increase in directivity with N_e and the exponential dependence of I_R on N_e . Another feature is the formation of side lobes as the pitch increases, this is shown by plotting $I_R = F^2(\theta, N_e)$ attributing to d values smaller (Fig. 4.12), and larger (Fig. 4.13) than the wavelength.

A further study on the effect of the pitch size on I_R is presented in Fig. 4.14 where the function $I_R = F^2(\theta, d)$ for given set of values of N_e, k and α is presented. It is possible to observe the progressive formation of side lobes, the increase in beam directivity with d.

The function $I_R = F^2(\theta, \alpha)$ for a given set of values of N_e, k is presented for two different values of d in Figures 4.15 and 4.16 respectively. It shows the maximum profiles of the acoustic fields generated using values of α ranging from -90° to +90°. It is possible to observe the control exerted by α on the steering angle θ and also the side lobes formation. The influence of d in the field directivity, in the sensitivity of θ to α, and in the tendency of side lobe formation can also be observed by comparing Figures 4.15 and 4.16

As w becomes significant the projection $P(\theta)$ and the diffraction $D(\theta)$ must be taken into account. In the model presented here the consequence is the distortion and limitation of the range of the acoustic field generated by the array of point sources.

The influence of projection in the intensity is represented by the vector $P^2(\theta) = \cos^2\theta$.

It is independent of the element width w however in order to compare projection with diffraction it is useful to present it here in the form of the array $P^2(\theta,w)$ (Fig. 4.17). The lines of $P^2(\theta,w)$ are $P^2(\theta)$ repeated the same number of times as necessary. In the particular example presented in (Fig. 4.17) there are as many lines as values of w employed in further calculations.

The function $I_{RP}(\theta, \alpha)$ obtained by performing the dot product of each line of $I_R(\theta, \alpha)$ by the vector $P^2(\theta)$ is presented in Fig. 4.18. It displays the maximum intensity profiles of the acoustic fields produced by line sources for α ranging from -90° to +90° taking into account the effect of the projection alone.

The effect of the diffraction is described by $D = sinc\gamma$ where $\gamma = \frac{kw}{2}\sin\theta = \frac{\pi}{2}\cdot\frac{w}{\lambda}\sin\theta$. It is dependent both on θ and on the ratio between w and λ as can be observed in $D^2(\theta, w)$ (Fig. 4.19).

$I_{RD}(\theta, w)$ is obtained by performing the dot product of each line of $I_R(\theta, \alpha)$ with the vector $D^2(\theta)_{w=a}$. (a corresponds to a particular value of w). $I_{RD}(\theta, \alpha)$ represents the maximum intensity profiles of the acoustic fields, produced by an array of line sources with a particular width $w = a$ for α ranging from -90° to +90° taking into account the effect of the diffraction alone (Fig. 4.20).

Comparing Fig. 4.17 with Fig. 4.19 it can be observed that, for small values of kW the influence of the projection is the most significant. For higher values of kW the situation reverses and the effect of the diffraction becomes the more significant.

The combined effect of projection and diffraction is represented by the dot product $D^2 \cdot P^2$ (Fig. 4.21).

I_{RDP} (Fig. 4.22) represents the maximum intensity profiles of the acoustic fields produced by line sources with a particular width $w = a$ and α ranging from -90° to +90° taking into account the effect of projection and diffraction. Its calculation consists in performing the dot product of each line of $I_R(\theta, \alpha)$ by $(D^2 \bullet P^2)_{w=a}$.

Fig. 4.23 a, b, and c presents the maximum intensity profiles of acoustic fields produced by line sources with the same width. Each diagram corresponds to progressively higher values of α. The dotted line represents the product $P(\theta)^2 \bullet D^2(\theta)_{w=a}$. The dashed lines represent of acoustic fields profiles generated by point sources $I_R(\theta, \alpha)$ and the solid line the acoustic field profiles generated by line sources $I_{RDP}(\theta, \alpha)$ (which are affected by projection and diffraction). Looking to the acoustic field profile in more detail it is possible to observe, in addition to the attenuation, a small distortion of the field profile. This distortion represents an effective decrease in the steering angle.

The effect of cross talk is characterised in Fig. 4.24 by presenting three cases: **a**) a case of no cross-talk where the effective element width is equal to w, **b**) a case where cross-talk is represented by attributing to the effective element width a value of $1.5 \times w$, **c**) a case where a higher degree of cross-talk is represented by attributing to the effective element width a value of $2 \times w$.

4.3 Summary

The theory presented in this section enables the construction of a mathematical model for a 1-D phased array transducer. This model is the basis for the subsequent stages of design, construction and evaluation of the transducer to be employed in the Doppler tracking instrument.

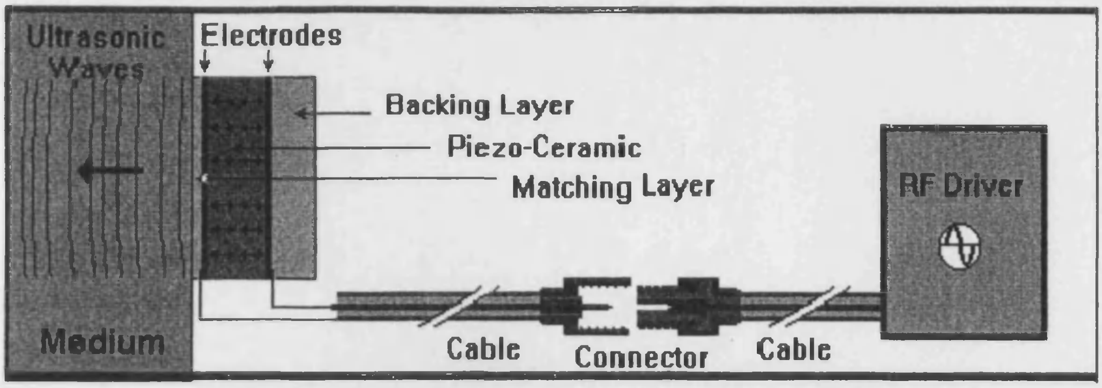

Fig. 4.1a Schematic representation of the transducer as a transmitter. The electrical signal generated at the driver generator is conducted through cables, connectors and electrodes to the piezo-ceramic. The electric field produces a strain in the ceramic crystalline structure generating pressure waves which are transmitted into the backing layer, and to the medium through the matching layer.

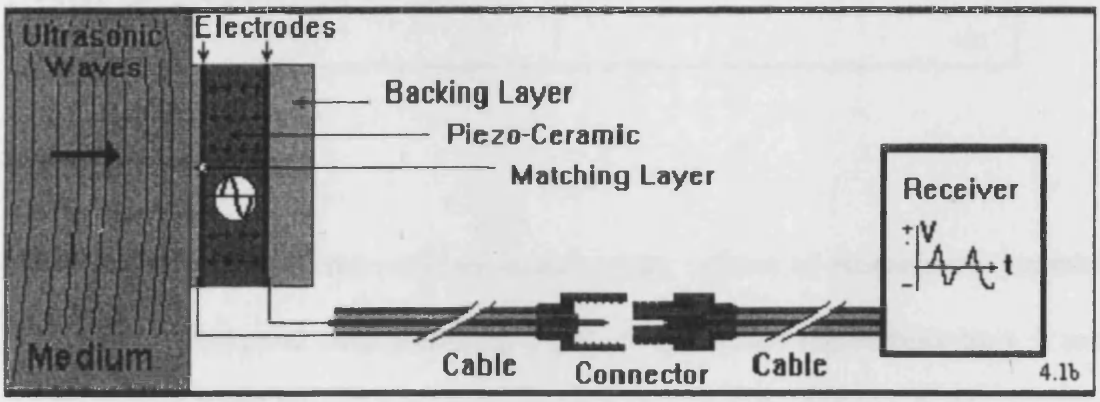

Fig. 4.1b Schematic representation of the transducer as a receiver. The pressure waves in the medium are transmitted through the matching layer to the transducer. The strained crystalline structure of the piezo-ceramic generates an electric field that is detected by the electrodes and transmitted through cables and connectors to the receiver electronic circuit.

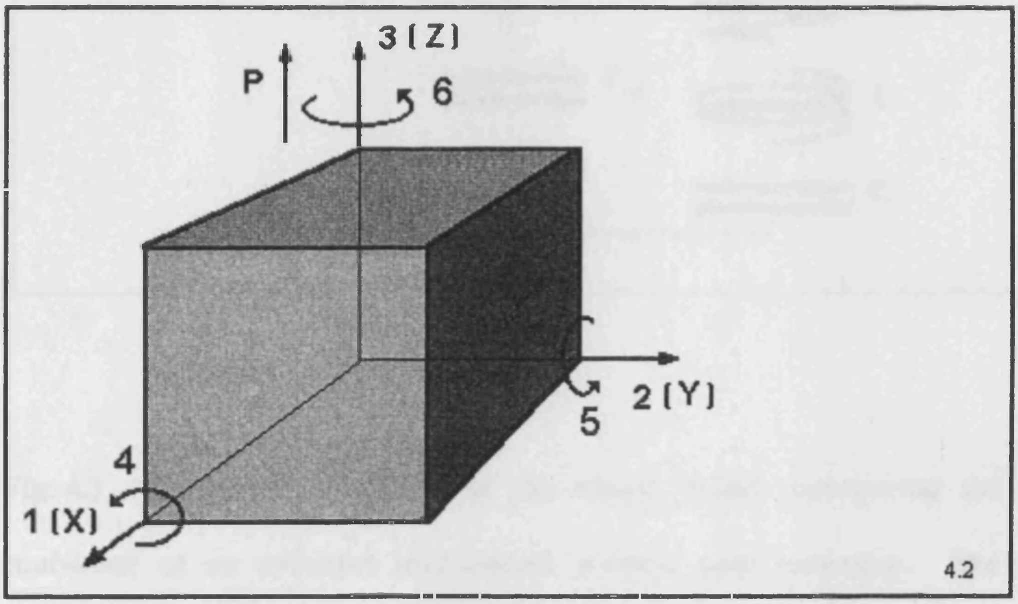

Fig. 4.2 Diagram representing an elementary volume of piezoelectric material in a system of orthogonal coordinates *X*, *Y* and *Z* represented respectively by **1**, **2** and **3**. The shear about the same axis is represented respectively by 4, 5 and 6. *Z* is designated as the polarization direction.

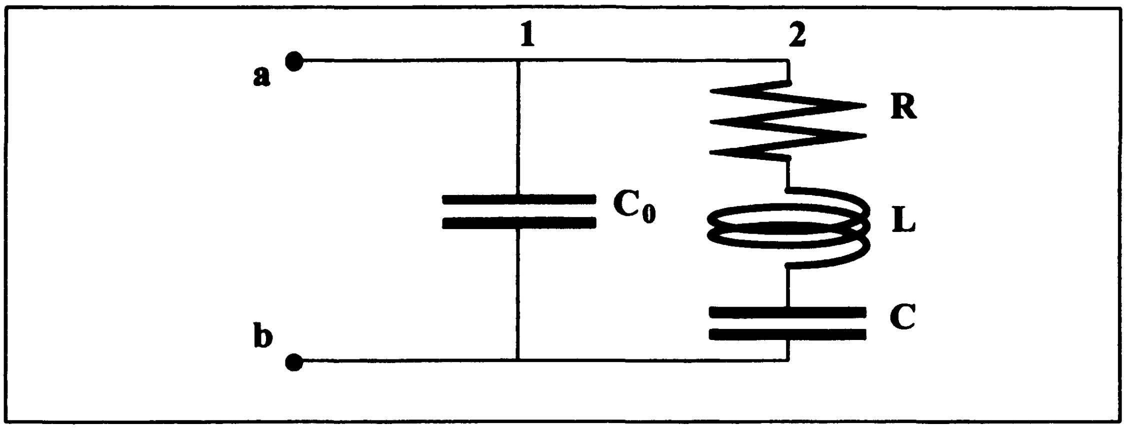

Fig. 4.3 Simplified version of the Mason model representing the electrical equivalent of an unloaded piezoelectric ceramic near resonance. The electrical impedance seen from terminals **a** and **b** reaches a minimum when the ***RLC*** circuit in branch **2** is excited at its serial resonance frequency (ceramic resonance). The electrical impedance seen from the terminals **a** and **b** reaches its maximum when the two branches are excited at their parallel resonance frequency (ceramic anti-resonance).

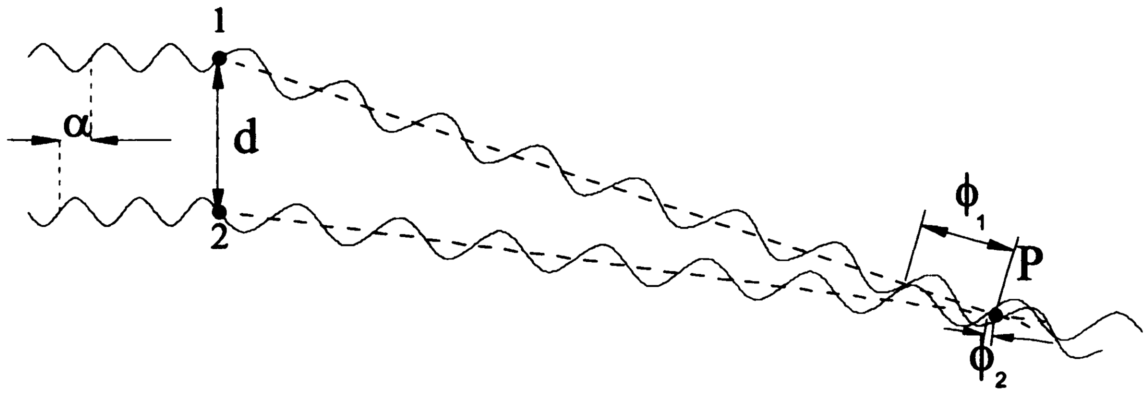

Fig. 4.4 Two point sources separated by a distance d are driven by signals of equal frequency and phase difference α. The resulting acoustic waves meet and add at a generic point P where each wave has a phase (ϕ_1 and ϕ_2 respectively). The difference between ϕ_1 and ϕ_2 is function of α and of the distance difference between each source to P expressed in radians.

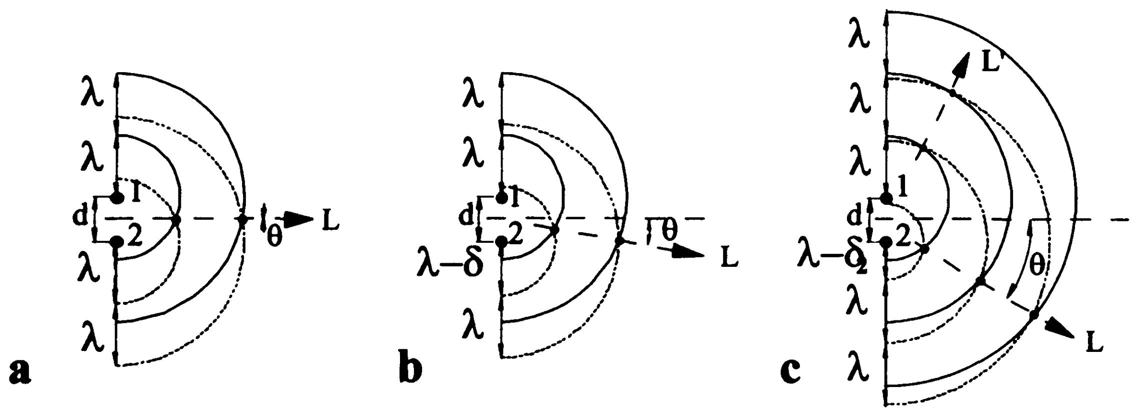

Fig. 4.5 In ***a***, ***b*** and ***c*** two sources **1** and **2** separated by a distance ***d*** driven by signals with the same frequency and phase difference α generate semi circular waves in the semi space limited on the left by a plane passing through **1** and **2**. For a given set of ***d***, λ and α there is a fixed phase distribution pattern determining how the waves generated at **1** and **2** interact locally as shown by the juxtaposition of the semi-circles centred at **1** and **2**. The semi-circles represent the cycle repetition, and are spaced by λ . The spatial phase difference at the origin is $\delta = \alpha\lambda/2\pi$. The axis ***L*** joining the intersections of the semi-circles mark the region of maximum constructive interference. In ***a***, where the case of δ equal to zero is represented, the direction of L coincides with the main axis. In ***b*** and ***c*** progressively higher values of δ and therefore of θ, which is the angle between ***L*** and the main axis are presented. For higher values of δ as shown in ***c*** there is a formation of another region of constructive interference in the direction ***L'***.

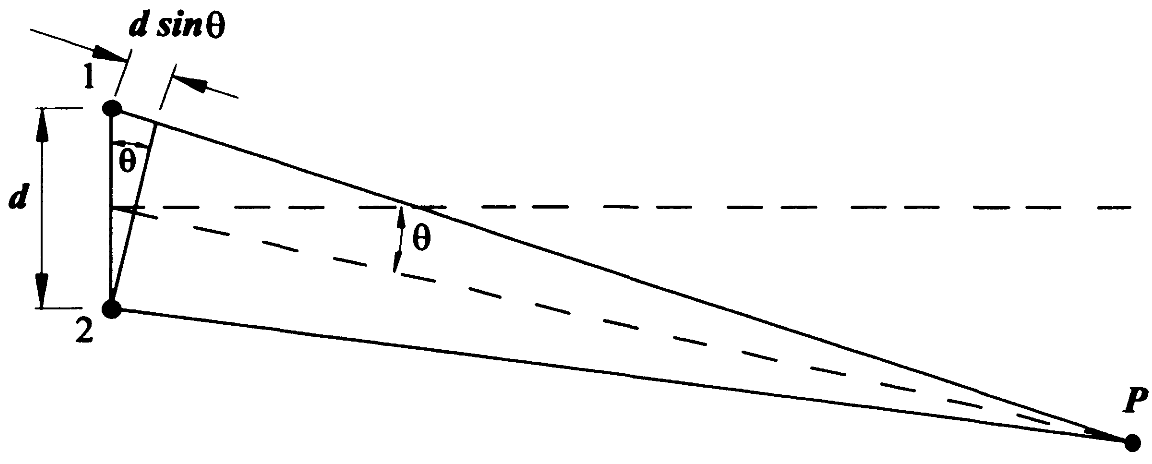

Fig. 4.6 Calculation of the difference in path length from two point sources **1** and **2** to a generic point ***P*** as a function ***d*** and θ. ***d*** is the distance between **1** and **2** and θ is the angle between **1*P*** and **2*P*** directions with the main axis assuming **1*P*** and **2*P*** to be parallel (possible for the case of **1*P*** and **2*P*** >> ***d***). In his case **1*P*–2*P*=*d***·sin·θ which when expressed in radians represents the phase difference ϕ between the waves generated in **1** and **2** when meeting at the point ***P***.

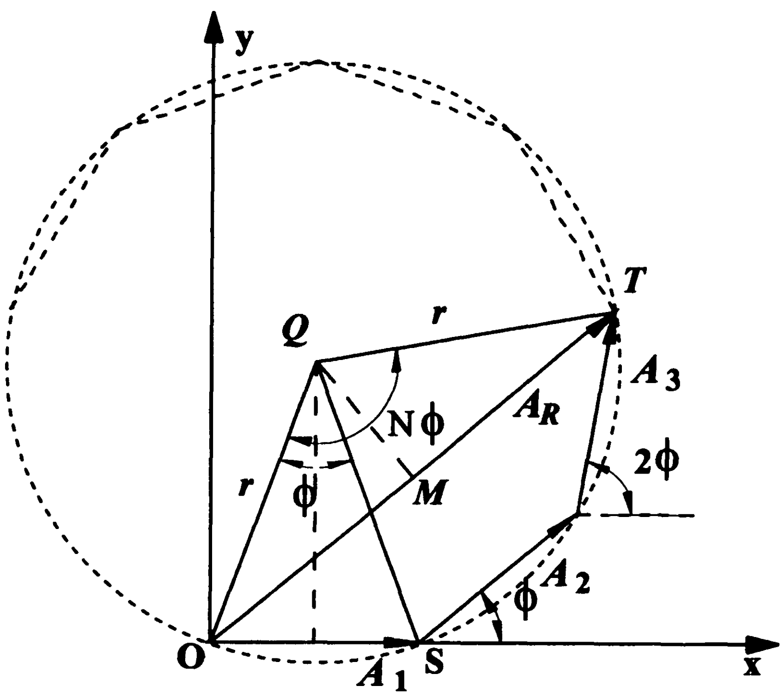

Fig. 4.7 Vectorial calculation of the amplitude A_R resulting from the sum of the contributions from N equally spaced elements of an array driven by equal amplitude signals A with regular phase increments ϕ.

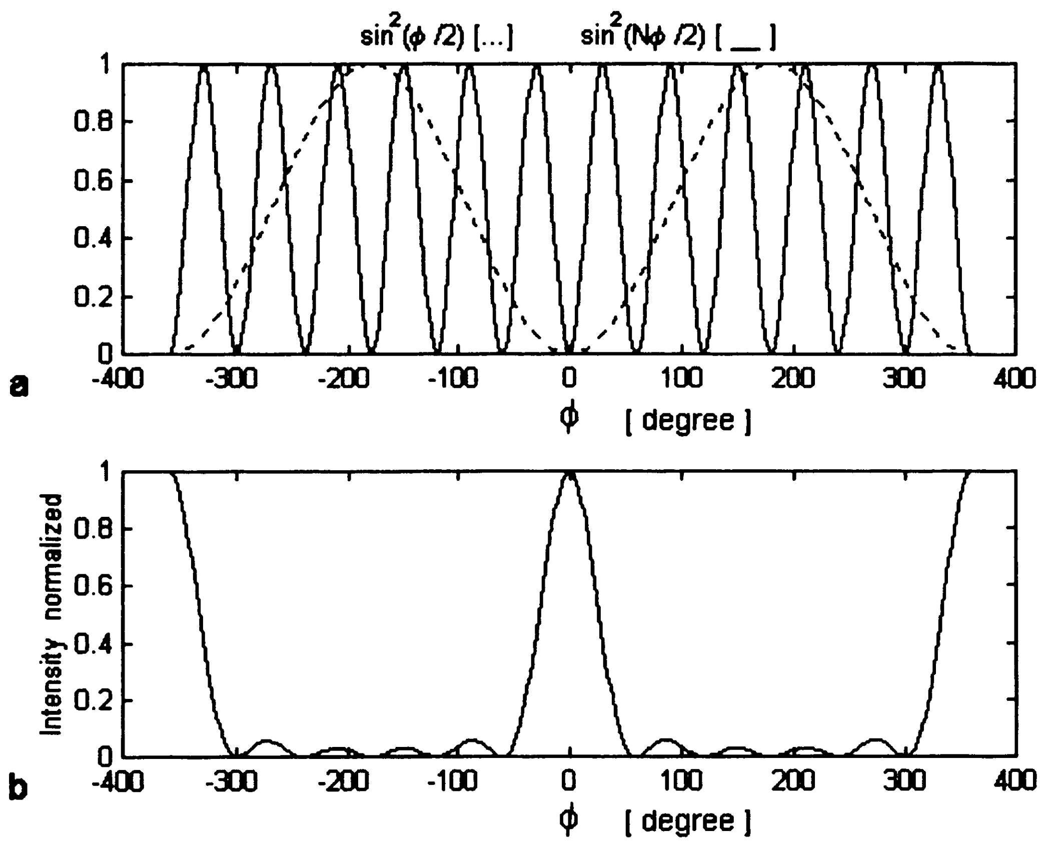

Fig. 4.8 **a)** The functions $\sin^2(\phi/2)$, $\sin^2(N_e\phi/2)$ are plotted together for a range of ϕ varying from **-360°** to **+360°** (in this example N_e=6). **b)** The function $I_R(\phi)$ is plotted for the same range of ϕ.

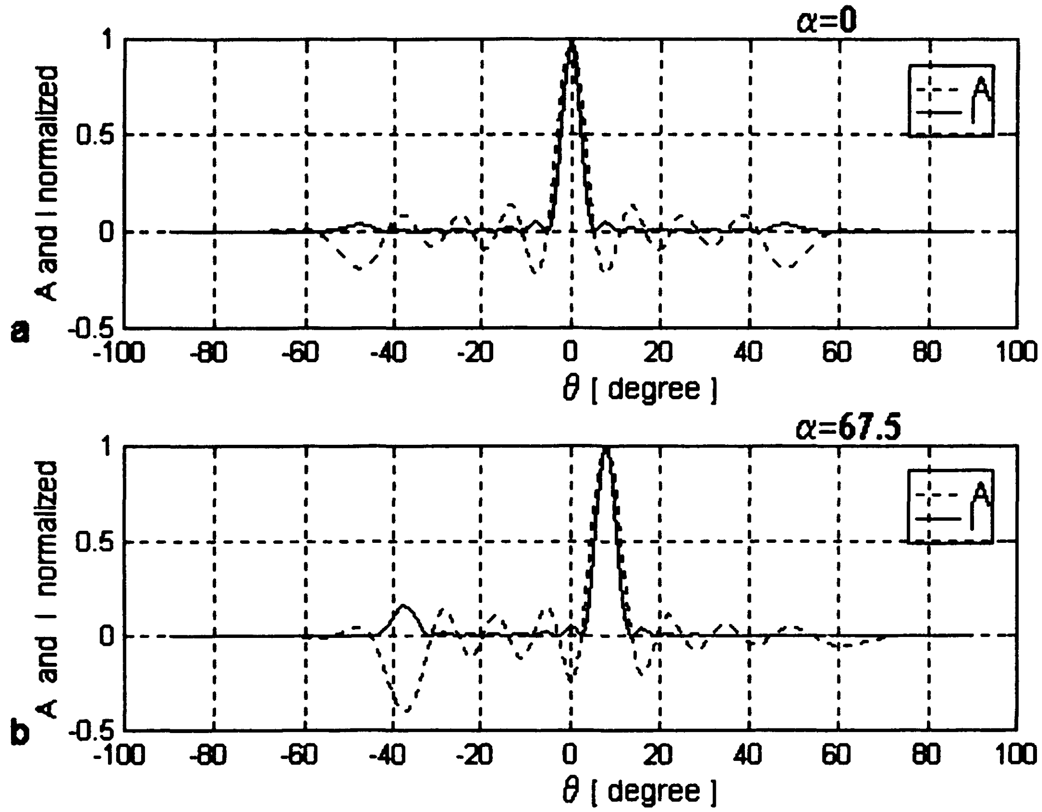

Fig. 4.9 The functions $A(\theta)$ and $I(\theta)$ normalized for θ ranging from **-90°** to **+90°** are presented. **a)** α = **0°**, **b)** α = **67.5°**.

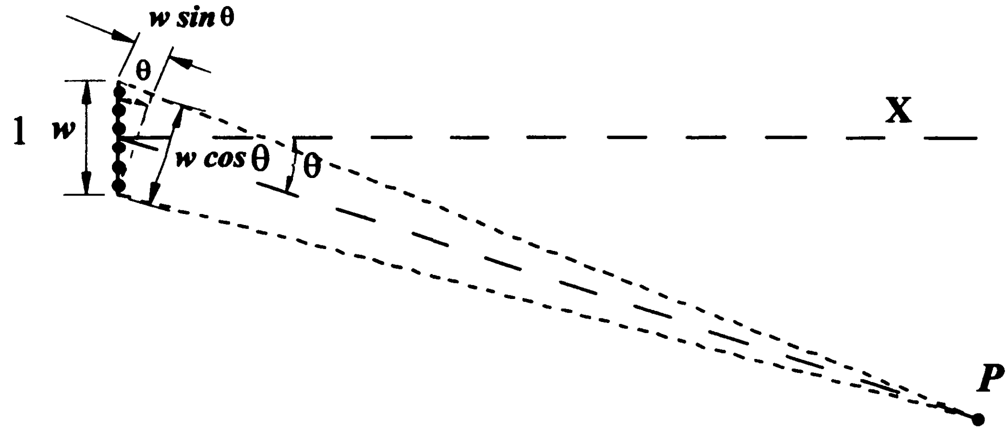

Fig. 4.10 A single array element **1** of length ***w*** is represented by a line constructed of ***N*** point sources. θ is the angle between the element axis and the straight line from the element axis origin to a generic point ***P***. The distance between consecutive point sources is ***w/N***. The difference between path lengths from any two points sources to ***P*** can be approximated by $(\Delta n/N)w\sin\theta$ where Δn the difference between the points order numbers. The source projection in P direction is given by ***w cos*** θ.

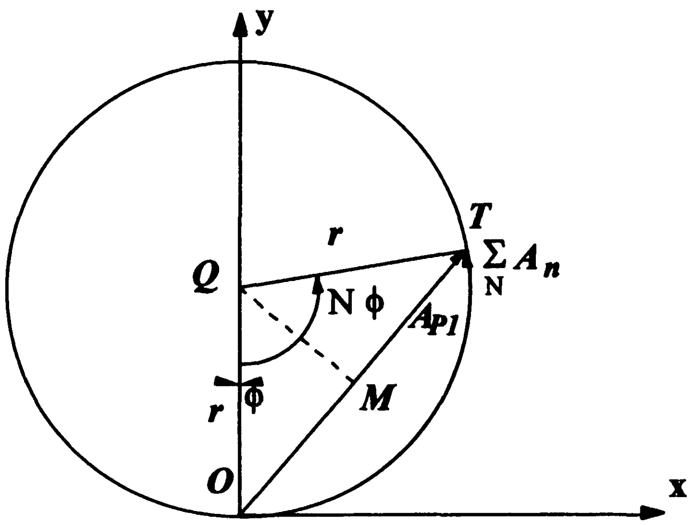

Fig. 4.11 Vectorial calculation of the resultant (A_{P1}) of the individual contributions (A_n) from N points representing a line source. In a line N tends to be large and therefore the angle ϕ between elements tend to zero and the vectors A_n tend to lie along the circumference arc ***OT***.

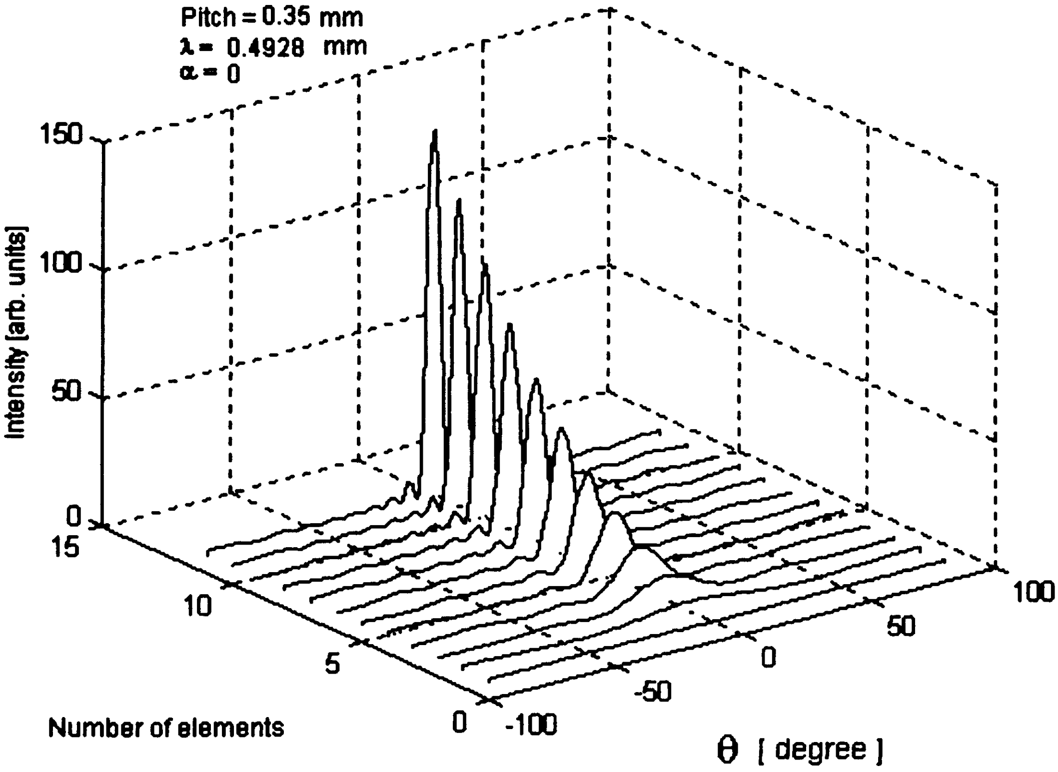

Fig. 4.12 Waterfall diagram of the function $I_R = F^2(\theta, N_e)$ for $N_e = 1, 2, 3, ...12$ point sources. A set of constant values of $\alpha = 0$, $\lambda \approx 0.5$ mm and $d = 0.35$ mm is adopted. The effect of the number of elements on the acoustic field generated by an array transducer is presented. The diagram shows the increase in directivity and amplitude with N and the proportionality between I and N^2. This particular example shows the case of the pitch smaller than the wavelength. Comparing with the case presented in Fig. 4.13 it is possible to observe a smaller directivity in the main (central) lobe and no side lobes

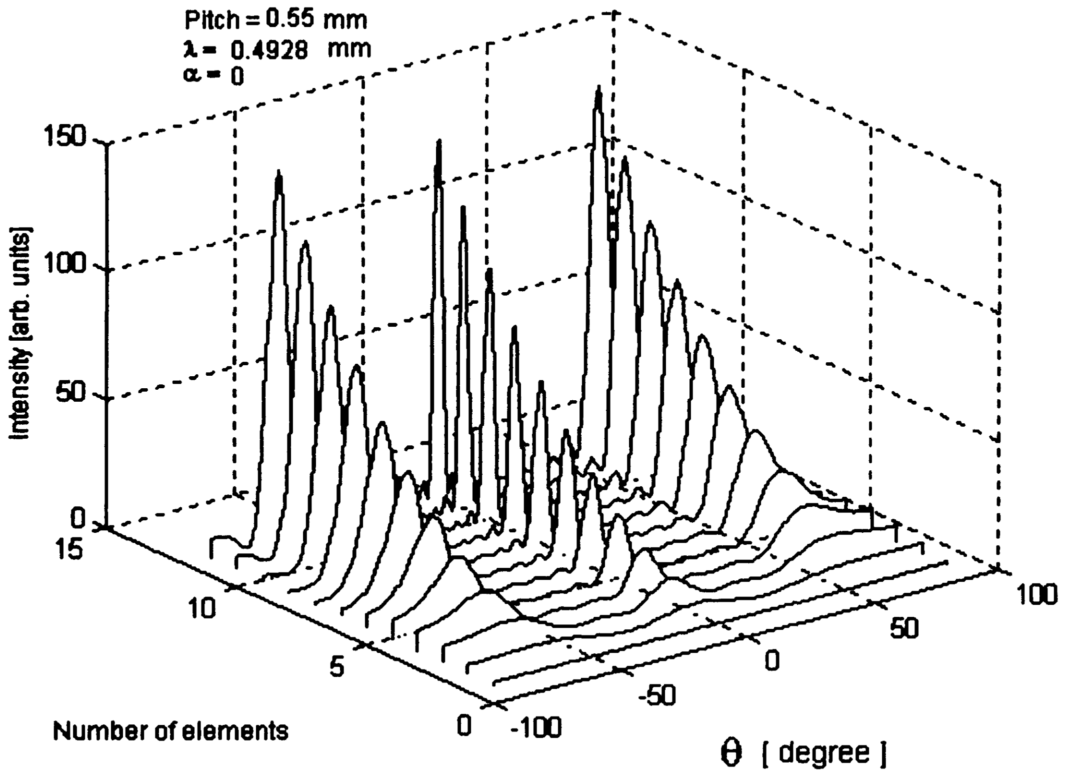

Fig. 4.13 Waterfall diagram of the function $I_R = F^2(\theta, N_e)$ for $N_e = 1, 2, 3, \ldots 12$ point sources. A set of constant values of $\alpha = 0$, $\lambda \approx 0.5$ mm and $d = 0.55$ mm is adopted. The effect of the number of elements on the acoustic field generated by an array transducer is presented. The diagram shows the increase in directivity and amplitude with N and the proportionality between I and N^2. This particular example shows the case of the pitch larger than the wavelength. Comparing with the case presented in Fig. 4.12 it is possible to observe a stronger directivity in the main (central) lobe and the formation of side lobes

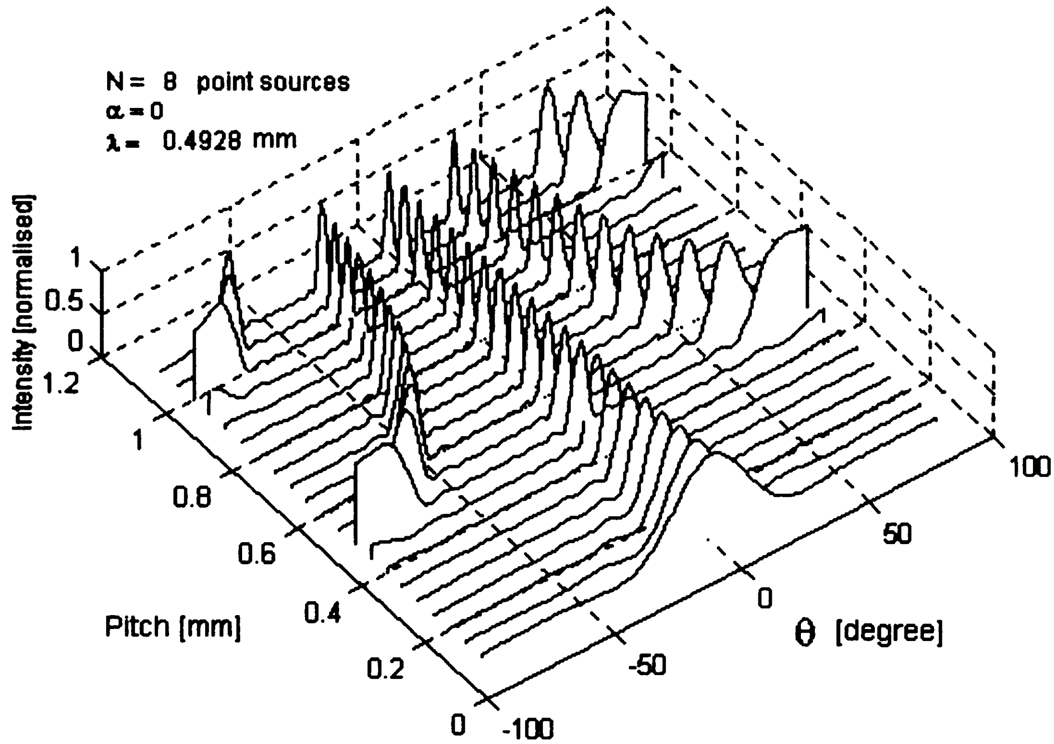

Fig. 4.14 Waterfall diagram of the function $I_R = F^2(\theta, d)$ for θ ranging from -90° to +90° and the pitch (d) ranging from 0.05 mm to 1.2 mm. A set of constant values are attributed to the number of elements $N = 8$, to $\alpha = 0$ and to $\lambda \approx 0.5$ mm. It is possible to observe that the beam directivity is inversely proportional to d. It also shows that higher pitch values lead to the formation of one or more side lobes closer to the main lobe.

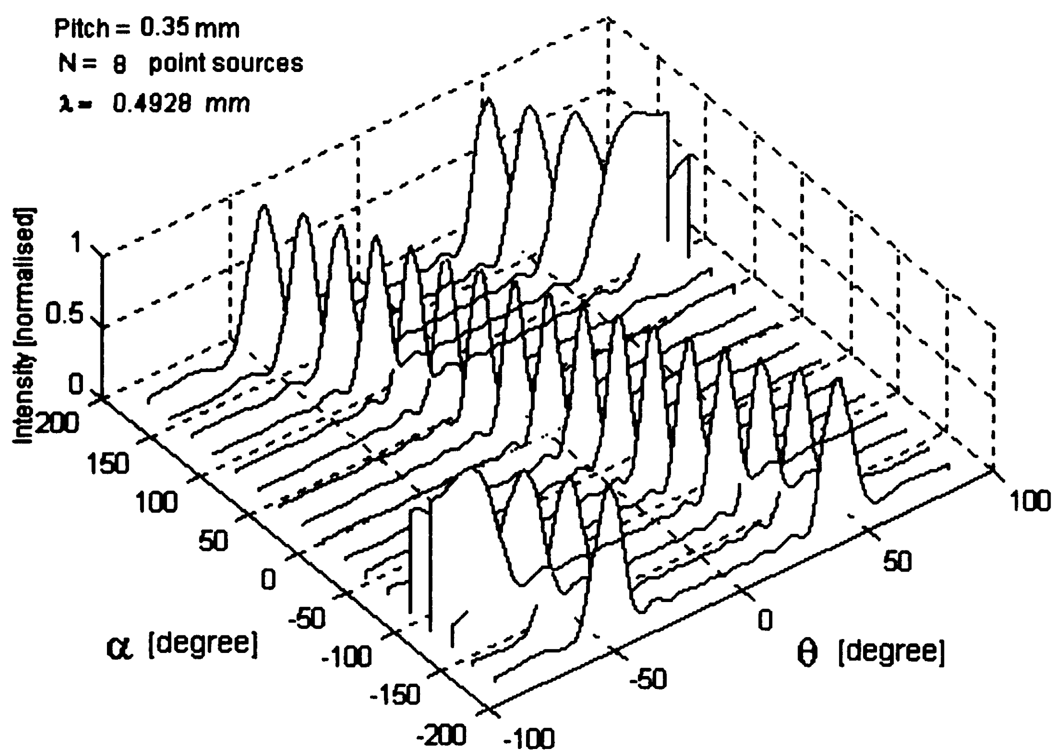

Fig. 4.15 Waterfall diagram of the function $I_R = F^2(\theta, \alpha)$ for θ ranging from -90° to +90° and α ranging from -180° to +180°. A set of constant values are attributed to the number of elements $N = 8$, to $d = 0.35$ mm, and $\lambda \approx 0.5$ mm. This diagram shows the effect of α on the beam steering and the formation of side lobes at extreme values of α and θ. Comparing this with Fig. 4.16 it is possible to observe that lower pitch values lead to increase of the sensitivity if of $I_R(\theta)$ to α, and decrease in the beam directivity

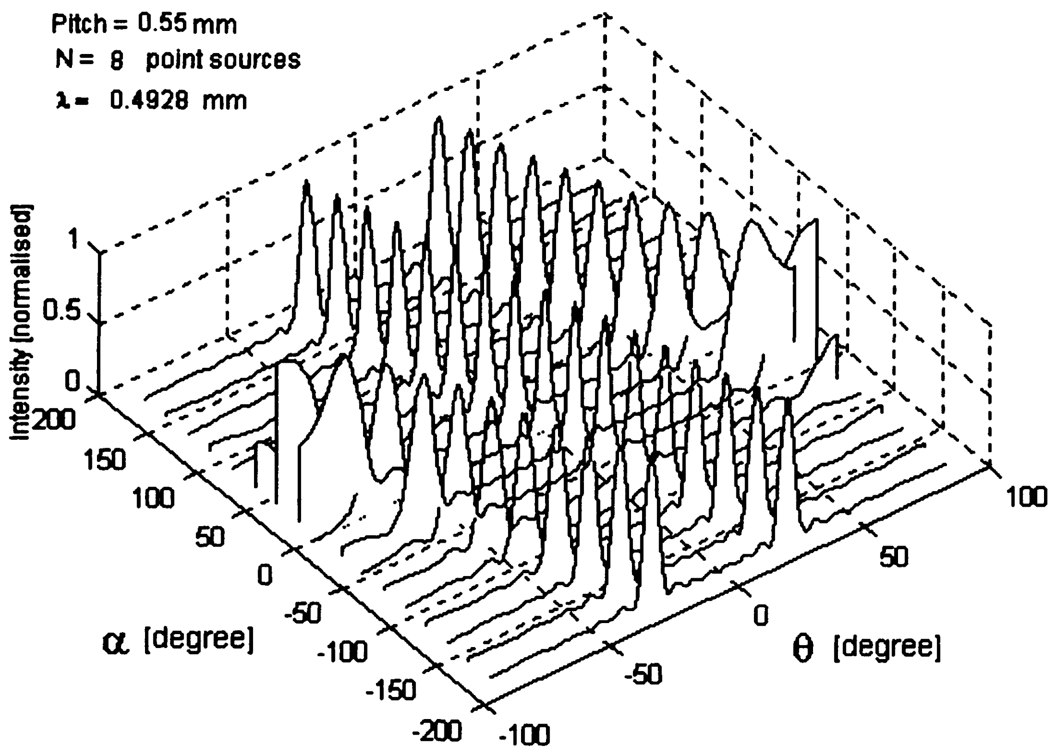

Fig. 4. 16 Waterfall diagram of the function $I_R = F^2(\theta, \alpha)$ for θ ranging from **-90°** to **+90°** and α ranging from **-180°** to **+180°**. A set of constant values are attributed to the number of elements $N = 8$, to $d = 0.55$ mm, and $\lambda \approx 0.5$ mm. This diagram shows the effect of α on the beam steering and the formation of side lobes at extreme values of α and θ. Comparing this with Fig. 4.15 it is possible to observe that larger pitch values cause a decrease of the sensitivity of $I_R(\theta)$ to α, and increase in the beam directivity

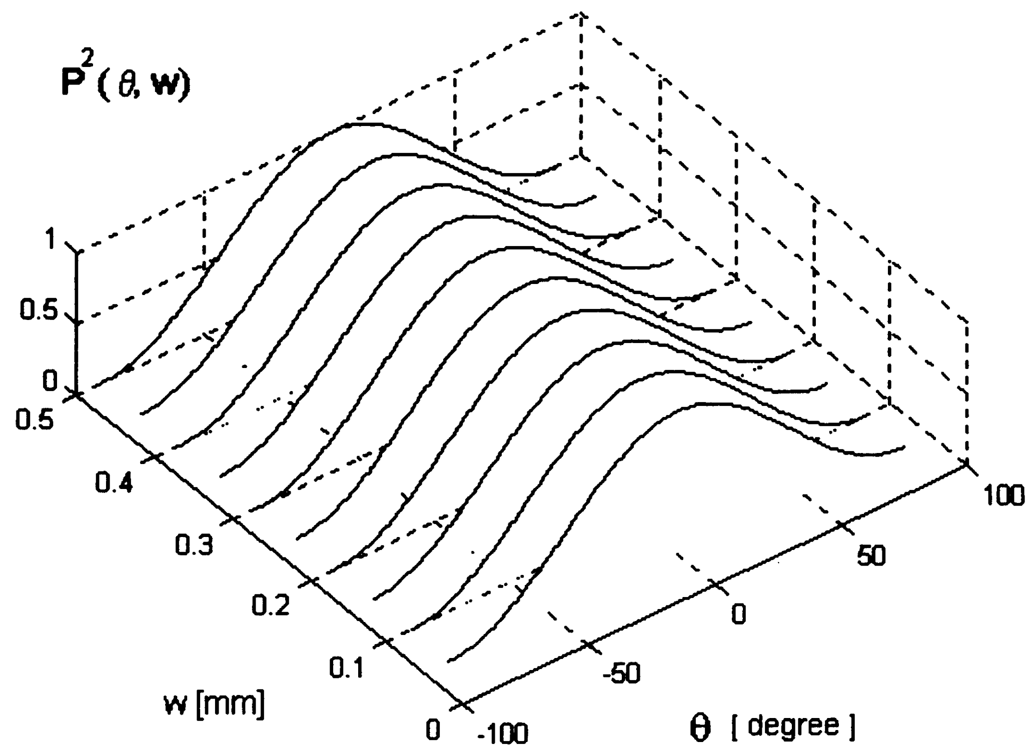

Fig. 4.17 Waterfall diagram of $P^2(\theta, w)$ for θ ***ranging*** from -90° to +90° and w ranging from 0.05 mm to 0.5 mm in intervals of 0.05 mm. Each line of this array represents the vector $P^2(\theta) = \cos^2\theta$ which represents the element projection as a function of the steering angle. P is independent of w and therefore all lines are equal. This representation enables the comparison between the effects of the projection and diffraction.

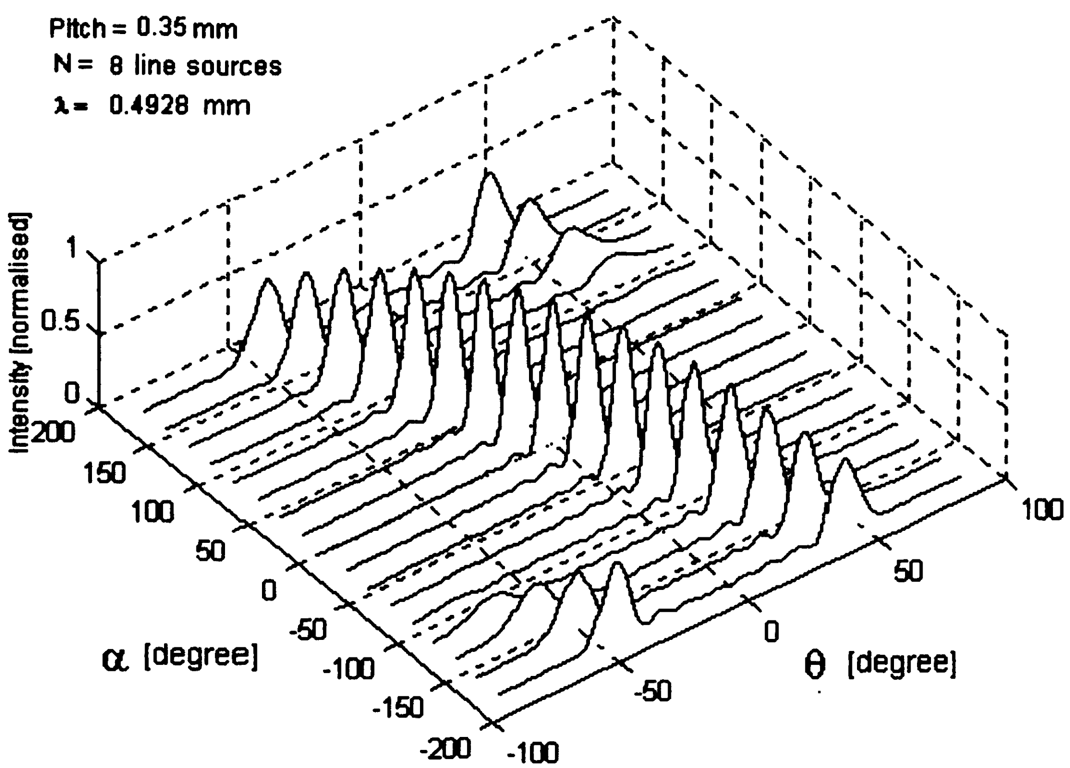

Fig. 4.18 Waterfall diagram of the function I_{RP} which is calculated by performing the dot product of each line of $F^2(\theta, \alpha)$[1] with $P^2(\theta)$ This diagram shows the attenuation caused by the projection in the amplitude of the steered acoustic field generated by an array of line sources. Comparing this with Fig. 4.15 it is possible to observe the stronger attenuation for larger values of θ as is the case of the side lobes and extreme steering angles.

[1] As presented in Fig. 4.15: For θ ranging from -90° to +90° and α ranging from -180° to +180°. A set of constant values are attributed to the number of elements $N = 8$, to $d = 0.35$ mm, and $\lambda \approx 0.5$ mm.

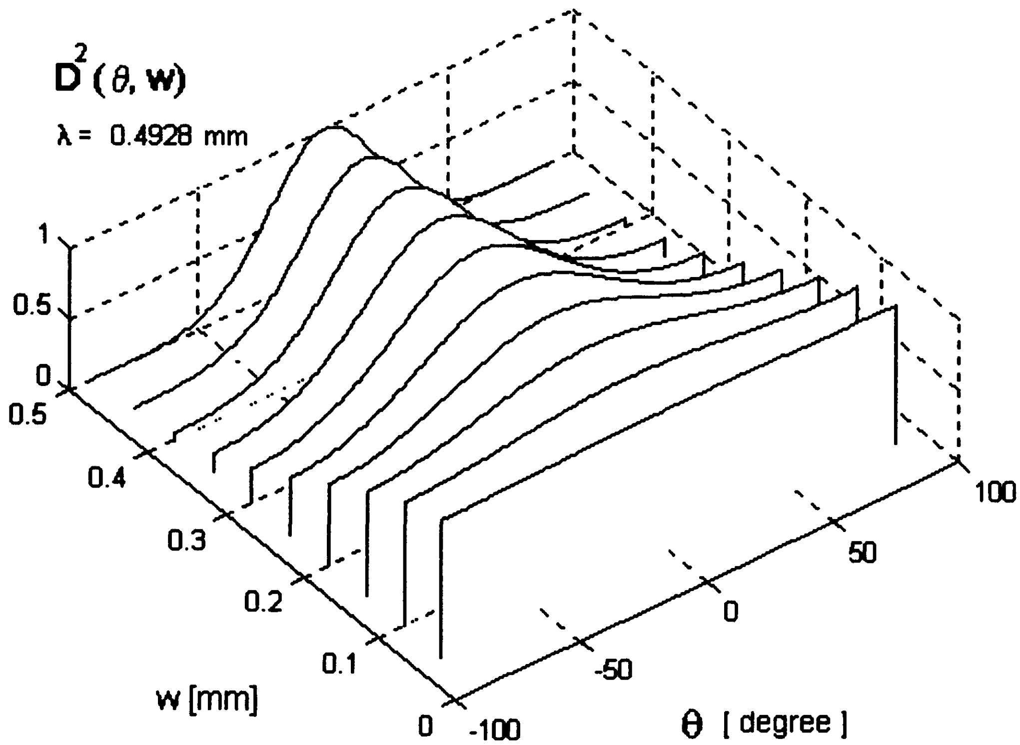

Fig. 4.19 Waterfall diagram of $D^2(\theta, w)$ for θ ***ranging*** from -90° to +90° and w ranging from 0.05 mm to 0.5 mm in intervals of 0.05 mm. Each line of this array represents the vector $D^2(\theta) = sinc^2\gamma$ where $\gamma = \frac{kw}{2}\sin\theta = \frac{\pi}{2}\cdot\frac{w}{\lambda}\sin\theta$. which represents the diffraction as a function of the steering angle and element width w. Comparing $D^2(\theta, w)$ and $P^2(\theta, w)$ shown in Fig. 4.17 is easy to see that, for small values of w, the influence of the projection is the most significant while the influence of the diffraction is negligible. For larger values of w the influence of the diffraction grows and its effect becomes the more significant.

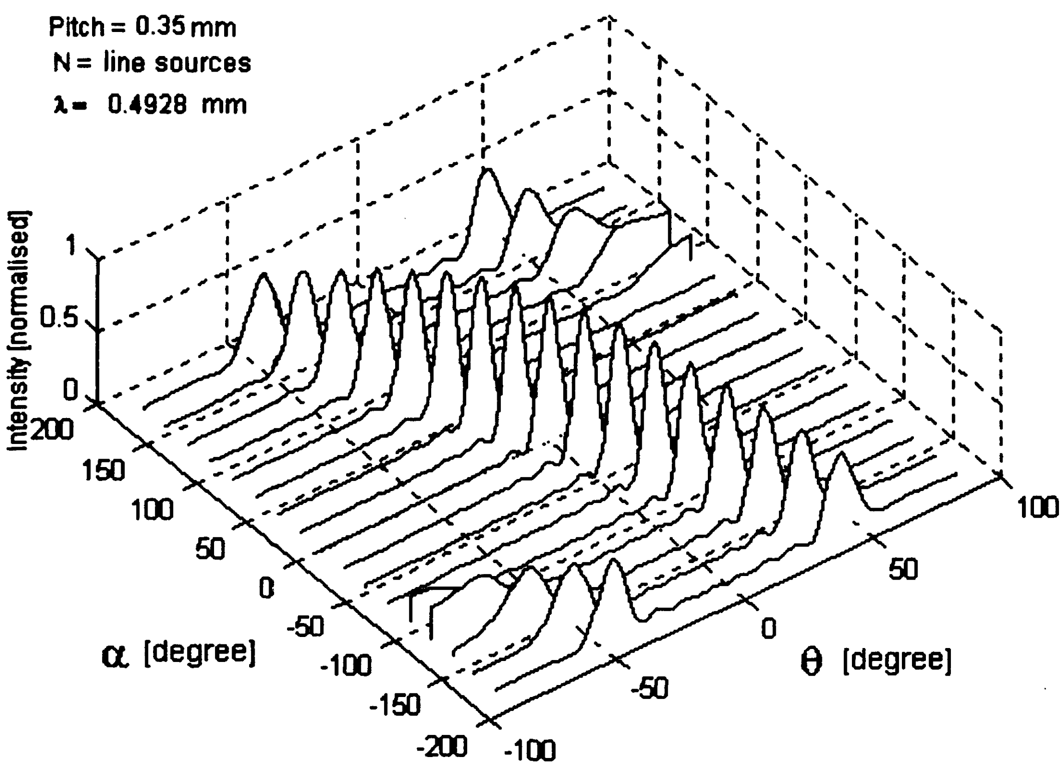

Fig. 4.20 Waterfall diagram of the function I_{RD} which is calculated by performing the dot product of each line of $F^2(\theta, \alpha)$[II] with $D^2(\theta, w)_{w=0.3}$ This diagram shows the attenuation caused by the diffraction in the amplitude of the steered acoustic field generated by an array of line sources. Comparing this with Fig. 4.15 it is possible to observe the stronger attenuation for larger values of θ as is the case of the side lobes and extreme steering angles. Comparing with Fig. 4.18 it is possible to see that for w=0.3 mm the effect of diffraction is less significant than the effect of the projection.

[II] As presented in Fig. 4.15: For θ ranging from -90° to +90° and α ranging from -180° to +180°. A set of constant values are attributed to the number of elements $N = 8$, to $d = 0.35$ mm, and $\lambda \approx 0.5$ mm.

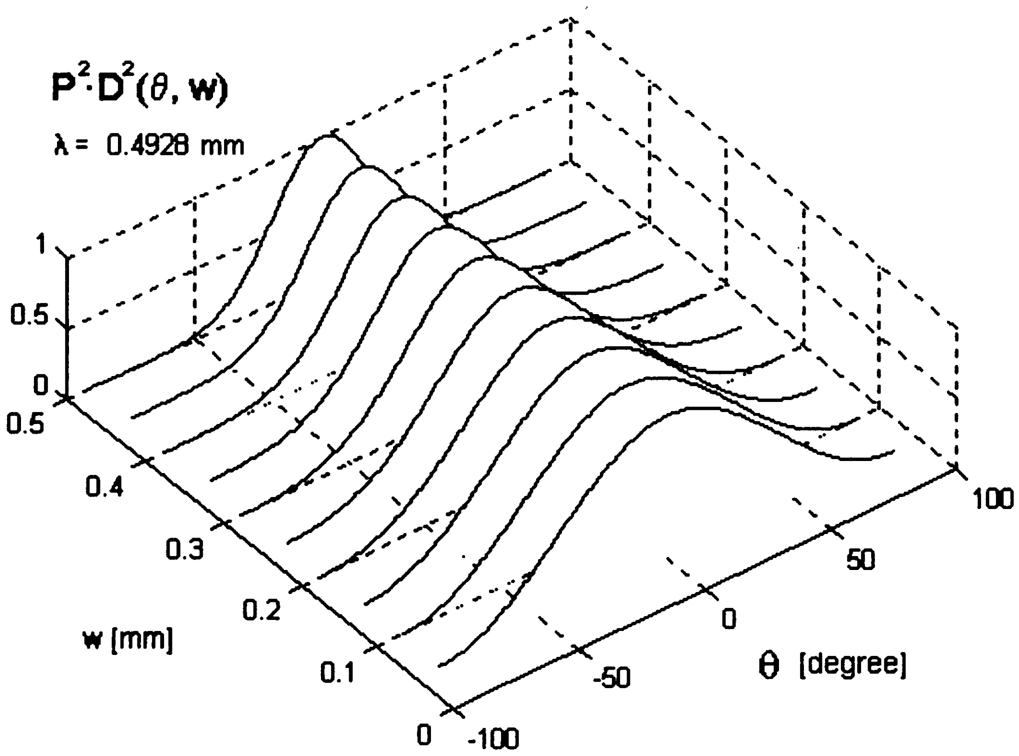

Fig. 4.21 Waterfall diagram of P^2 (θ, *w*)•D^2(θ, *w*) for θ ***ranging*** from -90° to +90° and *w* ranging from 0.05 mm to 0.5 mm in intervals of 0.05 mm. This presents the combined effect of projection and diffraction as a function of the steering angle θ and element width *w*.

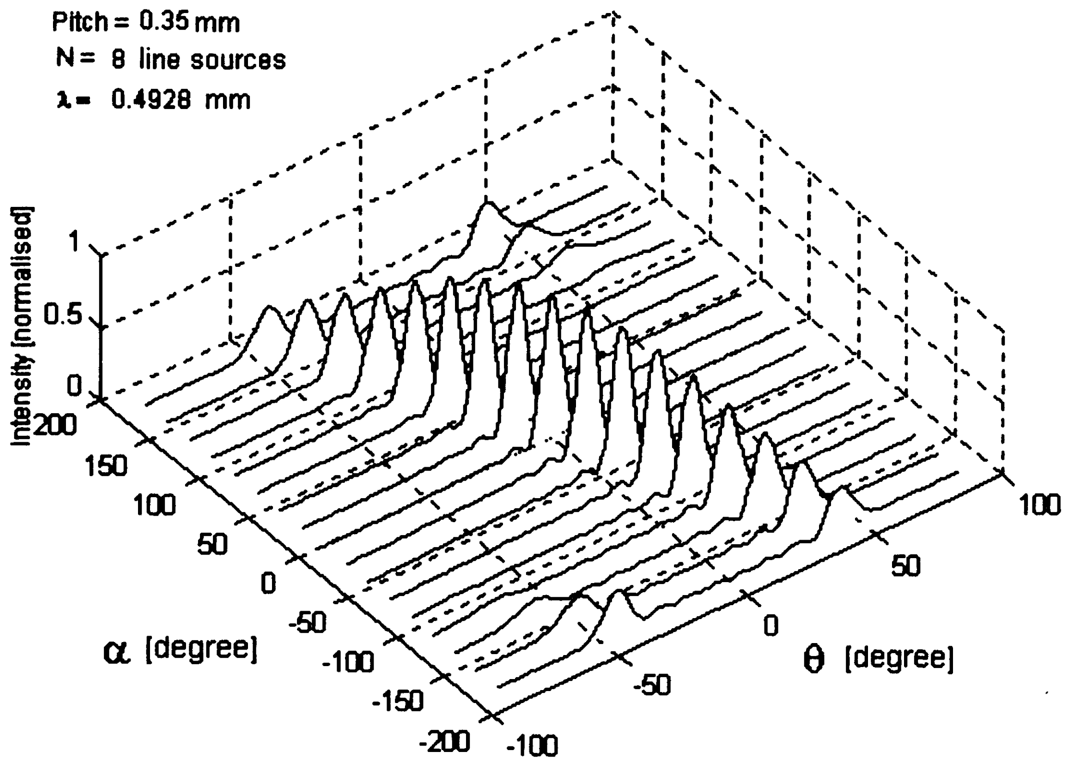

Fig. 4.22 Waterfall diagram of the function I_{RPD} which is calculated by performing the dot product of each line of $F^2(\theta, \alpha)^{III}$ with $P^2(\theta, w)\bullet D^2(\theta, w)_{w=0.3}$. This diagram shows the attenuation caused by the projection and diffraction in the amplitude of the steered acoustic field generated by an array of line sources.

[III] As presented in Fig. 4.15: For θ ranging from -90° to +90° and α ranging from -180° to +180°. A set of constant values are attributed to the number of elements $N = 8$, to $d = 0.35$ mm, and $\lambda \approx 0.5$ mm.

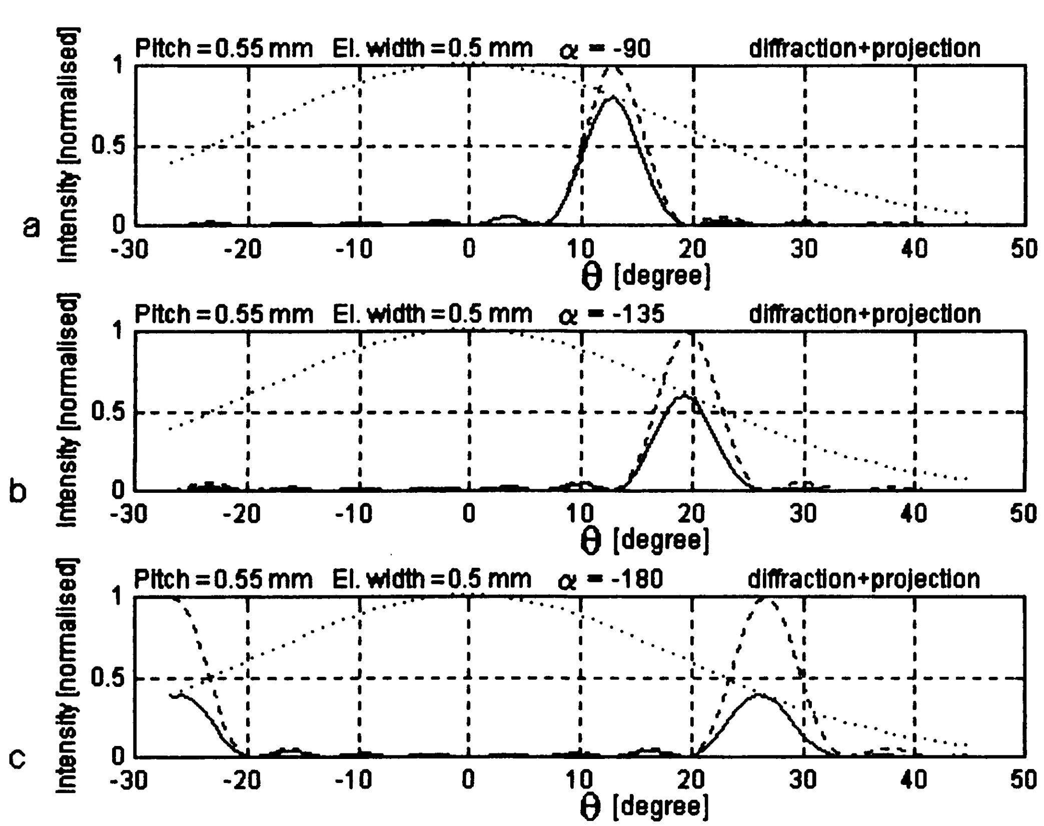

Fig. 4.23 The effect of projection and diffraction as a function of the steering angle θ. In all three diagrams the dotted line represents the product $P(\theta)^2 \bullet D^2(\theta)_{w=a}$. (for a = 0.5 mm). The dashed line represents the maximum profile of the acoustic field generated by an array of point sources $I_R(\theta, \alpha)$ (not affected by projection or diffraction). The solid line represents the acoustic field profile $I_{RDP}(\theta, \alpha)$ generated by an array of line sources measuring 0.5 mm (affected by projection and diffraction). (a, b, and c) correspond to progressively larger values of α (-90°, -135°, -180°). It is possible to observe that for higher values of θ the attenuation and distortion of the acoustic field as a consequence of diffraction and projection is also higher.

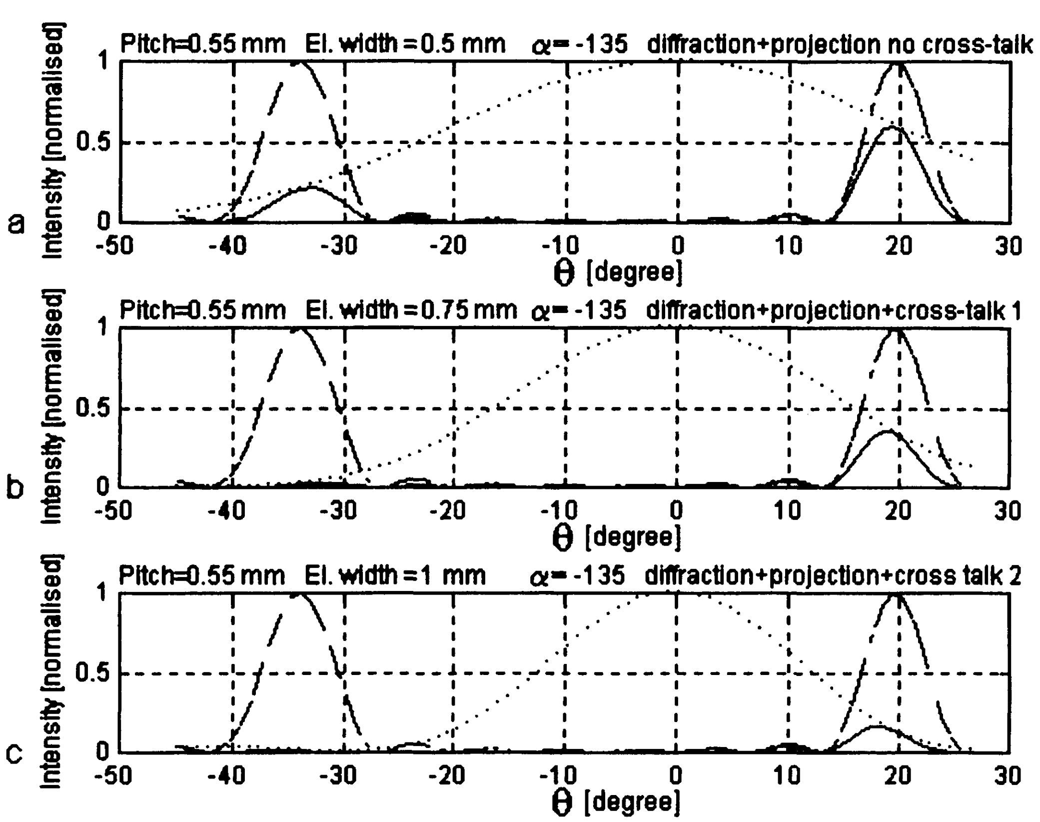

Fig. 4.24 The effect of progressively larger cross-talk as a function of the steering angle θ. In each diagram the dashed line represents the maximum profile of the acoustic field generated by an array of point sources $I_R(\theta, \alpha)$ (not affected by projection or diffraction). The solid line represent the acoustic field profile $I_{RDP}(\theta, \alpha)$ generated by an array of line sources (affected by projection and diffraction). The dotted line represents the product $P(\theta)^2 \bullet D^2(\theta)_{w=a}$. **a)** corresponds to the case of no cross talk where the effective **a** and real width *w*, are equal. **b)** corresponds to the case of cross-talk characterized by attributing to the effective width **a** of the element the value **1.5** × *w* **c)** corresponds to the case of cross-talk characterized by attributing to the effective width of the element **a** the value **2** × *w*.

Chapter 5

Array Transducer – Construction

5.1 Introduction

There are no CW Doppler array transducers commercially available and therefore it was necessary to construct one from scratch. The description of this work is presented in this chapter divided into two parts. The first part consists in a sequential description of the development of the four experimental prototypes during which progressive improvements and construction techniques where gradually introduced and tried. The second part consists in a detailed description of the construction of the latest version (fourth) which represents the last and most advanced stage of the transducer development achieved in this thesis.

5.2 Transducer development – Sequential description

5.2.1 First version

The first version of the transducer (Fig 5.1a) was designed with the purpose of overcoming the difficulty in handling the thin individual elements of the array: A single large rectangular piece of piezo ceramic transducer was glued with conductive epoxy (Circuit Works Conductive Epoxy) on top of a specially etched printed circuit designed to provide the individual electrical connections between the transducer elements and respective associated electronics. This ceramic was subsequently cut between the tracks with a diamond saw producing 20 elements with their rear faces electrically connected to the pins of a 'D' connector. The front faces of all elements were subsequently connected to the earth track with conductive paint. In this early version the use of PCB and differing methods of bonding and electrical connections to the ceramic were tested. Progressively smaller pitches were tried down to the limit of the equipment available for cutting the ceramic. This was a circular diamond disk 0.35 mm thick (Van Moppes model 1 A1R) assembled in a milling machine (Makers-Adcock and Shipley Ltd). The smallest pitch achieved with this equipment was 0.66 mm. This transducer was tried during the testing of the transmission circuits of the Doppler Ultrasound Phased Array Transceiver (DUPAT), however because of its very low acoustic output and strong RF noise generation it was soon replaced by an improved second version (Fig 5.1b).

5.2.2 Second version

In the second version the pitch size was 0.66 mm and the number of elements was limited to eight. It presented two new features: a) air backing which is more convenient for CW operation and improves the efficiency of acoustic generation, b) a matching layer which besides improving the acoustic efficiency protects the ceramic front electrode. It was constructed with a new shape, easier to attach to the acoustic tank window and also designed to provide better RF noise shielding. In order to prevent the coupling gel from entering the air backing space a low viscosity silicone rubber was employed for sealing the space between elements without producing strong acoustical cross talk. This transducer was employed in testing the transmission circuits of the DUPAT and in the first measurements of the acoustic field at different steering positions (Fig 8.7).

To test the DUPAT as a CW Doppler instrument two transducers were attached together, one for transmitting and one for receiving. It proved very difficult to align correctly both transducers and, in addition, the resulting transducer was cumbersome and difficult to hold in position. A new version was then constructed. (Fig 5.2).

5.2.3 Third version

This third version was also made with a pitch of 0.66 mm and incorporating all the new features of the previous version. Its main improvement consisted of the fact that the transmitter and receiver were constructed together. Such a transducer required a more elaborate and precise construction technique. The two ceramics had to be positioned at an angle necessary to make the beam converge in the same sample volume at about 30 mm from the transducer face. It was necessary to build a double support for the ceramics capable of holding them at an angle and also of supporting the extremities in order to maintain the air backing (Fig 5.2, a/b). Because of the angle between the ceramics the transducer face was modified. The flat surface of the matching layer which was simply made of epoxy and ground to the required thickness in the previous version was replaced here by a cylindrical surface having its centre of curvature at the point of convergence of the two ceramics axes (Fig. 5.6). This surface had to be made with the correct shape and dimensions because it could not be ground. For its manufacture a mould of Teflon® was made. It was positioned precisely above the ceramics in order to create a volume with the shape and dimensions of the required matching layer (Fig 5.2d). This volume was then filled with a mixture of epoxy and tungsten powder described in detail in the Section 5.3.4.2, see also (Figs 5.2e and 5.10). It was also necessary to align precisely the PCBs on the transmit and receive sides in order to make sure that each cut starting between two tracks in the transmit side would finish between the corresponding tracks on the receive side (Figs 5.2, f/g/h). The correct positioning of the saw between tracks was complicated by the fact that at the time of cutting, the tracks were hidden below the matching layer and the ceramic. The solution to this problem is described in section 5.3.4. It should be noted that besides providing the visualisation of the track position (Fig 5.2a and 5.2b) such a process was also useful in two other ways: a) It permitted the reversal of the direction of the PCB ground electrode towards the inside of the transducer (Fig 5.2, b/c). This enabled a stronger earth connection to the ceramic electrode. b) It also provided a support for the Teflon® mould during the making of the matching layer (Fig 5.2d).

An early version of the CW Doppler steering instrument consisting of the DUPAT equipped with the third version transducer was tested. This instrument was capable of generating steered acoustic fields such as the ones shown in Fig 8.7. Its performance however as a Doppler instrument was poor. The acoustic field generated by the transmitter side was weak and the audio signal output from the receiver side had a low signal to noise ratio. Interpreting this result from the transducer point of view it was concluded that this was a consequence of the relation between of the pitch size of 0.66 mm and wavelength of approximately 0.5 mm (3.125 MHz wave in tissue). As discussed in sections 4.2.3 and 4.2.5 such a relation between pitch and wavelength causes side lobe formation and a low main lobe energy. This led to the construction of a fourth version of the transducer with a pitch of 0.35 mm.

5.2.4 Fourth version

It was not possible to construct the fourth version just using only the facilities of the Department of Medical Physics. The PCBs were made using a lay-out produced in the

Departmental electronic workshop and exported as Gerber Files to P.W. Circuits Ltd who carried out the tasks of etching, gold plating and cutting them to the exact dimensions (Figs 5.3 a/b). In the Department these PCBs were cut and assembled together as described in Section 5.3.4 and Fig 5.7. They are also shown in Figs. 5.3, c/d and 5.4 b/c. The transducer was also constructed in the Department and the steps in the construction sequence are presented in Fig. 5.4. In Figs. 5.4, a/c/d/e/f/g, it is possible to observe how the transducer body was built to hold the ceramic with air backing. Figs 5.4 h/i/j show how the electrical connections to the ceramic were made to provide contact to each array element. Fig 5.4k shows the placement of the matching layer mould which was made in the same way as already described for version three (see also Section 5.3.4.2).

After construction the transducer was sent to Load Point LTD - Wiltshire where its face was cut with a diamond saw 0.05 mm thick (cuts shown in detail in Figs 5.3, e/g) and returned to the Department where the gaps between elements were filled with silicone rubber, and the electrical connectors fitted in position. The face and rear of the transducer can be seen in Fig 5.3e.

5.3 Description of the construction of the fourth version

The job of assembling the transducer was manually executed in the Project Lab of the Department of Medical Physics. Because of the small dimensions and tolerances, most of the assembly work was done under a binocular microscope with the help of micrometers and callipers. Measurements were also made with a Griffin Linear Vernier Microscope with a precision of 0.01 mm, and in some cases small drill bits or wires with known dimensions were also employed either as standards or as gauges to check depth or cavity diameter. This work was assisted by the Mechanical Workshop of the Department, which made the fibreglass parts and also the gigs and supports necessary to hold the parts in position for the grinding and glueing to the required tolerance.

5.3.1 Specifications

The construction of the transducer was guided by the following specifications:

- Continuous Wave Doppler Transducer (implying that was necessary to have two arrays, one for transmitting and one for receiving).
- Capable of "in plane" steering to ±20° both in transmission and in receiving mode.
- An operating frequency of 3.125 MHz (explained in section 7.2).

In order to specify the dimensions of the array to be constructed it is necessary to refer to the theory as presented in sections 4.2.

5.3.2 Dimensioning

Assuming a given element dimension, the sensitivity, power output and directivity can in principle be increased by increasing the number of array elements (Whittingham 1991). In order to limit the amount of electronics needed (each element requires an independent dedicated electronic circuit) eight was chosen as the maximum number of elements (N) of the array both for transmitting and receiving. Fig. 4.12 and Fig. 4.13 present the relative maximum intensity profiles $I_R(\theta,N)$ for a transducer with N equal to 1, 2, 3, ...,12 ($\alpha = 0°$ and pitch = 0.35 mm and 0.55 mm respectively).

Ideally an array pitch of less than half wavelength would allow steering of $\pm 90^0$ without producing secondary lobes (Whittingham 1991). A 3.125 MHz wave has a wavelength of 0.4928 mm in water assuming 1540 m/s as the propagation speed in this medium. (In the present work water was assumed to be the reference medium concerning sound velocity propagation. It is not very different from most soft tissues and the experiments were executed in an acoustic tank filled with water).

The construction of an array with a pitch of 0.25 mm is perfectly attainable today. P.W. Circuits LTD (the PCB manufacturer) and Loadpoint LTD, (the firm which cut the transducer) can easily meet accuracy levels better than ± 0.01 mm. However, to make an array with 0.25 mm pitch poses difficult problems for a non specialist laboratory like ours. After a careful assessment of our limitations it was concluded that a pitch of 0.35 mm would be a safe choice.

The element width is given by the pitch size less the space between elements. As the irradiation/reception capacity of the transducer is function of the transducer active area, the smallest possible spacing was sought and this was 0.05 mm. As a consequence the width of the elements was 0.30 mm.

The electronic circuit constructed to drive the array is explained in detail in Chapter 6. At this stage it is sufficient to point out that it is a digital circuit which synthesizes eight separate signals of 3.125 MHz which can be individually shifted in phase by increments of 1/16 of a cycle. This implies that, with the present electronics, the array elements can be excited by signals presenting a sequential phase difference α which can range from: $0°$ to $15\times360°/16$ in intervals of $360°/16$.

To perform a simulation of the projected array transducer operation the basic specifications of the array were: Pitch: 0.35 mm Element width: 0.30 mm

It was also assumed that the array elements were driven by sinusoidal signals of 3.125 MHz and the phase difference between these signals can range from 0° to 360° in steps of 22.5°.

The result of the simulation is presented in Fig. 5.5. It shows: The list of phase steps necessary to steer the beam between -20° and +20°; the overlap between the intensity profiles corresponding to each steering position; the formation of side lobes; the effect of the projection and diffraction. It was assumed there was zero cross-talk in this simulation because it was thought that this factor can be modified and minimised by improvements in transducer construction. To introduce a 'cross-talk index' at this stage would arguably not bring any benefit therefore it was chosen instead to perform an experimental evaluation of cross-talk with the transducer finished. This is presented in Chap. 8.

From the simulation it was found that nine steering positions can cover the range -20° to +20°. It was also observed that up to ± 20° the attenuation caused by diffraction and projection does not exceed 25% and it is possible to see that the decrease in range caused by distortion of the acoustic field profile is negligible.

Table 5.1 is constructed taking the nine phase values of (α): zero and the four values adjacent to zero. The corresponding main lobe directions (θ) are calculated by entering the values of α in equation (4.22). The "in plane" displacement of the main lobe at 30 mm from the transducer face ($X_{30} = 30 \cdot \tan\theta$) is also presented.

α [°]	**0°**	**± 22.5°**	**± 45°**	**± 67.5°**	± 90°
θ [°]	**0°**	**± 5°**	**± 10.1°**	**± 15.3°**	**± 20.6°**
X_{30} [mm]	**0**	**± 2.7**	**± 5.4**	**± 8.2**	**± 11.3**

Table 5.1 Tabulation of the steering angle θ equation (4.22) and the displacement of the beam axis at 30 mm from the transducer face X_{30} (X_{30} = 30·tanθ) corresponding to α equal to **0°, 22.5°, 45°, 67.5°** and **90°**.

5.3.3 Lay-out

The CW Doppler transducer developed here comprises of both the transmitter and the receiver parts. They are joined together at such an angle that they point to the same sample volume at a distance of about 30 mm (for the in vitro test this distance is defined as the distance from the intersection of the beams to the centre of the face of each transducer) (Fig. 5.6).

As already explained, the construction lay-out was designed to overcome the difficulty of handling the tiny individual elements. The chosen method was to produce a large single element transducer, having built in all the electrical connections required for the array and converting it into an array by a cutting process described later.

The first problem was to ensure that all the array elements had their electrodes electrically connected to their own associated electronics. For this purpose a special printed circuit board (PCB) was produced to be incorporated in the transducer body and to link the piezo-ceramic electrodes to a connector. Despite the fact that the array would have just eight elements, the PCB was designed with extra capacity so as to be capable of supporting an array with up to twelve elements as a provision for further developments. The PCB was double sided, and was designed to make contact with the piezo-ceramic at the extremity. One face had etched conductive tracks with the same pitch as the proposed array (0.35 mm) surrounded by a ground plane. The opposite face was a plain conductive surface connected to the ground plane by plated through holes on the connector side (Fig. 5.4 a, b).

5.3.4 Assembly

By a process of cutting, grinding and pasting, described in Fig. 5.7 and shown in Fig. 5.3, c/d and 5.4, b/c), the PCB extremity was adapted to provide strong electrical and mechanical bonds to the ceramic.

Besides its electrical function, the PCB assembly also has a mechanical role as a part of the transducer body. It supports one extremity of the piezo-electric ceramic on its tip that is ground at an angle of 6.5° (Fig. 5.6). Both receiver and transmitter employ one such assembly.

They are held apart precisely aligned front to front by two pieces of fibreglass (FG). These pieces have a groove in their middle in order to hold a slab (SL) which supports the other extremity of the piezo ceramic (CE) both from receiver and transmitter sides. These five parts joined together form a support capable of holding in place the two rectangular piezo ceramics. These ceramics measure 6.5 x 6.5 mm and are supported by only 0.5 mm of fibreglass at each of their extremities (Fig. 5.8). Such an arrangement ensures the creation of air backing convenient for CW operation.

5.3.4.1 Electrical connections

The ceramic rear electrodes are connected to the track face of the PCB with a strip of conductive epoxy placed at the corner made by the two converging surfaces. The ceramic front electrode is connected to the PCB back face and ground plane with a string of conductive epoxy bridging the gap between the ceramic and the PCB facing the gap. A detailed view of the electrical connections to the ceramic electrodes is shown in Fig. 5.9. The electrical connection between the ceramic electrode, the back of the PCB and ground plane in addition to supplying the necessary electrical connections to the elements, also provides electrical shielding for the tracks inside the transducer.

5.3.4.2 Matching layer

Once the ceramic is in place and all electrical connections made, a matching layer capable of improving the coupling between medium and transducer (Kossof 1966) is formed. This matching layer, besides enhancing energy transfer, has the additional benefit of providing insulation and protection to the ceramic.

As already presented in Section 1.3.1, the acoustic impedance Z of a material is given by $Z = \rho c$ where ρ is the density of the material and c is the propagation speed of sound in the material. The acoustic impedance Z_m of the matching layer can be calculated according to the formula proposed by Desilets et al (1978) in (Silk 1984):

$$Z_m = Z_l^{3/7} Z_c^{4/7} \tag{5.1}$$

The ceramic employed was a type of PZT, (PZ26 produced by Ferroperm, Denmark). The impedance Z_c quoted for this ceramic is 3.4×10^7 kg/sm^2 (Kossof 1966). The load may be an acoustical phantom, and will eventually be the body skin coupled to the transducer with gel. For our purposes a load impedance of 1.54×10^6 kg/sm^2 was assumed. Inserting this values into equation (5.1), leads to $Z_m = 9.0\times10^6$ kg/sm^2

A matching layer of Epoxy on its own would present an impedance of 3.2×10^6 kg/sm^2. In order to increase this impedance, tungsten powder can be added to increase the density ρ_m and consequently Z_m However, c in a mixture of Epoxy and tungsten is not a linear function of the tungsten concentration. The behaviour of velocity of propagation and impedance in mixtures of Epoxy and tungsten powder with different concentrations has been described in the literature (Kossof 1966, Silk 1984, and Sayers et al 1984).

Fig. 5.10 extracted from Silk (1984) presents a compilation of experimental values of c for mixtures of Epoxy and tungsten with different densities. It shows that as the tungsten concentration increases there is an initial sharp fall in c from around 2.5×10^3 ms^{-1} which is the average velocity propagation in pure Epoxy. This fall in c will reduce the increase in impedance caused by the growing density. As the concentration of tungsten increases further, c continues to fall with a tendency to stabilise at values of the order of 1.5×10^3 ms^{-1} staying almost constant around this value until concentrations on the order of 40% tungsten in volume are reached when it starts to grow progressively faster, reaching once again the value for pure epoxy at concentrations of the order of 70% in volume.

Adopting a mixture capable of presenting an impedance near 9×10^6 kg/sm^2 would present manufacturing problems, as its preparation would require the use of compression, and this could lead to the breakage of the air backed ceramic. In the present work, a mixture of Epoxy resin (MY 753 with catalyst HY951 10 to 1) and tungsten powder (0.5 μm) in proportions of 1:1 in mass was adopted. It requires no compression, corresponds to a concentration of 7.2% in volume, and a density of 2.2×10^3 kg / m^3. The value of c at this concentration is situated in the range of 1.8×10^3 ms^{-1} to 2.0×10^3 ms^{-1} corresponding to an impedance in the range of 4.0×10^6 kg / sm^2 to 4.4×10^6 kg / sm^2. This mixture is very simple to handle and will adhere well to the piezo electric element.

Besides the impedance, the thickness of the matching layer must be taken into consideration, it must measure an odd number of quarter wavelengths (McSkimin 1959). Assuming the velocity of propagation in the matching layer is in the range of 1.8×10^3 ms^{-1} to 2.0×10^3 ms^{-1} the wavelength λ, for an acoustic wave of 3.125 MHz ranges from 0.576 to 0.64 mm, and $\lambda/4$ from 0.144 to 0.160 mm. This is a very small dimension to be dealt with manually therefore the thickness adopted for the matching layer was $3\lambda/4$ thus ranging from 0.43 to 0.48 mm.

As explained before the transducer under construction consisted of both transmitting and receiving parts assembled together at an angle. A mould was employed to shape the layer on the front of both ceramics at the same time.

Fig. 5.11 presents the side view of the transducer facing upwards. The mould is placed on the top supported by the two external PCBs. The moulding surface is a plane cylindrical surface with a radius of 30 mm and width of 6 mm. The heights of the PCB supports on each side determine precisely the distance between the mould and the ceramic's surface. This space is then filled with the mixture of Epoxy and tungsten powder. The resin cures in 24 hours at room temperature and has low viscosity for the first 2 hours after preparation. Before application it is submitted to vacuum for 20 minutes in order to extract air bubbles trapped during the mixing process. The mould was made of Teflon because this material does not adhere to Epoxy and after setting, the mould is easily removed. As can be observed the distance between ceramic and mould is not constant as there is a slight curvature which will produce a slight 'out of plane' focusing .

5.3.4.3 Cutting

At this stage the transducer is ready for the cutting process which will the change it from a single element to an array transducer with all the elements having their own matching layer and electrical connections.

A set of 13 slits 0.05 mm wide, spaced by 0.35 mm are cut in the face of the transducer and are positioned precisely around the tracks with the help of the tracks visible on the outside surface. They are 2 mm deep which is enough to split the matching layer, the ceramics, and the strings of conductive Epoxy connecting the metallised face of the ceramics electrodes to the tracks (Fig. 5.12). The cutting was done at Loadpoint Ltd, Wiltshire-UK.

After cutting, all the tracks became electrically isolated from each other, individually linking the rear electrode of each element to a particular isle on the connector site in the PCB. The front electrodes remained electrically interconnected through the rear face of the PCB, linked to the ground plane on the track side of the PCB and also to the four external isles on the PCB connector site.

5.3.4.4 Filling the gaps between elements

The air gaps between elements must be filled to strengthen and seal the array, preventing the coupling paste entering the gaps and the air backing space. The filling material should maintain electrical and mechanical insulation between elements as cross-talk would compromise the array performance. The material adopted was a low viscosity RTV Silicone Rubber. The preparation of the Silicone Rubber was made by mixing the RTV Rubber Base with an RTV Catalyst in the proportions 20:1. The material has a low viscosity for about 2 hours after mixture and takes 48 hours to set. Before application the Silicone Rubber is submitted to vacuum for 5 minutes in order to extract air bubbles trapped during the mixing process. The liquid Silicone Rubber is applied in small amounts on the transducer surface over the tracks, where capillary action cause it to flow into the gaps, filling them completely. The capillary force is sufficient to hold the Silicone Rubber in place until set.

The last stage of manufacture is to solder the electrical connectors in place.

5.3.4.5 List of materials employed in the construction of the transducer

1. Piezo ceramics PZ26 (Ferroperm® Denmark).
2. Conductive Epoxy "CW2400 Conductive-Epoxy " Circuit Works® RS
3. Epoxy resin MY753 casting plus HY951 hardener
4. General Purpose Epoxy from ®Ciba (GP-Epoxy)
5. Tungsten (W) Powder (mean particle size - 0.5μ) - Goodfellow UK
6. RTV silicone rubber (Two parts- Rubber and Catalyst) RS.
7. Double face PCB 1.6 mm thick
8. Fibreglass boards

9. Connector M 100 16 pins right angled (Samteck UK)

5.4 Summary

The development and construction of the 'phased array CW Doppler transducer' built for this project was presented in this chapter. The fourth transducer version constitutes the latest stage of development achieved so far in this project and the description of its construction is detailed enough to allow its reproduction. This transducer still presents limitations and these are mainly caused by cross-talk as presented in Chapter 8. Nevertheless it is able to steer the beam over a limited range which is still larger than the range achieved with a non stereable transducer. The fourth version of the transducer was employed in the tests of the Doppler tracking instrument.

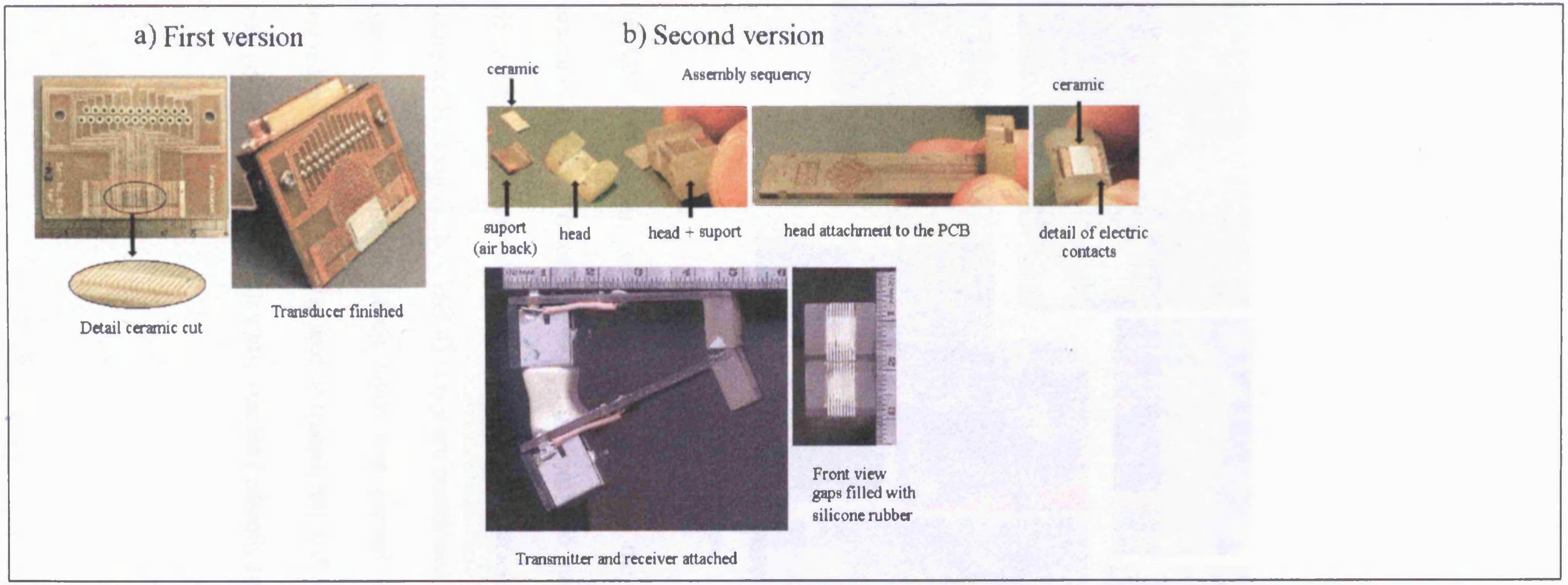

Fig. 5.1 **a**) Photographs presenting the first version of the array transducer. It consists basically of a diced ceramic glued with conductive epoxy to a PCB circuit especially made to provide individual electrical connections to each array element. **b**) Sequence of photographs showing the assembly sequence of the second version of the array transducer with a pitch of 0.66 mm. The 'head' of the transducer was designed to hold the ceramic with air backing, matching layer and better RF shielding. This was the first attempt to construct a CW Doppler array transducer by joining of the transmitter and receiver.

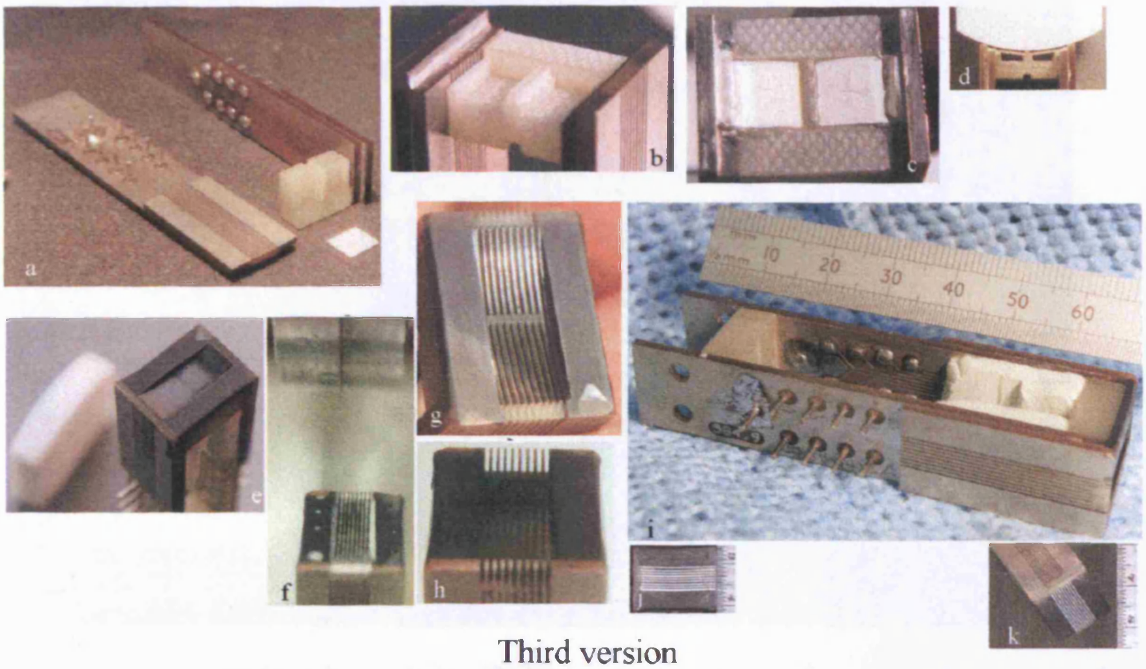

Third version

Fig. 5.2 Series of photographs showing the assembly sequence of the third version of the array transducer with a pitch of 0.66 mm. In this version both transmitter and receiver are constructed together. The two ceramics are held by their extremities to ensure air backing (**a**, **b**, **c** and **d**). They are positioned at the angle necessary to make the beam converge. The matching layer was curved and constructed to the required dimensions (**c**, **d** and **e**). The face of transmitter and receiver sides were cut at the same time, and the gaps filled with a low viscosity silicone rubber (**f**, **g**, **h**, **I**, and **k**).

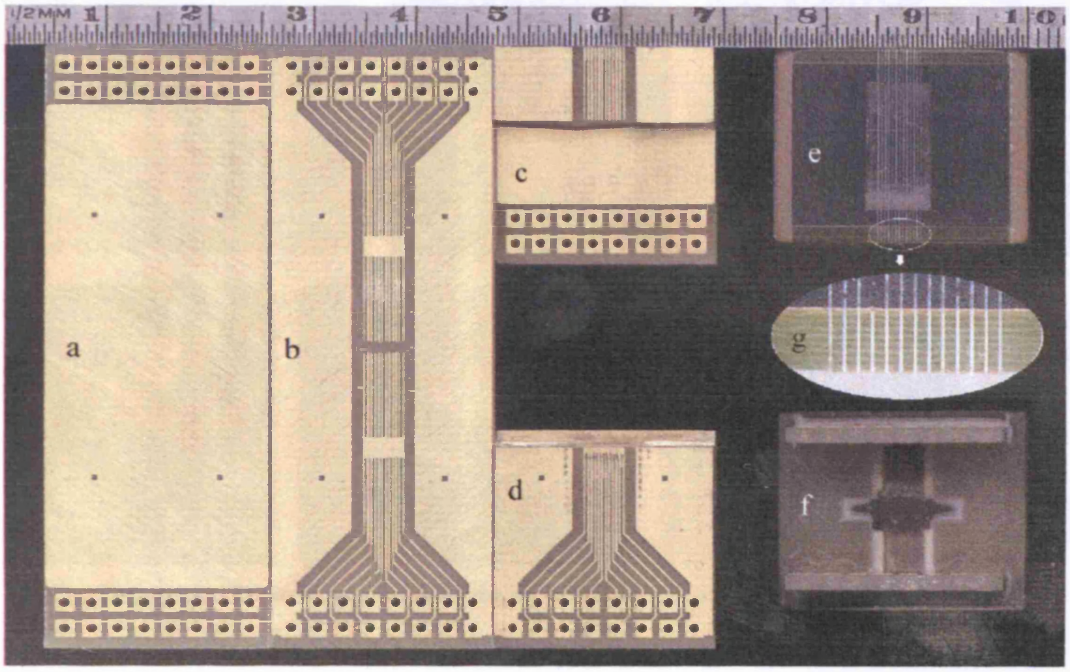

Fourth version (with scale) - PCBs , transducer face (cut), and back

Fig. 5.3 The back (**a**) and front (**b**) faces of the PCB made for the fourth version transducer are presented. In (**c**) and (**d**) it is shown how this PCB is cut and reassembled together. In (**e**) the transducer face is presented and in (**g**) the rear of the transducer is presented to show the air backing of the ceramic. In (**f**) an enlarged image of a part of the transducer face shows the cuts between elements.

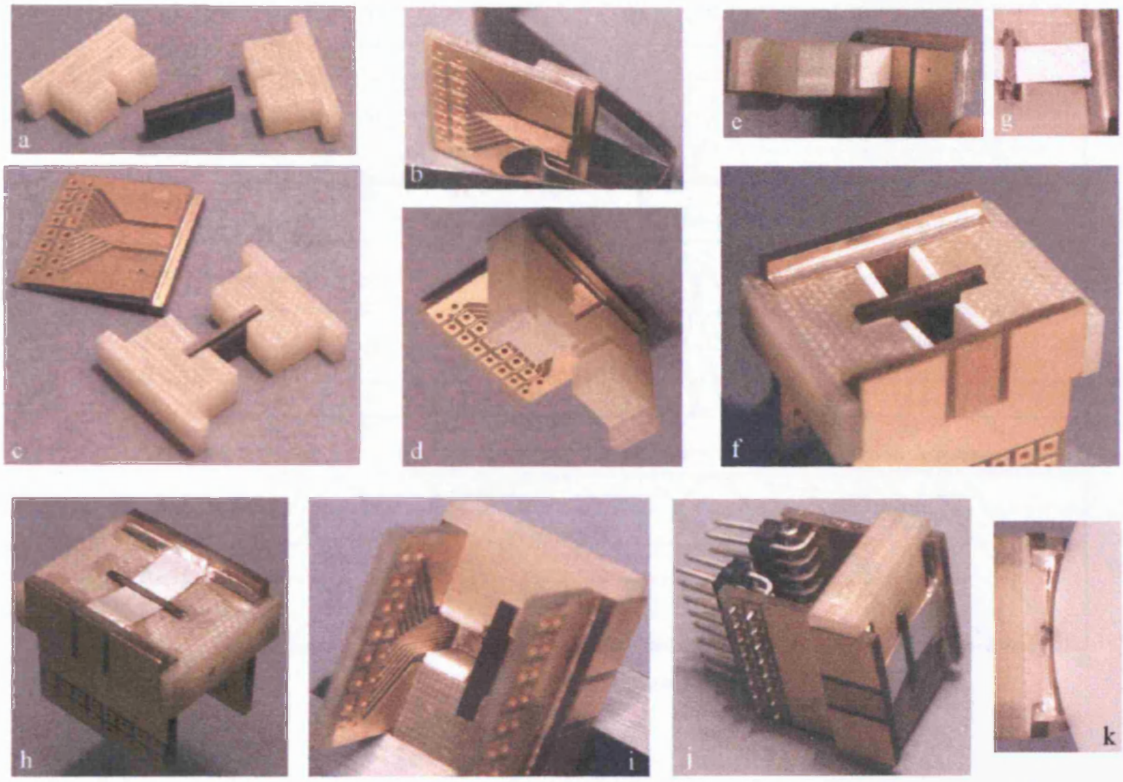

Fourth version - ceramic support, air backing, electrical connections, matching layer mould

Fig. 5.4 Series of photographs showing the assembly sequence of the fourth version of the array transducer. The parts assembly is shown in (**a**, **c**, **d**, and **e**). In (**b**) is presented a detail of the preparation of one PCB part. In (**e** and **f**) details of the ceramic support to ensure a correct angle are presented, it is also possible to see in (**f** and **i**), the air backing space. The ceramic held in position is shown in (**g**, **h**, and **j**), details of the electric connections to the ceramic and PCB are shown in (**h**, **i** and **j**). Detail of the placement of the mould above the face of the transducer to construct the matching layer in the correct dimensions is shown in (**k**).

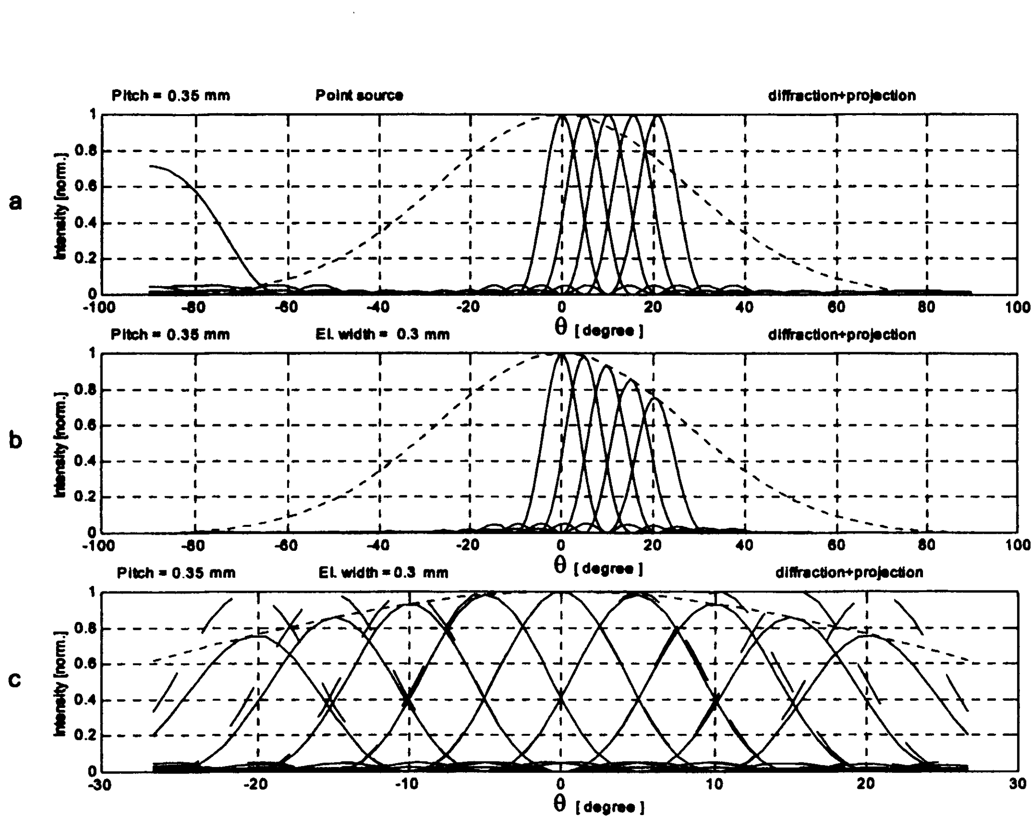

Fig. 5.5 Simulation of an array transducer with eight elements and 0.35 mm pitch. The maximum intensity profiles are represented by solid lines. The function representing the combination of diffraction and projection (calculated for the case of element width equal to 0.30 mm) is represented by the short dashed lines. **a)** Representation of five intensity profiles generated by an ideal array of point sources. θ ranges from -90° to +90° and α ranges from -90° to 0° in intervals of 22.5°. When α = -90°, the acoustic field is steered +20° and a side lobe is formed at -90°. **b)** Representation of five intensity profiles generated by an array of elements with width of 0.30 mm. θ ranges from -90° to +90° and α ranges from -90° to 0° in intervals of 22.5°. The diffraction and projection produce attenuation in the main lobe and eliminates the side lobe. **c)** Representation of intensity profiles corresponding to nine steering positions corresponding to α ranging from -90° to 90°. The long dashed lines represent the intensity profiles generated by an ideal point source transducer. θ ranges from -90° to +90°. It is possible to see that up to ± 20° the attenuation caused by diffraction and projection does not go beyond 25% and the shift in the peak position of any profile caused by distortion of the acoustic field is negligible.

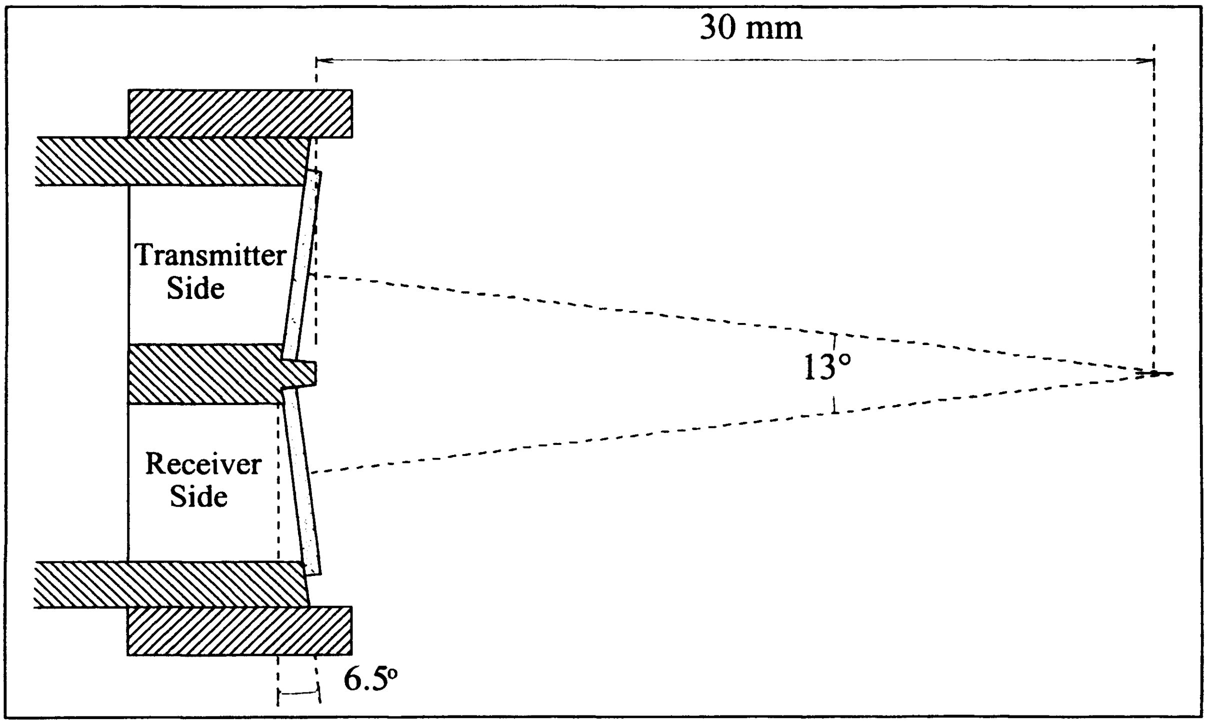

Fig. 5.6 Lateral cut through the transducer showing the positions of the two ceramics which are assembled at an angle in such way as to make their axes converge at a distance of 30 mm from the transducer face. Such a transducer would have its maximum sensitivity at that distance.

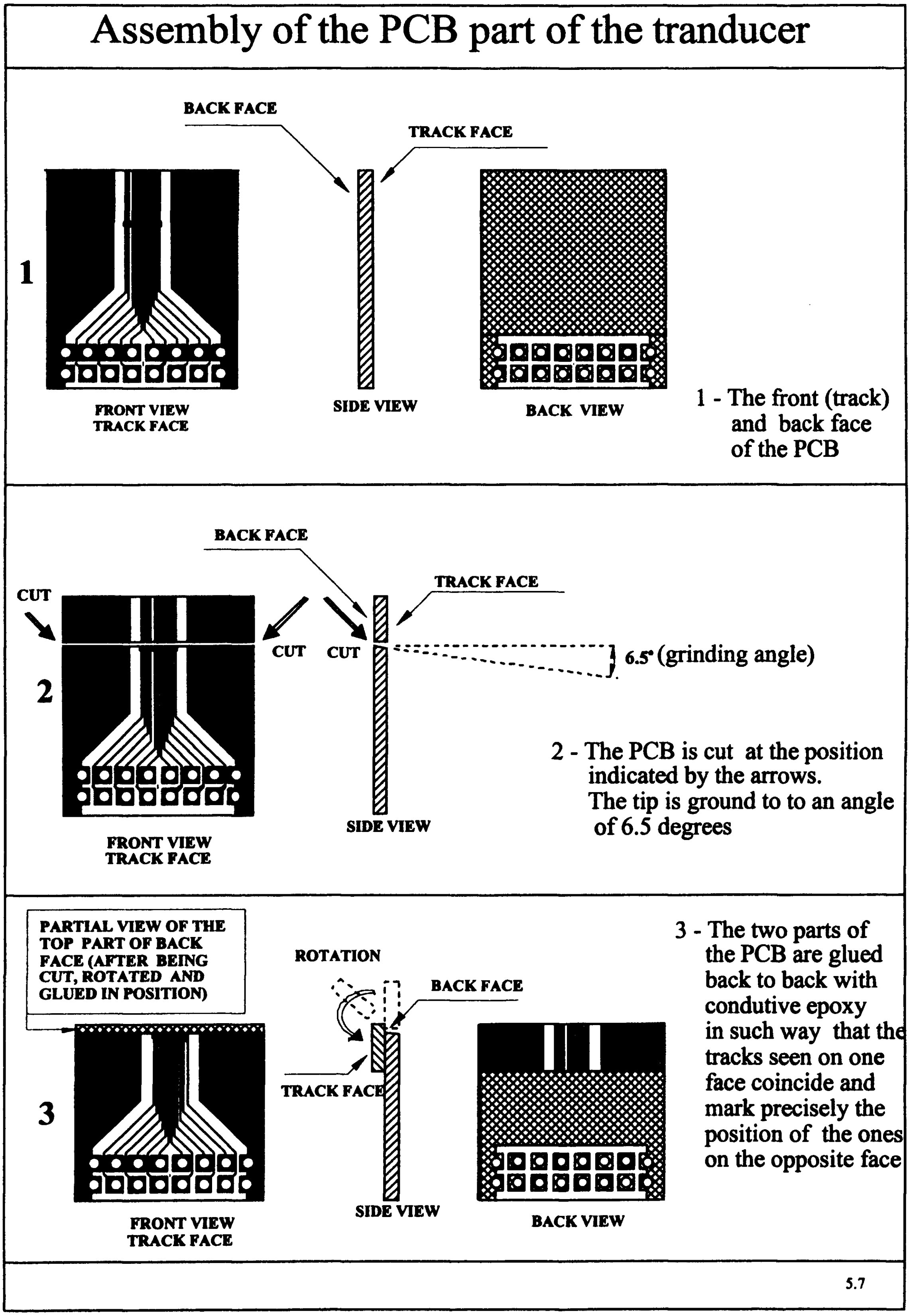

Fig. 5.7 Description of the assembly of the PCB part of the transducer.

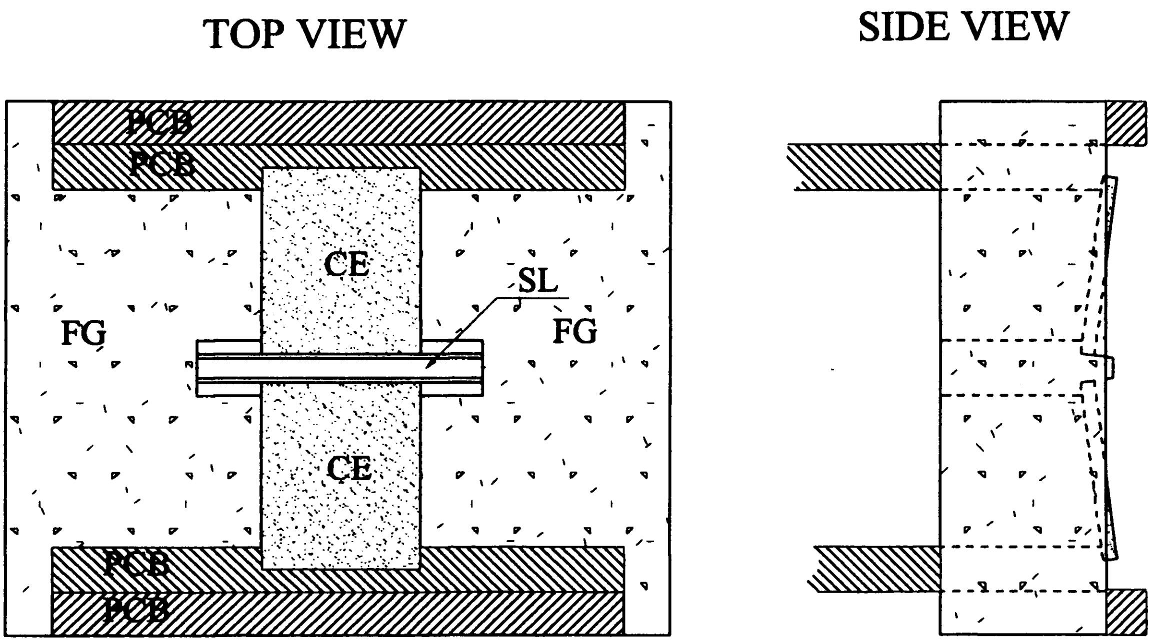

Fig. 5.8 Detailed view of the transducer construction: the two PCB assemblies are aligned and held in position by two fibreglass pieces (FG). These pieces have a groove in their middle designed to hold a slab (SL) also made of fibreglass. They form two cavities where the two ceramics (CE) are placed supported at 0.5 mm from each extremity.

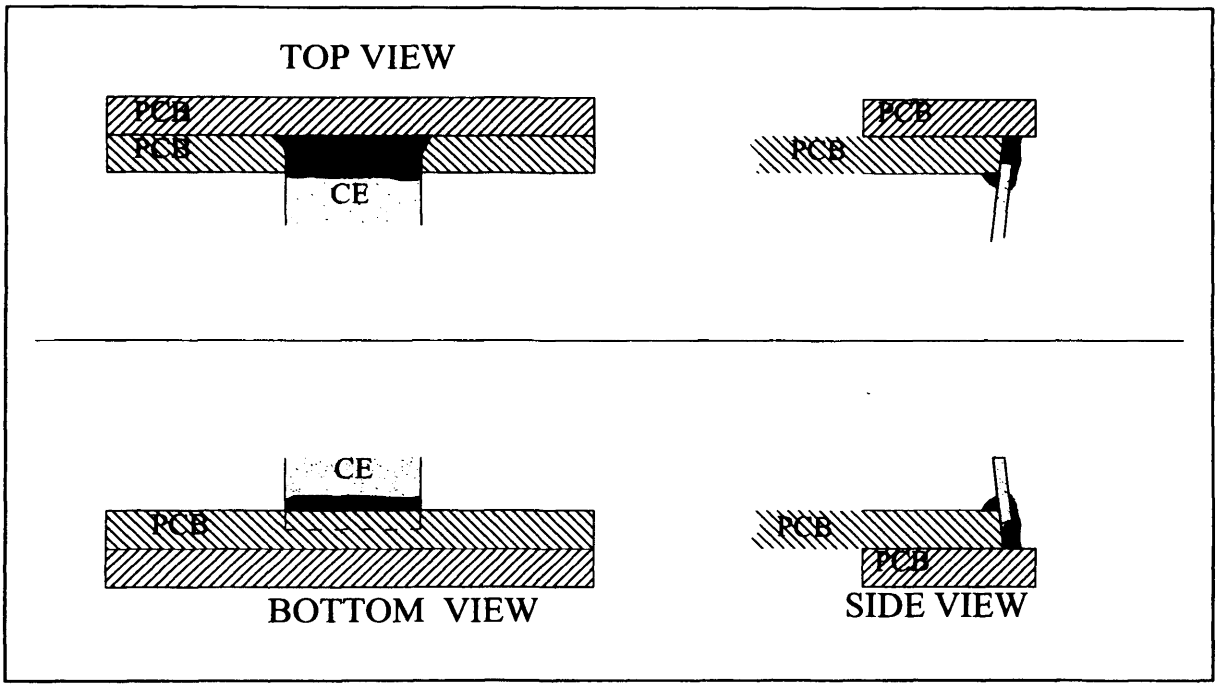

Fig. 5.9 Detailed view of the electrical connection of the ceramics (CE) to the PCB assembly. The top view shows how the conductive epoxy makes the electrical connection of the ceramic superior electrode to the back face of the PCB, and the bottom view shows how the conductive epoxy makes the electrical connection between the ceramic inferior electrode to the track face of the PCB.

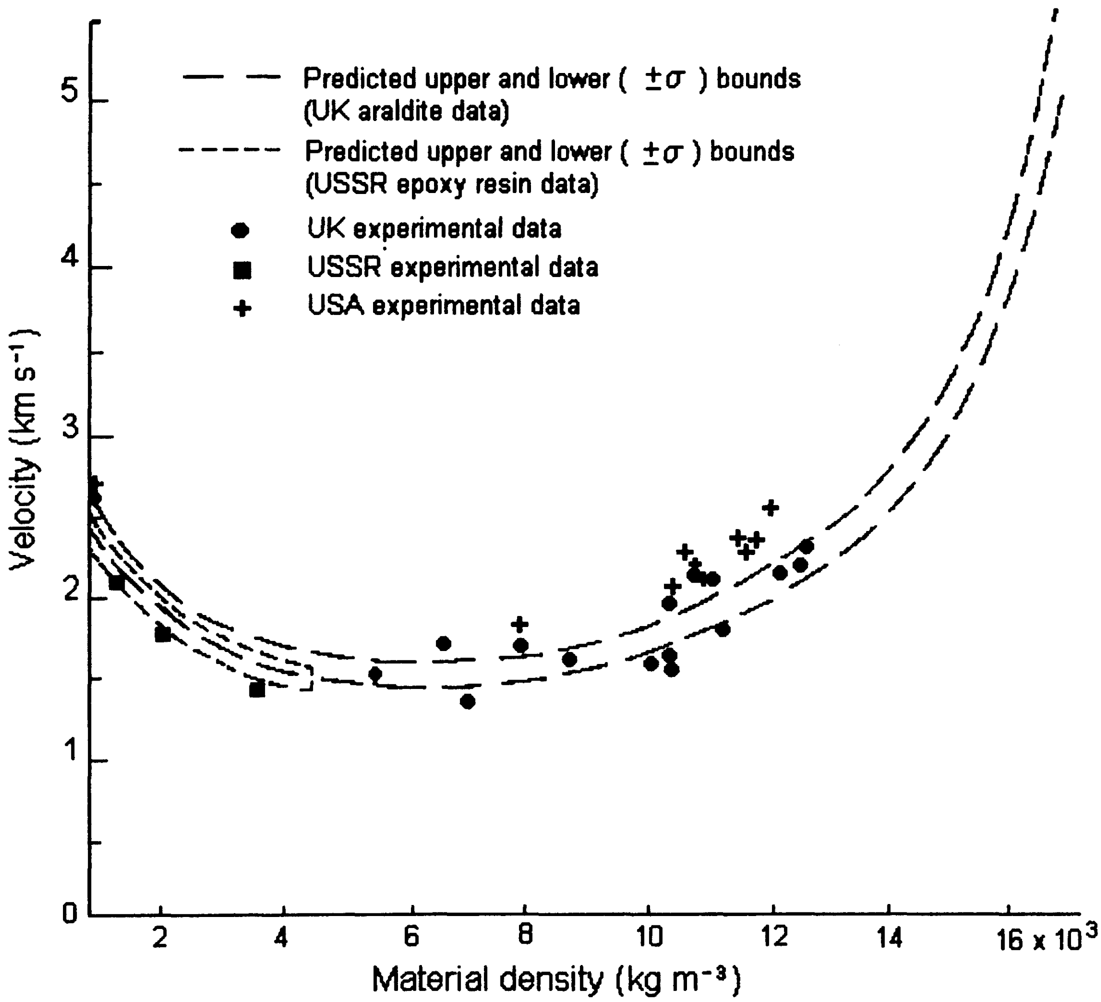

Fig. 5.10 Experimental data and theoretical estimates of the relationship between density and ultrasonic velocity for tungsten/araldite™ mixtures. (Extracted from Silk, M. G. 1984)

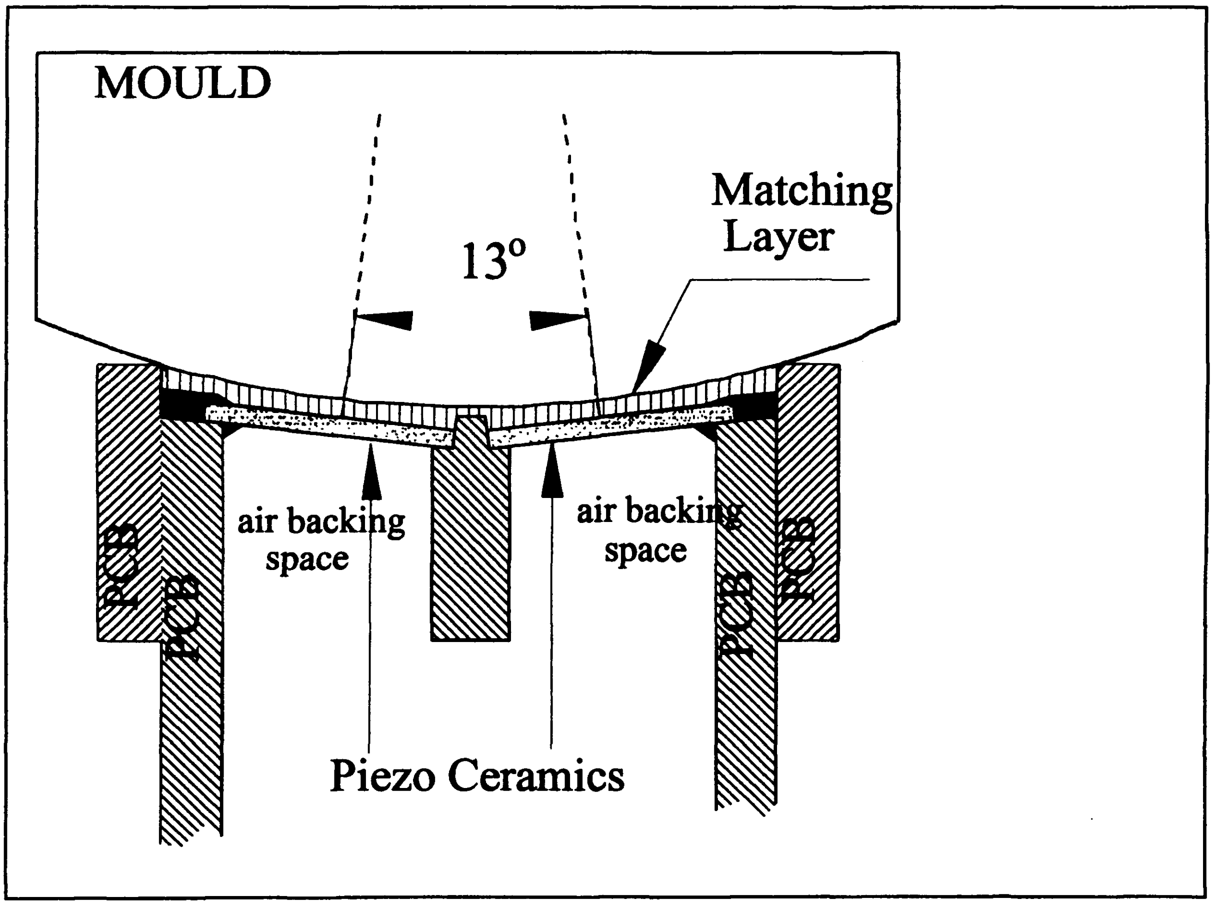

Fig. 5.11 Detailed view of the shaping of the matching layer. The mould is placed over the ceramics supported by the top of the PCB assembly at each side. The heights of the PCB supports determine the distance between the ceramics and the mould. This space is then filled with the epoxy mixed with tungsten powder.

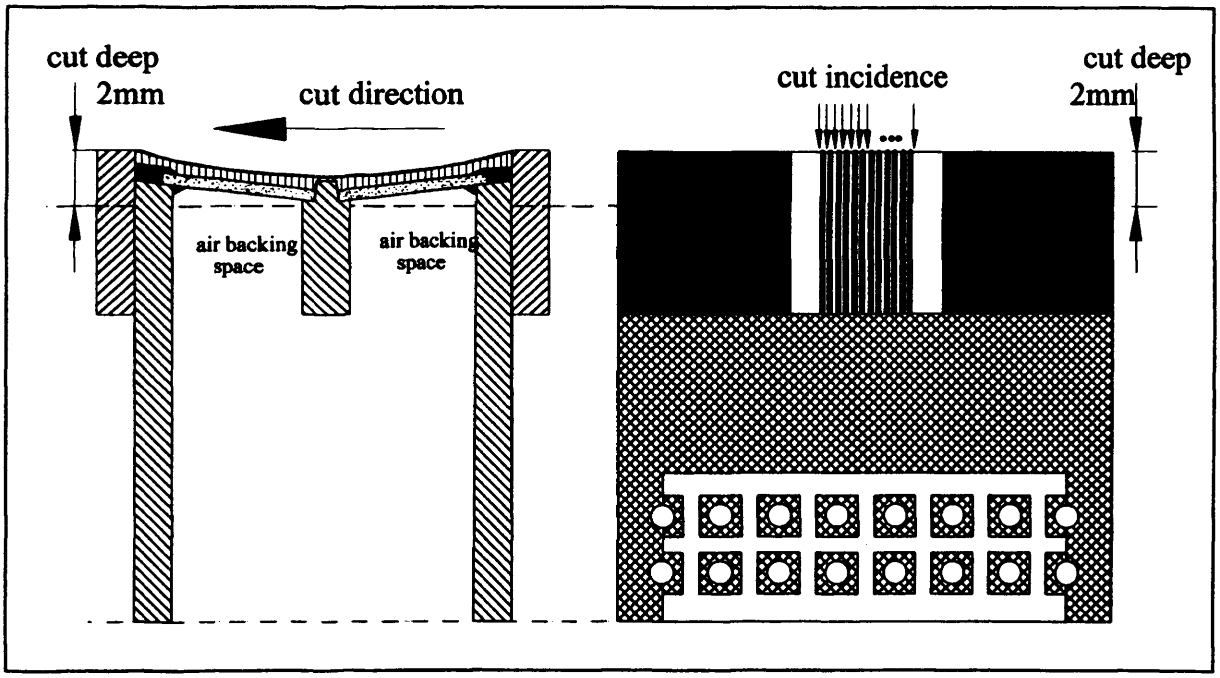

Fig. 5.12 Two lateral views of the transducer to show the depth and position of the cuts required to transform the single element transducer into an array transducer. The cuts must be deep enough to split completely the ceramic and conductive epoxy. They also are positioned exactly between the tracks.

Chapter 6

Doppler ultrasound phased array transceiver - DUPAT

6.1 Introduction

In the present chapter the operation of the electronics required to drive the Doppler array transducer is described. As already presented in section 4.2, it consists basically in an array of eight continuous wave (CW) Doppler circuits, each one connected to a pair of transmitting and receiving elements of the array transducer. The eight CW Doppler circuits are assembled together to work in synchronism in order to behave like a single CW Doppler system capable of performing the steering necessary to measure the blood flow velocity in a sample volume in a chosen direction.

On the transmitting side, what it is required is the ability to introduce a controlled and progressive phase difference in the RF signals driving the successive array elements to produce beam steering (Fig 6.1 a). On the receiving side the reverse procedure has to be applied to cancel the phase difference between the signals arriving at each successive array element in order to arrange for the individual reflections from the direction of interest to be in phase (Fig 6.1 b). In an analogue circuit it is possible to produce such a phase shift by inserting delay lines in the signal paths. (Powers et al 1980, Landini et al 1991). The solution adopted in the Doppler Ultrasound Phased Array Transceiver (DUPAT) (Aucott 2001) presented here is mainly digital. All eight Doppler circuits are similar, therefore describing one circuit is sufficient. However in order to understand their common output it is necessary to understand how they are interconnected.

6.2 RF signal and phase control

In all eight Doppler circuits, the RF signal is synthesised by a four stage synchronous binary counter (74AC163) running at a clock frequency of 50 MHz (IQXO - 1000C 50 MHz). The most significant bit (MSB) of the counter output has a cycle sixteen times longer than the clock cycle and corresponds to a frequency of 3.125 MHz. This is the signal employed both in driving the transmitting transducer and in the demodulation of the received signal. In Fig 6.2 a schematic diagram of the counter is presented, the clock signal and the output signal at each bit (from the least significant (LSB) to the most significant (MSB)) are also represented.

By loading the counter with a four bit binary word before it starts running, it is possible to introduce a initial phase shift in the MSB cycle. As a consequence when the counter runs, the MSB cycle starts from the phase defined by this word. In Fig 6.2 three examples of initial phase shift are shown in relation with the loaded word: a- 0000, b-0001, c- 1100. The phase shifts achievable by such a process are all multiples of the smallest possible phase difference which corresponds to the smallest word: 0001. That is 1/16 of the complete cycle, which corresponds to a time interval of 20 ns and also represents a phase angle of 22.5° for a frequency of 3.125 MHz.

In a similar way, a sequence of binary words in arithmetic progression can represent a sequence of progressive phase shifts. In the DUPAT such a sequence is generated in a set of eight 4-bit adders (74AC283) connected in series (Fig 6.3). The output of each stage is the sum of the output of the previous stage with the "common difference in the progression" representing the unit phase increment α. The output of each stage is then used to load each counter in order to set the initial phase shift in the MSB cycle.

As presented in the section 5.3.1 the beam steering excursion is ± 20° which would require from α an excursion of ± 90°. This value is four times the minimum phase shift either in the positive or negative directions. As a consequence just seven values of α are employed with the present system: -90°, - 66.5°, - 45°, - 22.5°, - 0°, +22.5°, +45°, +66.5°, and +90°. These correspond to the four bit words 1100, 1101, 1110, 1111, 0000, 0001, 0010 0011, and 0100 and represent nine possible unitary phase increments to be input in the chain of four bit adders presented in Fig 6.3.

Such a word is either manually input by a thumb wheel selector switch or by the computer controlled feedback loop (DT 302). When a change occurs the 'load' control circuitry responds automatically to re-initialise the counters. Each four bit counter continues to run with the phase which was set initially by their correspondent element of the phase shift sequence. As soon the this word is changed a new sequence of phase shifts is generated and the control circuitry generates a 'load' pulse which: 1 - Stops the counters, 2 - With the next active clock edge loads the new phase 'bits' into the counters, 3 - Release the counters to run again.

6.3 Transmission

In the block diagram of Fig 6.4 one module of the DUPAT circuit is shown, in this module two transmission circuits are presented. It has already been explained how the RF carrier signals are generated. It is just necessary to add that each MSB counter output signal drives the corresponding transmitting element of the transducer (T1, T2,...T8) through a buffer amplifier (EL2244) and the output voltage of all amplifiers are adjusted by a circuit which clamps the input swing.

6.4 Reception

In the block diagram of Fig 6.4 one module of the DUPAT circuit is shown, in this module two reception circuits are presented. The RF received signal is generated at the receiving transducer (R1, R2,...R8) when excited by the backscattered ultrasonic wave. It has a very small amplitude and therefore it needs to be amplified (RS1612C).

The next stage is the demodulator where the Doppler side bands are recovered. The process of demodulation employed here consists of multiplying the RF Doppler shifted signal by the RF carrier frequency.

Summarising the theory explained in the literature (Evans and McDicken 2000) it is possible to say that the received Doppler shifted signal is composed of three components:

$$\boldsymbol{S(t) = A_0 \cos(\omega_0 t + \phi_0) + A_f \cos(\omega_0 t + \omega_f t + \phi_f) + A_r \cos(\omega_0 t + \omega_r t + \phi_r)} \qquad (6.1)$$

where A is the amplitude, ω is the angular frequency and φ is the phase. The subscript ***0*** denotes the unshifted signal, the subscript ***f*** denotes the forward shifted signal and the subscript ***r*** denotes the reverse shifted signal.

Multiplying $\boldsymbol{S(t)}$ by $\boldsymbol{A_0 \cos(\omega_0 t)}$ and filtering the DC components and the RF components of the product the resultant demodulated signal is:

$$\boldsymbol{D(t)} = 1/2\,(\boldsymbol{A_f \cos(\omega_f t + \phi_f)}) + 1/2(\boldsymbol{A_r \cos(\omega_r t - \phi_r)}) \qquad (6.2)$$

In order to be able to separate the forward component from the reverse component, $\boldsymbol{S(t)}$ must be multiplied by $\boldsymbol{A_0 \sin(\omega_0 t)}$ which is the same carrier signal shifted by 90°.

After multiplying and filtering the DC and RF components the resultant demodulated signal is:

$$Q(t) = 1/2\ (A_f \cos\ (\omega_f t + \phi_f + \pi/2)\ ) + 1/2(A_r \cos\ (\omega_r t - \phi_r - \pi/2) \qquad (6.3)$$

$D(t)$ and $Q(t)$ are called quadrature signals and need to undergo further processing in order to get the full separation of the forward and reverse flow information.

In the DUPAT two demodulators (MC1496), (Fig 6.4), are employed in each Doppler circuit in order to get both quadrature components from each Doppler shifted signal. The MSB counter output is used in the demodulation of the RF received signal. Employing a dual input XOR gate (74AC86) with the next significant bit produces the quadrature components of the RF carrier signal. Each is connected to a demodulator in the receiving circuit.

Up to this point the fact that the signals are arriving with phase differences at the eight receiving elements has not been considered. In order to maximise the sum of the contribution of each element it is necessary to cancel these phase differences. Such phase differences between the signals arriving at each element of the transducer are a function of the incident angle in the same way as the phase differences between the signals driving each element of the transducer.

The process employed to cancel the phase differences between the receiving signals is simply to perform the demodulation using the carrier employed to drive the corresponding transmitting element. In Fig. 6.1a it is shown that in order to produce a wave front propagation in a given direction it is necessary to produce a phase lag in the signal driving the transmitting elements closer to the sample volume of interest. Regarding the reception Fig. 6.1b, the signals returning from the sample volume reach the elements closer to the source earlier and consequently their relative phase order is reversed. In the demodulator, the signal arriving at element number one has a relative phase lag equal to 7α. It is multiplied by the carrier signal which has a relative phase lag equal to 0α. The signal received at element number two with phase lag 1α is multiplied by the carrier signal with a phase lag of 6α, and so on. The advantage of this process is its simplicity and the fact that it does not require any additional components in the Doppler circuit.

Mathematically this procedure can be justified as follows:

Looking at the figure 6.1 it is seen that:

The signal arriving at the element number **1** is $R_1 = A_r \cos(\omega_r t - 7\phi)$, the signal arriving at element number **2** is $R_2 = A_r \cos(\omega_r t - 6\phi)$ and so on until the signal arriving at the element number **8** which is $R_8 = A_r \cos(\omega_r t)$.

The signal driving the element number **1** is: $T_1 = \cos(\omega_t t)$, the signal driving element number **2** is: $T_2 = \cos(\omega_t t - \phi)$ and so on until the signal driving element number **8** which is: $T_8 = \cos(\omega_t t - 7\phi)$.

Now carrying out the multiplication for element one we have:

$$R_1 \times T_1 = A_r \cos(\omega_r t - 7\phi) \times \cos(\omega_t t),$$

from the trigonometry we have:

$$R_1 \times T_1 = A_r/2\ \{\cos[(\omega_r t - 7\phi) + (\omega_t t)] + \cos[(\omega_r t - 7\phi) - (\omega_t t)]\}$$

$$\equiv A_r/2\ [\cos(\omega_r t - 7\phi + \omega_t t) + \cos(\omega_r t - 7\phi - \omega_t t)]$$

$$\equiv A_r/2\ \{\cos[(\omega_r + \omega_t)t - 7\phi] + \cos[(\omega_r - \omega_t)t - 7\phi)] \tag{6.4}$$

Again carrying the multiplication for element two we have:

$$R_2 \times T_2 = A_r \cos(\omega_r t - 6\phi) \times \cos(\omega_t t - \phi),$$

from the trigonometry we have:

$$R_2 \times T_2 = A_r/2\ \{\cos [(\omega_r t - 6\phi) + (\omega_t t - \phi)] + \cos [(\omega_r t - 6\phi) - (\omega_t t - \phi)]\}$$

$$\equiv A_r/2\ [\cos (\omega_r t - 6\phi + \omega_t t - \phi) + \cos (\omega_r t - 6\phi - \omega_t t - \phi)]\}$$

$$\equiv A_r/2\ \{\cos [(\omega_r + \omega_t)t - 7\phi] + \cos [(\omega_r - \omega_t)t - 7\phi)] \qquad (6.5)$$

Note that equations 6.4 and 6.5 are identical, which means also in phase, and it is easy to show that the same result would be achieved with $R_n \times T_n$ for any n.

The second term of equation 6.4 or 6.5 represents the Doppler signal and is separated from the first term by a low pass filter.

The mathematical demonstration is valid for both quadrature components.

The output of each of the eight receiver circuits consists of a pair of quadrature components. Each set of eight components in phase is added (TL072CP), and therefore the final output of the DUPAT consists of a single pair of quadrature components. These components are input into a DSP32C System Board (Loughborough Sound Images Ltd) installed in a personal computer. This board is operated by a Multi Channel Signal Analysis and Monitoring Program for Doppler Signal developed at the Dept of Medical Physics Leicester Royal Infirmary (Gibbons et al 1981, Prytherch and Evans 1985, Schlindwein et al 1988, Schlindwein and Evans 1989, Fan and Evans 1994a 1994b).

6.5 Discussion

The DUPAT was developed especially for the present project and the circuits were carefully conceived and executed. Indeed ingenious solutions were developed such as the process of cancelling the phase differences in the receiving circuit and also in the fast response to commands for changing the phase shift increment. In spite of that the intention was to make this first prototype as simple as possible. Using this philosophy standard logical devices were chosen instead of Digital Frequency Synthesis ICs and the receiver/detection circuits were only intended for moderate sensitivity laboratory application. As far as construction was concerned the modular lay out of the equipment was conceived taking into account the possibility of further improvements in the circuits and a simplified maintenance procedure.

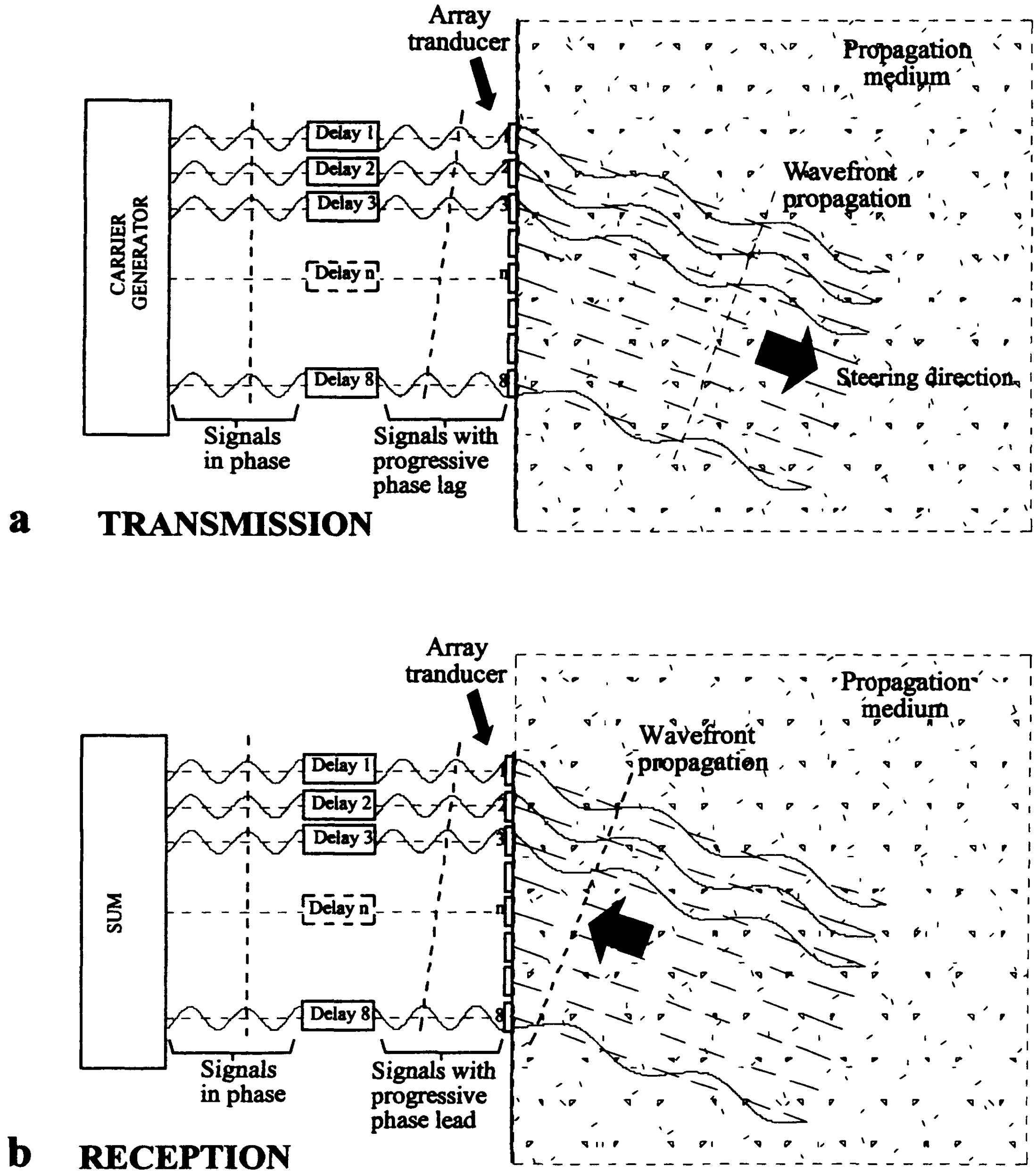

Fig 6.1 A schematic diagram of the eight-element phased array transducer, electronics and propagation medium is presented both for transmission (**a**) and for reception (**b**). During transmission, the successive transducer elements are driven by progressively staggered signals which are the result of a common carrier signal which was progressively delayed by an array of delay lines. In order to produce a wavefront propagation in a given direction it is necessary to produce a larger phase lag in the signals driving the elements nearer to the sample volume. On reception, the successive transducer elements detect the wavefront in sequence. In order to be added in phase they must suffer a progressive delay (in reverse order compared with the transmission).

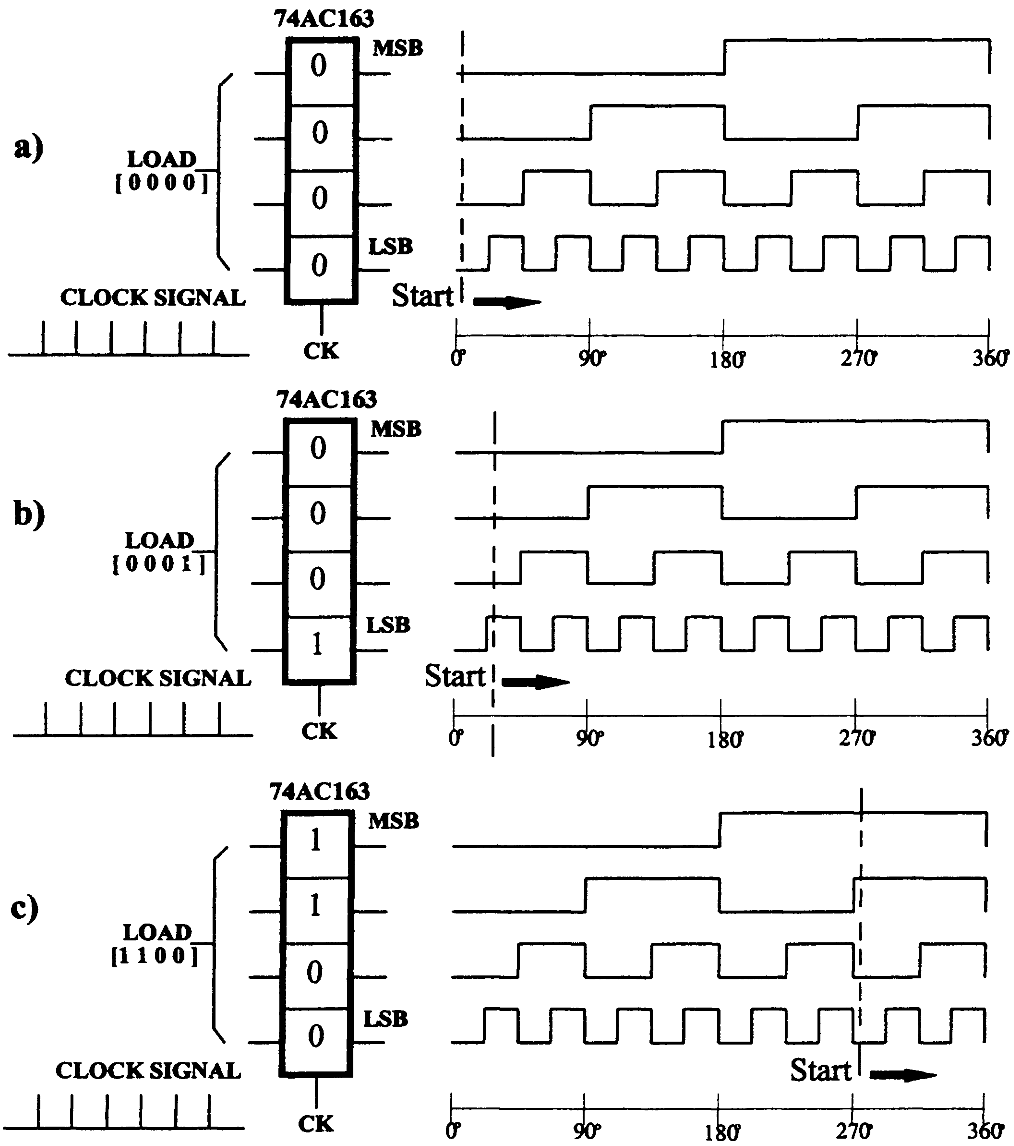

Fig 6.2 A schematic diagram of the four stage synchronous programmable counter (74AC163) is presented. While the counter is run by the clock signal, the least significant bit (LSB) produces a cycle which is two times longer than the clock cycle and each successive bit doubles this value until the fourth (MSB) which has a cycle sixteen times longer. Before starting the counter can be loaded with a binary word which sets the initial phase of the MSB cycle. Three different starting positions are presented: **a)** the loaded word is 0000 which corresponds to a cycle without an initial phase shift, **b)** the loaded word is 0001 and corresponds to 1/16 of the cycle and a phase shift of 22.5°, **c)** the loaded word is 1100 and corresponds to 12/16 of the cycle and a phase shift of 270°.

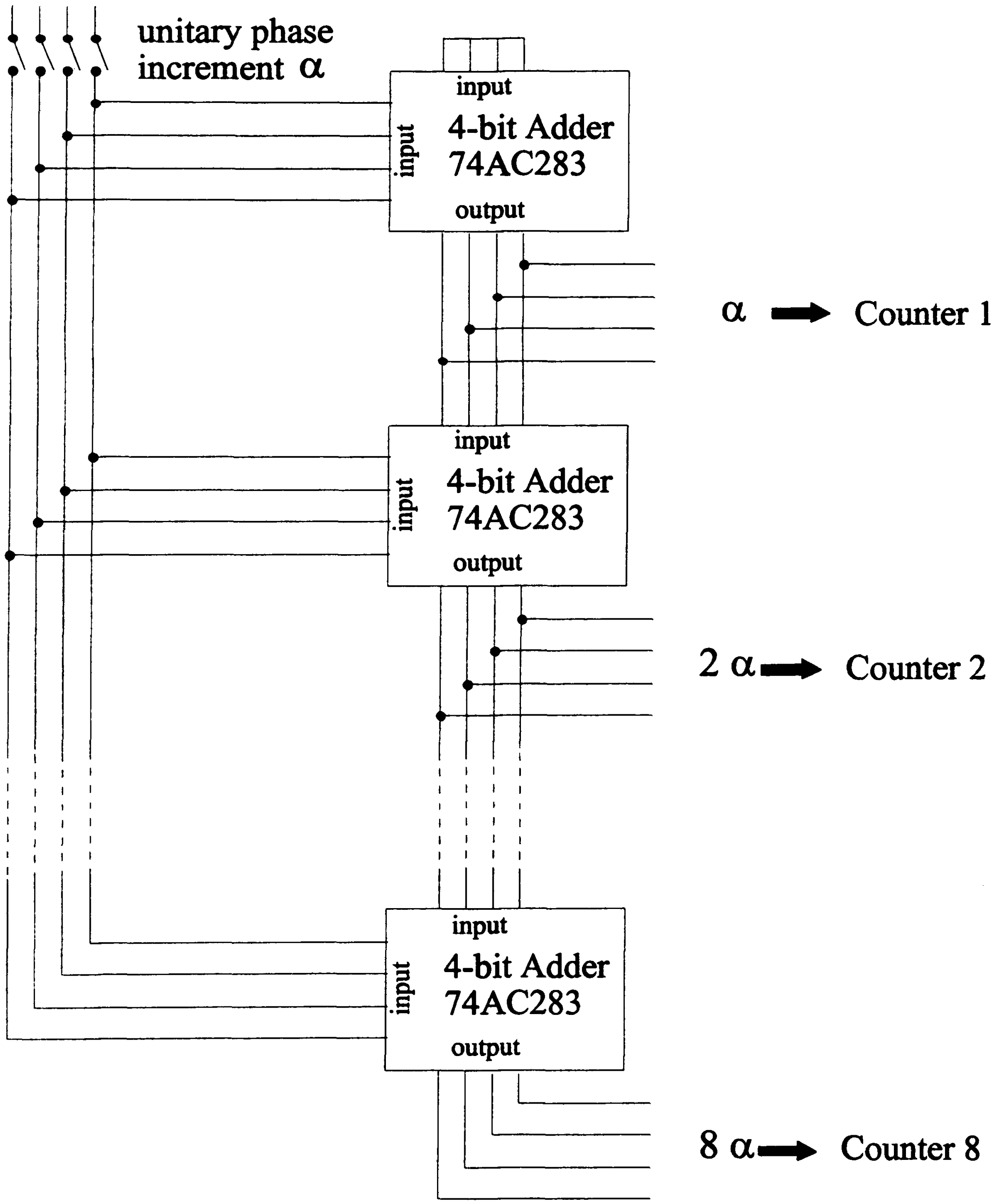

Fig 6.3 A schematic diagram of the set of eight 4-bit adders connected in series; the unitary phase increment is set by the switch and input to all eight counters. The output of each counter is input to the following, in order to generate an arithmetic progression where the "common difference in the progression" is the unitary phase shift. The output of each successive adder also loads the corresponding counter.

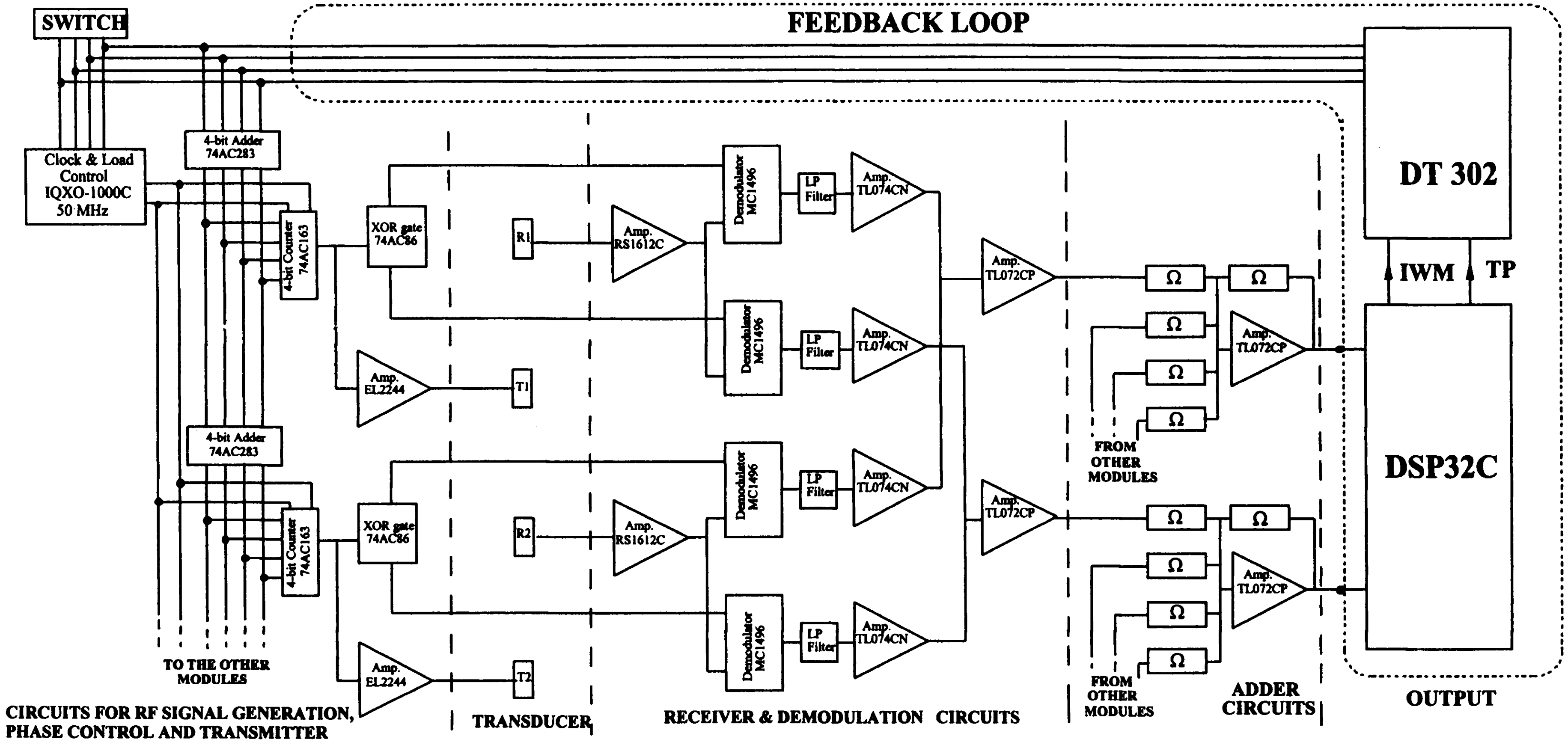

Fig. 6.4 A block diagram of a module of the DUPAT circuit is presented. It contains the thumb wheel switch, the clock, two complete transmitting/receiving circuits including their corresponding transducer elements and the two adding circuits which sum the quadrature signals from the other modules. The output of the DUPAT are two quadrature signals which are fed to the Feedback Loop consisting of DSP32C board and a DT302 board, each one fitted in a personal computer.

Chapter 7

The Feedback Loop

7.1 Introduction

In order to build a Doppler tracking system, a feedback loop implemented using two computers is added to the electronics already described. One machine is fitted with a DSP32C System Board (DSP32C PC System Board Loughborough Sound Images Ltd) operated by a Multi Channel Signal Analysis and Monitoring Program for Doppler Signals developed at the Dept of Medical Physics Leicester Royal Infirmary (Gibbons et al 1981, Prytherch and Evans 1985, Schlindwein et al 1988, Schlindwein and Evans 1989, Evans et al 1989e, Fan and Evans 1994a 1994b). The second machine is fitted with a data acquisition board (Data Translation DT 302) supported by the visual program language HP-VEE™ with the DT VPI™ data acquisition interface software. As already explained, the feedback loop can be implemented on a single board to be fitted inside the DUPAT. However at this development stage, the present configuration using the two computers presents the advantage of versatility, accessibility, easy adjustment and control over each stage. Referring to the block diagrams shown in Fig. 3.2 and Fig. 6.4, it can be observed that such a feedback loop begins at the input of the quadrature signals into the DSP32C and ends at the digital output of the DT 302. Between these two points a sequence of functions is performed in order to force the steering command response to the insonation measured through the parameters derived from the quadrature signals. The sequence is:

1. Acquisition

2. Conditioning
3. Parameter extraction
4. Comparison
5. Control

In the following sections, the feedback sequence is explained in detail.

7.2 Acquisition

The present configuration of the feedback loop is convenient for experimentation and for testing different solutions, but also involves a certain degree of redundancy. Such is the case for the acquisition process where the analogue data are converted to digital form in the first computer processed and returned to analogue form just to be transferred to the second computer, where they are again converted to digital form for further processing.

7.2.1 Acquisition by computer 1 (DSP32C)

The Doppler quadrature signals $\boldsymbol{D(t)}$ and $\boldsymbol{Q(t)}$ carry the total of the instantaneous contributions from each 'particle' crossing the beam. They present a mixture of signals which are difficult to interpret and need to undergo further processing in order for their information be presented in the form of a sonogram with full separation between the forward and reverse flow. The analogue quadrature signals generated at the DUPAT are acquired by the analogue to digital (A/D) input of a real-time fast Fourier transform (FFT) Analyser (which has an adjustable sampling rate of 1.28, 2.56, 5.12, 10.25 or 20.5 kHz, in the present work the sampling rate employed was 10.25 kHz). This Analyser consists of a personal computer fitted with the DSP32C board (Section 3.4,

Fig. 3.2 and Fig. 6.4). It is operated by the resident Multi Channel Signal Analysis and Monitoring Program for Doppler Signals and is actually a very powerful and flexible analysis system designed for advanced clinical research. It is capable of obtaining forward and reverse flow spectra separated into positive and negative frequencies by performing a complex FFT on the quadrature signals. These spectra can be displayed in real time in the form of a sonogram at a rate of one spectral line per 6.25 ms.

For the particular application of evaluating the degree of insonation, the bi-directional information is not required. As a consequence, just one quadrature signal is employed resulting in a spectrum with the positive part only. This sonogram still contains excess information and to achieve the fast processing time necessary for real time operation. it is necessary to reduce it to a selected number of parameters. Those parameters must be useful for the task of measuring the degree of insonation and must be able to be extracted rapidly.

In section 2.8 of this thesis the effect of insonation on the sonogram and on four parameters extracted from the sonogram, total power (***TP***), first moment (***M_1***), intensity weighted mean (***IWM***) and maximum frequency (***fmax***) were analysed. They have the advantage of representing a type of pre-processing as each line of 128 points in the sonogram is replaced by just four points, one each in the ***TP***, ***M_1***, ***IWM*** and ***fmax*** traces. From this analysis, it was concluded that:

1 Under good signal-to-noise ratio conditions, ***TP*** is clearly related to insonation.

2 Good signal-to-noise ratio conditions can be detected from the periodicity of waveform which can be extracted from envelope functions such as ***M_1***, ***IWM*** and

fmax

In the present work the combination of ***TP*** and ***IWM*** was chosen as a means of evaluating the degree of insonation.

The Analyser can be programmed to provide these two parameters in real time at its analogue output, updated 160 times per second.

7.2.2 Acquisition by Computer 2 (DT 302)

The ***TP*** and ***IWM*** signals are acquired at the A/D input of the data acquisition board (Data Translation DT 302) operated by the HP-VEE™ visual program in the second computer (Section 3.4, and Fig. 3.2 and Fig. 6.4). The maximum sampling rate of the A/D input in the DT 302 interface is 225 kHz, far beyond the update rate of the input signals (160 Hz). The DT 302 board contains sixteen single-ended or eight differential analogue inputs. In the present work, two differential analogue inputs were employed for digital conversion. Each A/D input can be individually configured to suit the extraction of the relevant information from each signal taking into account their individual differences.

The A/D subsystem operates in parallel with the rest of the program. It performs the analogue to digital conversion at a programmable sampling frequency which is chosen as a function of the frequency content of the signal, that is, at a pace adequate to preserve the relevant features of the signal. The acquired digital data is stored as a queue in a 'first in first out' (FIFO) memory.

The rest of the program operates at a much faster speed. The 'Get Data' object, which is the first step of the program, reads the data from the FIFO memory. It can be programmed to read the data in groups of specified size. The data are processed in one group at a time as read by the 'Get Data' object. Once the processing of a group is completed, the program is ready to work on the next group and waits for the queue to reach the specified group size. As soon this happens the new group is read by the 'Get Data' object and the processing restarts. The processing time must be shorter than the time taken by the A/D subsystem to acquire and store a group, otherwise the FIFO memory overflows causing the program to stop.

A schematic diagram of the operation of A/D subsystem and 'Get Data' object is presented in Fig. 7.1.

When there are more than one input channel, the A/D conversion for all channels is performed in parallel, therefore the total processing time available is limited by the time taken by the A/D subsystem to acquire and store enough data to fill the largest group. There are as many 'Get Data' objects as input channels in the A/D subsystem, each one corresponding to a program branch sharing, by a rapid alternation, the available processing time.

The analogue signals input at each channel of the A/D subsystem may have different frequency contents thus requiring different sampling rates. However, as they represent simultaneous events, their relative time reference must not be lost. This is achieved by programming the 'Get Data' objects in such way that the group sizes are proportional to the sampling rate of the respective input channel. This also means that, because the data are read at a speed proportional to their respective acquisition rate, there is always a complete renewal of the FIFO memory content and no problem of overflowing.

A diagram of the A/D subsystem and 'Get Data' object in the case of two channels is presented in Fig. 7.2

7.3 Processing

The processing is performed continuously in real time and its first stage consists of signal conditioning. This is removal or attenuation of noise and artefacts, which may affect the following processing stage, dedicated to the parameter extraction.

The method employed for reduction of high frequency noise involves the replacement of each group of points in the original signal by a single point. This reduction in number of points means that the sampling frequency of the conditioned signal is actually the 'group rate'. The sampling rate of the A/D conversion (S_{rate}) is calculated from the minimum number of points (N_{min}) capable of expressing the relevant signal features at the 'group rate' and from group size (G_{size}) which basically represents the total number of points processed each time.

i.e. $$S_{rate} = G_{size} \times N_{min} \tag{7.1}$$

From the processing point of view, for a given S_{rate}, a smaller G_{size} represents a worse case because the acquisition/processing time available is proportional to the group size. On the other hand, larger groups lead to smaller N_{min} and loss of frequency information in the conditioned signal. As a consequence of that, for a given S_{rate}, the available processing time ($\propto G_{size}$) is limited by the size of N_{min} required to carry the information necessary for monitoring the relevant variations of the signal. In the case of more than one channel, when the time reference is maintained and the processing is executed by alternation between branches, N_{min} is the same for all branches and must be specified as a function of the signal with highest frequency content.

A series of tests and trials were performed on real Doppler signals recorded both from patients and from a flow phantom (the flow phantom is described in Chap. 8). From these tests, it was found that, for the ***IWM*** and ***TP***, $N_{\min}$ corresponds to eight points per second because such a rate enables the relevant features of both signals to be displayed. Each point corresponds to a group and in order to define the minimum A/D sampling rate it is necessary to find the minimum size for the group. This is a function of the processing needed to filter out high frequency noises and artefacts. It must be noted that this minimal sampling rate and the size of the group are not absolute. they are dependent on the characteristics of the signal, and the determination of the minimum values is always an iterative process. One useful feature of the HP-VEE™ visual program is the facility for adjusting those values.

The second stage of the processing consists of parameter extraction, which is fundamentally the measurement of the signal parameters, which are chosen to estimate the degree of insonation. In this particular project, the parameters to be extracted from the ***IWM*** and ***TP*** signals are respectively the period and the intensity.

The comparison function interfaces the measurement with the control. By comparing the continuous stream of updated information about IWM period and TP intensity with thresholds, error signals capable of triggering the appropriate control response are generated.

The control module is constructed with a set of logic blocks whose complexity is a function of the amount information required to make a decision, and the range of decisions to be taken.

From the A/D subsystem the processing of the IWM and TP signals was executed in two distinct branches which are presented separately as follows.

7.3.1 *IWM* Branch

As already presented in Section 3.4, the function of the IWM branch is to test the reliability of the Measured TP signal as an indication of a 'good' degree of insonation and therefore this branch is active only when the TP level is above the threshold.

The ***IWM*** signal is an envelope function extracted from the sonogram, it is sensitive to blood velocity variations, and reproduces the pulsatile characteristics of the arterial blood flow. The simplest and most easily detectable parameter related to blood pulsatility is the period. In a noisy signal, the shape of the ***IWM*** deteriorates becoming erratic irregular and unrelated to the cardiac cycle; this feature can then be used as an indicator of low signal-to-noise ratio. In such a condition not only does the period of the IWM becomes irregular and unrelated to the cardiac cycle but also the TP signal contaminated with noise becomes unrelated to the degree of insonation. The object of the ***IWM*** processing in this program is therefore to provide an indication of when the signal-to-noise ratio becomes too low to prevent the use of the ***TP*** signal as an estimator of the degree of insonation.

7.3.1.1 Conditioning

Even in low noise conditions, the presence of artefacts in the ***IWM*** signal may lead to errors in the detection of the period of the cardiac cycle. The processing of the ***IWM*** signal starts by performing low pass filtering which consists of replacing a group of sequential points by their mean. It was found that a minimum sampling rate of 48 Hz in the A/D conversion, and a group size of six points for the 'Get Data' object was adequate for the filtering. The resulting conditioned signal is represented at a rate of eight points per second. The effect of signal conditioning is presented in Fig. 7.3, two segment of the same signal are presented, one before and another after conditioning.

7.3.1.2 Period measurement

The method of measuring the period length consisted of producing an off-set in the signal in order to force its excursion around zero, and then performing a zero crossing detection. The cardiac cycle period corresponds to the interval between two consecutive zero crossings in the same direction (positive to negative or vice versa).

To evaluate the accuracy of the period measurement it is necessary to refer it to a standard reference value. Considering that the length of the cardiac cycle, as for any physiological parameter, is not constant, its representation by a standard reference value is always based on an average value calculated over a chosen number of cycles. The cardiac cycle period also has trends and if instantaneous changes are to be monitored and compared over a long period of time, it is necessary to update the reference value continuously. In the present program, the average value of the ***IWM*** period, calculated over the last thirty consecutive periods, ($\boldsymbol{T}\mathrm{AV}_{30}$), was chosen as the standard reference value. The number of thirty cycles was empirically chosen to meet a compromise between stability and ability to auto adjust in response to normal variations of the cardiac cycle. The standard deviation of the last three periods, ($\boldsymbol{T}\mathrm{STD}_3$) was chosen as an indicator of variations in the cycle period. The length of three cycles was empirically chosen as a compromise between a fast response and the need to attenuate the response to transient noise.

7.3.1.3 Comparison function

Under normal sinus rhythm, for the transducer aligned with the vessel and in low noise conditions, the detected cardiac frequency/period averaged over thirty cardiac cycles ($T\mathrm{AV}_{30}$) does not show fast variations. In the event of a normal cardiac frequency increase or decrease, $T\mathrm{AV}_{30}$ decreases or increases slowly towards a new level. At the same time, $T\mathrm{STD}_3$ will show a small increase which is slow in the case of normal cardiac frequency variation. In any case, the response of the two parameters will be limited.

As the noise increases the ***IWM*** signal becomes distorted and as a consequence the periods measured by zero crossing detection become irregular. This is rapidly reflected in an increase in the amplitude of the $T\mathrm{STD}_3$ signal. At the same time, the signal will tend to a new average value (the higher the zero crossing detection rates, the lower the value of $T\mathrm{AV}_{30}$) which will be a function of the degree of distortion. The general rule describing the behaviour of both parameters in a higher noise condition is a higher value for $T\mathrm{STD}_3$ and lower value for $T\mathrm{AV}_{30}$. To use $T\mathrm{AV}_{30}$ as a threshold reference and $T\mathrm{STD}_3$ as index of signal-to-noise ratio, it is necessary to weight them conveniently in order to be able to enclose their excursions in a common reference frame. By this procedure it is possible to set as a threshold value, $\boldsymbol{TR} = \boldsymbol{M}\times T\mathrm{AV}_{30}$ and, as an index value, $\boldsymbol{ID}=N\times T\mathrm{STD}_3$. The multiplication factors can be found experimentally and it is convenient to be able to adjust them in order to meet a wide range of situations. Figures 7.4 to 7.6 show examples of ***TR*** and ***ID*** in response to different noise conditions. For the particular patient data shown in the example the values of 1.0 for ***N*** and 2/5 for ***M*** were found adequate. Figure 7.7 shows examples of ***TR*** and ***ID*** in response to cardiac variations, it shows an example of cardiac variation capable of producing false detection. This sort of problem can be addressed either by adjusting ***M*** and ***N*** or by establishing an allowed limit for the number of detection per minute.

7.3.1.4 Control

As already explained, the comparison function of the ***IWM*** program branch generates two responses: While the value of ***ID*** is smaller than ***TR*** it generates a signal indicating an acceptable signal-to-noise ratio, and when ***ID*** becomes larger than ***TR*** it generates a signal indicating an unacceptable signal-to-noise ratio. This signal can be used either to enable/disable a program branch or can simply be used to trigger an alarm. Considering that the present system is unable to improve the S/N ratio caused by external interference the later option was adopted.

7.3.2 *TP* Branch

TP is a function of the volume of moving blood within the beam and therefore very convenient as a measure of the degree of insonation. However, within the bandwidth of interest, it is indistinguishable from random noise, consequently when extracting information about insonation from the ***TP*** signal, it is first necessary to know if the signal-to-noise ratio is acceptable. Figure 7.8 shows an example of the ***TP*** signal obtained from a patient recording made with a conventional Doppler System. It also shows values of ***TP*** obtained from pure white noise and from a mixture of Doppler signal and white noise. As already presented, an acceptable signal to noise ratio is determined through the study of the ***IWM*** signal. If the period of the ***IWM*** detected automatically at the ***IWM*** branch presents a regular pattern characteristic of sinus rhythm it can be assumed that the measured ***TP*** signal intensity is not significantly affected by noise.

The real ***TP*** signal is much more related to the degree of insonation than to the blood velocity. Considering that the vessel cross section does not change very much during the cardiac cycle it would be fair to expect that the ***TP*** signal would also be almost constant during the cardiac cycle and also during a wide range of blood flow variations related to the patient's physiological conditions. However, because of the effect of interference on the returning ultrasound signals, it fluctuates quite considerably. Additionally, because of the signal processing, which involves filtering of the low frequency signals originating from the vessel walls, the ***TP*** signal obtained in practice presents some degree of dependency on the blood velocity as explained in Section 2.9.

7.3.2.1 Conditioning

The conditioning of the ***TP*** signal consists of cancellation or at least attenuation of artefacts in order to recover the information related to the moving volume of blood within the beam. The artefacts to be dealt with by the conditioning stage are: the random noise caused by electrical interference, the speckle, the decrease of power caused by the action of the high-pass filters and, particular to the present application, a surge in the ***TP*** signal caused by the change in the phase of the signals driving the array elements.

The first step for conditioning the ***TP*** signal, consists in replacing the points in each group by their median. This is effective in attenuating the fluctuations caused by electric interference and speckle because in such a case the median and the true signal mean have almost the same value. It also attenuates the observed decrease in power at the end of diastole and minimises the duration of reduced power. It cancels the spikes caused by phase changes as long as the spikes occupy less than half of the points in each group. Figure 7.9 recorded from patient and Fig 7.10 recorded from a flow phantom (described in Section 8.3.3.1) presents the action of the filtering on a raw ***TP*** signal.

When working with a small number of points the performance of a median filter for elimination of spikes can be optimised by processing groups with an odd number of points. This is because for an odd number of points the median corresponds to the value of the central point and in an even number of points the median corresponds to the mean of two values.

The ***TP*** signal can be digitised at a lower sampling rate ($\boldsymbol{S_{rate}}$) than the ***IWM*** because of its lower frequency content. Setting the $\boldsymbol{S_{rate}}$ for the ***TP*** analogue signal to 40 Hz, and taking into account that $\boldsymbol{N_{min}}$ is equal to 8 Hz, from equation 7.1 we have $\boldsymbol{G_{size}}$ equal to 5. This group size is convenient for attenuation of the fluctuations caused by interference, and the power decrease at the end of diastole caused by the high pass filters. Additionally, being an odd number, it is more effective in the cancellation of artefacts caused by the phase change.

The conditioning presented above was applied to ***TP*** signals extracted from two different signals: a) a Doppler signal recorded from a carotid artery (Fig 7.9) and b) a

Doppler signal recorded from a flow phantom. (Fig 7.10).

The carotid flow is unidirectional and presents a significant component of the velocity which is always above the cut-off frequency of the high pass filters, therefore the resulting ***TP*** signal is not significantly affected by velocity variations. Its processed ***TP*** signal presents oscillations of less than 5 dB.

The phantom flow is comparatively more pulsatile, and towards the end of the cycle a significant velocity component is below the cut-off frequency of the high pass filters, therefore the resulting ***TP*** signal presents a cyclic reduction. The conditioning was capable of reducing the amplitude of these oscillations to around 5 dB.

Figure 7.10 also shows the effect of a progressive misalignment between the beam and the phantom vessel where it is possible to observe that the conditioned signal does not reach the threshold prematurely.

The present conditioning routine was not developed to deal with extreme cases like an intermittent blood flow which would generate pulsed ***TP*** signals, however it is possible to adjust the routine to act as a peak detector which would generate envelope signals following the peaks of the ***TP*** signal.

It was observed that the sensitivity of the transducer and electronics vary with the steering angle. This is partly caused by the effects of projection and diffraction as already presented in Chapter 4, but is also a function of the present stage of development of the transducer and the electronics. The conditioning stage can also produce an equalisation of the output signals corresponding to each steering angle by applying calibration factors determined experimentally. It must be pointed out however that such a procedure just increases the accuracy of the vessel tracking without any gain in range or in the quality of the measured signal.

7.3.2.2 *TP* - Intensity measurement

For a given steering position, the average intensity of the ***TP*** conditioned signal is a function of the alignment between transducer and vessel. This is presented in Fig 7.10 where the change in ***TP*** level as a consequence of the transducer movement can be observed. Figure 7.11 shows the variation of ***TP*** when the transducer scans a vessel (Doppler phantom) maintaining a fixed steering position It is therefore expected that the intensity of the conditioned ***TP*** signal which enables direct comparison among the degrees of insonation is also a function of the intensity of the transmitted acoustic field at the different steering positions. Figure 7.12 **a** presents the theoretical maximum intensity profiles of the acoustic fields generated by a transducer with the same dimensions as the fourth version of the transducer. This diagram is basically the same presented in Fig. 5.5 **c**. Figure 7.12 **b** shows the same profiles on a dB scale.

Ideally $\boldsymbol{TP}(\theta)$ would be proportional to $\boldsymbol{I_{RDP}}(\theta)$ which takes into account just the effect of geometrical factors such projection and diffraction (as defined in Section 4.2.5) and assumes an ideal receiving circuit. These conditions would ensure the achievement of the predicted performance of the equipment and the basic feedback program was developed for such ideal conditions. At the present stage of development however these conditions are not achieved and alternative procedures had to be developed to cope with the situation. These are presented in Section 7.3.3, and also in Chap. 8 and discussed in Chap. 9.

The threshold values for the ***TP*** signal, unlike in the case of the ***IWM*** signal already discussed, must be constant. This is because the main objective of this project is to ensure the adequate quality of the Doppler signals recorded in long term monitoring. These thresholds are experimentally set by the operator when attaching the transducer to the patient before the system starts operation. At this stage, the feedback loop is disabled and the steering angle is set to zero. The operator then observes the sonogram or listens to the audio of the Doppler signal in order to find the best alignment. He/she is also able to adjust the gain of the Analyser (DSP32C) and choose the threshold levels required for the classification of the "quality" of the insonation. The thresholds levels are also represented in Fig 7.12 **a / b**

7.3.2.3 Comparison function

Two thresholds are chosen to enable the classification of insonation from the measured ***TP*** intensity in three distinct categories: a) 'Good' - above the first threshold, indicating good insonation and no need for the beam redirection. The first threshold level must be adjusted to ensure that the tracking routine is triggered only when the TP level corresponds to a Doppler signal of minimum acceptable 'quality' for recording. Such adjustment enable the maximum dynamic range of the equipment to be explored to deal with residual oscillations of the conditioned ***TP*** signal. However, in case of a progressive decrease of flow as might result from the patient's condition, as in the case of a failing graft, there is a limit beyond which the velocity of all particles in the blood vessel will be below the cut-off frequency of the high pass filters. In this case the TP signal will be interpreted as indicating insufficient insonation. b) 'Insufficient' - between the first and the second thresholds indicating an insufficient insonation corresponding to a Doppler signal detectable but below the minimum acceptable 'quality' for recording and the need for a minor redirection. c) 'Poor' - below the second threshold, indicating very low or no insonation and therefore a wide search is necessary.

When the system is set in operation, the intensity of the ***TP*** signal is continuously monitored and classified as belonging to one of these three categories.

7.3.2.4 Control

The control stage of the TP branch contains the strategy represented by the tracking routines triggered when the amplitude of the TP signal goes below the threshold levels. These routines are responsible for the generation of the feedback steering command, the binary word to be loaded in the first four-bit adder in the DUPAT. Whenever the insonation is classified as 'good', no signal comes out of the comparison stage, no tracking routines is activated and no command is sent to the DUPAT steering circuit. Consequently, the beam steering angle remains unchanged.

7.3.2.5 Summary

The feedback loop operates with two inputs, ***IWM*** (Intensity Weighted Mean) and ***TP*** (Total Power). The object of ***IWM*** processing is the evaluation of the signal-to-noise ratio. The IWM branch is active whilst the TP level indicates 'good degree of insonation' (substantial Doppler power). The object of the ***TP*** processing is the evaluation of the degree of vessel insonation. If the signal-to-noise ratio is high (as indicated by the ***IWM*** branch) it is assumed that the evaluation of the degree of vessel insonation by the ***TP*** branch is sufficiently reliable to perform the automatic activation of the tracking routine. If the signal-to-noise ratio is low it is assumed that the ***TP*** signal is not a reliable estimator of the degree of insonation. As consequence, the instrument is not capable of activating the tracking routine and an operator intervention is necessary. A diagram of whole program is presented in Fig. 7.13

7.3.3 Strategy - Tracking routines

Two sets of tracking routines were developed for the case where the insonation is not classified as 'good'. The first set was designed to cope with a possible nine steering directions necessary to track the vessel in the range of -20° to +20°, it consisted of a 'small adjustment routine' and a 'wide search routine'. In practice however, because of limitations of the transducer and electronics, many fewer steering directions were available and therefore a 'limited tracking' routine was also developed for experimental use with the current system.

7.3.3.1 Small adjustment routine

The classification 'Insufficient' indicates a condition of detectable but insufficient insonation. It activates a small adjustment routine based on the assumption that the best direction should be adjacent to the initial position, and requires at most two jumps. This small adjustment routine, once enabled, is capable of tracking the vessel in up two steering movements. These steps are described below and are also represented in the diagram of Figure 7.14 **a.**

Step one - Record the initial conditions: Store the present steering position **(S1)** classified in two categories: Internal (-3, -2, -1, 0, 1, 2, 3), or External (-4, -4).

Step two – First steering movement: The beam is steered to a second position **S2** which is always an internal position adjacent to **S1** (if **S1** is different from zero) or a position to the left of **S1** (only if **S1** is equal to zero).

If after the first steering movement **TP** becomes higher than the first threshold the tracking routine is disabled meaning that the first steering movement was enough to align beam and vessel. In case **TP** remains below the first threshold it means that the first steering movement was in the wrong direction and a further steering is necessary.

Step three – Second steering movement.

If **S1** was interior, the second steering movement called 'jump' is aimed to the second adjacent position.

If **S1** was exterior, the second steering reverses the first steering in a 'bounce' movement. It assumes that the tracking routine was triggered by artefact but may also indicate that the vessel is already in an unstable limit situation or out of range.

In case the vessel is not tracked after step three of the small adjustment routine, it is triggered again. If the first run was caused by artefacts, the second run may be successful in tracking the vessel. If the vessel is already in an unstable limit situation or out of range, the routine is repeated continuously.

7.3.3.2 Wide search routine

When the classification is 'poor', a wide search routine is activated. This tracking routine assumes that the beam is pointing away from the vessel and follows a pre-set sequence of steps described below. Figure 7.14 **b** helps the visualisation of this sequence.

Step one - Record the initial conditions: Store the present steering position **(S1)** classified in three categories: central **(0)**, negative **(-1, -2,-3, -4)** or positive **(1, 2, 3, 4)**.

Step two – First steering movement.

The first steering movement always brings the beam to the central position. If the initial position is already **0,** step two is skipped.

If after steering **TP** becomes higher than the first (higher) threshold it means that the first steering movement was enough to align beam and vessel and all tracking routines are disabled.

If after the first steering movement the **TP** value only raises above the second (lower) threshold the wide search routine is disabled and the fine adjustment routine takes over.

In the case that **TP** remains below the second threshold, it means that the first steering movement was incorrect and a further steering movement in the wide search routine is executed.

Step three – Second steering movement.

The second steering movement of the wide search routine points either to **-3**, in the case where the initial position **S1** was classified central or positive, or to **+3** in the case where the initial position was classified as negative. The same evaluation performed after the first steering is applied here and if required, the third steering movement of this routine is executed.

Step four – Third steering movement.

The third steering movement of the wide search routine is a 'mirror' of the second, it results in three possibilities: a) the vessel was successfully tracked, in this case all tracking routines are disabled. b) the TP value only raises above the second (lower) threshold. In this case the wide search routine is disabled and the small adjustment routine takes over, c) the vessel was well out of range, and in this case the wide search routine is triggered again taking the last steering position as the start point and the routine is repeated continuously.

In any case where the routine is repeated continuously, it is up to the operator to decide if the best option for this situation would be to sound an alarm or to let the instrument carry on trying until the vessel is inside the range again.

7.3.3.3 Limited tracking routine

This tracking routine was developed taking into account the reduction of the possible steering positions to four. In this case, just one threshold level was required for the classification of insonation from the measured ***TP*** intensity into two distinct categories: 'Good', above the threshold, indicating good insonation and no need for the beam redirection. 'Insufficient' below the threshold indicating low or no insonation and the need for adjustment.

The adopted strategy is presented below, it consisted of a sequence of steps of the 'limited tracking routine' triggered when the amplitude of the TP signal goes below the threshold level. Figure 7.15 helps the visualisation of its operation, which for the sake of clarity is represented in two diagrams. The first steering movement has no 'previous knowledge' and therefore represents a guess, which is identical in both diagrams. The second steering movement depends on whether or not the first step (guess) was in the correct direction, and these two scenarios are presented separately in **a** and in **b**.

Step one - Record the initial conditions: Store the present ***TP*** amplitude (**A1**) and the steering angle (**S1**) classified in two categories: Internal (-1 or 1) or External (-2 or 2).

Step two - Steer the beam: The beam is steered to a second position **S2** which is dependent on **S1**. In the case where **S1** is internal the beam is switched to its 'mirror' position. This steering movement can be called a 'switch'. In the case where S1 is external, it is steered to the nearest internal position closing the steering angle. This steering movement can be called a 'hop'. In any case, **S2** is always an internal position.

If, after steering, the amplitude of **TP** (**A2**) becomes higher than the threshold it means that the first steering movement was enough to align beam and vessel, then the tracking routine is disabled and after a small delay, the memory is reset erasing the values of **A1** and **S1**. In the case where the **TP** amplitude remains below the threshold it means that the first steering movement was not enough to align the beam and vessel and therefore further steps are required and the routine proceeds to the following step.

Step three - Comparison: **A2** is stored and subtracted from **A1**. This subtraction is a comparison test to find whether or not the first steering movement was in the correct direction to align the beam and vessel. If **A1-A2** is positive, the movement was in the wrong direction and if it is negative, it was in the correct direction. The next step of the program needs to consider this.

Step four - Steer the beam further: From S1 and A1-A2, the second steering can be decided.

If S1 was exterior and A1-A2 is positive, it means that the vessel is likely to be positioned on the same side as **S1** but lateral in relation to the transducer range. Step two must be reversed and this second steering movement can be called a 'bounce'. When a bounce occurs it also means that the position of the vessel may be out of range but there is a possibility that the tracking routine was triggered by a noisy **TP** signal, in any case it represents an unstable limit situation.

If **S1** is exterior and **A1-A2** negative it means that the vessel is likely to be positioned towards the closer opposite half of the transducer range in relation to **S1**. The beam must be steered one step further and this second steering movement can be called a 'skip in'. A skip also means that the vessel may be in a stable central situation.

If **S1** is interior and **A1-A2** is positive it means that the vessel is likely to be positioned on the same side as the **S1** but lateral in relation of the transducer range. The beam must jump back going beyond **S1** and this second movement can be called 'jump'. When a jump occurs it means that the vessel may be still be in a stable situation but near to the limit.

If **S1** is interior and **A1-A2** negative it means that the vessel is likely to be positioned on the far opposite side of the transducer range in relation to **S1**. The beam must step further skipping the present position. This second movement can be called 'skip out'. When a skip-out occurs, it also means that the vessel may still be in a stable situation but near to the limit.

This routine ensures that all possible options are tried in one or two steering movements and therefore as long as the vessel is contained inside the total range, it should be tracked by the above sequence of moves. This includes either the case of a long term monitoring situation when the instrument is on and the misalignment is a result of a transducer movement, or the case when the transducer is placed in an arbitrary position inside the range and the instrument is then switched on.

If the vessel is not tracked after the fourth step, the routine is triggered again before the memory is reset. In a second run, **S1** is replaced by **S2** of the first run. The second run can be caused either by artefacts or by the fact that the vessel is out of range. In the first case, the second run may be successful in tracking the vessel. In the second case, the routine is repeated continuously. It is up to the operator to decide if the best option would be to sound an alarm or to let the instrument carry on trying until the vessel is inside the range again.

7.4 Conclusion

The feedback system presented in this chapter is capable of processing the IWM and TP signals in real time in order to enable the Doppler tracking instrument to correct transducer-vessel misalignments.

The present feedback loop hardware, which is convenient as a development tool, lacks portability. In a future version of the equipment, designed for clinical use it can be replaced by a single board fitted inside the DUPAT.

The tracking routine presently in use was adapted to work with a smaller number of steering positions because of current limitations of the transducer and electronics.

The performance of the system is presented in Chapter 8 and the present limitations and future improvements are discussed in Chapter 9.

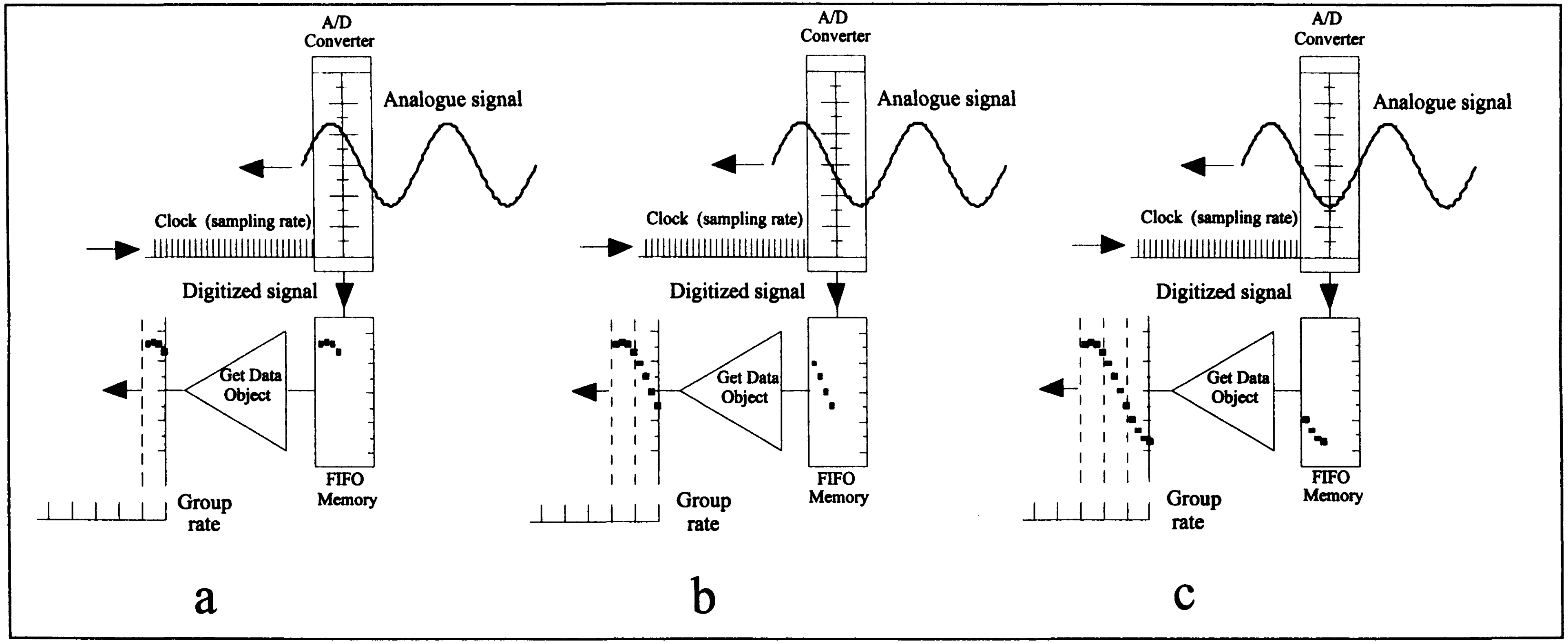

Fig. 7.1 Schematic diagram of the operation of A/D subsystem and 'Get Data' object. For one input channel, the A/D converter reads the voltage of the incoming analogue signal (represented by a sinusoid) with a chosen frequency (sampling rate). The successive digitised values are built up in the FIFO memory to form a group. As soon it reaches the programmed size, the group is read by the 'Get Data' object. By this process, the digitised signal is output in groups by the 'Get Data' object at a rate which can be called the 'group rate'. Three successive operations in the 'group rate' sequence are presented in parts **a**, **b** and **c**.

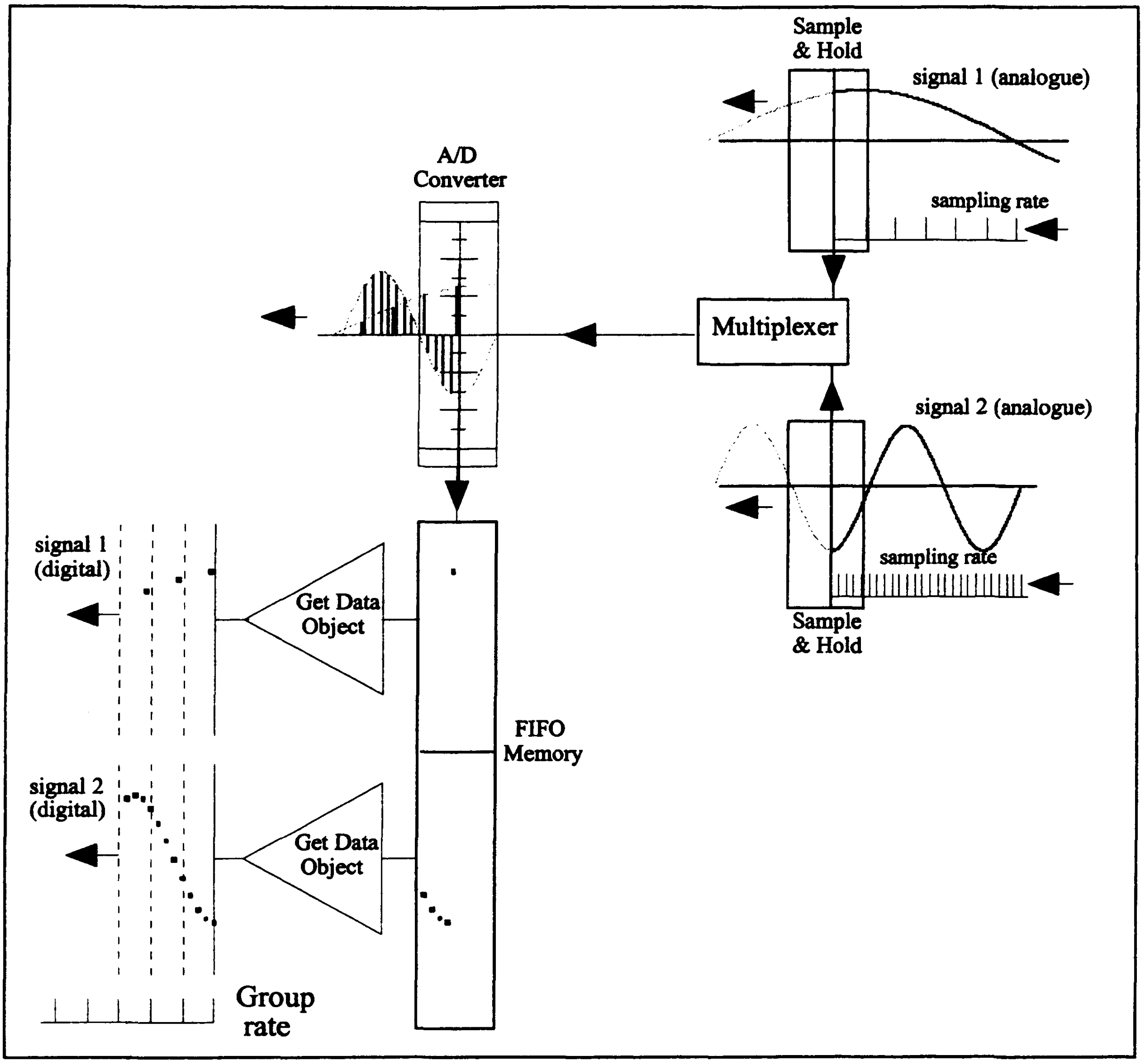

Fig. 7.2 Schematic diagram of the A/D subsystem and 'Get Data' object for the case of two channels. The A/D subsystem consists of two 'sample and holds', (one for each channel), a multiplexer and the A/D converter. Each 'sample and hold' can have a particular sample rate. In the example, the two sinusoids with different frequencies represent the input analogue signal. The sampling rates are different and in the example, channel two has a sampling rate four times faster than channel one. The samples are multiplexed in such way that their relative time reference is preserved. They are digitised in the A/D converter and queued in the FIFO memory (the time reference and channel information is also stored). As soon as the number of samples for a channel reaches the programmed group size, it can be read by the 'Get Data' object. The group size is inversely proportional to the sampling rate but the group rate is the same for all channels.

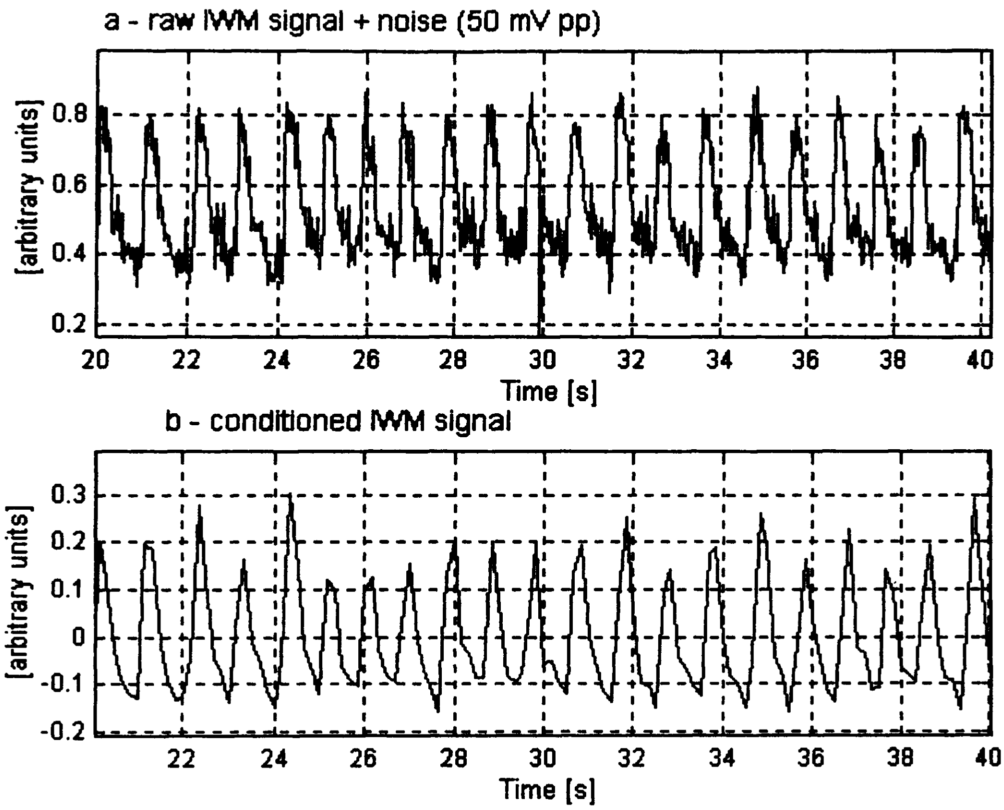

Fig. 7.3 The effect of IWM signal conditioning for the purpose of measuring the cardiac cycle by zero crossing detection. The same segment of an IWM signal obtained from a patient record which was mixed with a white noise 50 mV pp is presented twice. **a**) before conditioning. **b**) after conditioning.

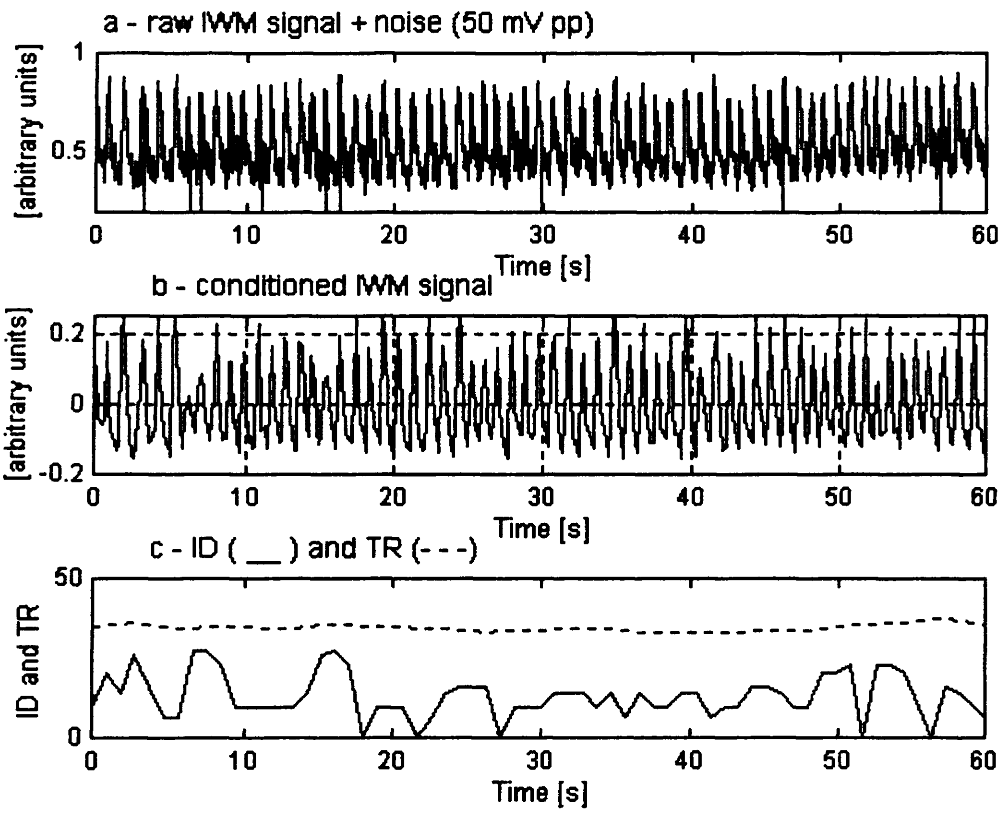

Fig. 7.4 Response of ***ID*** and ***TR*** to noise. **a)** Segment of IWM extracted from a patient recording. The audio signal was mixed with white noise of amplitude 50 mV. **b)** The same segment after conditioning in order to extract the cardiac frequency. **c)** Behaviour of ***ID*** and ***TR***. is not significantly affected. This figure can be compared with Fig. 7.5 and Fig. 7.6, where the same patient signal segment was employed.

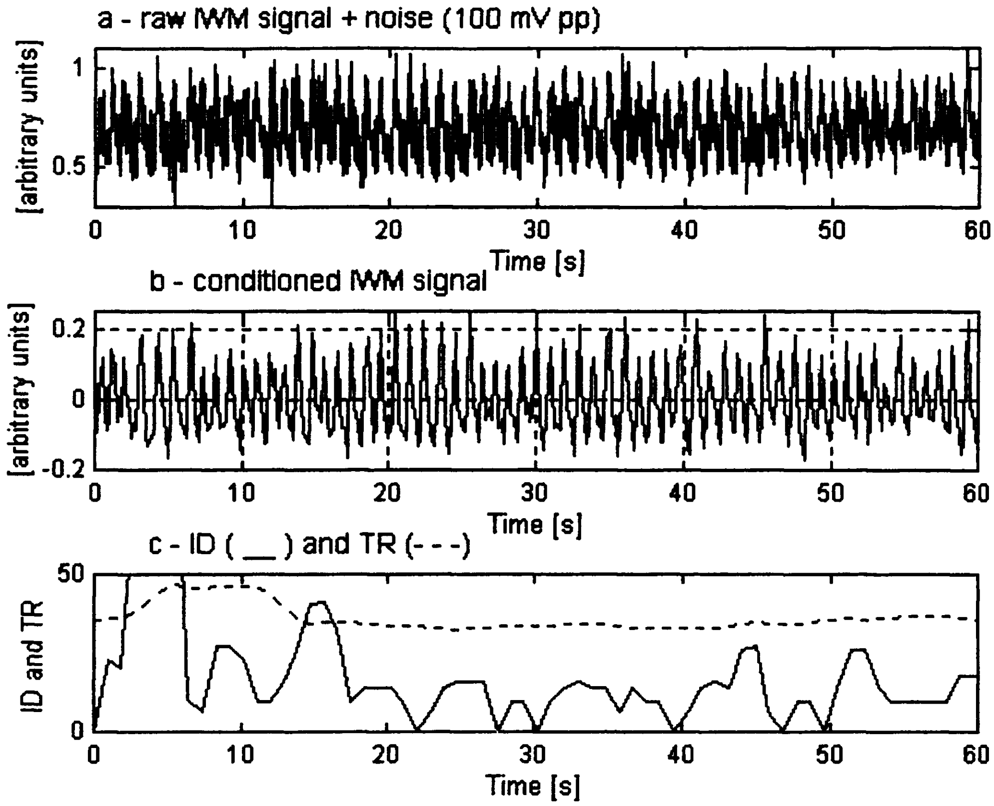

Fig. 7.5 Response of ***ID*** and ***TR*** to different noise levels. **a**) Segment of IWM extracted from a recording of a patient; the audio signal was mixed with white noise of amplitude 100 mV. **b**) The same segment shown in **a** after conditioning in order to extract the cardiac frequency. **c**) Behaviour of ***ID*** and ***TR***. in response to the noise. This figure can be compared with Fig. 7.4 and Fig. 7.6, where the same patient signal segment was employed.

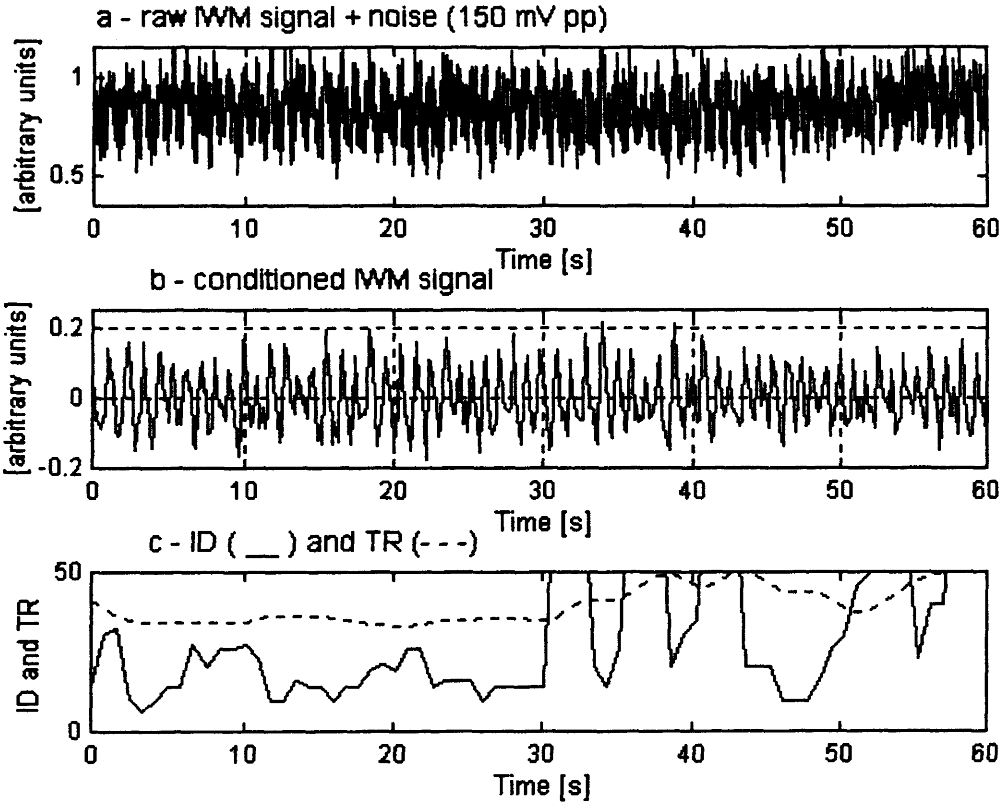

Fig. 7.6 Response of ***ID*** and ***TR*** to different noise levels. **a)** Segment of IWM extracted from a recording of a patient; the audio signal was mixes with white noise of amplitude 150 mV. **b)** The same segment shown in **a** after conditioning in order to extract the cardiac frequency. **c)** Behaviour of ***ID*** and ***TR***. in response to the noise. This figure can be compared with Fig. 7.4 and Fig. 7.5, where the same patient signal segment was employed.

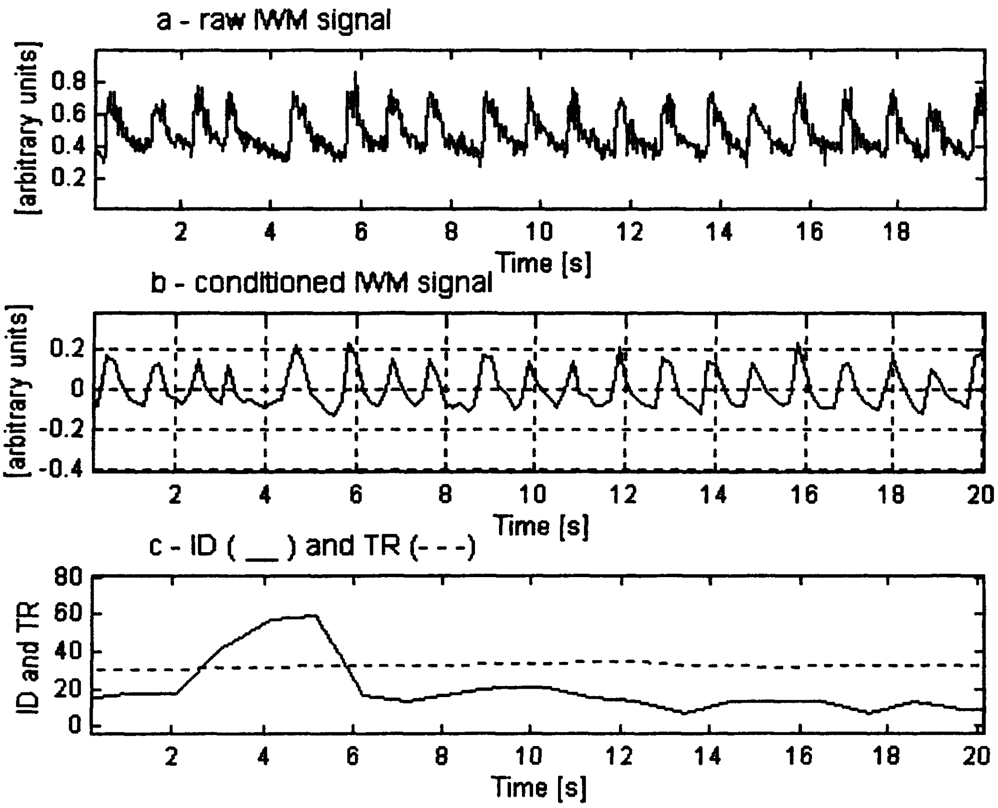

Fig. 7.7 Effect of cardiac variations on ***TR*** and ***ID***. **a**) Segment of ***IWM*** extracted from a recording of a patient; it is possible to observe the cardiac variations. **b**) The same segment shown in **a** after conditioning in order to extract the cardiac frequency. **c**) Behaviour of ***ID*** and ***TR***. in response to the cardiac variations. For normal sinus rhythm, ***ID*** is smaller than ***TR*** as can be observed between 6 and 20. Larger variations in cardiac cycle (between 2 and 6) can cause increase in ***ID*** beyond ***TR***.

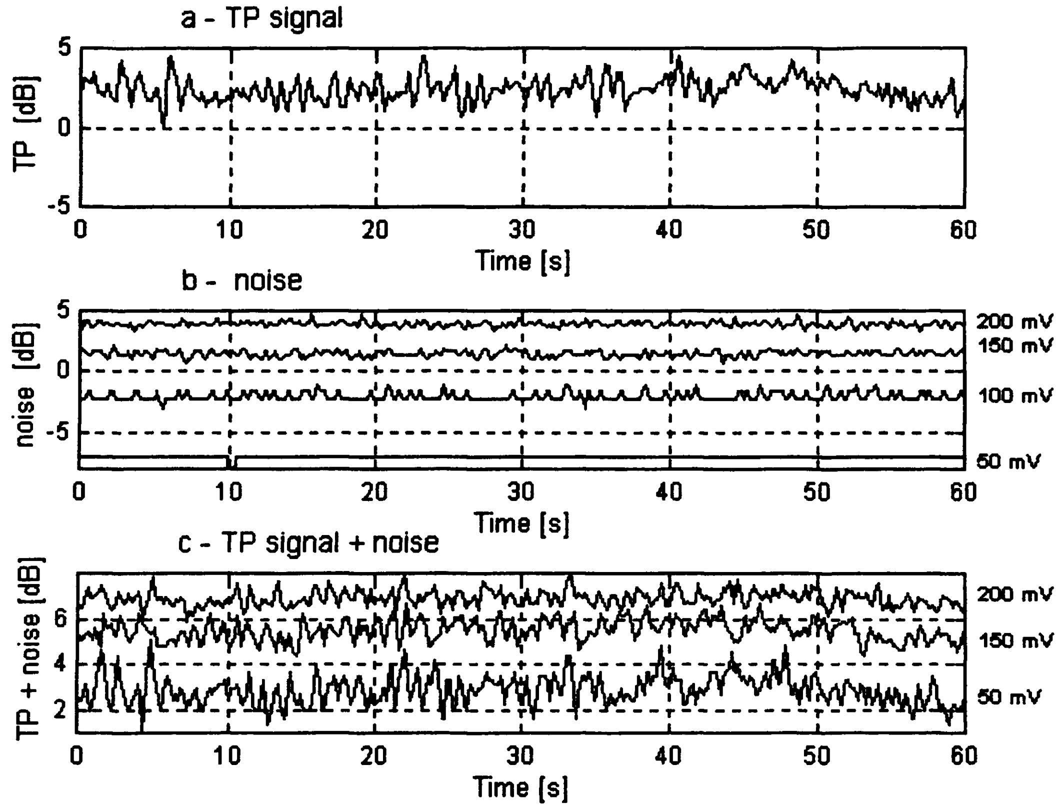

Fig, 7.8 *TP* from signal and noise. **a)** Example of ***TP*** signal extracted from patient recording. **b)** ***TP*** signal obtained from pure white noise (in four different levels: 50 mV pp, 100 mV pp, 150 mV pp, and 200 mV pp). **c)** ***TP*** signal extracted from the mixture of the signal shown in **a** with the noise shown in **b**. It can be observed that the noise alone can produce a ***TP*** signal on a level equivalent to the true patient Doppler signal. It can also be observed that the noise added to the true patient signal causes an increase in the ***TP*** signal.

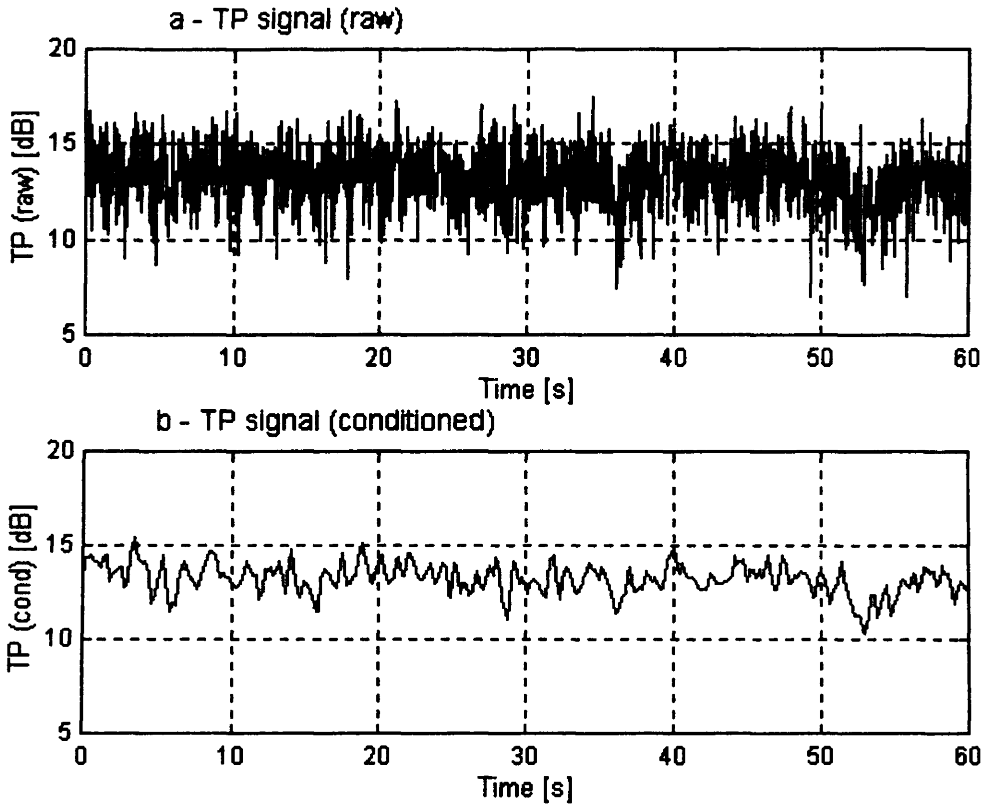

Fig. 7.9 Filtering a raw *TP* signal. **a)** Example of a *TP* signal extracted from patient recording before conditioning, the presence of fast oscillations and spikes which produces a fluctuation of *TP* in a 10 dB range can be observed. **b)** The same signal segment after conditioning which eliminates the fast oscillations and spikes reducing the *TP* fluctuation to less than 5 dB.

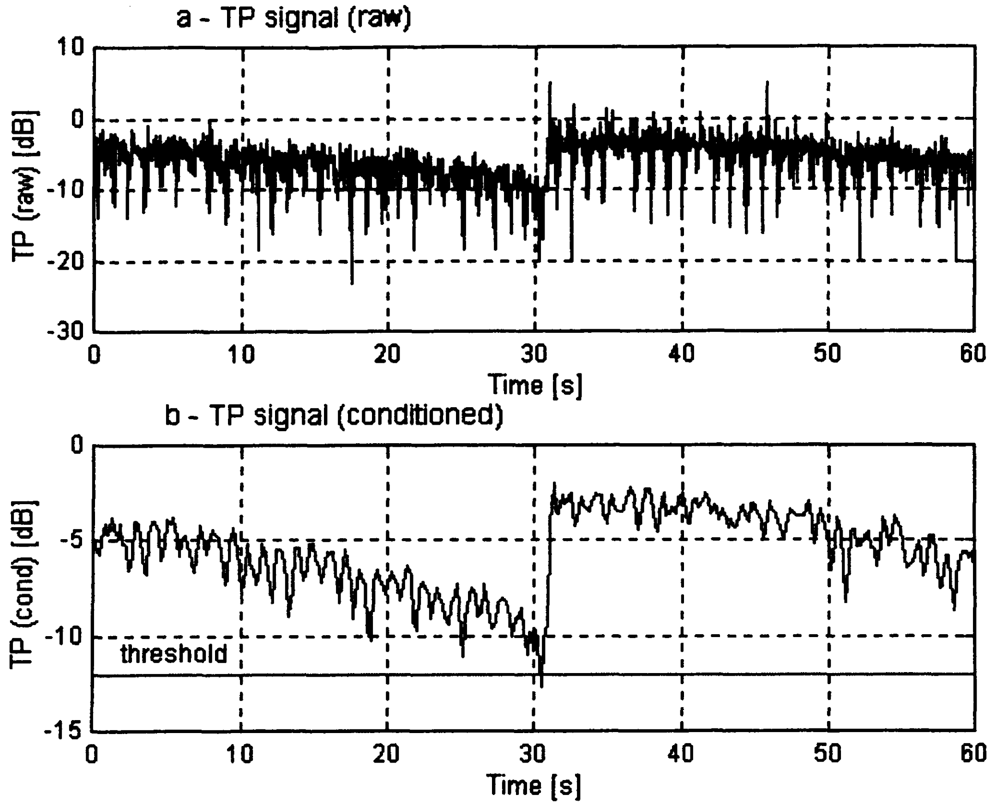

Fig. 7.10 A segment of ***TP*** signal where the action of signal conditioning and slow and fast variation of insonation are presented. For the duration of the recording the transducer was scanned across the vessel (Doppler phantom) with uniform movement. From zero onwards the alignment between beam and vessel decreased causing the fall in the ***TP*** level. When the ***TP*** fell below the threshold (approximately 31 ***s***) the tracking mechanism was triggered and the beam steered, restoring the alignment. **a**) The raw signal presents fast oscillations and spikes causing fluctuation in ***TP*** in a range larger than 20 dB. Particular to the present application, another artefact is also shown, It is caused by the rapid change in phase of the elements which produces an apparent transient Doppler shift and a surge in the detected ***TP*** signal immediately after the phase change. **b**) The same signal segment after conditioning which eliminates the fast oscillations and spikes reducing the ***TP*** fluctuation to less than 5 dB.

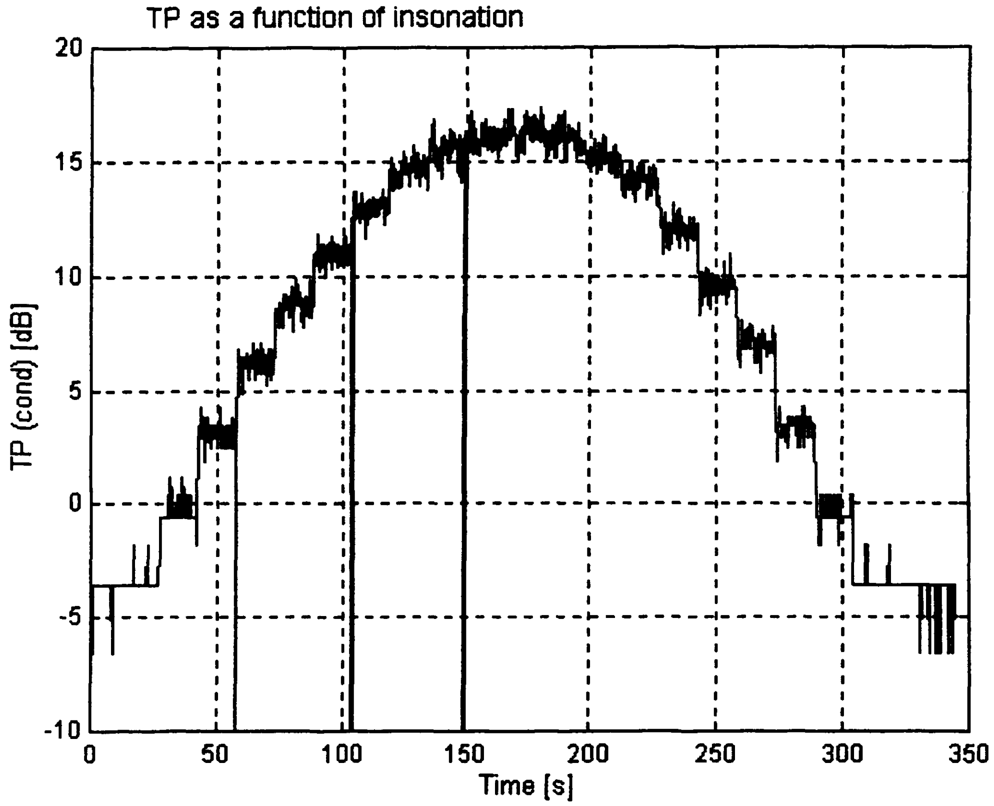

Fig. 7.11 *TP* as a function of the insonation. This *TP* profile was constructed operating the transducer in a fixed steering position. It was scanned across the vessel (Doppler phantom) in steps of 0.5 mm. After each movement it was kept still for approximately 20 seconds and then moved again. Each step in the profile represents 20 seconds recording in a stationary position spaced 0.5 mm from the previous position.

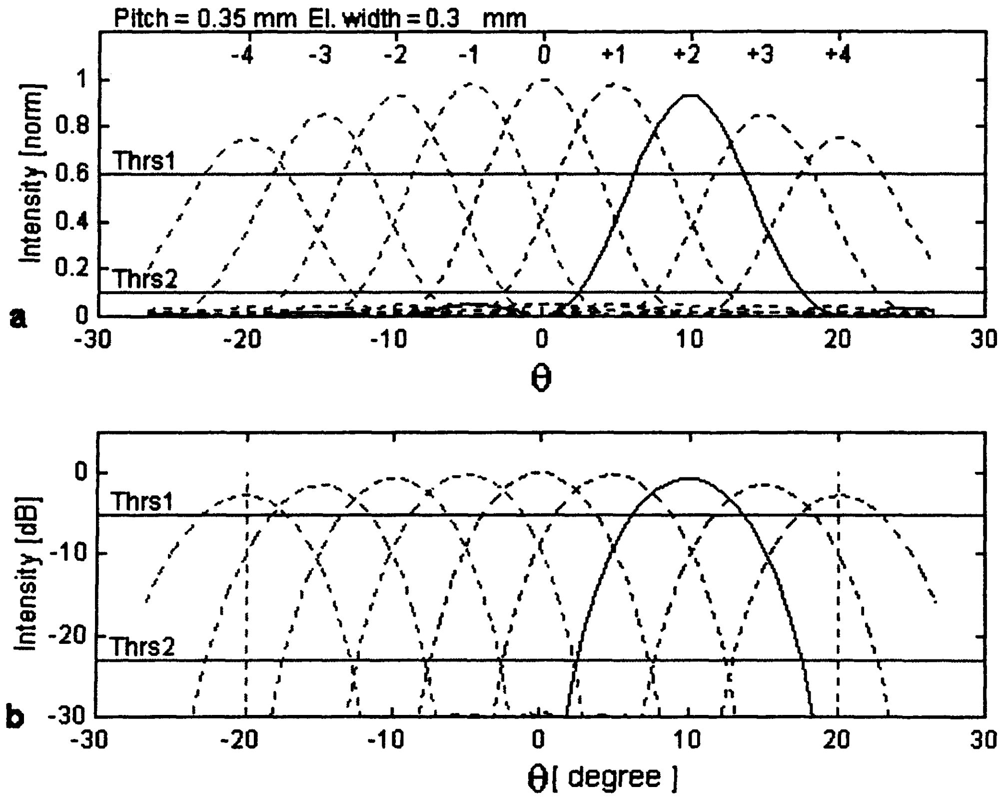

Fig. 7.12 Simulations of the maximum intensity profiles of nine acoustic fields corresponding to nine steering positions which are sufficient to cover the range -20° to +20° as specified in chapter 5. The profiles are generated by a 1-D array transducer with pitch = 0.35 mm, element width = 0.30 mm taking into account the effect of projection and diffraction. **a)** Reproduces the profiles already presented in Fig. 5.5. **b)** Shows the same profiles on a dB scale. The thresholds (**Thrs1** and **Thrs2**) are represented in both diagrams. The region above **Thrs1** correspond to insonation classified as 'good', the region between **Thrs1** and **Thrs2** correspond to an insonation classified as 'insufficient', the region below **Thrs2** corresponds to a classification of 'poor'.

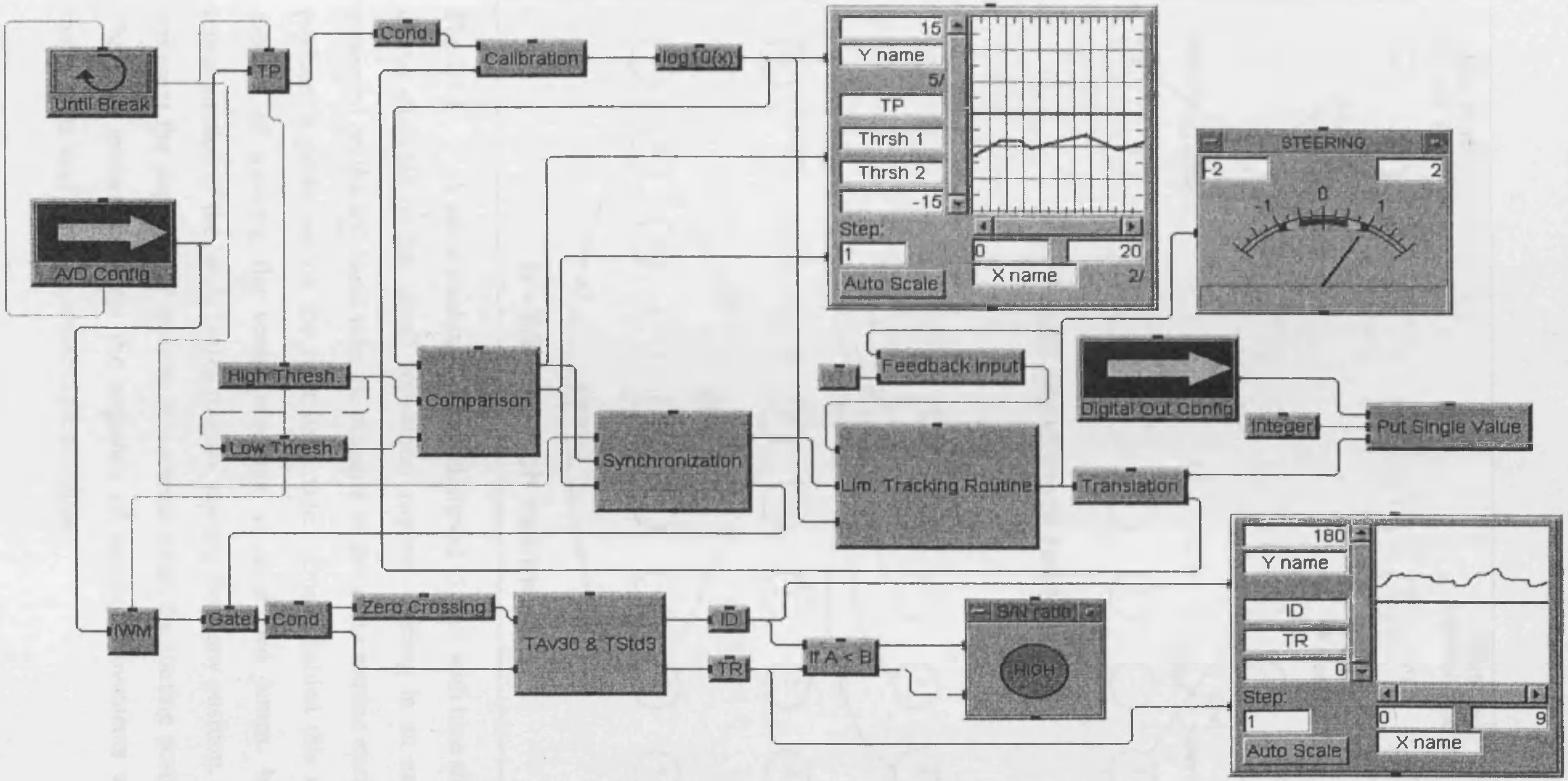

Fig. 7.13 Diagram of the HP-VEE program with two branches designed to process the ***TP*** and ***IWM*** signals. The ***TP*** branch is explained in Sections 7.3.2 to 7.3.2.4. When the ***TP*** level is lower than the 'high' threshold, the synchronization function activates and sets the step pace of the 'Limited tracking routine' This routine reads the ***TP*** level and the present steering position exporting the steering commands to the DUPAT via the digital output. The ***IWM*** branch is explained in Section 7.3.1 to 7.3.1.4. It is enabled by the synchronization function of the ***TP*** branch when the ***TP*** level is higher than the 'high' threshold. An alarm is set when the signal-to-noise ratio is low.

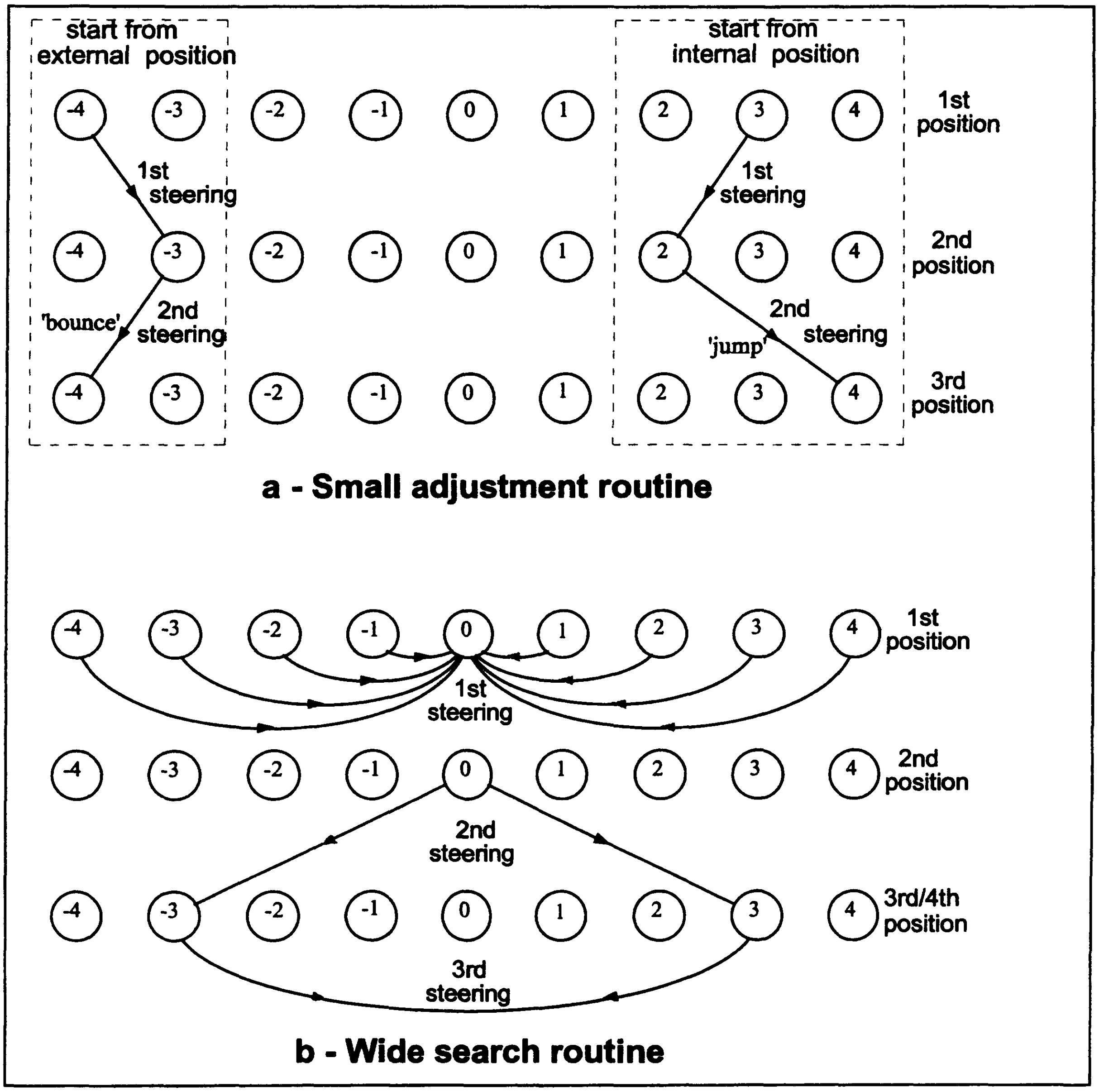

Fig. 7.14 A set of tracking routines designed to cope with nine steering positions. **a)** An example of the 'small adjustment routine' starting in an external position is presented on the left hand side; an example of the same routine starting in an internal position is presented on the right hand side. Once enabled this routine should be capable of tracking the vessel requiring at most two jumps. **b)** The schematic representation of the 'wide search routine' starting from any position. The black arrows represent the sequence of steering movements when the starting position is on the left. The grey arrows represent the sequence of steering movements when the steering movements start from the centre-right positions.

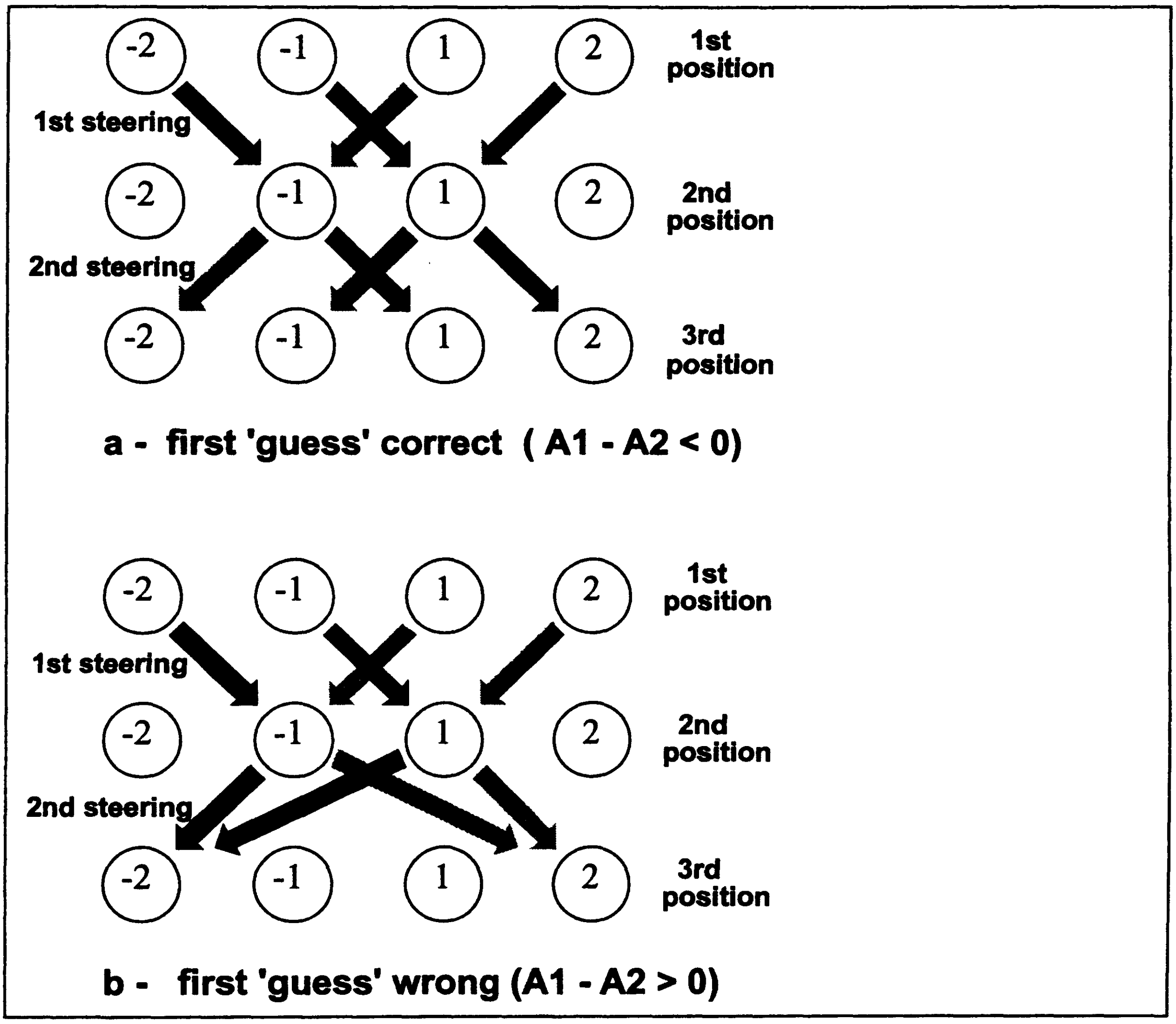

Fig. 7.15 The adopted strategy consisting of a sequence of steps of the 'limited tracking routine'. The illustration is divided into two for clarity. The back arrows represent movements starting from left-hand side positions, and the grey arrows represent movements starting from right hand side positions. The first steering movement has no precondition representing a guess, therefore is identical in both diagrams. The second steering movement depends on whether or not the first step (guess) was in the correct direction; these two hypotheses are presented separately. **a)** Represents the case where the first step was made in the correct direction and any further transducer movement will be moving forward. **b)** Represents the case where the first step was in the incorrect and direction the next steering movement will be backwards.

Chapter 8

Results

8.1 Introduction

The subject of this chapter is the presentation of the experiments performed and the results achieved during the development and at the conclusion of this project. For each stage the experimental technique employed is described and the results are displayed either as tables or figures. The discussion of the results is presented in chapter nine.

The first part of the project was dedicated to the development of the transducer and the electronics required to drive the transducer. CW Doppler array transducers and CW Doppler steereable array flowmeters were not commercially available and therefore it was necessary to construct them from scratch. The description of the transducer development and construction is presented in Chapter 5 and the description of the electronics in Chapter 6. The second part consisted of the setting up of the whole system, with the implementation of the feedback loop and the development of the tracking program. For this stage the hardware was available and therefore the work consisted of assembling the units together and developing the software necessary to drive the system. The software is presented in Chapter 7. The presentation of the results is organized to follow the same order.

8.2 Tests

Periodic tests and measurements were made regularly to confirm the success of each stage of the transducer manufacture. In the following sections the tests performed since the early stages of construction of this transducer are presented. These tests can be classified into, electrical, acoustic and Doppler. The tests performed on the DUPAT alone during its development in the Electronic Workshop of the Department of Medical Physics are not presented here. However the DUPAT was effectively tested when the steereable Doppler instrument was tested either to plot its acoustic field or to measure its Doppler tracking range.

8.2.1 Electrical tests

The electrical tests, applied at early stages of transducer construction, when the measurement of the acoustic output was not yet possible, ranged from simple continuity measurements to more elaborate tests based on electrical equivalent models of the transducer (Silk 1984). In these, simultaneous electrical input and output measurements were performed over a known frequency range enabling the observation of the transducer input impedance and phase as a function of frequency. These impedance and phase measurements can be more precisely made with a Vector Impedance Meter, however for qualitative and comparative purposes a simplified set-up was employed.

This set-up (Fig. 8.1) consists of a Signal Generator (Philips PM 5134) connected to the device $\boldsymbol{Z}$ to be measured through a known series resistance $\boldsymbol{R}$. A dual channel oscilloscope (Gould OS 1420) and a frequency-meter are employed for the measurements. The voltages V_1 and V_2 at respectively the output of the signal generator and after the series resistance are measured.

It is then possible to visualize on the screen of the oscilloscope the variations in amplitude of V_1, V_2 and the phase difference α between them as a function of the frequency. These experimental values of voltage phase and frequency could be sequentially sampled in the range of interest and then typed into a worksheet constructed with Microsoft Excel where automatic calculations are performed to provide calibration normalization and a plot of the results (Table 8.1).

Table 8.1 - Measurement of Frequency Delay and Voltage
Calculating & Plotting: Frequency, Phase and Voltage

Device: Loose ceramic - number 10
Ceramic: PZ27 Ferroperm Dimensions: 6.5 x 7.5 x 0.475 (mm)

Settings:	INPUT DATA				OUTPUT DATA			
Func. Gen.	F(MHz)	Delay	Ch1 (I)	Ch2(o)	Freq.(Hz)	Phase	Vnor. %	Vnor.
Freq.	1.00E+06	0.00E+00	0	0		Degree	100	17
(MHz)	2.969	3.0	16.0	12.5	2.97E+06	33.06	78.13	0.78
1.00E+06	3.319	2.0	15.0	13.0	3.32E+06	24.64	86.67	0.87
	3.516	1.5	15.0	13.4	3.52E+06	19.57	89.33	0.89
	3.782	1.0	15.0	13.8	3.78E+06	14.04	92.00	0.92
Oscillosc.	3.921	0.5	14.5	14.0	3.92E+06	7.28	96.55	0.97
Ch1	4.15	0.0	14.5	14.5	4.15E+06	0.02	100.00	1.00
(V/trace)	4.265	-0.5	14.5	14.5	4.27E+06	-7.91	-100.00	1.00
0.1	4.336	-1.2	15.0	14.0	4.34E+06	-19.31	-93.33	0.93
Ch2	4.437	-2.0	15.0	14.5	4.44E+06	-32.93	-96.67	0.97
(Volts/trace)	4.556	-3.5	17.0	11.0	4.56E+06	-59.18	-64.71	0.65
0.1	4.62	-3.0	18.0	7.5	4.62E+06	-51.44	-41.67	0.42
Scan	4.674	-1.5	18.0	5.5	4.67E+06	-26.02	-30.56	0.31
(ns/trace)	4.739	0.0	19.0	2.5	4.74E+06	0.02	13.16	0.13
1.03E-08	4.884	1.5	18.0	7.0	4.88E+06	27.19	41.18	0.41
	5.038	2.0	17.0	10.5	5.04E+06	37.40	61.76	0.62
	5.378	1.5	16.0	12.3	5.38E+06	29.94	79.35	0.79
	5.872	0.8	15.5	14.0	5.87E+06	17.43	90.32	0.90

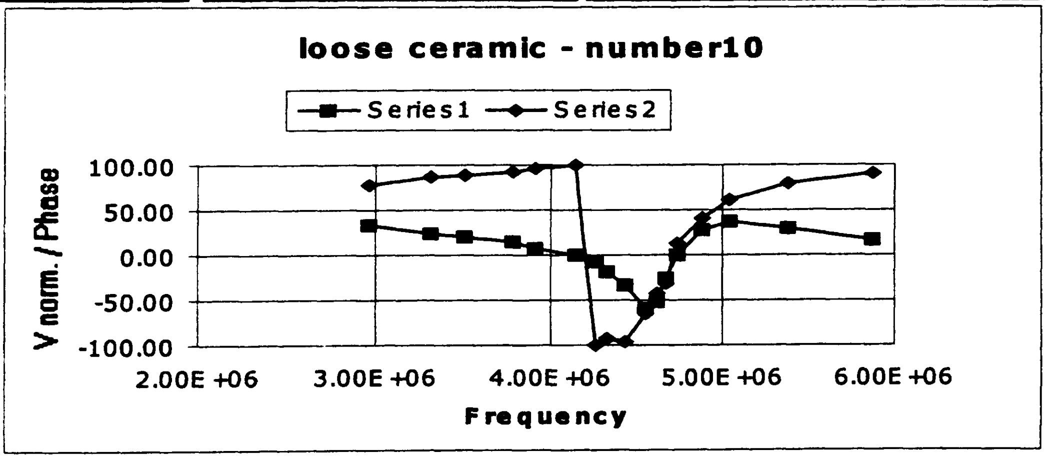

Table 8. 1 Worksheet to process $V1(f)$, $V2(f)$ and their phase difference $\alpha(f)$, and to display $\alpha(f)$ (Series 1) and $V(Z(f))$ (Series 2).

At the series (resonance) frequency fs and at the parallel (anti-resonance) frequency fp, α is equal to zero. It is known that the frequency corresponding to the maximum output of a piezoelectric transducer is situated between fs and fp (Berlincourt et al 1964).

This method was manual and time consuming therefore an alternative quick method consisting of the observation of $Z(f)$ over a desired frequency range was also employed, (Fig 8.2).

In this case the Function Generator is replaced the by a Sweep Generator, the sweep frequency is adjusted to span the range of interest, and the voltage $V_{f1 \rightarrow f2}$ is applied to the RZ series circuit. The oscilloscope is operated in the XY mode, the saw tooth wave $V(f)$ (available from the sweep generator) is input to channel 1 (X). $V(Z(f))$, taken between R and Z is the input to channel 2 (Y). Adjusting the sensitivity of channel 1 it is possible to display $V(Z(f))$ in the frequency domain over the range $f1$ *to* $f2$.

This method, useful in monitoring the construction process through repetitive measurements, has the advantage of providing a quick and dynamic visualization of $Z(f)$, which is proportional to $V(Z(f))$. The disadvantage is that it does not provide a measurement of the phase of the signal.

The functions $V(Z(f))$, obtained with a series of known impedances were recorded over the frequency range of interest. From these records it was possible to build a reference scale to measure the impedances of the ceramics. In Fig. 8.3 the test of a fourth version transducer in the frequency range of 2 MHz to 5.5 MHz is presented. Z_t and Z_r and Z_e represent the values of $Z(f)$, respectively for the transmitter array, for the receiver array and for one single element of an array. In the same diagram are also shown the records of ***Z(f)*** for resistances of 75Ω, 175Ω, 444Ω and 1075Ω.

In fig 8.4 the simultaneous plots of ***Z(f)***, for eight elements of one array in the frequency range of 2 MHz to 5.5 MHz are shown.

8.3.2 Acoustic tests

When it was possible to operate the transducer as an ultrasound generator its acoustic field could be plotted in an acoustic tank. (fig 8.5)

The Beam Plotting Tank (BPT)* of the Department of Medical Physics in Leicester Royal Infirmary was employed in the present work. It consists basically of a water tank having in one lateral wall an ultrasound transparent window made with a polyethylene film. Inside the tank there is an submersible hydrophone** held in place by a frame operated by 3 stepper motors capable of positioning it precisely in a XYZ system of coordinates. In the present work all measurements made in the BPT employed an hydrophone with 0.5 mm diameter.

8.3.2.1 Acoustic field measurements

An ultrasonic transducer attached to the window generates an acoustic field in water, which is then sampled by the hydrophone. The block diagram in Fig 8.6 shows the present electrical layout of the BPT.

---

* The Beam Plotting Tank (BPT) developed in the department of Medical Physics by N. Dahoun and S. Colligans in 1987 and upgraded in 1998 by J. Gittins.

** The hydrophone set used in the BPT was made by Precision Acoustics Ltd, it consists of: a Buffer, a Submersible Pre Amp. and four interchangeable tips with active areas made of PVDF (diameters: 1.00 mm, 0.50 mm, 0.25 mm and 0.075 mm).

The Data Acquisition and Control Board (DACB) is inserted in a personal computer. It has 8 A/D Input channels and 8 Digital Output channels. The computer drives three stepper motors positioning the hydrophones via the DACB by sending control pulses to the Beam Plotter Driver (the stepper motor drive electronics of the BPT). The signal produced by the ultrasound pressure wave detected at the tip of the hydrophone is amplified, filtered and can be visualized with an oscilloscope. The 3.25 MHz ultrasound wave is too fast for the A/D conversion rate of the DACB and so the alternative is to plot the acoustic field based on the peak values of the ultrasonic wave. A peak detector is inserted between the Amplifier/Filter and the A/D input of the DACB and converts the peak value of the ultrasound wave to a proportional DC level which is easily digitized. The DACB board is versatile enough be employed as a general tool for data recording and is also employed for recording the function $V(Z(f))$, described previously.

For beam plotting a C++ program operates the DCAB both for positioning of the hydrophones and also for data acquisition at the A/D converter. The data acquisition is programmable, the resolution along the axes X, Y and Z can be defined, and it is also possible to choose which plane to sample, (i.e. XY, XZ, or YZ) or optionally to sample an entire XYZ volume. A Matlab program capable of storing and displaying the results directly in real time reads the digitized data.

A plot of the acoustic field generated by a pitch 0.66 mm transducer (version two) is presented in Fig 8.7. It was noticed that in versions two and three of the transducer, (0.66 pitch), the output was not much affected by the steering angle as can be observed from the comparison between Fig 8.7 and the theoretical model presented in Fig 4.16.

Unfortunately these versions presented low outputs and imperfections as can also be observed in the Fig. 8.7.

Figure 8.8 presents nine plots of the acoustic field of the fourth version of the transducer. Comparing this figure with the one obtained from the theoretical model and presented in Fig 4.15, the stronger dependence of the amplitude of the experimental acoustic fields on the steering position, is clearly noticeable. According to the literature (Kino and DeSilets 1979, von Ramm and Smith 1983, Wojcik et al 1996) this can be explained by cross-talk between elements.

The comparison between the theoretical and experimental acoustic fields is more accurately visualized in Fig 8.9 where amplitude and location (θ) of the maximum intensity profiles of the experimental and theoretical acoustic fields are displayed

Compared to the theoretical predictions, the experimental acoustic fields present two important differences: a) The amplitude falls more rapidly with the steering angle. b) There is a progressive discrepancy between the locations (θ) of the theoretical and experimental acoustic fields profile peaks.

To test experimentally the hypothesis that cross-talk was responsible for these differences, the acoustic field generated by one element of the array was mapped using the same experimental setup already described. The acoustic field in an area, normal to the transducer main axis and at 30 mm from the transducer face was mapped with 0.5 mm resolution along the horizontal (in plane, θ) direction and 1 mm in the vertical direction (out of plane, ψ). The sampling plane was centered on the position corresponding to the maximum received signal. This acoustic field is presented normalized (Fig. 8.10).

From the general model described by the equations 4.35 and 4.36 a normalized model of an equivalent acoustic field with amplitude equal to:

$$A_{nor} = (D(\theta) \cdot P(\theta) \cdot (D(\psi) \cdot P(\psi) \qquad (8.1)$$

was constructed.

Such an acoustic field was fitted to the experimental data by adjusting the value of the element width (w) and element length (l). The adjustment was executed by iterative program in Matlab which uses the function FMINS. The program returns the parameters which maximizes the correlation between experimental and estimated acoustic fields. The parameters were: the effective element width (w= 1.39 mm) and the effective element length (l = 4.39 mm). The simulated acoustic field generated by an element with such dimensions is presented in Fig. 8.11.

The effective element width of almost five times the real width (0.30 mm) suggests the existence of significant cross-talk between elements in the 'in plane' direction. Regarding the 'out of plane' direction the closer agreement between the real (0.55 mm) and effective length suggests negligible cross talk. Such a behavior is predictable taking into account the shape and relative position of the array elements.

Inserting the effective value of w in the equations 4.35 and 4.36 and recalculating the functions $I(\alpha, \theta)$ it is possible to draw the acoustic field profiles shown in the diagram **a** of Fig 8.12 which is similar to the experimental profiles drawn in Fig 12 **b**. The dotted lines around both diagrams represents $D(\theta) \cdot P(\theta)$ also calculated using the effective value of w. The difference between the two diagrams requires a further investigation but this is outside of the scope of the present thesis. It may suggest the need for: a) refining the model to take into account 2-D or 3-D modes of oscillation and/or the coupling between ceramic and matching layer (Wojcik et al 1996), b) refining the adjustment method, or c) improving the data collection methodology. Alternatively it could be explained by the fact that the transducer excitation produced by the DUPAT is also dependent on the phase (α).

The characterization of cross-talk is difficult. It could be electrical and/or mechanical, localized or diffused, symmetrical or not. However with the use of the model described it was possible to calculate the effective element length. This value can be taken as an index and a form of cross-talk characterization. Such an index can be useful in evaluating the effectiveness of materials, design and procedures to reduce cross-talk.

This is discussed in detail in chapter nine.

8.3.2.1.1 Safety

Despite the fact that the present equipment is not yet intended for 'in vivo' measurements some safety assessments were made.

The measurement of the power output (W) of the transducer for the five central steering positions (-2, -1, 0, 1, 2) was made with a radiation balance using the same settings used for tests on tracking. Because of the difficulty in reproducing the alignment between transducer and balance a sequence of four measurements were made. The maximum measurements obtained from each steering position are presented in Table 8.2. The calculation of the intensity close to the face of the transducer (I) was performed by dividing W by the transducer aperture which is equal to $0.1513\ cm^2$.

Using equation A.1, and assuming a frequency of 3.125 MHz, a distance of 30 mm, and an attenuation coefficient of 0.3 dB cm^{-1} MHz^{-1} a derating factor (φ) of 0.52 was calculated. The derated power ($W_{0.3}$) and the derated intensity ($I_{0.3}$) are presented in Table 8.2. The Thermal indices ***TIS***, ***TIC*** and ***TIB*** were also calculated using equations A.4, A.5, A.7, A.8 and presented in Table 8.2.

TABLE 8.2					
St. Positions	**-2**	**-1**	**0**	**1**	**2**
W [mW]	**25**	**31**	**36**	**29**	**19**
$W_{0.3}$ [mW]	**13**	**16.12**	**18.72**	**15.08**	**9.88**
I **[mW / cm]**	**165.29**	**204.96**	**238.02**	**191.74**	**125.62**
$I_{0.3}$ [mW / cm]	**85.95**	**106.58**	**123.77**	**99.70**	**65.32**
TIS (scan)	**0.37**	**0.46**	**0.54**	**0.43**	**0.28**
TIS (unsc)	**0.37**	**0.46**	**0.54**	**0.43**	**0.28**
TIC (sacan/unscan)	**0.74**	**0.92**	**1.07**	**0.86**	**0.56**
TIB (unsc)	**0.67**	**0.83**	**0.96**	**0.78**	**0.51**
φ = 0.52					

Table 8.2 Table summarizing results of the safety tests performed on the five central steering positions (-2, -1, 0, 1, 2) of the fourth version transducer driven by the DUPAT using the same settings used for the tests on tracking. The following abbreviations have been used: W - output power, I - average intensity close to the transducer face, $W_{0.3}$ - derated output power, $I_{0.3}$ - derated average intensity, φ - derating factor, ***TIS***, ***TIC*** and ***TIB*** are the thermal indices (scanned and unscanned) for soft tissues, cranial bone, and for soft tissues with bone at the focus respectively.

All these values are relatively low, and would probably be acceptable for use in peripheral artery monitoring in adult but not for long term monitoring of neonatal brain. For neonatal application the present device needs to be made more efficient in order to operate at lower energy levels.

8.3.2.2 Frequency response of the transducer.

Another test performed employing the Beam Plotting Tank consisted of the measurement of the relative distribution of the acoustic output pressure p as function of frequency. This complements the impedance measurements previously described, therefore the experimental set-up is partly the same. The sweep generator excites the transducer and drives the **X** sweep of the oscilloscope in the same way. The difference is that the input signal in channel 2 (Y) of the Oscilloscope is the output from the hydrophone $V(p(f))$ (Fig. 8.13).

This test was made in the acoustic tank with the hydrophone static and positioned on the axis of the transducer in the region where the fields of the transmitter and receiver overlap.

The procedure was similar to that described in the case of relative impedance measurement, and here a DACB was also employed. It consisted of sampling the values of pressure $p(f)$ at progressive frequency values in a range including the interval fs to fp.

It was observed that these frequency response measurements were sensitive to the transducer-hydrophone alignment and also to the thickness of the coupling layer represented by the gel-window attachment. Therefore care was taken to always reproduce the alignment and the transducer pressure against the window.

The simultaneous plots of the voltage output $V(p(f))$ in the frequency range of 2 MHz to 5.5 MHz for the transmitter array (**t**) and receiver array (**r**) for the fourth version transducer are presented in Fig. 8.14.

8.3.3 Doppler tests

To test the DUPAT and transducer as a stereable Doppler instrument an experimental set-up was assembled. It consisted of: a) DUPAT and transducer, b) another computer fitted with a DSP board (described in section 7.2.1), c) a flow phantom described below. With this set-up it was possible to obtain, record and process the Doppler shift signals corresponding to different alignments between the Doppler transducer and blood vessel. The tests employing the IWM signal to detect noise have already been presented in Chap. 7 and therefore they are not presented here.

8.3.3.1 Flow phantom

As already mentioned in section 3.1 the working model used in this thesis was the case of arterial blood flow in femoro-distal grafts. It represents the situation of a blood vessel of around 4 mm diameter running straight, between 20 mm and 30 mm below the skin surface. When the transducer is applied to the patient it points towards the in-flow so as to achieve an insonation angle of between 30° and 60°.

The flow phantom designed to reproduce this condition was basically a closed hydraulic circuit where the blood mimicking fluid (BMF) (Ramnarine et all 1998) is pushed through a segment representing a vessel.

In order to have either a peristaltic flow or a constant flow, this phantom can be assembled in two different ways. In the first case the BMF is pushed through the vessel by a peristaltic pump (Fig 8.15 **a**). It is possible to exert some control on the wave-shape of the peristaltic flow by adjusting the size of an air bubble introduced into the pipe between the pump and vessel model. By this method it is possible to obtain an approximation of a ‘physiological’ wave shape.

In the second case, the BMF is allowed to flow between two reservoirs placed at different heights and connected to each extremity of the vessel model (Fig 8.15 **b**). The flow rate is function of the difference in height (***h***) in BMF level of the two reservoirs and therefore the pump rate had to be adjusted to maintain this difference as constant as possible.

8.3.3.1.1 Blood mimicking fluid

The blood mimicking fluid (BMF) employed was the prepared according to the IEC 1685 Draft following the procedure described by Ramnarine et al 1998. The preparation procedure is described in the Table 8.3 which is a copy of the excel spreadsheet which lists all the preparation procedures, and calculates the weighs of the ingredients necessary to produce a desired mass of BMF.

TABLE 8.3 - Blood mimicking fluid worksheet					
Enter in CELL " H1 " the desired mass of BMF [grams] =================>				1000	
Order	**Procedure**		**% mass**	**mass [g]**	**Cumulative mass [g]**
1	Weigh the container ============>	Container*	************	518.2	518.2
2	Add to the weight ==============>	orgasol (4)	1.82	18.2	536.4
3	Add to the weight and mix ========>	surfactant (5)	0.9	9	545.4
4	Add to the weight and mix well ====>	glycerol (2)	10.06	100.6	646.0
5	Add to the weight and mix well ===>	water (1)	83.86	838.6	1484.6
6	Add to the weight and mix well ====>	dextran (3)	3.36	33.6	1518.2
7	Sieve with the 38 micron sieve > 5 X	BMF	100	1000	1518.2
8	Vacuum for about 1 hour				
9	Sieve at least once more	* Value for the 2000 ml Fisherbrand container			

Ingredients		
1	Pure Water	
2	Pure Glycerol	
3	Dextran	Sigma D4876 average molecular weight 187000D
4	Orgasol	ELF Atochem, France; particle diameter 5 micron
5	Surfactant	ICI synperonic N

Table 8. 3 Worksheet describing the procedure and calculating the weights of components to produce a specified mass of blood mimicking fluid (BMF) according to the IEC 1685 Draft following the procedure described by Ramnarine et al 1998. The production 1000 g of BMF is shown as an example

8.3.3.1.2 The vessel box

The segment representing the blood vessel is a silicone tube of 3.5 mm internal diameter and a wall thickness of 0.5 mm. It is contained in a rectangular box of Perspex, and is aligned with the long axis of the box. The box is open at the top and filled with water which besides representing the tissue surrounding the artery also provides a flexible coupling between transducer and vessel. A more detailed diagram of the box is shown in Fig 8.16 where it can be seen that a platform is assembled on one of the borders of the box and tilted -45° towards the inside. On top of this platform the transducer is held by a case with its face submersed at a distance of 30 mm from the vessel axis.

8.3.3.2 Static Doppler steering test - (SDS)

Attaching the case to a micro-manipulator it was possible to scan it sideways. A sequence of alignment conditions was then generated as the transducer moved 'in plane' in steps scanning its axis across the vessel at an angle of 45°, (Fig 8.17 **a**). For each step $\boldsymbol{d_i}$, with the feedback loop inactive and using the thumb wheel selector switch (described in Section 6.2), the beam could be manually steered 'in plane' to any of the possible steering directions $\boldsymbol{st_1}$ to $\boldsymbol{st_n}$ (Fig 8.17 **b**). For each combination of step and angle, the corresponding quadrature signal could be listened to through an audio system, observed on an oscilloscope screen, and also processed to be presented and recorded as sonograms, total power (***TP***) signals, or intensity weighted mean (***IWM***) signals.

This open loop test, the "Static Doppler steering test" (SDS) was designed to study the range of each individual steering position ($\boldsymbol{st_i}$). It consisted of recording the function ***TP(d, st)*** which is an array of ***TP*** values with as many lines as ***st*** positions and as many columns as ***d*** positions. Each line of this array represents the directivity and sensitivity of each particular steering position $\boldsymbol{st_i}$.

8.3.3.2.1 SDS test procedure

In the SDS test, the steering positions (***st***) were the same as the presented in the Table 5.1; they are here designated as: **-4,-3, -2, -1, 0, +1, +2, +3,** and **+4**, while ***d*** represents the position of the transducer and ranges from 0 to 21 mm in steps of 0.5 mm. Before starting the data collection the transducer was moved manually to the initial position d_1 (0 mm) and then a HP-VEE program specially written for this test was started. It would first steer the beam to the position -4, and then sample 250 ***TP*** points at that position storing them in a file named '-4'. Next, the program would steer the transducer to the position -3 repeat the same procedure storing the ***TP*** values in a file named '-3'. This was repeated for all the steering positions and after storing the data in the file named '+4' the program would stop. Then the transducer was manually moved to the position d_2 and the program was started again. The data recorded in this and in all subsequent program runs were appended to the data string already recorded. At the end of the collection (d_{43},-21 mm) the string of data in each one of the nine files consisted of a sequence of segments of 250 points, where each segment represented a point in a line of the array ***TP(d, st)***. These strings were processed for elimination of spikes and reduction in the number of points. After this processing each line had 43 points representing the values of ***TP*** in the range of 0 to 21 mm in steps of 0.5 mm. ***TP(d, st)*** is presented in waterfall diagram in Fig. 8.18.

8.3.3.2.2 Selection of the operational steering positions

From Fig. 8.18 it is clear that the sensitivity of the instrument at the positions **-4**, **-3** and +3, and **+4** is too low to be used, therefore these four positions were discarded. Displaying the five remaining curves in a 2D plot (Fig. 8 19) it can be observed that the ***TP*(d, 0)** signal corresponding to the position **0** is always smaller than the ***TP*(*d*, -1)** and ***TP*(*d*, +1)** signals corresponding to the neighboring positions **-1** and **+1**. Because of this the position **0** could also be discarded. The sensitivities of the external positions, (**-2** and **+2**) are one order of magnitude lower than the sensitivity of the internal positions (**-1** and **+1**) as can be observed in their corresponding ***TP*(*d*)** curves. Nevertheless, as the external steering positions have enough sensitivity to provide a good quality Doppler signal they can be used. From the above considerations it is possible to state that at the present stage of development the instrument can operate employing four steering positions: **-2, -1, +1,** and **+2.**

8.3.3.2.3 Total range and threshold

The range of one individual steering position is defined as the scanning region where the amplitude of ***TP*(*d*, *st*$_i$)** detected by the transducer set at ***st*$_i$** is larger than the amplitude chosen as the threshold. By extension, the total range of the Doppler tracking instrument having ***n*** steering positions is the combination of the individual ranges with overlap. It can be visualized as the width of the envelope constructed by the superposition of the traces of ***TP(d, st)*** corresponding to the workable steering positions. The four traces corresponding to the selected steering position are presented in Fig. 8.20**a**, however because of the large dynamic range involved they can be better observed on a dB scale (Fig. 8.20**b**). A threshold of -15 dB is also represented in order to define the individual and total ranges.

The bar graphs of Fig. 8.21 illustrate the effect variation of the threshold level in the width of the ranges. Each diagram corresponds to a threshold level. In each graph the first four bars refer to the individual ranges (-2, -1, +1, +2) always in that order. The fifth bar represents the total range which (assuming that the ranges overlap) corresponds to the distance between, the first limit of the first range and the last limit of the last range. For progressively higher thresholds a decrease in the length of the ranges is observed. The decrease is not always proportional because of the differences in the shape of the TP(d) curves for each steering position. The lowest possible threshold level must be above the noise level for any steering position and ensure a minimal signal quality. The lower the threshold the wider the range.

The calculation of the ranges were made by measuring the positions of the intersection of each line with the threshold. The Table 8.4 presents the intersections and ranges calculated from the same data represented in Fig 8.20 **b** adopting a threshold of -15 dB

Table 8.4 Passive ranges corresponding to a threshold level of									-15	**dB**
Steering Position	-2		-1		+1		+2		Transducer	
Intersection with threshold [mm]	4.35	8.33	5.37	13.6	8.23	16.8	14.1	17.9	4.35	17.9
Range [mm]	3.98		8.25		8.57		3.77		13.54	

Table 8.4 SDS test. Summary of measurements of individual ranges ('-2, -1, +1, +2') and total range ('Transducer'). Example based in data presented in Fig. 8.20 **b** and threshold of -15 dB.

8.3.3.3 Dynamic Doppler steering test - (DDS)

8.3.3.3.1 Introduction

To test the tracking performance of the instrument with the feedback loop active another test, the "Dynamic Doppler steering test" (DDS) was designed. In this closed loop test the automatic steering was observed while manually scanning the transducer with the micro manipulator. The performance of the system as a Doppler tracking instrument results from the combined performance of the individual steering positions. From the SDS tests described in Section 8.3.3.2 it can be assumed that at the present stage of development of the DUPAT and transducer, the instrument can operate with up to four steering positions (**-2, -1, +1, +2**). The present tracking routine, developed for that configuration, was presented in the Section 7.3.3.3 of this thesis.

8.3.3.3.2 Dynamic Doppler steering test procedures

The procedure was to scan the transducer across the vessel with the micro manipulator starting at one side and finishing on the other side. The transducer was moved in steps, always in the same direction. At the start and the end positions the vessel would be totally out of range.

During the initial part of the scanning while the vessel was still out of range, the amplitude of the ***TP*** signal was below the threshold causing the transducer to steer the beam in all possible directions. As soon as the scanning movement brought the vessel in range, the ***TP*** signal corresponding to the nearest steering position increased and became higher than the threshold. This disabled the tracking routine and fixed the steering angle. The transducer position (d_1) when the steering angle becomes fixed for the first time marks the beginning of the total range. As the transducer was moved forward, the ***TP*** signal increased first and then started to decrease in response to the location of the vessel inside the range of the current steering position. The ranges of the consecutive steering positions overlap above the threshold and therefore when the ***TP*** signal hits again the threshold level the vessel is already inside the range of the next steering position. As soon as the ***TP*** signal equals the threshold level triggering the tracking routine the beam is steered and finds the position corresponding to the range containing the vessel. The ***TP*** signal then rises above the threshold disabling the tracking routine and fixing the steering angle again. As the transducer is moved forward the same process is repeated again and again until the last steering position is reached. The transducer location where the vessel becomes out of range marks the second limit (d_n) of the total range. This occurs when in the last possible steering position, the TP signal equals the threshold and triggers the tracking routine which is no longer able to find the vessel.

8.3.3.3.3 Prediction of the DDS Ranges.

In the diagrams of Figure 8.22 the behavior of TP in the DDS test is predicted based on the data collected in the SDS test.

The bar graph diagrams presented in Fig. 8.23, are also based in the SDS test. Assuming a particular threshold level they show the prediction of what will be the share between the individual ranges when the feedback loop is active and the transducer is moving in a given direction. In bar graph **a,** the individual and total ranges obtained with the SDS test is presented. In diagrams **b** and **c** the first four bars represent the distribution of the share of the total range between the four steering positions when the tracking routine is in operation and the transducer scans from left to right **b**, or right to left **c**. The fifth bar represents the total range, and is always the sum of the four preceding bars. As the threshold increases there is a redistribution of the shares as a function of shape and relative position of the curves ***TP(d)***.

8.3.3.3.4 Recording of the tracking action

The final goal of the present project is to produce an instrument capable of tracking the vessel, the procedure designed to record this function is presented as follows. With the transducer in the initial position (0.0 mm) and the flow phantom operating in pulsatile mode, the tracking program was switched on. From that instant on all the values of the raw ***TP*** (***TPr***) signal, the conditioned ***TP*** signal in dB (***TPcdB***) and the steering position (***stp***) corresponding to each point in ***TPcdB*** were simultaneously sampled, and recorded in three different files. During five cycles of the pulsatile flow the position of the transducer was left constant and then moved manually to the position 0.5 mm where it would stay for another five cycles. This was repeated until the 21 mm position was reached when the program was switched off. The same procedure was repeated in the opposite direction (21 mm to 0 mm) with the same setting. In the end of the data collection six files ***TPr***(0-21), ***TPr***(21-0), ***TPcdB***(0-21), ***TPcdB***(21-0), ***stp***(0-21) and ***stp***(0-21) were acquired.

These data are presented in the diagrams **a**, **b** and **c** of Fig. 8.24 (direction 0 to 21) and Fig. 8.25 (direction 21 to 0). For this presentation the ***TPr*** data had to be processed and conditioned in order to reduce spikes.

The horizontal scale in all graphs is in mm and represent the same length of 21 mm although this scale is not precise. This is because the transducer movement was done manually (subjected to imprecision in the positioning), based on a subjective time measurement and with variable movement duration. Therefore the diagrams in Fig. 8.24 and Fig. 8.25 do not match perfectly despite the fact that the diagrams **a**, **b** and **c** in either figure are perfectly synchronized. The threshold level is presented in diagrams **b** in both figures. It can be observed that the position of the intermediary transitions are dependent on the direction of the movement. Particularities in these results are discussed in chapter nine.

8.4 Summary

This chapter presented experiments (materials, methods, procedures and results) considered relevant in testing the performance of the parts and of the entire Doppler tracking instrument designed and constructed during this project.

The results obtained so far are sufficient for demonstration that Doppler tracking is achievable. In addition to this the results also reveal the points which need to be further developed in order to improve the performance of the equipment. A more detailed discussion of the results is presented in chapter nine.

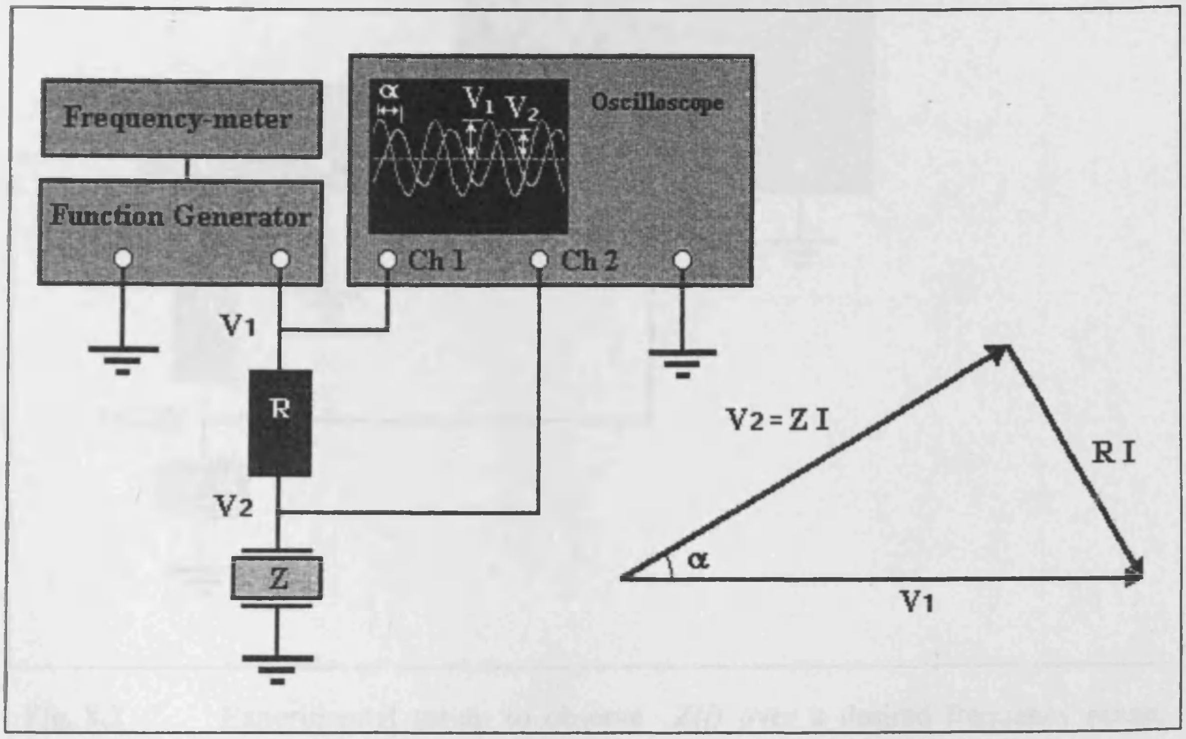

Fig. 8.1 Experimental set-up to measure the Impedance *Z(f)* and phase *α(f)* of a ceramic. A signal generator is connected to the device *Z* to be measured through a known series resistance ***R***. The voltages V_1 and V_2 at respectively the output of the signal generator and, after the series resistance are measured. It is then possible to visualise on the screen of the oscilloscope the variations in amplitude of V_1, V_2 and the phase difference α between them as a function of the frequency. Values of voltage phase and frequency could be sequentially sampled in the range of interest. From this data it is possible to calculate ***F1(f)*** and ***F2(f)*** respectively proportional to *Z(f)* and α(*f*). At the series (resonance) frequency *fs* and at the parallel (anti-resonance) frequency *fp*, α is equal to zero.

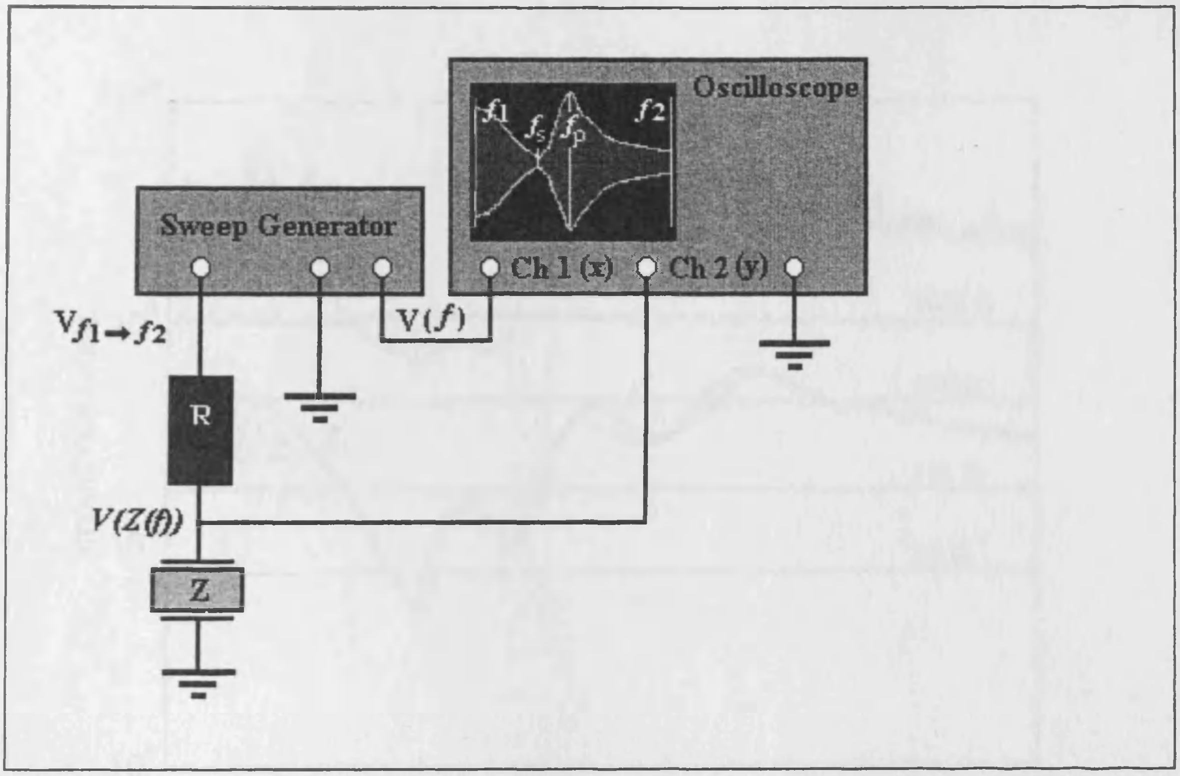

Fig. 8.2 Experimental set-up to observe *Z(f)* over a desired frequency range.

A Sweep Generator is employed to apply a voltage $V_{f1 \rightarrow f2}$, to the ***RZ*** series circuit. The sweep frequency limits (f_1 and f_2) are chosen to span the range of interest. The oscilloscope is operated in the *XY* mode, the saw tooth wave *V(f)* (available from the sweep generator) is input to channel **1** (*X*). *V*(*Z*(*f*)), taken between ***R*** and ***Z*** is the input to channel **2** (*Y*). Adjusting the sensitivity of channel **1** it is possible to display *V*(*Z*(*f*)) in the frequency domain over the range f_1 to f_2. This method, useful in monitoring the construction process through repetitive measurements, has the advantage of providing a quick and dynamic visualisation of *Z*(*f*), which is proportional to *V*(*Z*(*f*)). The disadvantage is that it does not provide a measurement of the phase of the signal.

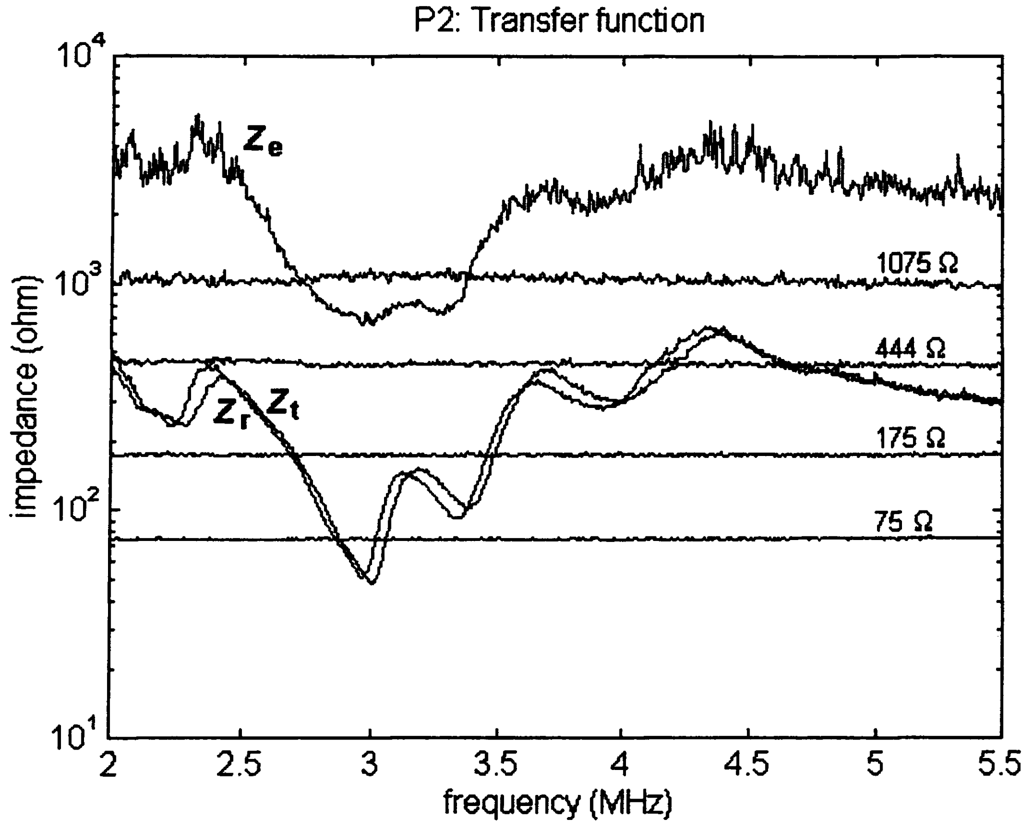

Fig. 8.3 *Z(f)* plots from a fourth version transducer using the experimental set up as described in Fig 8.2. The measurements were made over the frequency range of 2 MHz to 5.5 MHz. The vertical scale is logarithmic and calibrated in Ohms. The impedance of the transmitter array is represented by Z_t, the receiver array by Z_r and a single array element is represented by Z_e. The calibration resistances 75Ω, 175Ω, 444Ω and 1075Ω are also represented.

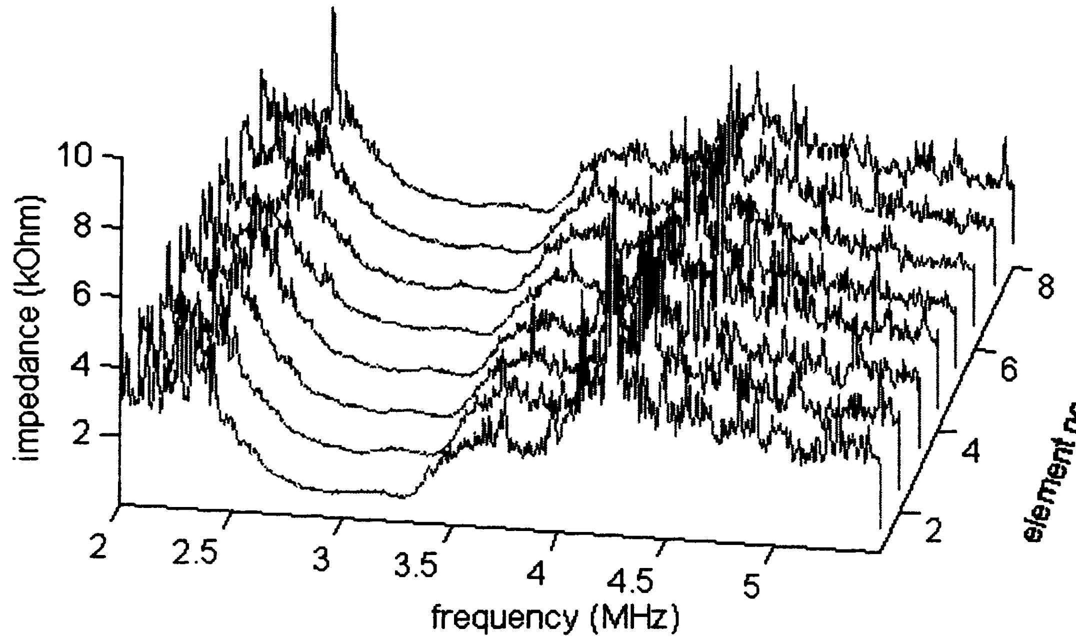

Fig. 8.4 Simultaneous $Z(f)$, plots for eight elements of one array using the experimental set-up described in Fig 8.2 The measurements were made over a frequency range of 2 MHz to 5.5 MHz. It is possible to observe that all the elements present the same behaviour. This test is useful in checking the individual array elements for faults or differences.

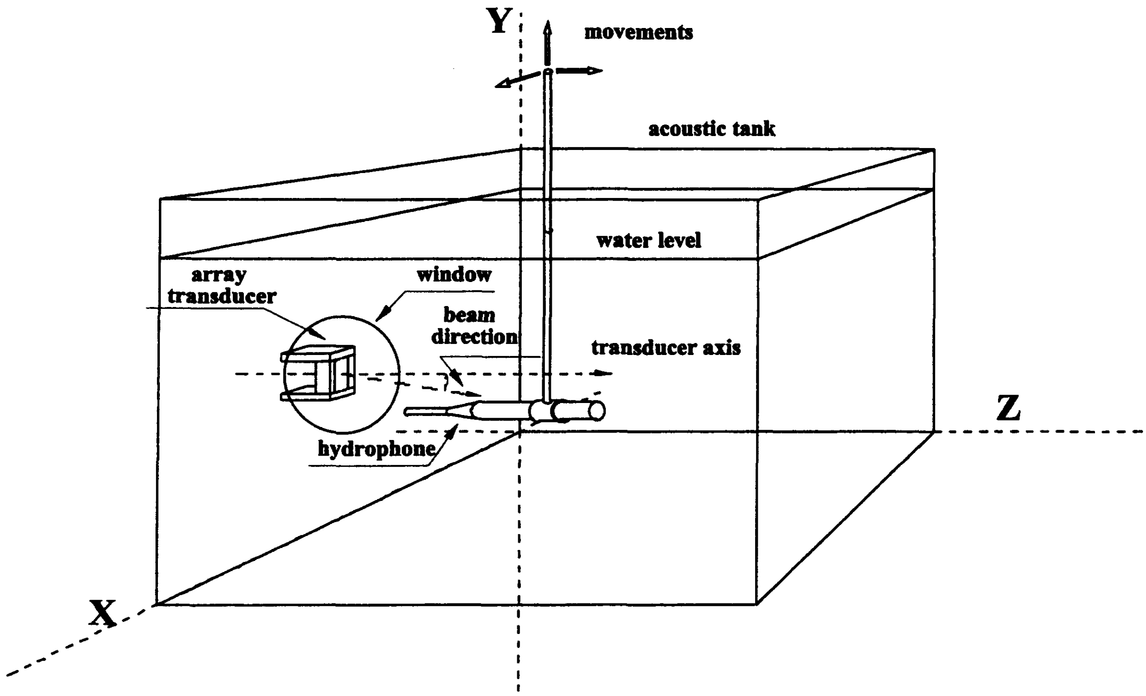

Fig. 8.5 Schematic drawing of the Beam Plotting Tank (BPT) employed in the acoustic measurements. The transducer attached to a polyethylene window from the outside generates an acoustic field in the water inside the tank. A submersible hydrophone samples the acoustic field pressure, it is held in place by a frame operated by three stepper motors capable of positioning it precisely in a *XYZ* system of co-ordinates.

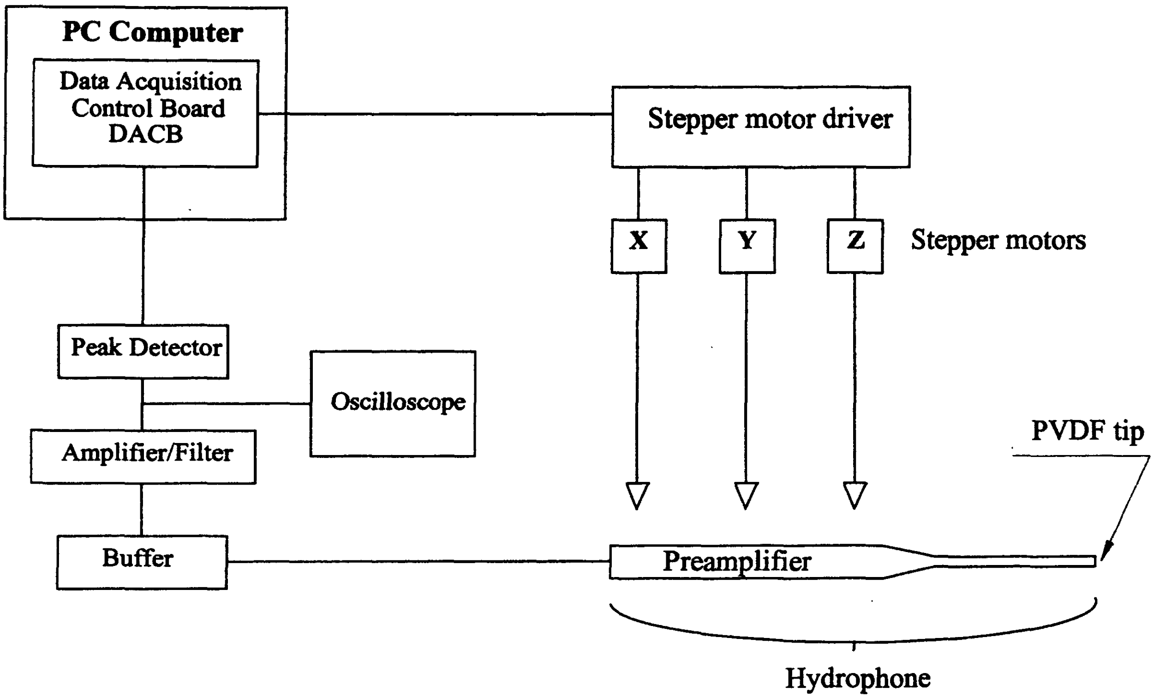

Fig. 8.6 Block diagram showing the present the electrical layout of the BPT. The Data Acquisition and Control Board (DACB) with A/D input channels is inserted in a personal computer. The computer drives three stepper motors positioning the hydrophone via the DACB by sending control pulses to the Beam Plotter Driver (the stepper motor drive electronics of the BPT). The signal produced by the ultrasound pressure wave detected at the tip of the hydrophone is amplified, filtered and can be visualised with an oscilloscope. The 3.25 MHz ultrasound wave is too fast for the A/D conversion rate of the DACB and so the alternative is to plot the acoustic field based on the peak values of the ultrasonic wave. A peak detector is inserted between the Amplifier/Filter and the A/D input of the DACB and converts the peak value of the ultrasound wave to a proportional DC level which is easily digitised.

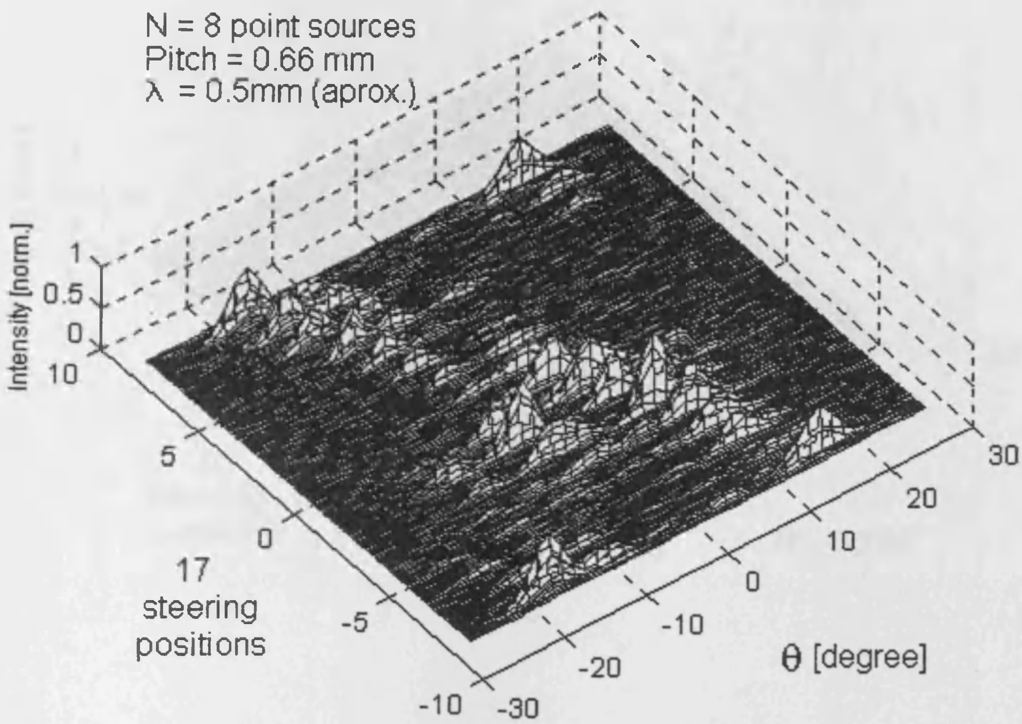

Fig. 8.7 The acoustic fields of a 0.66 pitch transducer generated in the plane *XY* (parallel to the face of the transducer) 30 mm from the transducer face. Seventeen 3D acoustic field plots are staggered together. To each plot corresponds one steering position. The resulting figure shows the relative intensities at each steering position and their relative locations relatively to the steering angle (θ). The side lobes can be observed at extreme steering positions. The non uniform distribution can be attributed to faulty array elements. This Figure can be compared with a theoretical prediction presented in Fig 4.16

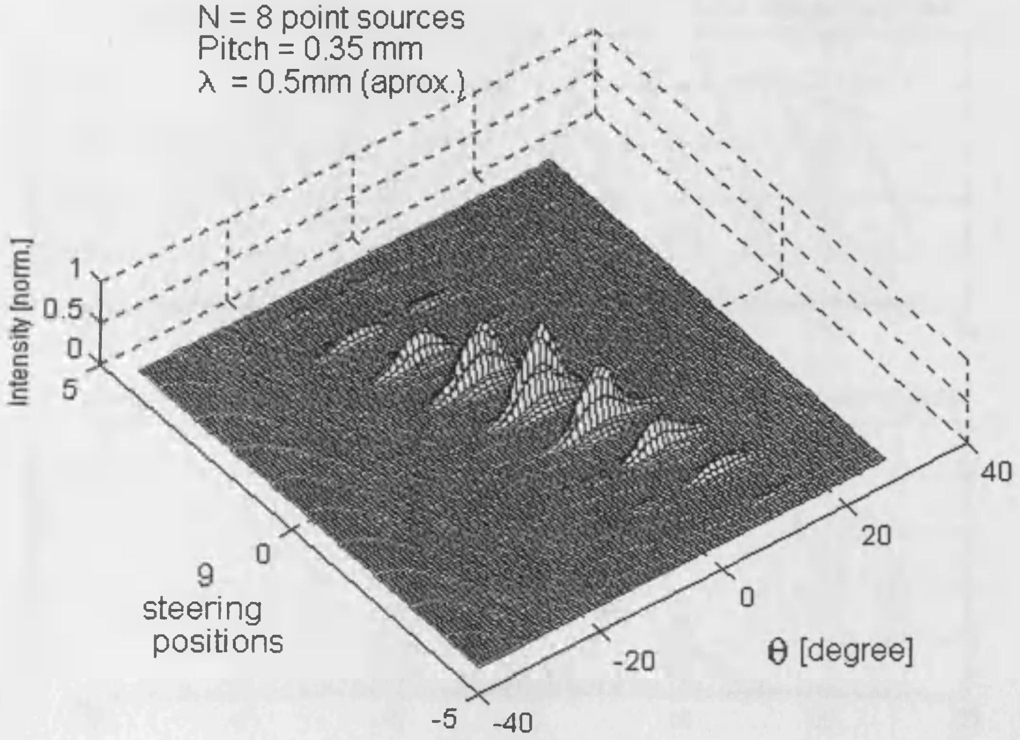

Fig. 8.8 The acoustic field of a fourth version transducer (pitch 0.35 mm) generated in the plane ***XY*** 30 mm from the transducer face. Nine 3D acoustic field plots are staggered together. Each plot corresponds to one steering position. The resulting figure shows the relative intensities at each steering position and their relative locations relatively to the steering angle (θ). Comparing the present figure with Fig. 8.7, it is possible to observe the absence of side lobes and a requirement of less steps to achieve an equivalent lateral displacement. The decrease in amplitude with steering angle suggests a likely cross-talk between elements. This Figure can be compared with a theoretical prediction presented in Fig 4.15

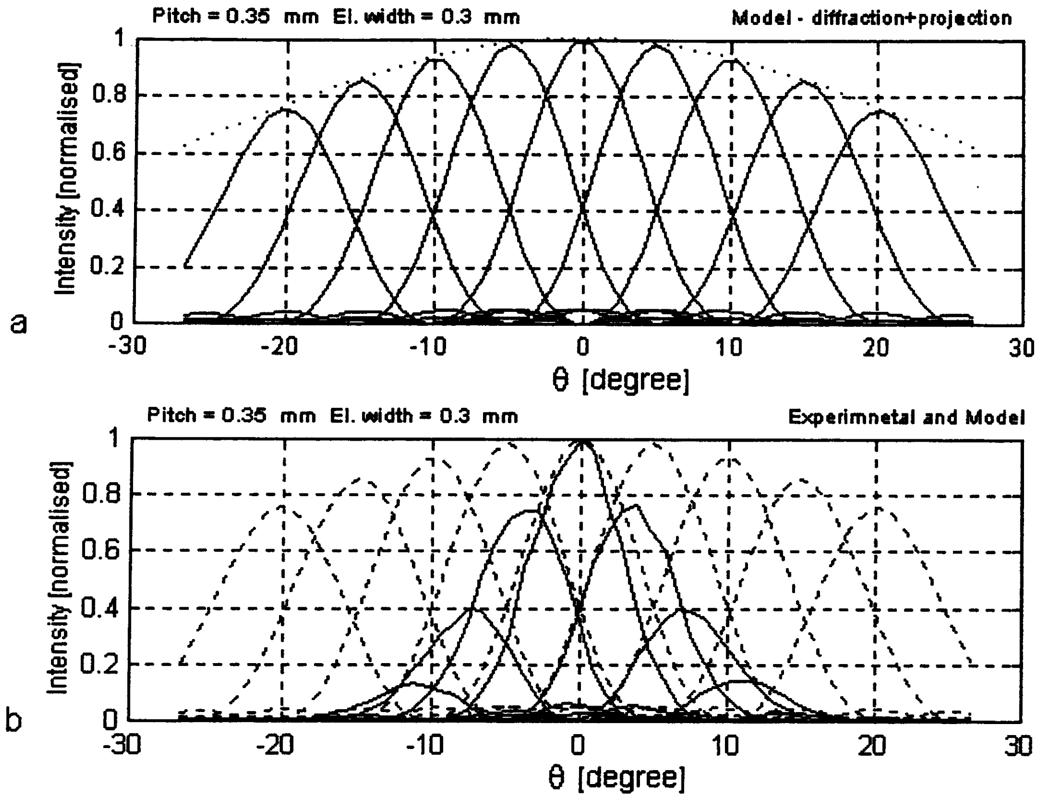

Fig 8.9 Comparison between prediction and experiment. **a)** The maximum intensity profiles and relative peak positions of nine (theoretical) acoustic fields produced by a model with the same dimensions as the fourth version transducer. In this simulation, projection and diffraction effects are assumed (represented by the dotted line). It is also assumed there is no cross-talk. **b)** The maximum intensity profiles of the acoustic fields experimentally generated by the fourth version transducer (shown in Fig. 8.8). The interrupted line represents the same theoretical profiles shown in **a.** It can be observed that the experimental acoustic fields present a significant decrease in amplitude for progressively higher values of θ. Additionally, a shift in the peak positions towards the centre can be noticed.

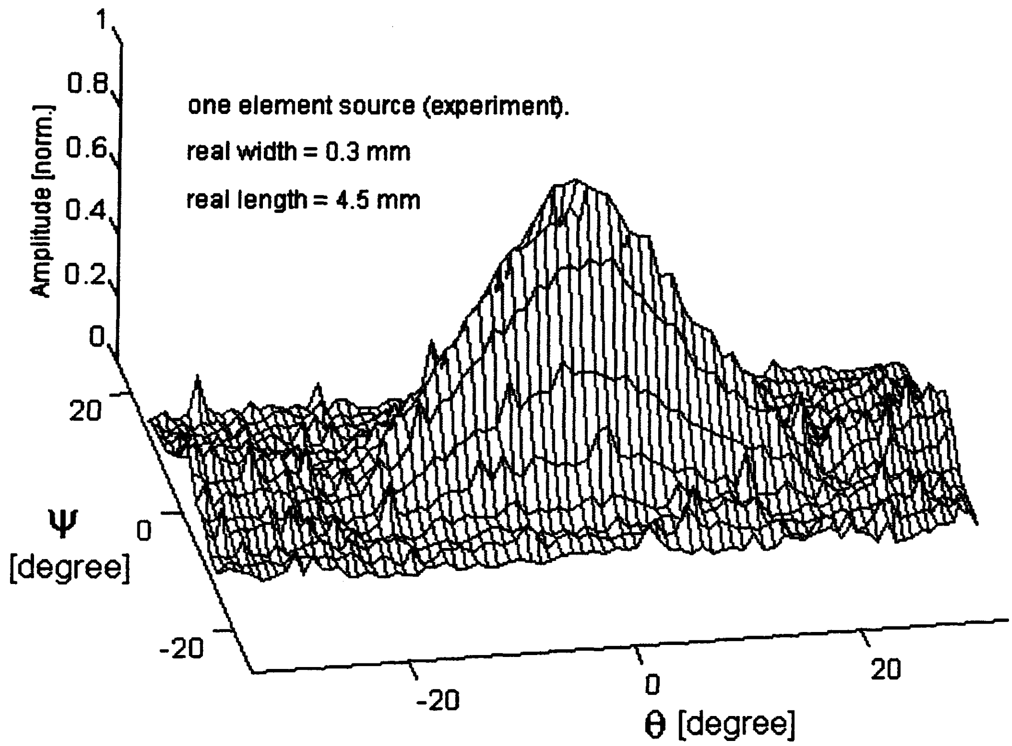

Fig. 8.10 Acoustic field generated by a single array element of the fourth version transducer. It was measured in a plane normal to the transducer axis and at 30 mm from the transducer face. The element face is rectangular and measures 4.50×0.30 mm. The axis θ is parallel to the element width (0.30 mm) and the axis ψ is parallel to the element length (4.5 mm).

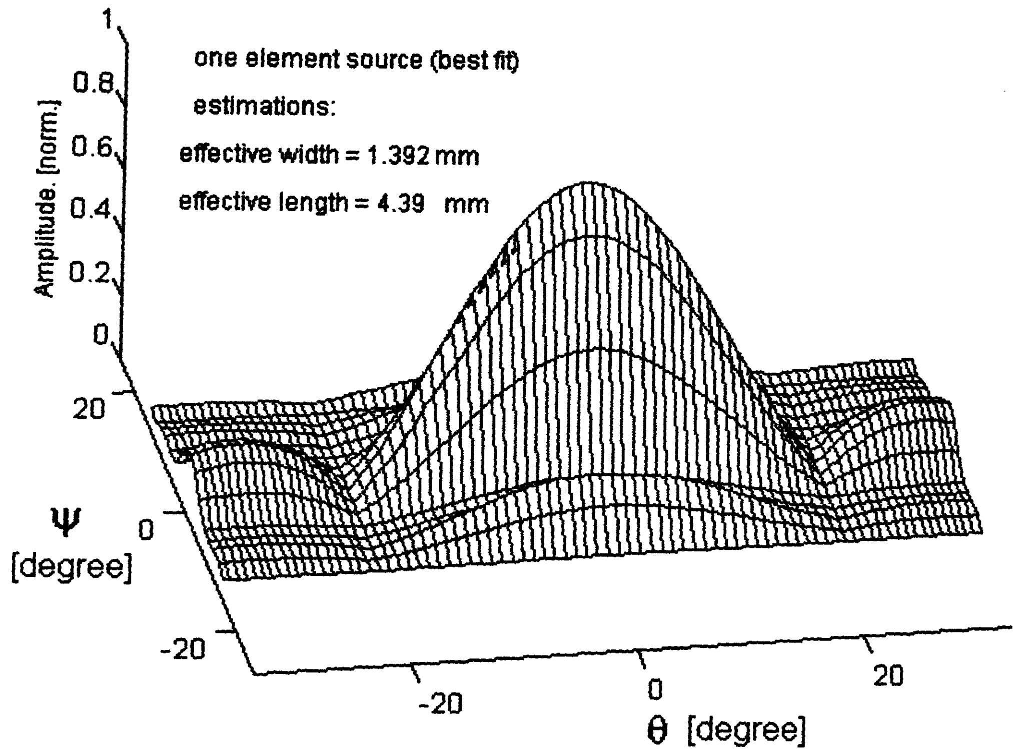

Fig. 8.11 Simulation of the acoustic field which corresponds best to the experimental acoustic field presented in Figure 8.10. The model parameters, ***w*** (1.392 mm) and ***l*** (4.392 mm) were obtained by an iterative program.

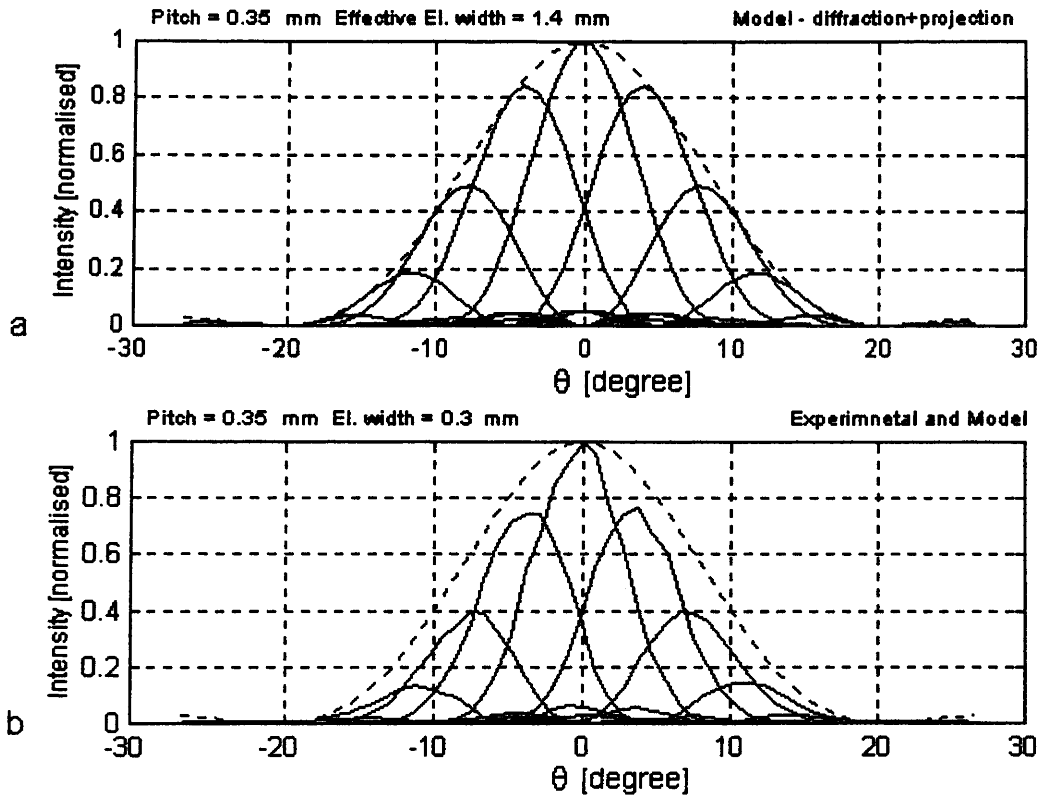

Fig 8.12 The maximum intensity profiles and relative peak positions of nine acoustic fields corresponding to nine steering angles. **a)** The estimated profiles employing the model described by equations 4.35 and 4.36 and the effective value of width (w = 1.4 mm) and pitch (d = 0.35 mm). **b)** The experimental profiles obtained with the fourth version transducer (w = 0.30 mm and d = 0.35 mm). The dotted lines around the estimated and experimental profiles represent the effects of projection and diffraction employing the effective value of w = 1.4 mm.

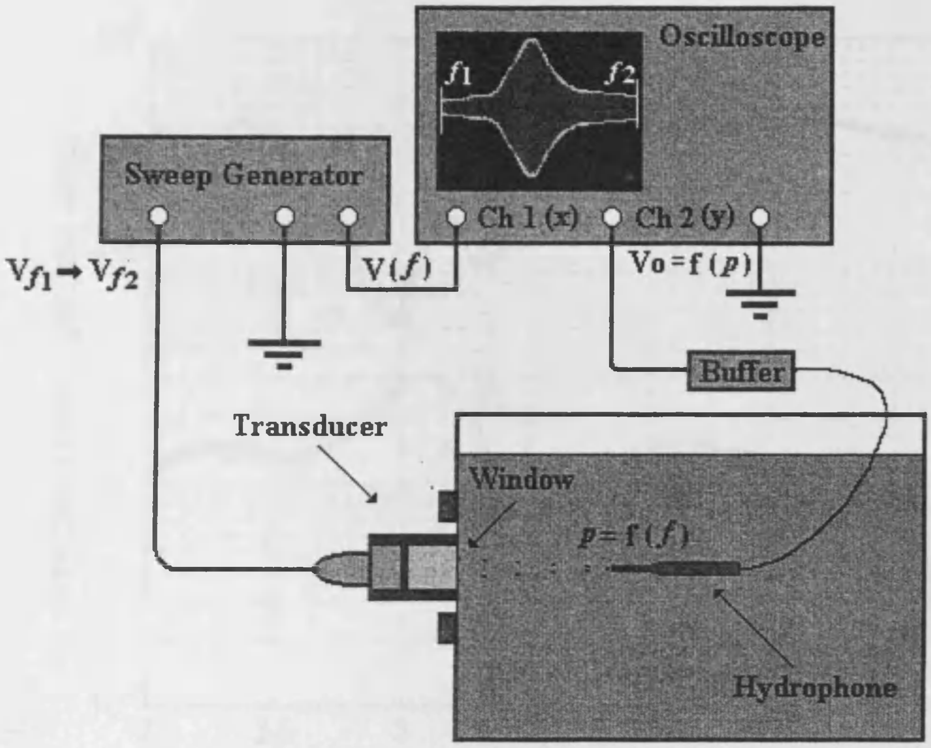

Fig 8.13 Experimental set-up to observe the frequency response of the transducer by displaying the distribution (relative values) of the acoustic output pressure ***p*** as a function of frequency. It complements the impedance measurements previously described, therefore the experimental set-up is partly the same. The sweep generator excites the transducer and drives the oscilloscope sweep (*X*) in the same way. The difference is that the signal input in channel 2 (*Y*) of the oscilloscope is *V(**p**(f))* output from the hydrophone (placed in the tank, positioned on the transducer axis 30 mm from its face). *V(**p**(f))* is a function of the transducer output which is dependent on the excitation frequency. The sweep rate is very slow compared to the generator frequency therefore what is shown on the oscilloscope screen is the excursion of *V(**p**(f))* moving with a speed given by the sweep rate. Varying the sweep rate and adjusting the sensitivity of the channel 2 (*X*), it is possible to display, on the whole extension of the screen, the frequency response of the transducer in the range of interest. If it is desired to register this signal the peak detector can provide the envelope of *V(**p**(f))* which is then easily recorded with the same system employed to map the acoustic field.

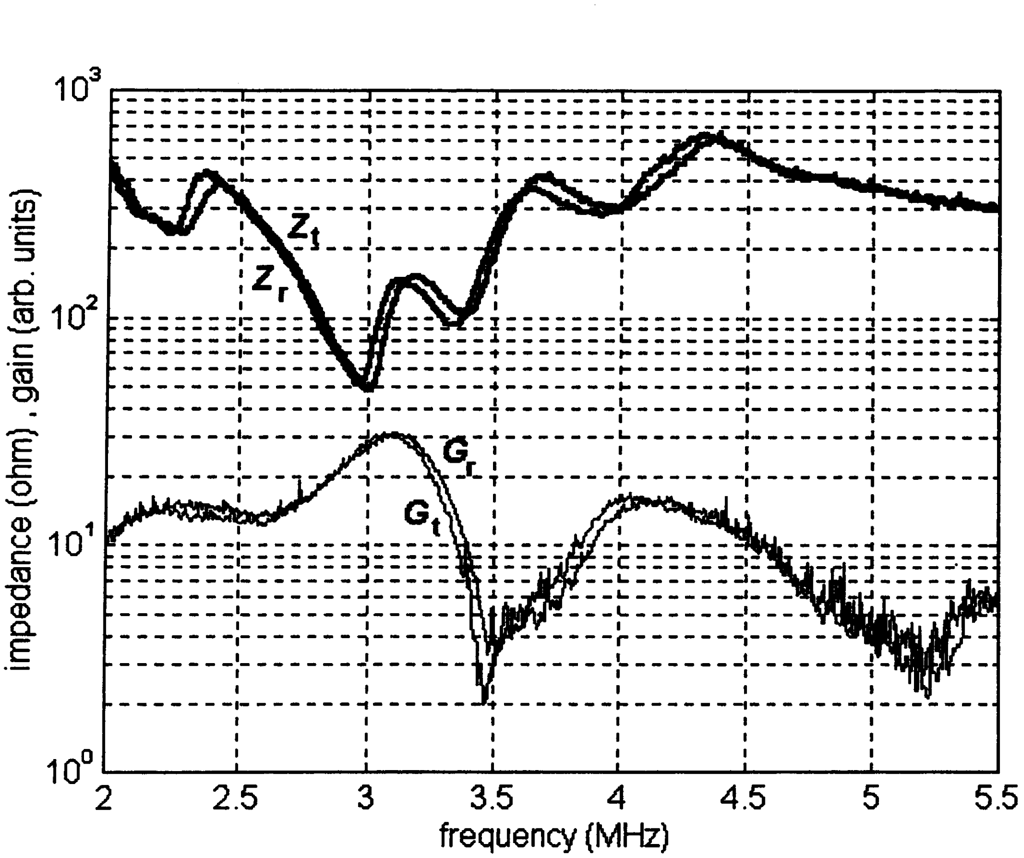

Fig 8.14 Frequency response of a fourth version transducer using the experimental set-up described in Fig 8.13. The measurements were made over the frequency range of 2 to 5.5 MHz. $V(p(f))$ of the transmitter and receiver arrays are represented respectively by G_t and G_r. Both are presented in arbitrary units on logarithmic scales, superimposed on a graph where Z_t and Z_r are also represented. It shows that: **a)** similar impedance traces corresponds to similar frequency response traces. **b)** the transmitter and receiver have a similar behaviour. Despite the fact that the prediction of the transducer frequency response based on the impedance measurements ($Z(f)$) alone is difficult, the observation of the impedance trace can help in the location of the resonance region where the maximum acoustic output occurs. A reliable method for studying the frequency response of the transducer involves necessarily the measurement of acoustic field parameters.

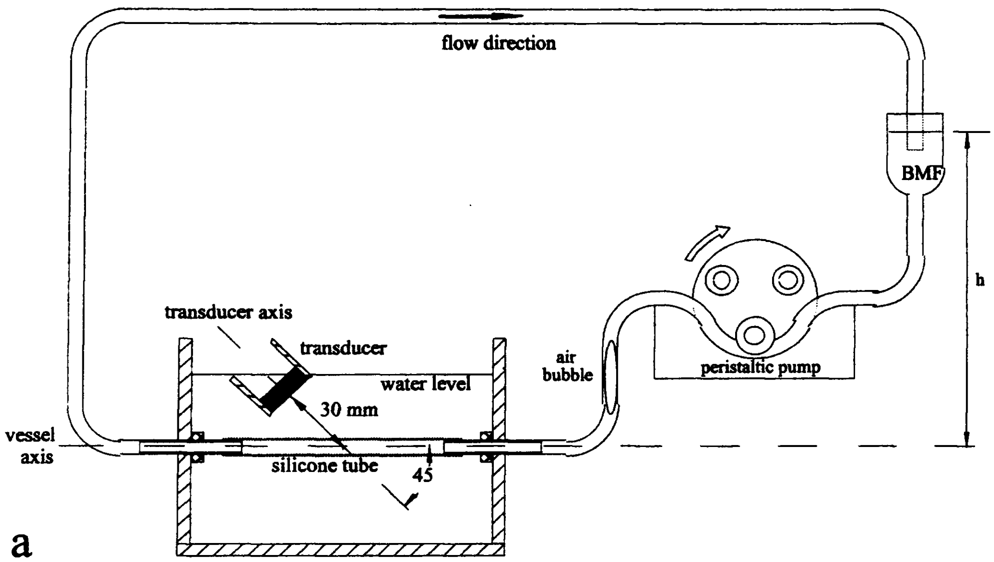

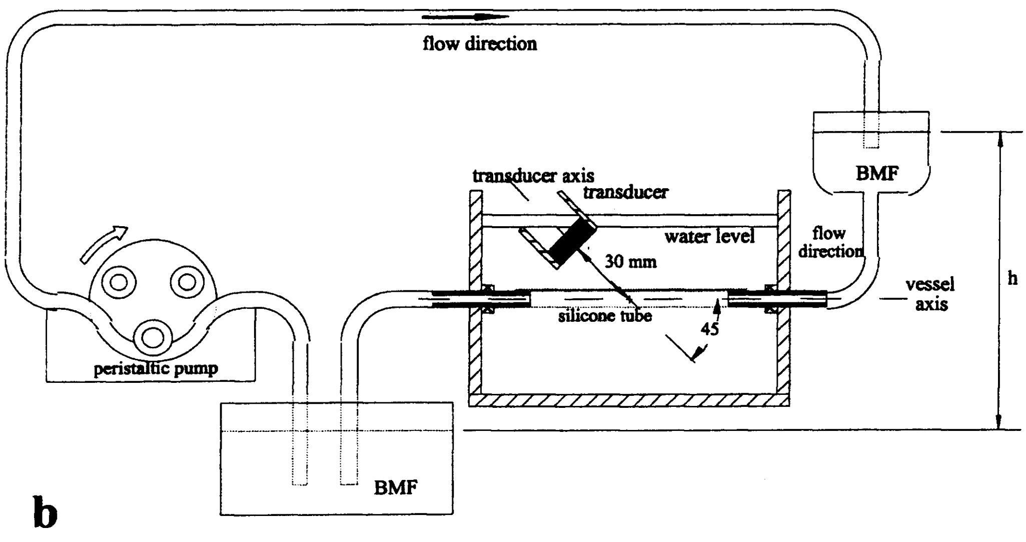

Fig 8.15 Schematic diagram of the flow phantom in two different configurations: **a)** To reproduce a pulsatile flow the blood mimicking fluid (BMF) is pushed through the vessel by a peristaltic pump. To exert some control on the wave-shape of the pulsatile flow the size of an air bubble introduced in the pipe between the pump and vessel model can be adjusted. **b)** To reproduce a constant flow the BMF is allowed to flow between two reservoirs placed at different heights and connected by the vessel model. The flow rate is a function of the difference in high (***h***) in BMF level.

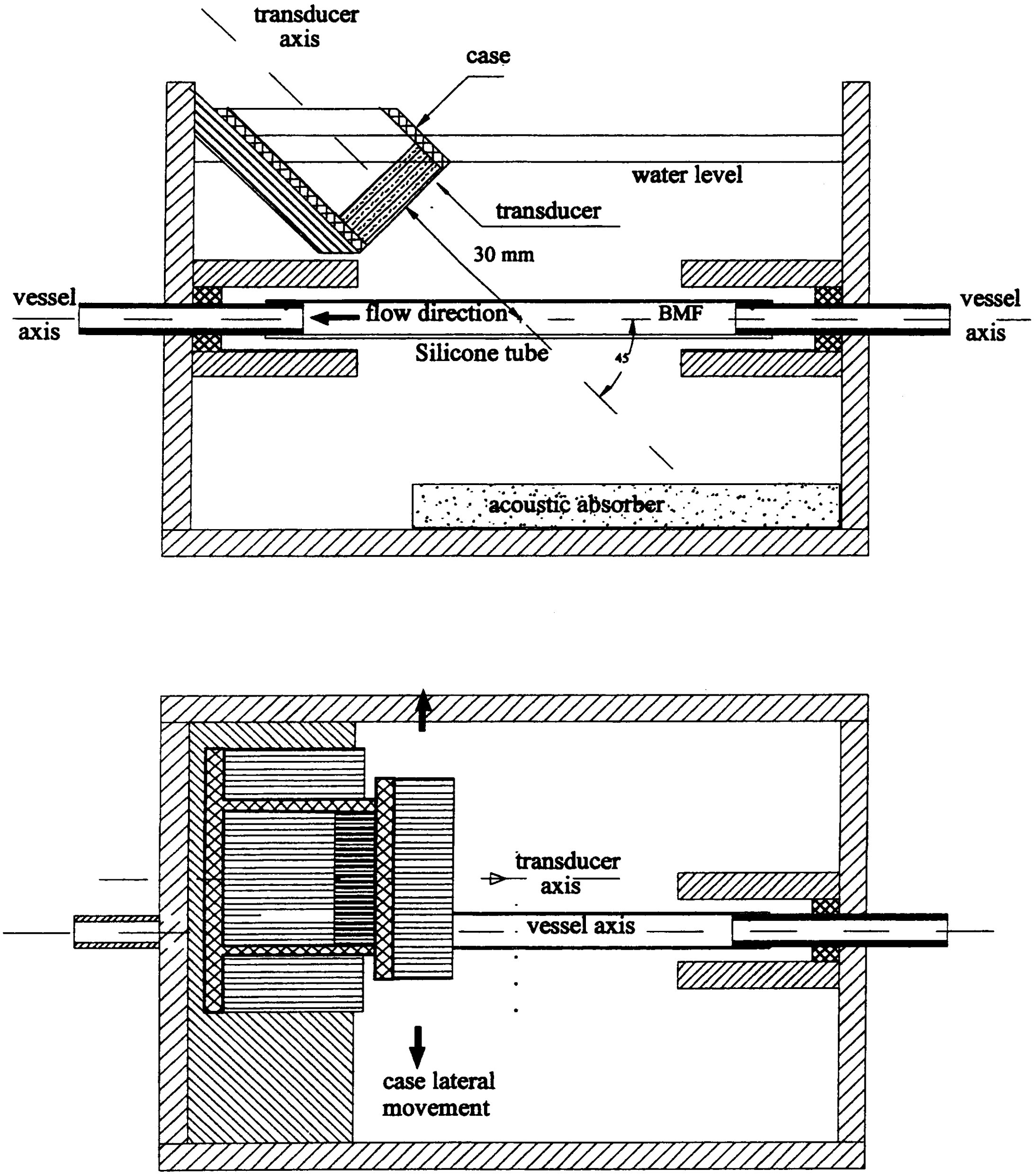

Fig 8.16 Detailed diagram of the box containing the segment representing the vessel. The box is filled with water representing the tissue surrounding the vessel and produces the coupling between transducer and vessel. It also contains a support for the transducer which maintains a constant insonation angle of 45° and allows a precise 'in plane' scanning movement. To avoid undesirable echoes an acoustic absorbing material was paced in the bottom of the box.

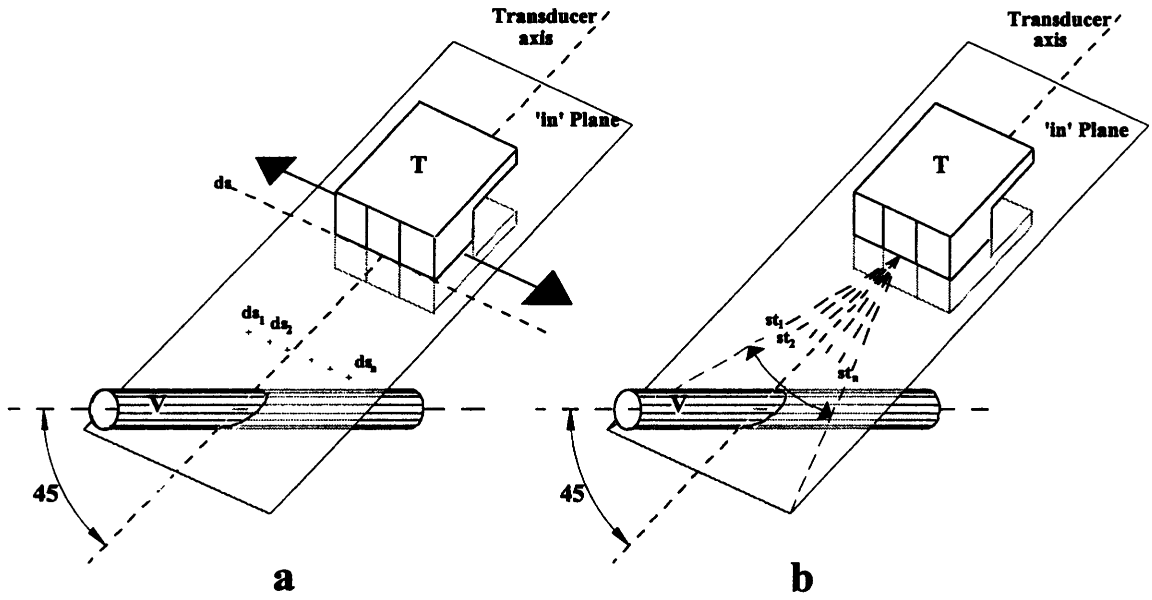

Fig 8.17 Schematic diagram representing the 'in plane' relative positions of transducer and vessel. **a)** The lateral transducer movement along the direction ***ds*** representing the different alignment situations ***ds***$_i$. **b)** The beam steering movement ***st***$_i$ aimed to correct the misalignment caused by the lateral movement.

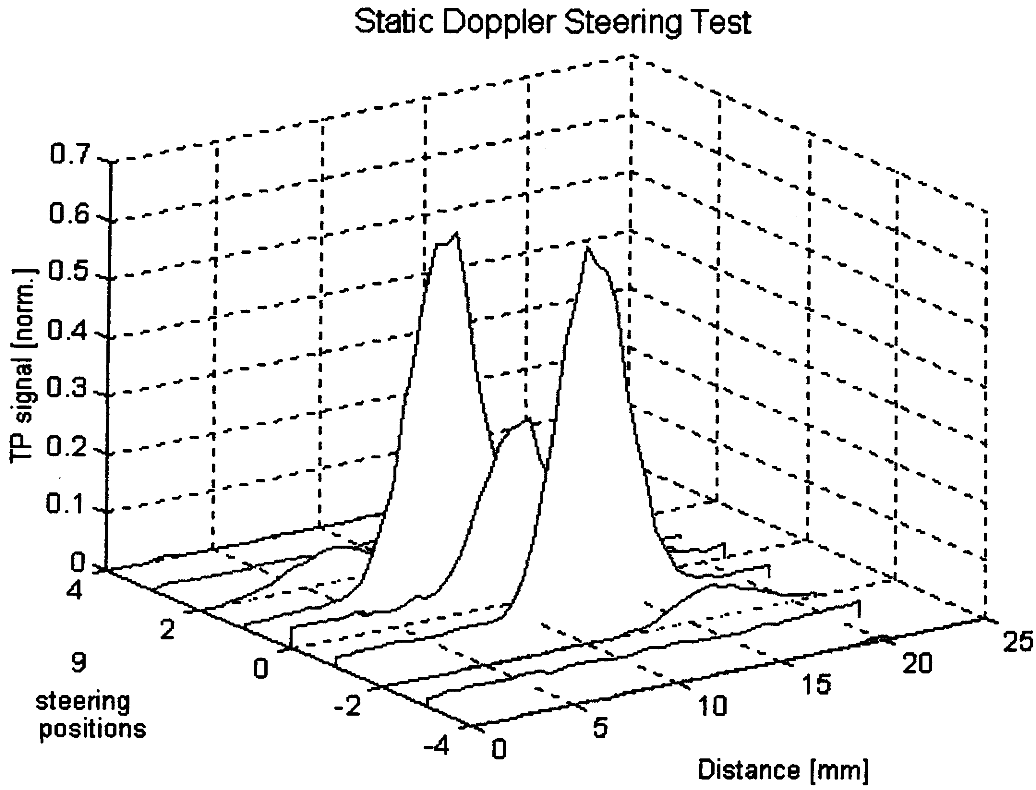

Fig. 8.18 Waterfall diagram of the array ***TP*(*ds, st*)** as measured in the SDS test. Each line represent the amplitude of the ***TP*** signal detected by the transducer as it scans the vessel moving in the 'in plane' along the distance ***ds***. It can be observed that the steering positions **-4, -3, +3** and **+4** have such a low sensitivity they can be discarded. The five remaining positions show different sensitivities which are position related.

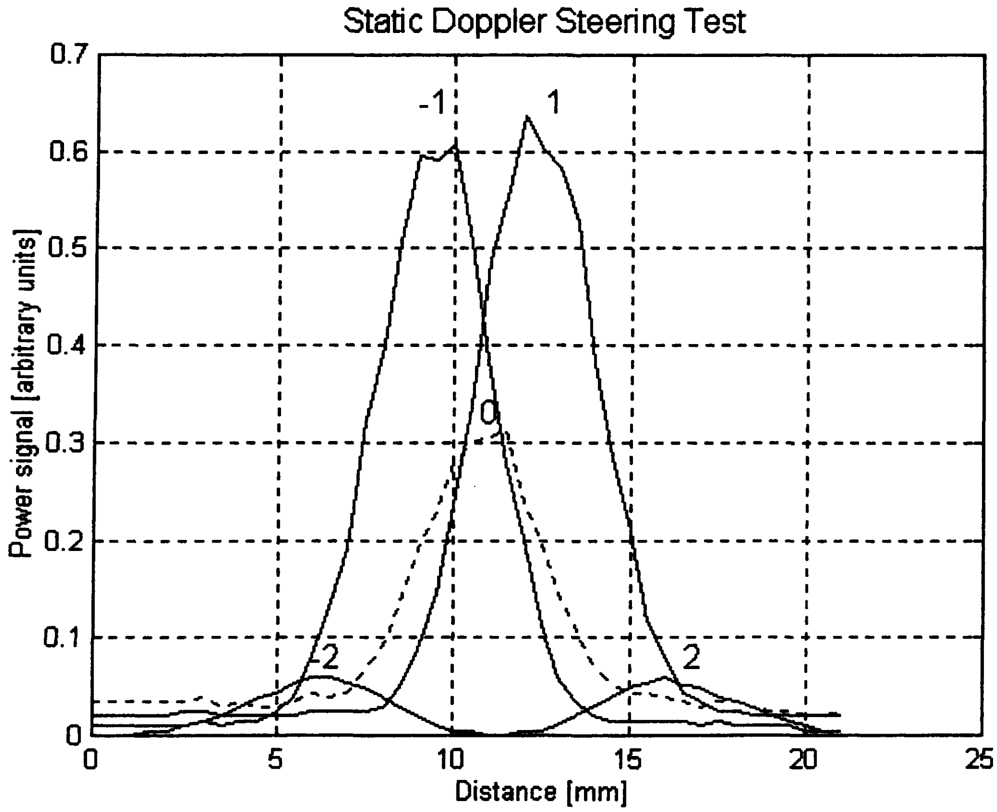

Fig 8.19 A 2D representation of the five central lines of the array ***TP*** (***ds, st***) superimposed. The horizontal axis represent the scanning displacement along the distance ***ds*** and the vertical axis represents the intensity scale. It is possible to observe that the sensitivity of the position **0** (represented in interrupted lines) is such that it can be replaced with advantage by positions **-1** and **+1**. The sensitivity of the external positions **-2** and **+2** are one order of magnitude smaller than the internal positions **-1** and **+1**. However, as the external positions cover a different range, their use extends the tracking range.

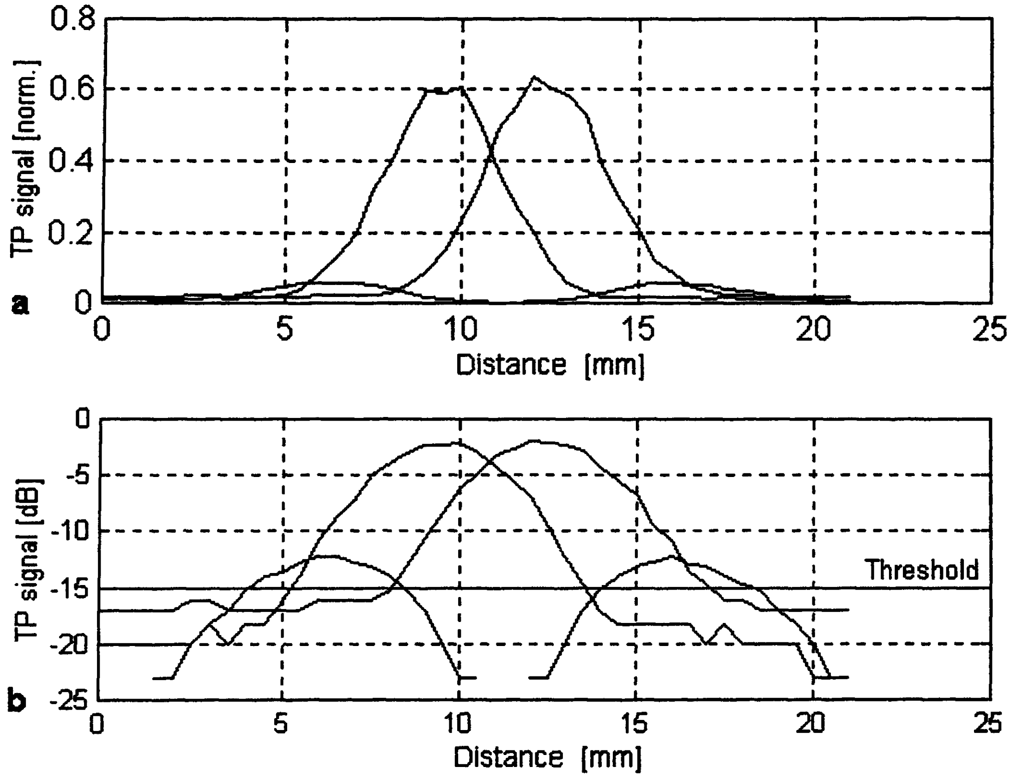

Fig 8.20 Representation of the four chosen tracing positions -2, -1, +1, and +2 and threshold. **a**) Superposition of the four central lines of the array ***TP*** (***ds, st***) already presented in Fig 8.18. **b**) The same array ***TP*** (***d, st***) represented in **a** but in dB. A threshold line is placed at -15 dB. The intersections of the curves with the threshold define the position and width of the individual ranges. The total range is the defined by the interval comprised between the first and last intersection of the first and last steering position respectively.

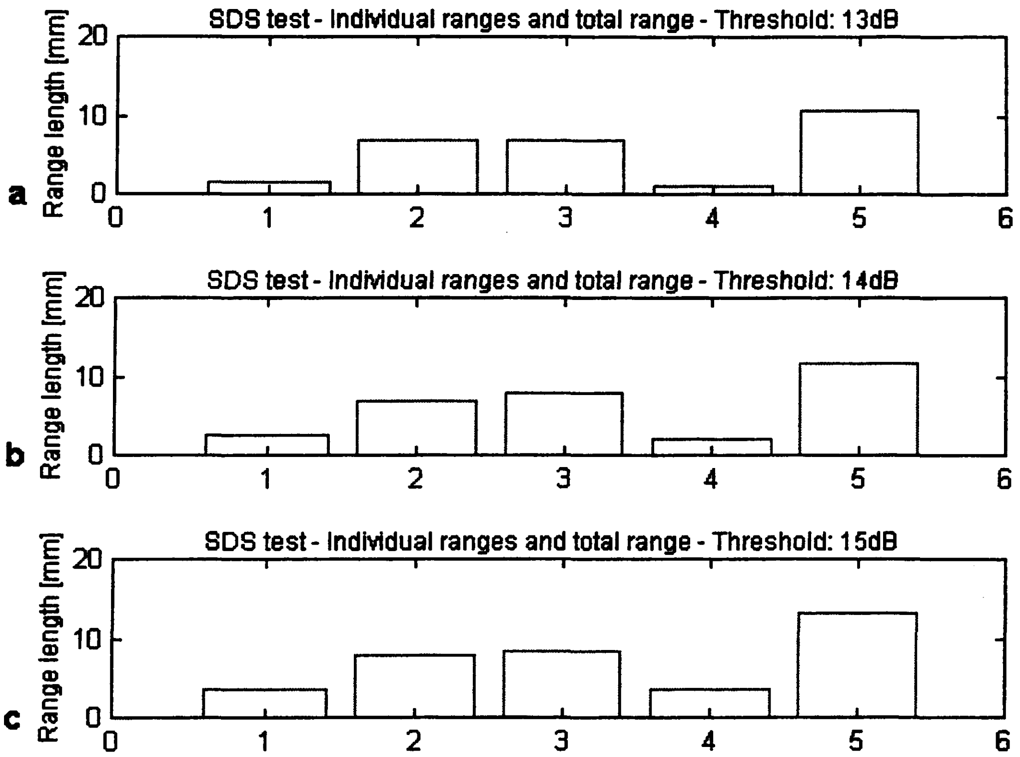

Fig. 8.21 The effect of the threshold in the ranges of individual steering positions and in the total range. Each diagram, correspond to a threshold level: (**a** -13 dB, **b** -14 dB, and **c** –15, dB). In all diagrams the first four bars refer to the individual ranges (-2, -1, +1, +2), always in that order. Progressively low thresholds lead to an increase in the length of the ranges.

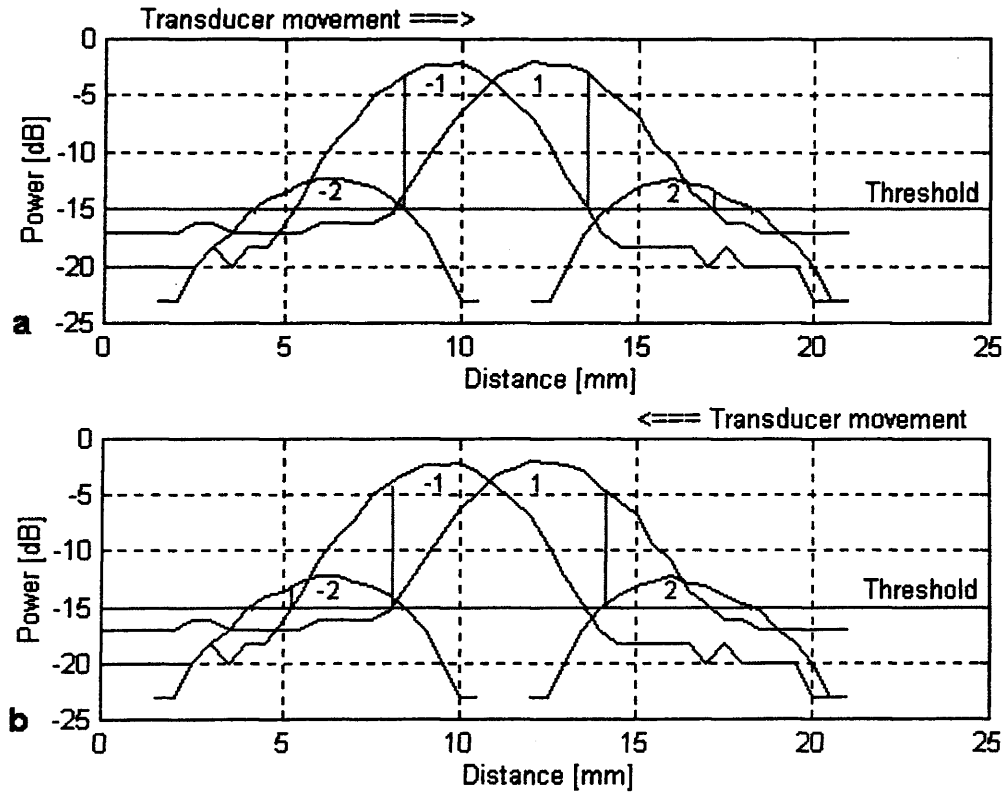

Fig. 8.22 Prediction of the behaviour of the function ***TP*(*d*)** of the Doppler tracking instrument from the results of the **SDS** test. Each diagram presents the cases of the transducer moving from left to right (**a**) and from right to left (**b**). **a)** When the transducer moves from left to right the first steering position is –2. The range of –2 ends inside the –1 range and the vertical line represents the jump from –2 to –1. The same process repeats in the transition from –1 to +1 and +1 to +2. The configuration presented exemplifies a situation of ambiguity: The range of the –2 position ends inside the –1 ranges and also inside the +1 range. This can result in a incorrect change. Such a situation can be corrected either by increasing the threshold level or by decreasing the relative sensitivity of position +1.

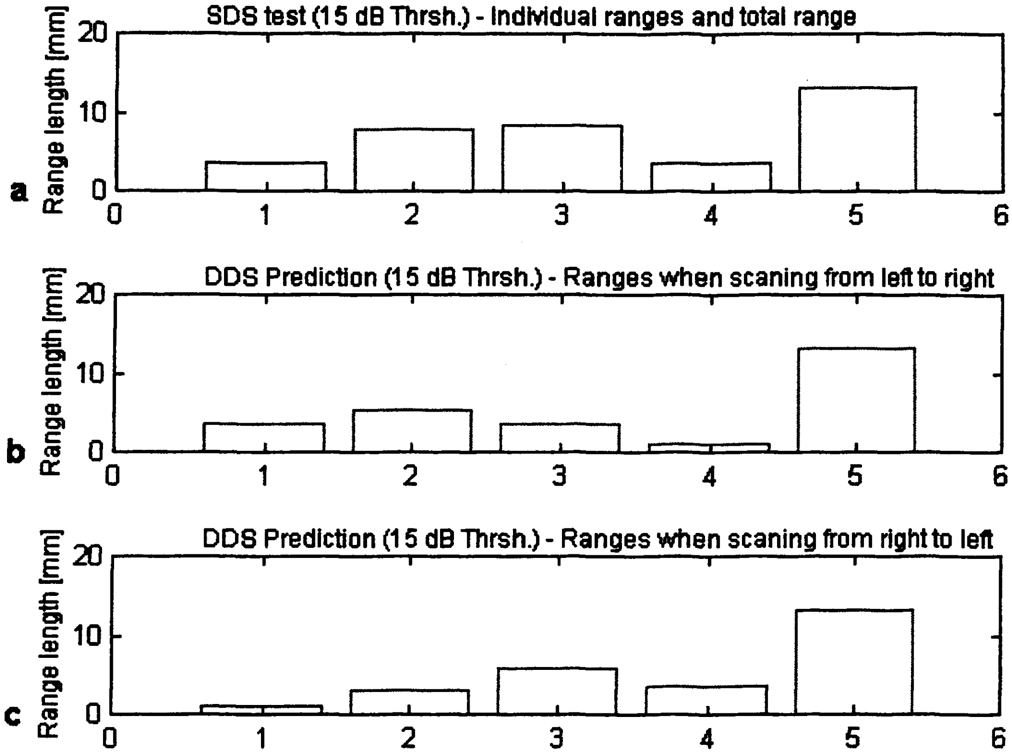

Fig. 8.23 Comparison between static and dynamic ranges assuming a fixed threshold of -15 dB. **a)** Represents the static ranges for the threshold of –15 dB as presented in diagram c of Fig 8.21. **b** and **c)** Represent the dynamic ranges of positions –2 (1), -1 (2), +1 (3), +2 (4). The sum of the four dynamic ranges (5) is exactly the same as the overlapping of the four static ranges as presented in **a** 5. The case of the transducer moving from left to right is represented in **b** and the case of the transducer moving from right to left. Is represented in **c**.

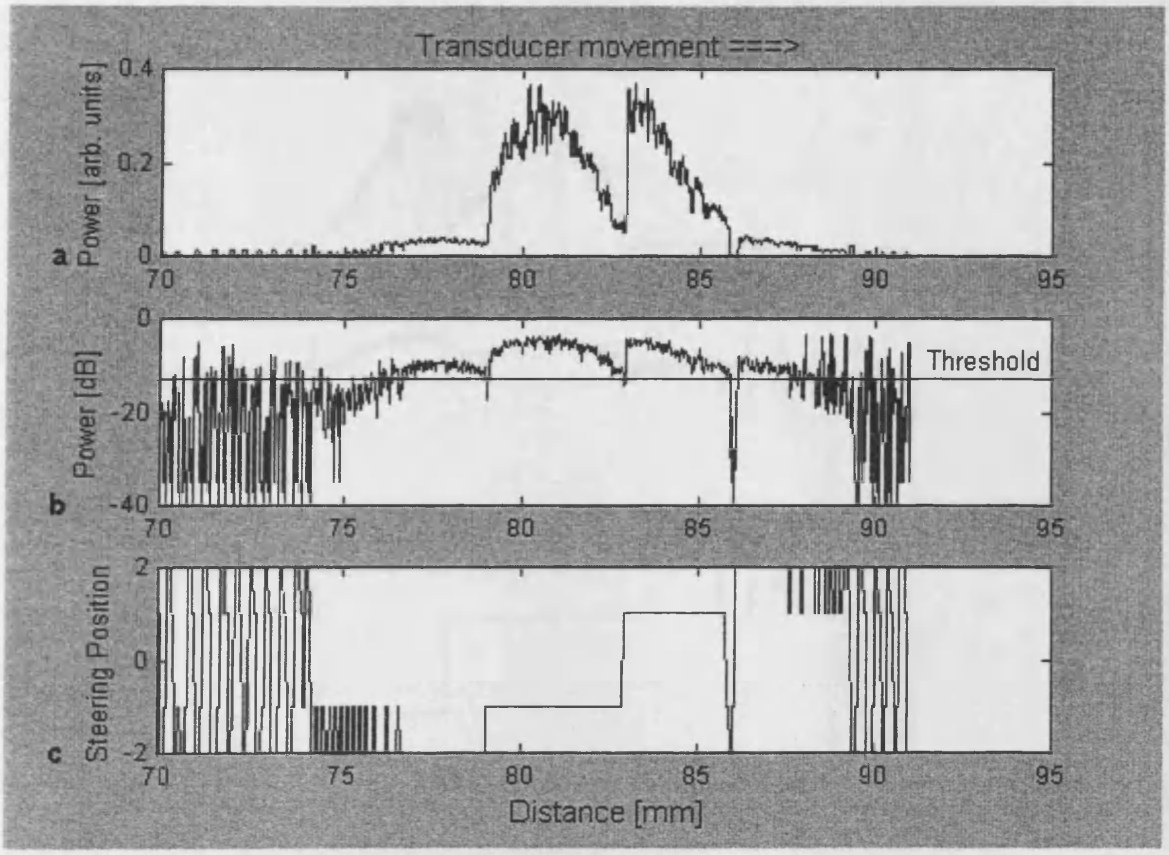

Fig. 8.24 Presentation of the results obtained in the DDS test when the transducer movement was from left to right. The values of total power (***TP***) are presented in **a**. ***TP*** (conditioned and on a dB scale) (***TPcdB***) is presented in **b**, and the steering position ***stp*** presented in **c**. The horizontal scale on all graphs is in mm and represents the same length of 21 mm but it is not precise because the transducer movement was made manually, however diagrams **a**, **b** and **c** in each figure are perfectly synchronised. Diagram **c** shows the erratic hunting movement outside the total range. As soon the vessel is inside the total range the hunting stops and a sharp transition marks the change in steering position to track the moving vessel. The diagram also shows a case of a non smooth transition (+1 to +2) which could be caused by noise or an incorrect threshold.

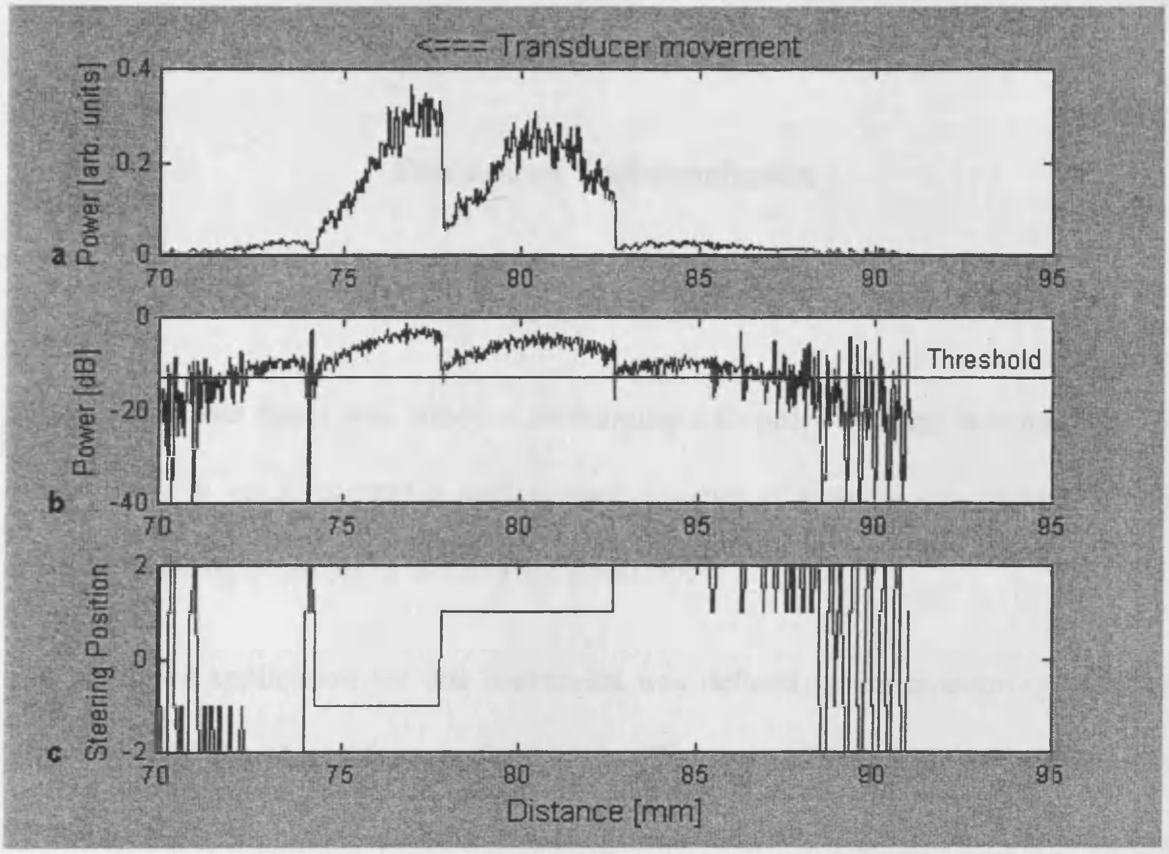

Fig. 8.25 Presentation of the results obtained in the DDS test when the transducer movement was from right to left. The values of total power (***TP***) are plotted in **a**. ***TP*** (conditioned and on a dB scale) (***TPcdB***) is presented in **b,** and the steering position ***stp*** presented in **c**. The horizontal scale on all graphs is in mm and represents the same length of 21 mm but it is not precise because the transducer movement was made manually, however diagrams **a**, **b** and **c** in each figure are perfectly synchronised. Diagram **c** shows the erratic hunting movement outside the total range. As soon the vessel is inside the total range the hunting stops and a sharp transition marks the change in steering position to track the moving vessel. The diagram also shows a case of a non smooth transition (-1 to -2) which could be caused by noise or an incorrect threshold.

Chapter 9

Discussion and conclusion

9.1 Introduction

The work in this thesis was aimed at developing a Doppler tracking instrument to the stage where it could present a performance capable of proving the viability of the Doppler tracking principle in monitoring blood flow.

The proposed application for this instrument was defined as the monitoring of blood flow with CW Doppler in femoro-distal grafts (Thrush and Evans 1990). The reason for focusing on a typical application was that this would provide guide lines for deciding the dimensions and shape of the transducer and also the specification of the electronics.

The instrument can be divided into three parts, the transducer, the electronics (DUPAT), and the feedback loop. Each of these will be discussed in turn.

9.2 Transducer

The work on the transducer was aimed at the development of a small and light device which could eventually be attached to a patient. For this purpose the design and construction of a small phased array transducer was chosen because its of its versatility and potential for miniaturization.

For the proposed application a 1-D array is sufficient, and the construction of a mathematical model of an 1-D array with N elements of width w and pitch d is presented in section 4.2. With such model it was possible to specify the size and dimensions of the array and also to evaluate of the cross talk between elements.

A series of four versions of the transducer were produced. From one version to the next, progressive improvements both in the design and construction techniques were achieved.

The first version basically represented a test of the facilities in the department for producing an array of piezo ceramics. At the same time the strength of the bonding between PCB and ceramics with different conductive bonding materials was also tested.

The second version represented the first effort towards miniaturization. It was a successful attempt in producing a proper CW phased array transducer with air backing and matching layer.

The third version was a CW phased array Doppler transducer. The transmitter and receiver were built together and this required a much more precise construction method. For this transducer however the pitch was still dictated by the limitations of the facilities of the departmental workshop.

The fourth version represented a step forward because of the adoption of dimensions more consistent with the mathematical model. For its construction it was necessary to use the facilities of the industrial sector in two instances: a) to produce the PCBs with dimensions compatible with the element dimensions, b) for making the cuts between elements. This was the transducer showing the best performance but unfortunately it also presented a strong cross-talk between the elements which reduced significantly its performance. The occurrence of such cross-talk which was much stronger than that observed in the previous versions can be explained by the very substantial reduction of the spacing between elements from 0.35 mm to 0.05 mm

Even with the limitations imposed by cross-talk, the fourth version still represents the most advanced stage of transducer development and was the best in terms of performance. Because of that it was the transducer employed in the most recent tests of the equipment reported in this thesis. As can be seen from its potential performance, shown in the section 4.2, a successful correction of cross-talk could increase the sensitivity in the lateral steering positions. This would result in an increase of the signal-to-noise ratio in these positions and also the multiplication of the present maximum range by more than three. There are two immediate options to tackle the problem of mechanical cross-talk. One is to maintain the present dimensions and employ a better material for mechanical isolation between elements. Another is increasing slightly the spacing between elements and at the same time finding the best compromise between element width and pitch. To tackle the problem of electrical cross-talk the first option is the use of connectors and cables more adequate to RF signals, a further option would involve the redesign of the PCB employed in the construction of the transducer.

As far as miniaturization is concerned it can be observed that the active area of the transducer is already very small. The present dimensions of the whole transducer are dictated by the connector and cable sizes. Considering that at the present stage the problem of cross-talk is still to be solved, there is no justification yet for employing expensive cables and connectors. Once the problem of cross-talk is corrected there will be no difficulty in producing a miniature transducer employing cables and connectors adequate for the attachment to the patient.

9.3 The electronics (DUPAT)

As already mentioned in chapter six the present version of the electronics was designed for the purpose of laboratory application and therefore to be as simple as possible. This first prototype of the Doppler Ultrasound Phased Array Transceiver (DUPAT) performed well during the development and testing of the transducer, and also in its role in the Doppler tracking instrument with the flow phantom. In order to test the instrument in a real blood vessel its reception circuits need to be enhanced by increasing the signal-to-noise ratio and sensitivity.

During the tests, a remarkable decrease in the signal-to-noise ratio and in the sensitivity of the Doppler signal was observed at the central (**0**) steering position. This is interpreted as possible saturation of the receiving circuits because of the higher amplitude of the transmitted signal at the **0** steering position. It had no negative effect on the performance of the instrument because it was possible to suppress the **0** position replacing it by the combination of the two neighboring positions **-1** and **+1** without any loss of performance.

It was also observed that the instantaneous change in phase of the driving signals, designed to steer the beam, produces an apparent instantaneous Doppler shift in the received signal. The signal conditioning of the Feed-Back Circuit has to cancel the resultant surge in the detected TP in order to perform the tracking function. This is difficult in real time and some times fails. This artifact will be recorded together with the flow signal when the instrument performs long term monitoring. This problem suggests that a continuous phase shift may be a better alternative.

In conclusion, in order to be able to work with real blood flow signals the present DUPAT version requires further improvement in its reception circuits. It is necessary to improve the signal-to-noise ratio and it is necessary to increase the gain. Making the reception gain variable with the steering position would be useful in compensating for small differences in sensitivity caused by diffraction, projection and cross talk. However it must be pointed out that in the case of strong cross-talk such corrections will have a limited effect. This emphasizes that as far as the range is concerned the role of the electronics is limited by the transducer performance.

9.4 The feedback loop

The present configuration of the feedback loop can be divided in two blocks. The first block is a real time analyzer consisting of a DSP board (DSP32C) fitted in a personal computer. The second block is a programmable logic controller consisting of a data acquisition board with digital output (DT-302) fitted in a second personal computer. The Doppler signal output from the DUPAT is input into the A/D converter of the DSP32C where it is processed in real time by a resident program to extract Intensity Weighted Mean (IMW), and Total Power (TP) signals. At the analog output of the DSP32C these signals are updated 160 times per second and then input into the A/D converter of the data acquisition board (DT-302) in the second computer. The data acquisition and processing is operated by a HP-VEE™ visual program which analyzes the data and commands the beam steering in the DUPAT via the digital output.

This arrangement lacks the portability necessary for clinical use but is convenient for laboratory testing and experimenting with different solutions because it permits accessibility, easy adjustment and control over each stage. It entails, however, some degree of redundancy, unnecessary capacity and a slow response. The velocity response does not represent a serious problem as the frequency content of the TP and IWM signals is low.

In an optimized version of the instrument the feedback loop could be simplified and the functions of real time analysis and digital control performed by in a single DSP board operated by a fast resident program. It would even be possible to load that program into the DSP from a ROM on an auxiliary board thereby dispensing with the use of any computer.

In the present configuration, the extraction of the IWM and TP signals in the first block is performed fast and efficiently by the analyzer. However, in order to obtain information about the alignment from these signals they must undergo further conditioning in the second block. This conditioning is designed to compensate for artifacts in the TP signal: the speckle, the cyclic variation during the cardiac cycle caused by the action of the low pass filters, and the surge caused by the instantaneous transducer phase change. Some fluctuations cannot be completely eliminated because they would also result in the reduction of the sensitivity for variations in TP caused by sudden changes in alignment. Consequently, even after conditioning, the continuous sequence of TP values representing in real time the degree of alignment between transducer and vessel still fluctuates. While the beam and vessel are aligned, the TP value is much higher than the threshold and therefore its fluctuations cause no problems. The tracking routine stays disabled while the TP signal remains above the threshold as this represents a good alignment condition. When the TP signal falls below threshold the tracking routine is triggered. Looking at the diagrams of Figs 8.19 and

8.20 is possible to observe the overlap between the ranges of neighboring steering positions. Such overlap forces the range of one position to finish well inside the range of the neighbors therefore as soon the tracking routine finds the best position the TP signal rises well above the threshold where the fluctuations have no effect. In the present stage of development the Doppler tracking instrument uses four steering positions. The external positions (2 and -2) are more susceptible to TP fluctuations either because their lower sensitivity places the TP signal closer to the threshold or because they are on the borders of the total range. This reaffirms the dependence of the system on the performance of the transducer. The general performance of the instrument would improve by increasing the sensitivity of the lateral steering positions and increasing the number of steering positions. Both can be achieved by decreasing cross-talk.

The tracking routine drives the DUPAT via the digital output of the feedback loop. This routine implements the strategy designed to find the steering position corresponding to the best alignment between beam and vessel. Such a routine must be based on the steering options of the instrument and therefore has been developed according to the number of steering positions available which are presently four. The present tracking routine, based on four steering positions, was conceived to track the vessel with a strategy consisting of two steering movements. The first movement is simply a guess based on the initial position. The second movement is based on the knowledge of the previous position and on the comparison between the TP values before and after the first movement. The vessel tracking can take one or two movements as the routine can be interrupted at any time by the TP rising above the threshold. The strategy was tested successfully in tracking the vessel during a continuous monitoring by moving the transducer within the total range. It was also able to track the vessel by switching on the instrument after placing the transducer in an arbitrary position inside the total range. In most of the tests the routine could track the vessel with one or two steering movements. On some occasions however the first two steps were unsuccessful, in these cases the routine was automatically repeated starting from the previous end position. The reason for the repetition can be interpreted as a consequence of failure in the signal conditioning.

The tracking routine is to some extent limited by the performance of the transducer and electronics, and improvements in these aspects of the system will inevitably lead to an improvement in tracking.

Another important consideration which is independent of any tracking procedure is the signal quality in terms of information about the degree of insonation. A noisy Doppler signal can lead to a high TP regardless of the degree of insonation. Despite the fact that the instrument cannot correct this situation, it can at least identify that this is taking place and trigger an alarm. By observing the degree of difficulty of measuring the period of pulsatile flow from the IWM, the instrument is able to identify noisy signals.

9.5 Future developments

From the previous discussions it is clear that the next development of this project must be to reduce the transducer cross-talk. There are a wide range of options, ranging from laboratory investigation of new materials for mechanical insulation, to the use of cables and connectors more adequate for use with RF signals. A significant reduction in cross-talk will result in a considerably enhanced capture range and stability.

The increase in possible steering positions obtained from the reduction in cross-talk will require the adaptation of the tracking routine in order to make use of these new positions.

To be able to use the instrument for tracking real blood vessel the reception circuits of the DUPAT will require enhancement in the signal-to-noise ratio and in sensitivity. It may be useful to investigate the possibility of employing continuous steering to avoid the surge of TP that is caused by the sudden phase change in the transducer. In this case it would be necessary to change the tracking routine.

It will be necessary to reduce the transducer size and employ special cables in order to use the instrument in long term monitoring. Also for long term monitoring it will be important to measure and adjust the output power of the transducer to ensure it is operating within the current safety levels.

The present progress in electronics, computation and DSP technology offer a wide range of options for refinement of the feedback loop. This is the part of the system which enjoys the best prospects of upgrading in terms of miniaturization, processing speed, and versatility. For practical use with patients a drastic reduction in the size of the feedback loop hardware will be required. Some possible options are discussed in the section 9.4

The use of the instrument for patient monitoring will clearly need to be preceded by a comprehensive series of clinical trials.

9.6 Conclusion

The blood flow to a particular organ or region of the body is of considerable interest because it is directly related with the health and to the physiology of that region or organ. The monitoring of blood flow is crucial in situations were a clinical condition, a medical intervention or a physical activity is likely to interfere with the blood flow to an extent that the biological processes in an individual can be significantly affected. Extended monitoring is necessary when the occurrence of modifications in the blood flow are expected to be either slow, or to be repetitive, or occurring at an uncertain occasion in time.

Doppler ultrasound is a powerful clinical tool because it is a reliable and noninvasive method of measuring blood flow in real time. The development in understanding of the physical processes in the formation of the Doppler signal associated with the recent progress of electronics and computerization has widened the range of information that can be extracted from the Doppler signal. For all these reasons Doppler ultrasound has great potential for monitoring blood flow. There are however difficulties which prevent the establishment of blood flow monitoring as a valuable clinical resource.

Amongst these difficulties the one which appears to be the most important is the difficulty in fixing the transducer to the patient in order to prevent misalignment between ultrasound beam and vessel caused by patient movement. A Doppler tracking instrument which is able to adjust its beam direction automatically to ensure correct alignment between the beam and vessel would be valuable in overcoming this difficulty.

The work developed in this thesis led to the design, construction, and testing of such an instrument. With its operation it was possible to demonstrate the principle of Doppler tracking, which can open a wide area of monitoring to clinical ultrasound.

Presently this equipment is comprised of a number of components, some of which have been adapted from other applications and some of which have been developed from scratch. The development of this instrument was a valuable learning experience in terms of gaining theoretical and practical knowledge of the design, construction and tests of different parts of the equipment, and also the way in which such parts interact with each other and with other apparatus. From the construction point of view, this equipment was useful in identifying some guide lines to be followed in order to turn it into a device which can be used as a clinical tool.

Appendix 1

Safety

A.1 Introduction

The awareness about hazard concerning the interaction between ultrasound and tissues is even older than its application in medicine. For many years it was assumed that ultrasound was more hazardous than x-rays and the bitter experience which led to the reversal of this expectation left diagnostic ultrasound with a label of safe, a reputation which is still supported by the lack of confirmed reports of deleterious effects.

There are however several research papers reporting on potentially hazardous effects, particularly at higher intensities, resulting in an increased concern about the safety of diagnostic ultrasound. This is even more relevant now when the progress of ultrasound in medicine, characterized by the remarkable improvement in the quality of diagnostic information extracted from the patient, is followed by a pressure to increase the energy levels employed because: a) This is a simple method to increase the signal to noise ratio. b) Higher frequencies which improve resolution, also lead to a more rapid attenuation of ultrasound. c) With an expanding range of applications, new situations are appearing which means that patients are exposed to ultrasound irradiation more frequently and for greater time periods. One such example of this trend is the use of long term monitoring of blood flow which the main subject of this thesis.

A.2 Overview

An initial attempt to establish some sort of safety level for the medical use of ultrasound was simply to limit the power output of the transducer to a level assumed safe. An average intensity of $100\ mW/cm^2$ is generally considered a safe limit for long term continuous exposure. For short term exposure much higher intensities are believed to be acceptable. (Evans and McDicken, 2000). This is clearly a crude rule of thumb because it does not take into account the shape and size of the acoustic field, nor the characteristics of the irradiated tissue.

For more refined work it is necessary to incorporate ideas like exposure and dose; in this case the size and shape of the acoustic field are taken into account and attention is paid to the mechanisms of interaction between ultrasound and the different tissues.

To relate exposure and dose to the power output of a transducer, it is important to consider energy deposition along the path of the transmitted beam to the region of interest. In each particular application the anatomy of the irradiated region is of prime concern because different tissues are differently affected by ultrasound, and in addition interfaces can reshape the acoustic field and also create regions of enhanced energy deposition rate.

Finally it is important to take into account the risk factor for each particular case because it is necessary for instance to take into account that the potential risk of irradiating the brain of a premature baby is much higher than the potential risk of irradiating the brain of an adult patient recovering from vascular surgery.

A.3 Estimation of exposure

A method to overcome the difficulty of measuring the acoustic field in the body is by estimation of 'in situ' acoustic exposure in tissue. This method has been accepted since 1980 by the Food and Drug Administration of the USA (FDA) and is based on specifying different correction factors called derating factors φ. Those factors are specified for each different type of clinical application. They are used to convert exposure measurements made in an acoustic tank filled with water to estimated 'in situ' exposures for each particular ultrasound clinical application. Owing to the broad spectrum of applications of ultrasound uses, and the difficulty of modeling the acoustical behavior in the body, this estimation is a rough approximation and expected only to represent on average the worst case.

The calculation of φ is made according to equation (A1), where it is assumed that an attenuation coefficient α [dB cm^{-1} MHz^{-1}] represents the equivalent attenuation coefficient of the irradiated tissue.

$$\varphi = \exp(-0.23\,\alpha f_c x) \qquad (A.1)$$

where 0.23 converts dB to nepers, f_c is the central frequency of the wave and x is the distance in cm in the region of interest from the transducer face. As an example, 0.3 dB cm^{-1} MHz^{-1} is adopted as a typical for the value of α in case of a tissue predominantly composed from soft tissue and fluids (Evans and McDicken, 2000, Haar and Duck 2000). The 'in situ' value for a parameter of the acoustic field, (amplitude or intensity) is calculated by multiplying the parameter measured in water by φ (in case of intensity) or $\varphi^{0.5}$ (in case of amplitude).

A.4 Thermal Index and Mechanical Index

The modern approach to safety in clinical use of ultrasound represents a trend towards making the rigid limits and thresholds based only on the exposure estimation more flexible. The present knowledge of the mechanisms of action of ultrasound in tissues and the ability to control the shape and the focus of the acoustic field enables the implementation in the machines of an active monitoring of the exposure and a continuous estimate of parameters which are believed to be related to the likelihood of producing relevant biological effects. When these parameters exceed certain thresholds the operator is automatically warned. The strength of the biological effects are represented by indices divided in two categories, mechanical indices and thermal indices.

The mechanical effects presently taken into account are those caused by the negative part of the pressure wave which may potentially cause cavitation. These are only relevant in the case of large amplitude pulsed wave (PW) ultrasound and can be neglected in applications employing low amplitude waves. The are represented by the Mechanical Index (***MI***)

$$MI = \frac{P_{-,d}}{\sqrt{f}} \tag{A.2}$$

where $P_{-,d}$ is the derated negative peak pressure and f the frequency of the wave. The maximum mechanical index accepted for all applications is 1.9 except in ophthalmology where it is 0.23.

Thermal effects are common both to PW and continuous waves (CW) and refers to the temperature elevation caused by the ultrasonic irradiation over a certain length of time. The thermal effects are represented by the thermal index (***TI***).

$$\boldsymbol{TI = \frac{W}{W_{DEG}}} \tag{A.3}$$

where $\boldsymbol{W}$ is the acoustic power in the region of interest and $\boldsymbol{W_{DEG}}$ represents the acoustic power necessary to produce an elevation of temperature by 1°C in tissue. In order to represent the wide range of possibilities in terms of different tissues ***TI*** is divided into three subcategories: a) the thermal index for soft tissues ***TIS***, b) the thermal index for soft tissue containing bone ***TIB***, c) the thermal index for the case of tissues containing bone close to the transducer, as it is the case of cranial irradiation, ***TIC***. Each new category can be further divided to represent the several beam geometries, focusing possibilities, and scan regimens. Examples of ***TIS***, ***TIB*** and ***TIC*** are presented below

$$\boldsymbol{TIS(scanned) = \frac{W_1 f_c}{210}} \tag{A.4}$$

$$\boldsymbol{TIS(unscanned) = \frac{W_0 f_c}{210}} \quad (\text{for } A < 1 \text{ cm}^2) \tag{A.5}$$

$$\boldsymbol{TIS\ (unscanned)} = \text{the lower of } \boldsymbol{\frac{W_{0.3} f_c}{210}} \text{ or } \boldsymbol{\frac{I_{0.3} f_c}{210}} \quad (\text{for } A > 1 \text{ cm}^2) \tag{A.6}$$

$$\boldsymbol{TIC(scanned\ /\ unscanned) = 0.025 W_0 \sqrt{\frac{\pi}{4A}}} \tag{A.7}$$

$$\boldsymbol{TIB\ (unscanned)} = \text{ the lower of } \boldsymbol{\frac{\sqrt{W_{0.3} I_{0.3}}}{50}} \text{ or } \boldsymbol{\frac{W_{0.3}}{4.4}} \tag{A.8}$$

where W_0, W_1 and $W_{0.3}$ are the time averaged power output of the transducer in mW/cm ^{2} respectively, measured at the source, emitted from the central 1 cm^2 of the source, and derated (at 0.3 dB cm^{-1} MHz^{-1}) , A is the area of the source in cm^2 and $I_{0.3}$ is the intensity derated (at 0.3 dB cm^{-1} MHz^{-1}). The thermal indices have to be displayed when larger than 0.4 and the maximum value accepted in all applications is 6 except for ophthalmology when it is 1.

These formulae are the results of calculations assuming simple models of the anatomy and taking into account factors like perfusion and bone heating. They are far from exact and should not be taken as absolute.

A.5 Recommendations

Irrespective of the value of any index, the principle of ALARA (As Low As Reasonably Achievable) is a major safeguard to be followed in all cases. A list of recommendations is presented by Evans and McDicken (2000) as a procedure for Doppler examinations which can reduce the total amount of ultrasonic energy delivered to the patient for a factor of up to 1000, they are:

1. Use the lowest transmitted power that will give a result

2. Use the minimum duration of scanning

3. Use the lowest PRF of the pulsed Doppler until that will allow the highest velocity to be measured

4. Use CW rather than PW Doppler if it will give a result

5. Do not leave the Doppler beam irradiating a particular region for longer than necessary. With a duplex system switch back to the imaging mode as soon as the Doppler recording is completed.

Detailed information can be found in the regulation standards (AIUM/NEMA 1992, FDA 510(k), Duck and Henderson 1998, Evans and McDicken, 2000a, Haar and Duck 2000).

Safety considerations and calculations relevant to the Doppler tracking instrument are presented in Section 8.3.2.1.1.

References

AIUM - American Institute of Ultrasound in Medicine (1987), Acoustical data for diagnostic ultrasound equipment.

AIUM/NEMA - American Institute of Ultrasound in Medicine and National Electrical Manufacturers Association (1981). Safety standard for diagnostic ultrasound equipment. Standard publication UL

AIUM/NEMA - American Institute of Ultrasound in Medicine and National Electrical Manufacturers Association (1992). Standard for Real-ime Display of Thermical and Mechanical Acoustic Output Indices on Diagnostic Ultrasound Equipment.

ALDIS G.K. THOMPSON R. S., (1992) Calculation of Doppler spectral power density functions. IEEE Transactions on Biomedical Engineering 39 1022-1031

ANTHONY M. Y., EVANS D. H., LEVENE M. I. (1991) Cyclical variations in cerebral blood flow velocity. Archives of Diseases in Childhood 66 12-16

AUCOTT G. C. (2001) Technical Note on phased-array ultrasound transducer electronics. (In preparation)

BASCOM P. A. J., COBBOLD R. S. C. (1990) Effects of transducer beam geometry and flow velocity profile on the Doppler power spectrum: A theoretical study. Ultrasound in Medicine and Biology 16 279-295

BASCOM P. A. J., COBBOLD R. S. C. (1996) Origin of the Doppler Ultrasound spectrum from blood. IEEE Transactions on Biomedical Engineering 43 562-571

BERLINCOURT D. A., CURAN D. R., JAFFE H. (1964) Piezoelectric and Piezomagnetic Materials - Physical Acoustics Edited by MASON W.P. Academic Press Volume 1A 169-270

BJORN A. J. A., TORP H., HOLM S., KRISTOFFERSEN K., WHITTINGHAM T.A. (1995) Which transducer array is best? European Journal of Ultrasound 2 151-164

BODE H. (1991). Cerebral blood flow velocities during orthostatic and physical exercise. European Journal of Pediatrics. 150 738-743

BRENNAN J. A., THRUSH A. J., EVANS D. H, BELL P. R. F. (1991) Perioperative monitoring of blood flow in femoroinfragenicular vein grafts with Doppler ultrasonography: A preliminary report. Journal of Vascular Surgery 13 468-474

BRENNAN J. A., THRUSH A. J., EVANS D. H, BELL P. R. F. (1992) Intensive blood flow monitoring following femoro-distal bypass: Can early outcome be really predicted? European Journal of Vascular Surgery 6 148-152

COBBOLD R. S. C., VELTINK P. H., JOHNSTON K. W. (1983) Influence of the beam profile and degree of insonation on the CW Doppler ultrasound spectrum and mean velocity. IEEE Transactions on Sonics and Ultrasonics SU 30 364-370

COUGHTREY H., RENNIE J. M., EVANS D. H., (1992) Postnatal evolution of slow variability in cerebral blood flow velocity. Archives of Diseases in Childhood 67 412-415

DAHNOUN N., THRUSH A. J., FOTHERGILL J. C., EVANS D. H. (1990) Portable directional ultrasonic Doppler velocimeter for ambulatory use. Medical & Biological Engineering & Computing 28 474-482

Data Translation Product Handbook 2000, Data Translation Inc.

DIAS A. T., (1962) Curso de Calculo Infinitesimal. Fundacao Gorceix Ouro Preto Brasil

DSP32C PC System Board User Manual Issue 2.02 1991, Loughborough Sound Images Ltd

DUCK F. A., HARTMAN C. L. (1998) Acoustic output of modern ultrasonic equipment is increasing ? Safety of Diagnostic Ultrasound. Edited by Barnett S. B. and Kossoff G., Parteneon Publishing |Group, New York 15-26

DUCK F., MARTIN K. (1993) Exposure values for medical devices. - Ultrasonic exposimetry. Edited by ZISKIN M. C. and LEWIN P. A. CRC Press, Boca Raton Chapter 11

EVANS D. H., McDICKEN W. N. (2000a) Doppler Ultrasound: Physics, Instrumentation and Signal Processing. John Wiley & Sons Chichester Chapters 4, 10, 13, 14.

EVANS D. H., McDICKEN W. N. (2000b) Doppler Ultrasound: physics, instrumentation and signal processing. John Wiley & Sons Chichester Chapter 12 Section 12.2.4.

EVANS D. H., McDICKEN W. N., SKIDMORE R., WOODCOCK J. P. (1989a) Doppler Ultrasound: Physics, Instrumentation and Clinical Applications John Wiley & Sons Chapters 14 and 15

EVANS D. H., McDICKEN W. N., SKIDMORE R., WOODCOCK J. P. (1989b) Doppler Ultrasound: Physics, Instrumentation and Clinical Applications John Wiley & Sons Chapter 13

EVANS D. H., McDICKEN W. N., SKIDMORE R., WOODCOCK J. P. (1989c) Doppler Ultrasound: Physics, Instrumentation and Clinical Applications John Wiley & Sons Chapter 8 and 9

EVANS D. H., McDICKEN W. N., SKIDMORE R., WOODCOCK J. P. (1989d) Doppler Ultrasound: Physics, Instrumentation and Clinical Applications John Wiley & Sons Chapter 2

EVANS D. H., SCHLINDWEIN F. S., LEVENE M. I. (1989e) Automatic system for capturing and processing ultrasonic Doppler signals and blood pressure signals. Clinical Physics and Physiological Measurement 10 241-251

EVANS D.H. (1982) Some aspects of the relationship between instantaneous volumetric blood flow and continuous wave Doppler ultrasound recordings–I. Ultrasound in Medicine and Biology 8 605-609

EVANS D.H., PARTON L. (1981) The directional characteristics of some ultrasonic Doppler blood flow probes. Ultrasound in Medicine and Biology 7 51-62

FAN L., EVANS D.H. (1994a) A real-time and fine resolution analyzer used to estimate the instantaneous energy distribution of Doppler signals. Ultrasound in Medicine and Biology 20 445-454

FAN L., EVANS D.H. (1994b) Extracting instantaneous mean frequency information from Doppler signals using the Wigner distribution function. Ultrasound in Medicine and Biology 20 429-443

FDA 1993, Revised 510(k) Diagnostic Ultrasound Guidance for 1993

FENSTER A., DOWNEY (1996) 3-D ultrasound imaging: A review. IEEE Engineering in Medicine and Biology 15 41-51

FENTON A. C., EVANS D.H., LEVENE M. I. (1990) On line cerebral blood flow velocity and blood pressure measurement in neonates: a new method. Archives of Diseases in Childhood 65 11-14

FEYNMAN R.P., LEIGHTON R. B., SANDS M., (1963). The Feynman Lectures on physics. Addison-Wesley Publishing Company Vol. I Chapters 47-51

FRANKLIN D. L., SCHLEGEL W., RUSHMER R. F. (1961). Blood flow measured by Doppler frequency shift of backscattered ultrasound. Science 134 564-565

FRANKLIN D. L., SCHLEGEL W., WATSON N. W., (1963). Ultrasonic Doppler shift blood flowmeter: circuitry and practical applications. Biomedical Sciences Instrumentation. 1 309-311

GIBBONS D. T., EVANS D. H., BARRIE W. W., COSGRIFF P. S. (1981) Real time calculation of ultrasonic pulsatility index. Medical & Biological Engineering & Computing 19 28-24

GILL R. W., (1985) Measurement of blood flow by ultrasound: accuracy and sources of error. Ultrasound in Medicine and Biology 11 625-641

GREISEN G., JOHANSEN K., ELLISON P. H.,FREDERIKSEN P. S., MALI J., FRIIS-HANSEN B. (1984) Cerebral blood flow in the infant: Comparison of Doppler ultrasound and ^{133}xenon clearance. Journal of Pediatrics 104 411-418

HAAR G. ter, DUCK F. A. (2000) The Safe Use of Ultrasound in Medical Diagnosis. The British Medical Ultrasound Society / The British Institute of Radiology

HENNERICI M. G., MEAIRS S. P. (1999). Cerebrovascular ultrasound. Current Opinions in Neurology. 12 57-63

HOLESTROM-WESTAS L., BELL A. H., SKOV L.,GREISEN G., SVENNINGSEN N. W. (1992) Cerebroelectrical depression following surfactant treatment in preterm neonates. Pediatrics 89 643-647

HOSKINS P. R. (1991b) An investigation of simulated umbilical artery Doppler waveforms. II. A comparison of three Doppler waveform quality indices. Ultrasound in Medicine and Biology 17 23-30

HOSKINS P. R., LOUPAS T., McDICKEN (1990) A comparison of three different filters for speckle reduction of Doppler spectra. Ultrasound in Medicine and Biology 16 375-389

HOSKINS P. R., LOUPAS T., McDICKEN (1991a) An investigation of simulated umbilical artery Doppler waveforms. I. The effect of three physical parameters on the maximum frequency envelope and pulsatility index. Ultrasound in Medicine and Biology 17 7-21

HUETER T. F., BOLT R. H. (1955). Sonics. John Wiley & Sons New York

HUSSEY M. (1975) Diagnostic Ultrasound. Backie London

IEC - International Electrotechnical Commission, (1991a) Measurement and characterization of ultrasonic fields using hydrophones in the frequency range 0.5 MHz to 15 MHz. Publication 1102.

IEC - International Electrotechnical Commission, (1991b) The absolute calibration of hydrophones using the planar scanning technique in the frequency range 0.5 MHz to 15 MHz. Publication 1101.

IEC - International Electrotechnical Commission, (1991c) The characteristics and calibration of hydrophones for operating in the frequency range 0.5 MHz to 15 MHz. Publication 866.

KINO G. S., DeSILETS C. S. (1979) Design of slotted transducer arrays with matched backings. Ultrasonic Imaging 1 189-209

KINSLER L. E., FREY P. (1962). Fundamentals of Acoustics. John Wiley & Sons New York

KOFKE W. A. (1999) chapter 14 -Transcranial Doppler ultrasonography in anesthesia. in Transcranial Doppler ultrasonography 2nd Ed. Edited by :BABIKIAN V. K., WESHLER L. R. Butterworth Heineman

KOSSOF G. The effects of backing and matching on the performance of piezoelectric ceramic transducers, IEEE Transactions on Sonics and Ultrasonics SU-13 1966 20-31.

KRIMHOLTZ R., LEEDON D. A., MATHAEI G. L. (1970) New equivalent circuits for elementary piezoelectric transducers. Electronics Letters 6 398-399

LANDINI L., SANTARELLI F., POMATA F.,VERRAZZANI L. (1991) Dynamically variable electronic delays for ultrasound imaging. Journal of Biomedical Engineering 13 469-472.

LARSEN F. S., OLSEN K. S., HANSEN B. A., PAULSON O. B., KNUDSEN G. M. (1994) Transcranial Doppler is valid for determination of the lower limit of cerebral blood flow autoregulation. Stroke 25 1985-1988

LARSON J. D. III (1983) An acoustic transducer array for medical imaging - Part I. Hewlett Packard Journal 10 17-22

LOCKWOOD G. R., TURNBULL D. H., CHRISTOPHER D. A., FOSTER F. S. (1996) Beyond the 30 MHz. IEEE Engineering in Medicine and Biology, 15 60 71

LUNT M. J. (1975) Accuracy and limitations of the ultrasonic Doppler velocimeter and zero crossing detector. Ultrasound in Medicine and Biology 2 1-10

LYNN P. (1989) An introduction to the analysis and processing of signals MacMillan Press Ltd chapter 5 section 5.3

MASON W. P. (1948) Electromechanical transducers and wave filters. 2nd Edition Van Nostrand Co. Inc. New Jersey

MATLAB Reference Manual (1995) The Math Works Inc. Prentice Hall

McDonald D. A. (1974) Blood flow in arteries. Edward Arnold, London Chapter 5.

McLEOD F. D. (1967). A directional Doppler flowmeter. Digest 7th International Conference of Medical & Biological Engineering. 213

MICHEL E., ZERNIKOV B., RABE H., JORCH G. (1993). Adaptive multipurpose probe fixation device for use on newborns. Ultrasound in Medicine and Biology 19 581-586

MILLER D. G. (1983) An acoustic transducer array for medical imaging - Part II. Hewlett Packard Journal 10 22-26

MO L. Y. L., COBBOLD R. S. C. (1986) "Speckle" in continuous wave Doppler ultrasound spectra: A simulation study. IEEE Transactions on Ultrasonics, Ferroelectrics, and Frequency Control UFFC33 747-753

MO L. Y. L., COBBOLD R. S. C. (1992) A unified approach to modeling the backscattered Doppler ultrasound from blood. IEEE Transactions on Biomedical Engineering 39 450-461

MORSE P. M., INGARD K. U. (1968) Theoretical Acoustics. McGraw Hill, New York

MOULSON A. J., HERBERT J. M. (1990) Electroceramics. Chapman and Hall, Cambridge.

NCRP - National Council on Radiation Protection and Measurement (1983). Biological Effects of Ultrasound: Mechanisms and Clinical Implications. Report No 74

NCRP - National Council on Radiation Protection and Measurement (1992). Exposure criteria for medical diagnostic ultrasound I. criteria based on thermal mechanisms. Report No 113

NEWHOUSE V. L. , FURGASON E. S., JOHNSON G. F., WOLF D. A. (1980) The dependence of ultrasound Doppler bandwidth on beam geometry. IEEE Transactions on Sonics and Ultrasonics SU 27 50-59

POWERS J. E., PHILLIPS D. J., BRANDESTINI M. A., SIGELMANN R. A., (1980) Ultrasound phased array delay lines based on quadrature sampling techniques. IEEE Transactions on Sonics and Ultrasonics SU 27 287-294

PRYTHERCH D. R., EVANS D. H. (1985) Versatile microcomputer-based system for the capture storage and processing of spectrum analyzed Doppler ultrasound blood flow signals. Medical & Biological Engineering & Computing. 23 445-452

RABE H., GROHS B., BRESSER B. W., JORCH G., (1990) Die kontinuieriche Dopplersonographie: Ein newe Methode Uberwashung der zerebralen Zirkulation des sehr kleinen Fruhgeborenen. Kliniche Pediatrie 202 383-386

RAMNARINE K. V., NASSIRI D. K., HOSKINS P. R., LUBBERS J. (1998) Validation of a new blood-mimicking fluid for use in Doppler flow test objects. Ultrasound in Medicine and Biology 24 451-459

SAINI V. D., MAULIK M., NANDA N. C., ROSENZWEIG M. S. (1983) Computerized evaluation of blood flow measurement indices using Doppler ultrasound. Ultrasound in Medicine and Biology 9 657-600

SALIBA E., CHANTEPIE A., AUTRET E., GOLD F., POURCELOT L., LAIGIER J. (1991a). Effects of indomethacin on cerebral hemodynamics at rest and during endotracheal suctioning in preterm neonates. Acta Pediatrica Scandinavica. 80 611-615

SALIBA E., CHANTEPIE A., GOLD F., MARCHAND M., POURCELOT L., LAIGIER J. (1991b). Intraopertive measurements of cerebral hemodynamics during ductus arteriosus ligation in preterm infants. European Journal of Pediatrics. 150 362-365

SATOMURA S. (1959). Study of the flow patterns in peripheral arteries by ultrasonics. Journal of the Acoustical Society of Japan 15 151-158

SAYERS C. M., TAIT C. E. (1984) Ultrasonic properties of transducer backings. Ultrasonics 22 57-70.

SCHLINDWEIN F. S., SMITH M. J., EVANS D. H. (1988) Spectral analysis of Doppler signals and computation of the normalized first moment in real time using a digital signal processor. Medical & Biological Engineering & Computing 26 228-232

SCHLINDWEIN F. S., EVANS D. H. (1989) A real time autoregressive spectrum analyzer for Doppler ultrasound signals. Ultrasound in Medicine and Biology 15 263-272

SHUNG K. K., SIGELMANN R. A., REID J. M. (1976) Scattering of ultrasound by blood. IEEE Transactions on Biomedical Engineering BME 23 460-467.

SILK M. G. (1984) Ultrasonic transducers for non destructive testing. Adam Hilger Ltd, Bristol

STEPANISHEN P. R. (1981) Pulsed transmit/receive response of ultrasonic piezoelectric transducers. Journal of the Acoustical Society of America 69 1815-1827

THOMPSON R. S., ALDIS G.K. (1996) Effect of a cylindrical refracting interface on ultrasound intensity and the CW Doppler spectrum. IEEE Transactions on Biomedical Engineering 43 451-459

THOMPSON R. S., ALDIS G.K., LINNETT I. W.(1990) Doppler ultrasound spectral power density distribution: measurement artifacts in steady flow. Medical & Biological Engineering & Computing 28 60-66

THRUSH A. J., EVANS D. H. (1990) Simple system for automatic intermittent recording of blood flow in femoro-distal bypass grafts using Doppler ultrasound. Medical & Biological Engineering & Computing. 28 193-195

VON RAMM O. T., SMITH S. W (1983) Beam steering with linear arrays. IEEE Transactions on Biomedical Engineering 30 438-452.

WELLS P. N. T. (1969). A range gated ultrasonic Doppler system. Medical & Biological Engineering. 7 641-652

WELLS P. N. T. (1977). Biomedical ultrasonics. Academic Press, London.

WHITTINGHAM T. A. (1981) Real time Ultrasonic Scanning - Physical Aspects of Medical Imaging. Edited by Moores B. M, Parker R. P., Pullan B. R. John Wiley and Sons. 153-165.

WHITTINGHAM T. A. (1991) Resolution and information limitations from transducer arrays. Physics in Medicine and Biology 36 1503-1514.

WHITTINGHAM T. A. (1995) Modern developments in diagnostic ultrasound - I Transducer and signal processing developments. Radiography 1 61-73

WHITTINGHAM T. A. (1996) Modern developments in diagnostic ultrasound - II High frequencies, new types of image and safety. Radiography 2 311-325

WHITTINGHAM T.A. (1997) New and future developments in ultrasonic imaging. The British Journal of Radiology 70 S119-S132

WOJCIK G., DeSILETS C., NIKODYM L.,VAUGHAN D.,ABBOUD N., MOULD J. Jr. (1996) Computer modeling of diced matching layers. IEEE Ultrasonics Symposium 1503-1508

WU S. J., SHUNG K. K., (1996) Cyclic variation of Doppler power from whole blood under pulsatile flow. Ultrasound in Medicine and Biology 22 883-894

ZISKIN M. C., LEWIN P.A. (1993) Ultrasonic exposimetry. CRC Press, Boca Raton